Optimization of Radiation Sensors
for a
Passive Terahertz Video Camera
for
Security Applications

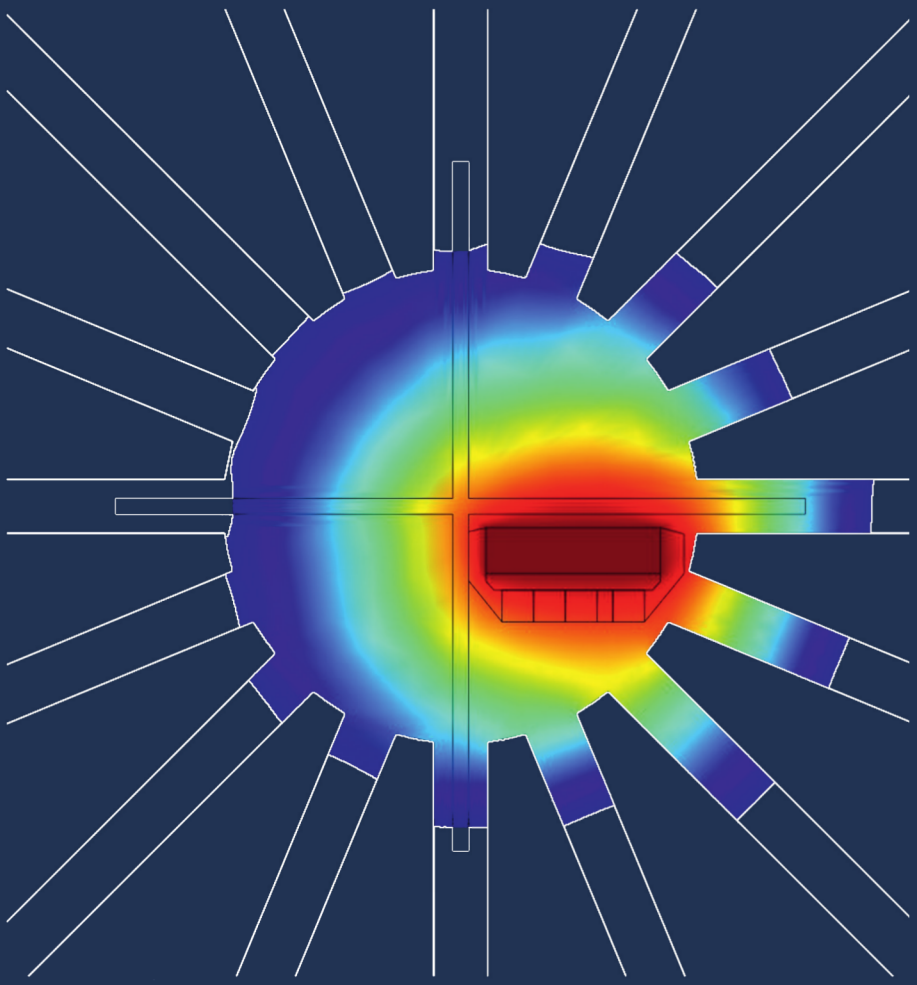

Gabriel Zieger

OPTIMIZATION OF RADIATION SENSORS FOR A PASSIVE TERAHERTZ VIDEO CAMERA FOR SECURITY APPLICATIONS

Gabriel Zieger

PhD Committee

Chairman/Secretary:		
	dean	University of Twente
Supervisor:		
	Prof. Dr. H. Rogalla	University of Twente
Assistant supervisor:		
	Prof. Dr. H.-G. Meyer	IPHT Jena, Germany
Members:		
	Prof. Dr. H. Hilgenkamp	University of Twente
	Prof. Dr. M. ter Brake	University of Twente
	Prof. Dr. H.-W. Hübers	German Aerospace Center (DLR), Germany
	Dr. E. Kreysa	Max Planck Institute for Radio Astronomy, Germany

Front cover: Thermal gradient on the Si_3N_4 platform of a 1A TES determined from FEM simulations (see figure 8.6 for details).

Back cover: Single frame of a THz video of a person hiding several objects (see figure 7.10 for details).

The work described in this thesis was performed at the Leibniz Institute of Photonic Technology (IPHT) in Jena, Germany in collaboration with the Low Temperature Division at the University of Twente, Netherlands.

G. Zieger
"Optimization of Radiation Sensors for a Passive Terahertz Video Camera for Security Applications"

PhD Thesis, University of Twente, Enschede, The Netherlands.
Printed by Ipskamp Drukkers B.V. Enschede, The Netherlands.

ISBN: 978-94-6259-293-3

OPTIMIZATION OF RADIATION SENSORS FOR A PASSIVE TERAHERTZ VIDEO CAMERA FOR SECURITY APPLICATIONS

DISSERTATION

to obtain
the degree of doctor at the University of Twente,
on the authority of the rector magnificus,
prof. dr. H. Brinksma,
on account of the decision of the graduation committee,
to be publicly defended
on Thursday September 4^{th}, 2014 at 12.45

by

Gabriel Zieger

born on october 24^{th}, 1980
in Stuttgart, Germany

This dissertation has been approved by:

Prof. Dr. H. Rogalla (promotor)
Prof. Dr. H.-G. Meyer (assistant promotor)

Contents

1 Introduction

1.1 Motivation and overview

Big events and mass transportation have become inherent parts of our everyday life. While this entails many security implications, ideally, they are handled flawlessly and unnoticed. However, incidents in the last years have revealed vulnerabilities concerning mass security screenings: They can neither efficiently handle the amount of people to be screened nor detect most of the possible threats. Concerning transportation, an increased demand for comprehensive security checks combined with growing numbers of travelers lead to the necessity of faster controls with additional detection capabilities at the same time. In general, mass security controls suffer from a fundamental conflict between speed and precision. Any false negative like a missed dangerous object can be extremely threatening and should therefore be avoided[1]. Thus, methods usually tend to prefer false positives which lead, as a consequence, to additional individual personal screenings, so called "pat downs", or even strip searches. The fact that the common security screening with metal detectors only detects metallic objects is a severe limitation and actually implies pat downs for every screened person. Newer technologies try to address the problem of limited detection capabilities by using X-rays or microwaves which allow to detect a wide variation of materials[2]. However, X-ray exposure of humans for non-medical purposes is considered critical by many people and even illegal e.g. in Germany[3]. The European Union explicitly banned X-ray body scanners[4].

In addition, X-ray backscattering as well as microwave scanners unavoidably produce nude images due to their active illumination of the human body[5]. A common and in most cases compulsory way to protect privacy is an automatic analysis of the image with a resulting transformation to an abstract representation with markers showing possible threat locations. Since 2013, this is mandatory in the USA[6]. However, this additional intermediate processing step increases the risk of detection errors, which usually is trimmed to false positives due to the aforementioned reasons. The implied additional "pat downs" made necessary by this again cause a severe reduction in throughput, which usually is acceptable only up to a certain level[7]. Furthermore, all of these technologies still rely on a portal, which acts as an unflexible bottleneck and limits the stream of people. To achieve an acceptable throughput and limit the effects on convenience and the protection of the private sphere, a common, but dissatisfactory compromise is to apply pat downs only on randomly chosen persons.

Because of these reasons, future security controls have to improve in speed, flexibility, detection capability and convenience at the same time. An ideal technology would

therefore detect simultaneously any threat in any location in real-time without violating the private sphere in any way, ideally even without any noticeable interaction with the scanned person. The concept of a passive terahertz video camera, which is described in chapter 1.3, promises to come closer to this ideal.

Like X-ray and microwave systems, it allows to detect and locate different materials, like metals, ceramics, glass and explosives[8]. In addition, a terahertz video camera has several advantages over X-Ray and microwave systems. First, it avoids any kind of irradiation and thus legal restrictions or social conflicts. For the same reason, this technology does at no point produce pictures with an impression of nudity. This fact strongly adds to the applicability, because there is no general need for obscuring software like in other technologies[9] which reduces the detectability and increases the complexity of the system. The fact that there is no binding to a radiation source except the examined person itself uncouples the system location and the controlling area. This opens up the possibility to flexibly scan at variable locations within short time using adapted optical systems. No additional bottleneck as a portal is necessary.

Sufficient resolution from distances of several meters are possible (see section 1.2), facilitating a real camera. Therefore, it is able to follow movements in real-time without touching, irradiating or virtually undressing people. At high frame rates, this would allow for speeding up security checks. Also applications needing a secure distance become possible.

Thus, passive terahertz detection is an upcoming challenge for security applications. This requires highly sensitive detection of small radiation differences under a significantly higher background load, as shown in section 1.3.

Astronomical exploration systems have shown that it is possible to use transition edge sensors (TES) to passively detect terahertz radiation with high sensitivity[10]. However, sampling of frames with several thousand pixels, as needed for a security camera, is always a compromise between integration time and array size. Compared to the very expensive astronomical tools looking at nearly static objects, the requirements of speed are severely stressed for security purposes while complexity and production cost play an important role for realistic application scenarios.

These special requirements are analyzed in this thesis with respect to practical applicability, production costs and long term stability, focusing on the resulting demands concerning the sensors. In detail, general properties of voltage biased TES in bolometric mode are discussed based on a common lumped model to define the necessary steps to adjust them to fulfill these requirements (see chapter 2). Starting from the TES design used in a single pixel demonstrator, optimization steps concerning reproducibility and long term stability are presented and discussed in chapter 3. Based on a detailed analysis of the characteristic properties of the initial design in comparison to the theoretical predictions in chapter 4, a computer simulation model was created that allows to reproduce the behavior of the TES and to analyze deviations from the lumped model in chapter 5. In the following, it was used to improve the sensor time constants (chapter 6). This allowed to reduce the time constants of the sensor compared to the reference design by

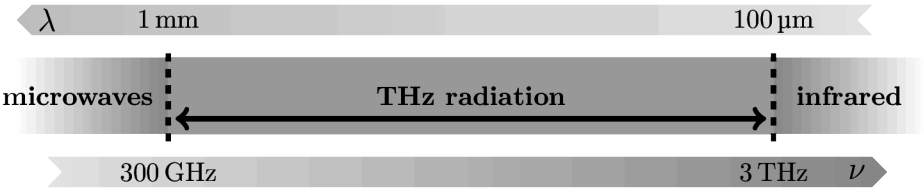

Figure 1.1: Definition of the THz band in the electromagnetic spectrum.

a factor of approx. four at nearly the same noise level. Also the radiation coupling efficiency could be maintained by optimizing the sensor integration setup. Their applicability could be shown in a demonstrator system presented in section 6.5 that was capable to visualize hidden objects of different materials at frame rates up to 10 Hz with a sensor array consisting of 20 TES.

The analysis and reduction of interference effects of the TES with the readout electronics are presented and discussed in section 7. The enhanced stability could be demonstrated in an advanced camera system containing 64 TES. In section 7.4 results of real time imaging at 25 frames per second are presented. They demonstrate that the time constants of the sensors are low enough to achieve a spatial resolution close to the theoretical diffraction limit while their improved stability allows for undistorted video streams without sensor outages. Hence, no redundant sensors (including the corresponding readout components) are necessary, which reduces the production cost of such a system.

Finally, an advanced design that combines the previously ascertained improvements is presented and discussed in chapter 8. It promises faster sensors with an extended stable working range and hence further enhancements for future camera systems.

1.2 Choice of the optical frequency range

Terahertz (THz) radiation is a rather newly defined electromagnetic band. It is settled in between microwaves and infrared, filling a (former) technical gap between electrical and optical technologies. Because of this technically induced definition and the advancing technical development, different definitions of the borders of this band can be found (for example in [11] and [12]). However, a quite common definition of the lower end of the THz band is derived from the upper limit of the EHF radio band, which is the upper range of the microwave band, at a frequency of $\nu_{opt} = 300\,\mathrm{GHz}$[1]. As an upper limit, oftentimes 3 THz can be found. This corresponds to wavelengths[2] λ of 1 mm to 100 µm (see figure 1.1). Thus, this range is also called submillimeter band. In this thesis, the

[1] In this thesis, the subscripts 'opt' and 'el' will be used to denote properties of electromagnetic radiation and and electrical signals, respectively.

[2] Wavelengths refer to vacuum and in good approximation to air as the optical medium.

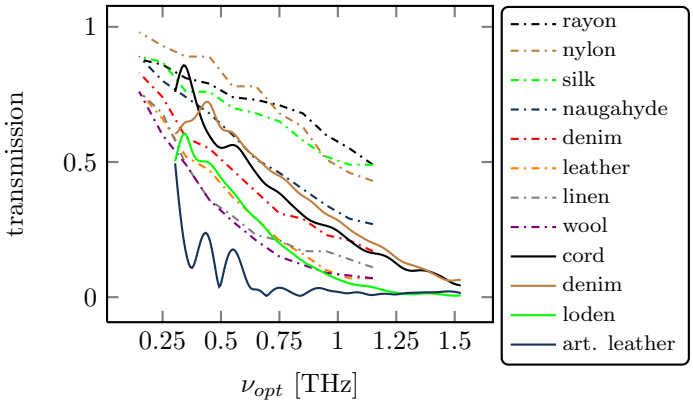

Figure 1.2: Transmission through different materials used to produce clothing for typical thicknesses. In the shown range, transmission decreases strongly with rising radiation frequency. The data are taken from [15] (dash-dotted lines) and measured at IPHT (solid lines).

terms "THz" and "THz band" will be used as synonyms for the range from 300 GHz to 3 THz, which corresponds to the ITU frequency band number 12, as defined in [13].

As for microwaves, a lot of dielectric materials show high transmission for THz radiation, especially many materials used to produce clothing[14][15][16]. However, this effect which is essential for security controls reduces with increasing frequency (see figure 1.2).

These low frequencies compared to the visible light range and the corresponding large wavelengths of up to one millimeter let diffraction become significant for stand-off applications. As spatial resolution is one of the key parameters of a camera system, its dependency on the chosen frequency has to be taken into account as part of specifying the system parameters of a THz camera.

Spatial resolution can be defined as the minimum distance r_{min} of two objects that still can be separated. According to the Rayleigh criterion, two objects are just resolved when the distance of the maxima of their diffraction patterns is as large as the distance of the first minimum to the maximum, the so called airy disc radius r_{airy}.

For a circular aperture with the diameter d_{AP},

$$r_{airy} = 1.22 \cdot \frac{d_{obj} \cdot \lambda}{d_{AP}} = 1.22 \cdot \frac{d_{obj}}{d_{AP} \cdot \frac{c}{\nu_{opt}}} \tag{1.1}$$

if d_{obj} is the distance to the object and c the speed of light in vacuum. According to this, resolution improves with rising frequency. As figure 1.3 shows, with an aperture of half a meter, microwave based full body scanners working at 35 GHz or at 94 GHz[17][18], are limited to distances of 1 m and 2.6 m, respectively, to still achieve a spatial resolution of 2 cm. A camera system working at THz frequencies above 300 GHz can achieve the same

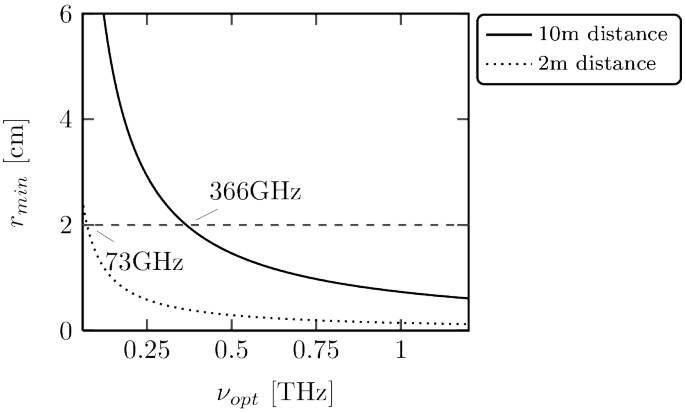

Figure 1.3: Diffraction limited spatial resolution using an aperture of 0.5 m. The dependency on frequency is shown for different distances of the object. While a resolution of 2 cm is achievable for frequencies above 73 GHz at a distance of 2 m, at least 366 GHz are necessary if the object is 10 m away.

resolution from at least 8 m distance, e.g. 350 GHz would allow for about 10 m.

Terahertz radiation is strongly absorbed in water[19]. Accordingly, the human bodies thermal emission can be approximated as a blackbody of approx. 310 K. Corresponding to Planck's law (equation 1.2), a blackbody emits incoherent continuous radiation.

The power P_{bb} emitted by a blackbody at the absolute temperature T from an area A and the frequency interval $\left[\nu_{opt} - \frac{\Delta\nu_{opt}}{2}, \nu_{opt} + \frac{\Delta\nu_{opt}}{2}\right]$ is given by

$$P_{bb}(T) = \int_A \int_{\nu_{opt}} M_{e\nu}(T) dA \; d\nu_{opt} = \int_A \int_{\nu_{opt}} \frac{2\pi h \nu_{opt}^3}{c^2} \frac{1}{e^{\frac{h\nu_{opt}}{k_B T}} - 1} dA \; d\nu_{opt} \tag{1.2}$$

$$[M_{e\nu}] = \frac{W}{m^2 \cdot Hz} \tag{1.3}$$

With h being the Planck constant, k_B the Boltzmann constant, T the absolute temperature in Kelvin, ν_{opt} the center frequency, $\Delta\nu_{opt}$ the bandwidth and $M_{e\nu}$ being the spectral radiant emittance. In case of an emitting area A at constant temperature, the surface integral simply results in a constant factor A. If $M_{e\nu}$ in good approximation is a linear function within the optical bandwidth $\Delta\nu_{opt}$, the expression for $P_{bb}(T)$ can be simplified to

$$P_{bb}(T) = \frac{2\pi h \nu_{opt}^3}{c^2} \frac{1}{e^{\frac{h\nu_{opt}}{k_B T}} - 1} \cdot A \cdot \Delta\nu_{opt} \tag{1.4}$$

A real object will always emit less than a blackbody, though it can be very close to it. Therefore, a more general model of an object emitting thermal radiation is the graybody. Its emitted power at temperature T

$$P_{gb}(T) = \epsilon \cdot P_{bb}(T) \tag{1.5}$$

$$0 \leq \epsilon < 1 \tag{1.6}$$

is the blackbody radiation power for the same temperature scaled by the emissivity ϵ of the object. In the THz band, the reflectivity of the skin decreases with increasing frequency[20]. At 350 GHz, a remaining value of $r_{skin} \approx 18\,\%$ for normal incidence was found by[16].

Figure 1.4 compares the spectral radiant emittance of a the human body to the one of the surrounding at an assumed temperature of 295 K. For the human body, a temperature of 310 K is assumed and the emission is calculated as

$$M_{e\nu}^{body} = 0.82 \cdot M_{e\nu}(310\,\mathrm{K}) + 0.18 \cdot M_{e\nu}(295\,\mathrm{K}) \tag{1.7}$$

As can be seen, total power as well as the signal difference to room temperature background increase with rising frequency (figure 1.4 C and D).

As THz radiation strongly interacts with different oscillation modes of water molecules, also water vapor[21] and therefore air shows significant absorption. This becomes relevant for stand-off detection from distances of several meters. Figure 1.5 shows the transmittance of air at 295 K, 1013 mbar and 30 % relative humidity. In the considered range, in principle, the transmittance declines with increasing frequency. However, there are certain regions (atmospheric windows), in which the transmission is significantly higher compared to their surrounding frequency ranges. These atmospheric windows are preferable working points for systems with object distances of several meters.

Combining these properties, a compromise is necessary to define the wavelength of choice for a THz security camera. It is mandatory to pick one of the atmospheric windows, and stay below 0.5 THz to achieve good transmission through most types of clothing. This thesis focuses on sensors for the 345 GHz window (see figure 1.5), corresponding to a wavelength of 870 µm, where a spatial resolution of 2 cm still can be achieved with an aperture of 0.5 m diameter from 10 m distance and the emittance of the human body is still high. However, the sensors described in this thesis can be easily adapted to different frequencies in the THz band, and the discussed optimizations are in principle independent of the chosen frequency.

1.3 Concept and requirements of a THz Camera

A THz security camera setting consists of mainly three components: The first is the object space which in general can be separated into the screened person, objects in between the person and the camera and the background, which includes everything else

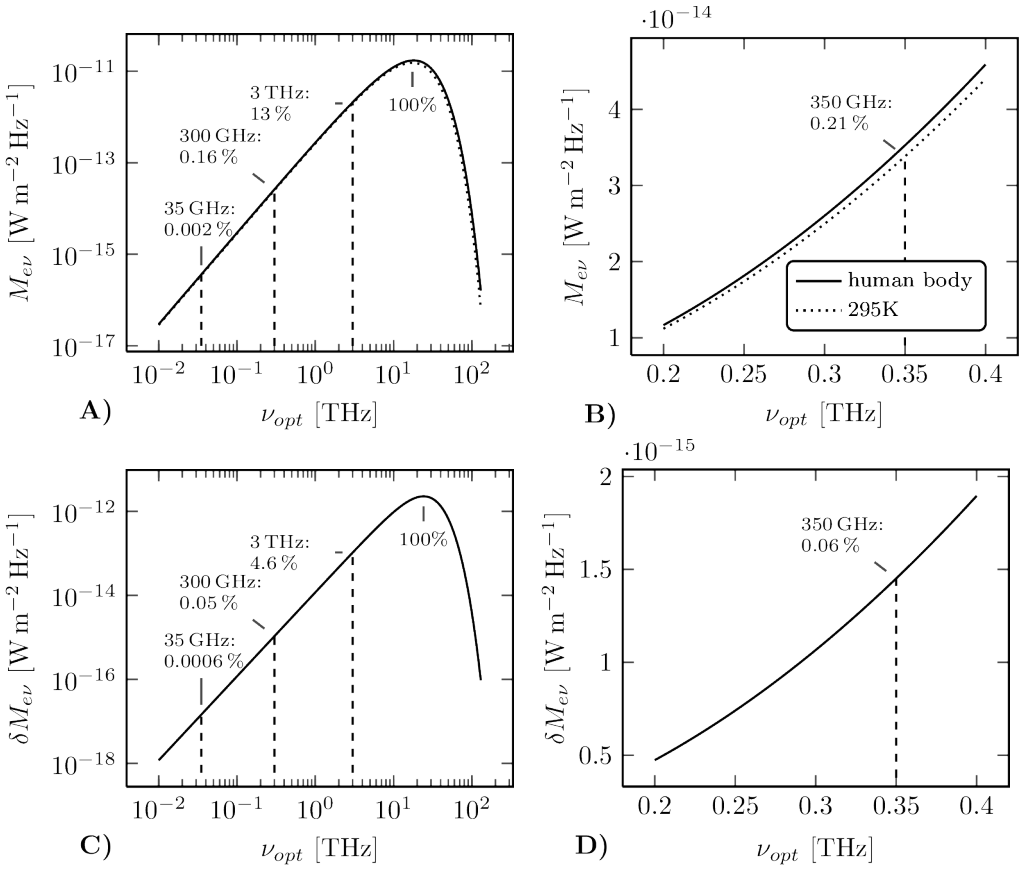

Figure 1.4: Left: Spectral radiant emittance of the human body and a blackbody at 295 K. The relative fraction of the maximum at 295 K is marked for the borders of the THz band and for the 35 GHz microwave window for comparison. B) Magnification of the range from 0.2 THz to 0.4 THz. C) Difference between the curves shown in A). The relative fraction of the maximum is marked for the borders of the THz band and for the 35 GHz microwave window for comparison. D): Magnification.

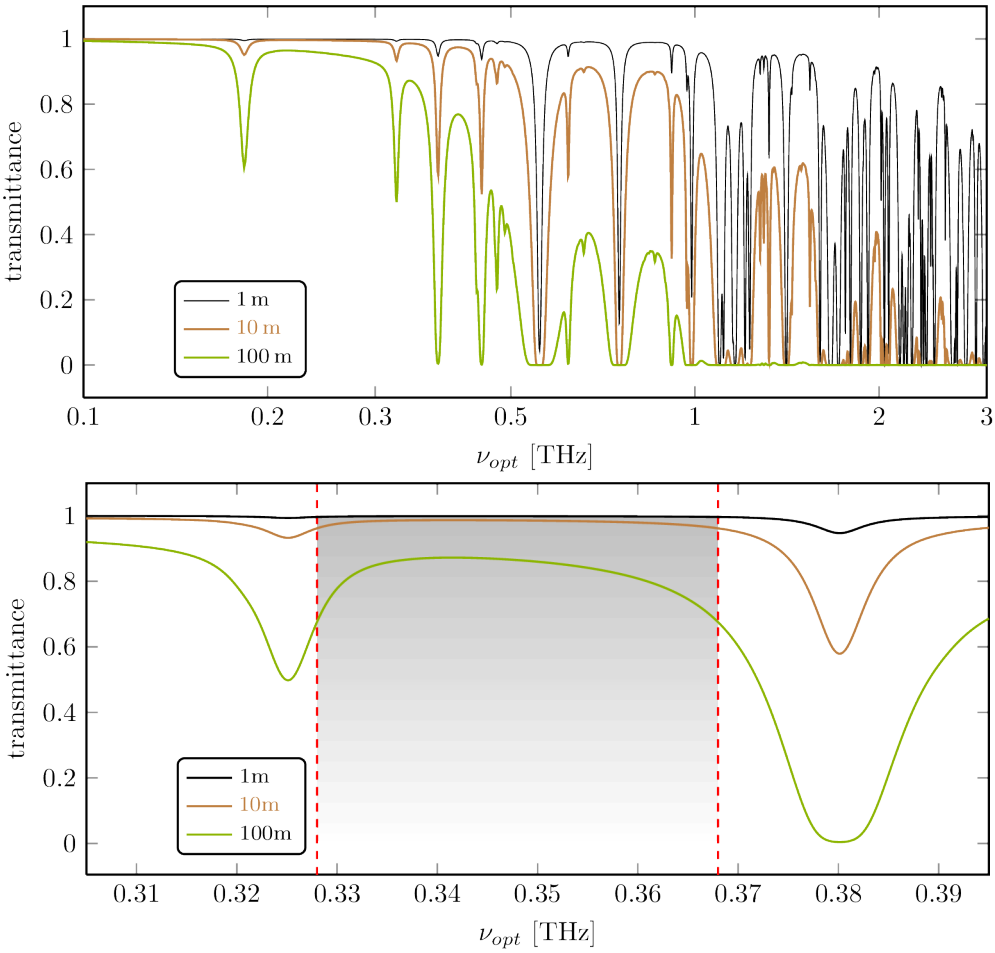

Figure 1.5: Upper graph: Transmittance of air at 295 K, 1013 mbar and 30 % relative humidity for different object distances. The shown data was calculated using [22]. Lower graph: The range of (348 ± 20) GHz is shaded. Because of the asymmetry of the transmittance, its maximum is shifted to lower frequencies compared to the center of this window.

that contributes to the resulting image. A natural demand concerning the object space for a THz camera for person screening is the possibility to map a whole person, which defines a minimum of the necessary lateral dimensions. Depending on this setting and the objects that have to be detected, sensitivity and spatial resolution of the camera have to be adapted. Depending on the aspired scenario and security demands, an appropriate distance between object space and camera has to be chosen. It is called working distance.

The second component is the optical system, the "objective" of the camera. It defines the dimensions and location of the object space. The parameters of the optics result in a maximum solid angle that can be mapped. It is referred to as the angular field of view which in combination with the working distance results in the size of the area that is actually being screened. The field of view (FOV) is oftentimes referred to as the size or diameter of this area in combination with the working distance. Combined with the depth of field, it describes the section of space in which objects can be pictured with the required spatial resolution.

For a given working distance and optical wavelength, the aperture of the optical system defines a lower limit of the achievable spatial resolution (see equation 1.1), which corresponds to the case of diffraction limited imaging. Due to the large optical wavelengths in the THz band, the diffraction limited case usually is aimed for as the ideal optical system. However, the effective aperture size can be smaller than its physical dimensions due to shadowing effects or limited use of the available cross section. This can be accounted for by using this effective value for calculations.

Also the received radiation power is defined by the optical system. Depending on its efficiency and setup, a certain amount of the emitted radiation power from the different locations in the object space will be guided into the camera. For a passive system, this is defined by the spectral radiant emittance of the objects as described in the previous section and their optical characteristics. Also the efficiency of the optical system affects the received radiation. For a diffraction limited system with negligible losses, the received radiation power per sensor is independent of the optical system parameters as the aperture size, the working distance and the resolution, as will be shown below. This is also the case if an effective aperture size has to be taken into account, as long as the system still behaves as an ideal diffraction limited system with the appropriate aperture. In this case, the received power per sensor only depends on the chosen frequency, bandwidth and emission characteristics, so it is defined by the object space independent of the optics.

The third component is the "camera body" containing the sensor, but also the necessary optical filters, readout electronics, power supply and control units. In this thesis, the filters and readout components will be assumed as given, so only the sensors and the essential components for their integration into the system will be discussed in detail.

To define the requirements concerning the sensitivity of the sensors, the received radiation power has to be estimated. The radiation signal received by the THz security camera can be described by the radiation power per sensor P_{sig}. In the most simple case, it only consists of radiation from the surrounding background with the power P_{bg}. A

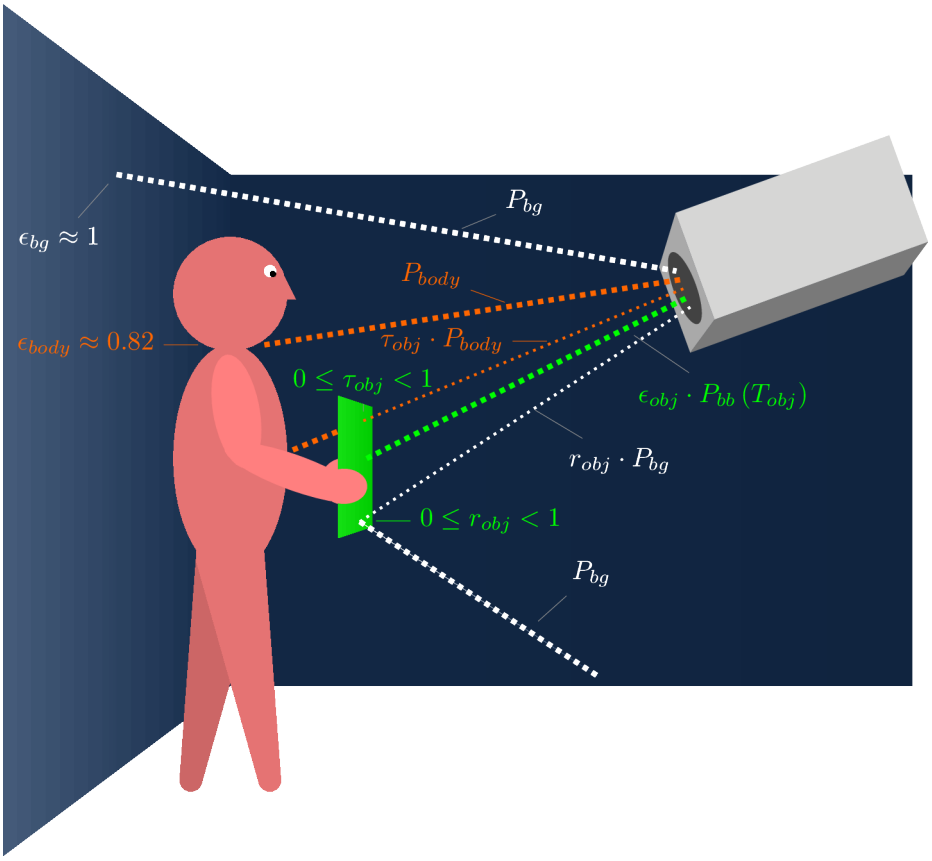

Figure 1.6: Composition of the received radiation power of a THz security camera: The signal is a combination of emission from the surrounding background P_{bg}, from the human body P_{body} and objects in between the body and the camera. The latter partly transmits radiation from the body and reflect the background, depending on its transmittance τ_{obj} and reflectivity r_{obj}. In general, the received signal can be described as in equation 1.20.

person stepping into the field of view changes the signal to P_{body}. If an object is placed in front of the body the received power is P_{obj}. The definition of these power levels will be given in the following.

In an idealized environment, the background radiation results from materials at a common and constant temperature. In this case, reflected and transmitted radiation usually originates from the background, as well. Therefore, independent of reflectivity and transmissivity of the materials, they act as an effective background that behaves like a nearly ideal blackbody (see equation 1.2). Hence, the radiation power received from the background can be described as

$$P_{bg} = \epsilon_{bg} \cdot P_{bb}(T_{bg}) \tag{1.8}$$
$$\epsilon_{bg} \approx 1 \tag{1.9}$$
$$\Rightarrow P_{bg} \approx P_{bb}(T_{bg}) \tag{1.10}$$

where ϵ_{bg} is the effective emissivity of the background with the effective temperature T_{bg}.

The human body shows no significant transmission τ_{body} in the used frequency range. However, the reflectivity of $r_{body} \approx 18\,\%$ can not be neglected (see section 1.2). Hence, the radiation received by the camera from the human body is a combination of its thermal emission and reflected radiation from the background:

$$P_{body} = \epsilon_{body} \cdot P_{bb}(T_{body}) + r_{body} \cdot P_{bb}(T_{bg}) \tag{1.11}$$
$$r_{body} \approx 0.18 \tag{1.12}$$
$$\tau_{body} \approx 0 \tag{1.13}$$
$$\epsilon_{obj} + \tau_{obj} + r_{obj} = 1 \text{ (Kirchhoff's law of thermal radiation)} \tag{1.14}$$
$$\Rightarrow \epsilon_{body} \approx 1 - r_{body} \tag{1.15}$$
$$\Rightarrow P_{body} \approx 0.82 \cdot P_{bb}(T_{body}) + 0.18 \cdot P_{bb}(T_{bg}) \tag{1.16}$$

where ϵ_{body} is the emissivity of the human body at the effective temperature T_{body}.

An object at temperature T_{obj} in between the human body and the camera in general can reflect the background, transmit radiation from the covered body and emit thermal radiation (see figure 1.6). Hence, the received signal is the sum of these three components:

$$P_{obj} = \epsilon_{obj} \cdot P_{bb}(T_{obj}) + \tau_{obj} \cdot P_{body} + r_{obj} \cdot P_{bg} \tag{1.17}$$
$$0 \leq \tau_{obj} < 1 \tag{1.18}$$
$$0 \leq r_{obj} < 1 \tag{1.19}$$

with ϵ_{obj}, τ_{obj} and r_{obj} being emissivity, transmittance and reflectivity of the object, respectively.

In a real environment, combinations of several different object layers can be described by a single virtual object with chosen parameters that result in the same received power. Similarly, the emission from the background as well as the uncovered body can be de-

scribed the same way as received from a perfectly reflective and transparent object, respectively. This allows also to account for complex reflection and transmission paths without considering them explicitly by integrating them into the effective values, including inhomogeneous background settings, if necessary.

Hence, the general description of the received signal in all cases is

$$P_{sig} \approx \epsilon_{obj}^{eff} \cdot P_{bb}\left(T_{obj}^{eff}\right) + \tau_{obj}^{eff} \cdot P_{body} + r_{obj}^{eff} \cdot P_{bg} \tag{1.20}$$

while the used properties ϵ_{obj}^{eff}, τ_{obj}^{eff}, r_{obj}^{eff} and T_{obj}^{eff} of the object are effective values, possibly representing different object layers.

If one assumes that

$$T_{body} \geq T_{obj}^{eff} \geq T_{bg} \tag{1.21}$$

the maximum signal difference to be expected is given by

$$\Rightarrow P_{body} \geq P_{sig} \geq P_{bg} \tag{1.22}$$

$$\Rightarrow (\Delta P_{sig})_{max} = P_{body} - P_{bg} \tag{1.23}$$

The combination of equations 1.2 and 1.23 shows, that for $T_{bg} = 295\,\mathrm{K}$ and $T_{body} = 310\,\mathrm{K}$ at $\nu_{opt} = 345\,\mathrm{GHz}$ the maximum signal difference $(\Delta P_{sig})_{max}$ will be approx. 4.3 % of the background signal P_{bg}, when the reflectivity of the human skin is taken into account.

To evaluate the emitted power by a spot in the object space mapped to a sensor, a circular area with the same radius as the airy disc r_{airy} can be used in the case of a diffraction limited system. The blackbody emission from this disc can be calculated using equation 1.2. However, due to its strong inhomogeneity, the intensity distribution across the airy disc has to be taken into account. It is rotationally symmetric and given by

$$I_{airy}(r) = I_0 \cdot \left(\frac{J_1(2\pi r)}{\pi r}\right)^2 \tag{1.24}$$

where r is the distance from its center and J_1 the normalized Bessel function of the first kind and of order one. The surface integral over the normalized airy disc up to its radius r_{airy} results in $\zeta \approx 0.23$. Thus, the radiation from a circular spot with radius r_{airy} has to be scaled with ζ.

Ignoring higher orders of the diffraction pattern does not give exact results as in the case of an ideal circular aperture the airy disc contains only approx. 84 % of the total power[23]. In real cases, however, the exact value depends on the specific properties of the optical system due to varying diffraction patterns. With respect to these variations, the assumption of only the airy disc being the source of the radiation leads to good

approximation of the general case.

Moreover, the actually received power is further reduced by the fact that only a small portion of the emitted radiation is caught by the aperture. Thus, a diffraction limited system with an airy radius of r_{airy}, an aperture diameter of d_{AP} and an object distance of d_{obj} receives the background radiation power of (see equation 1.4)

$$P_{bg} \approx \frac{2\pi h\nu_{opt}^3}{c^2} \frac{1}{e^{\frac{h\nu_{opt}}{k_B T}} - 1} \cdot \Delta\nu_{opt} \cdot 0.23 \cdot \pi r_{airy}^2 \cdot \frac{\pi \left(\frac{d_{AP}}{2}\right)^2}{2\pi d_{obj}^2} \tag{1.25}$$

As a result of equation 1.1, this value is unchanged for any diffraction limited system at the same frequency, temperature and bandwidth:

$$P_{bg} \propto \left(r_{airy} \cdot \frac{d_{AP}}{d_{obj}}\right)^2 = (1.22\lambda)^2 \tag{1.26}$$

$$\Rightarrow P_{bg} \approx \frac{\pi^2 h\nu_{opt}}{e^{\frac{h\nu_{opt}}{k_B T}} - 1} \cdot \Delta\nu_{opt} \cdot 0.085 \tag{1.27}$$

Therefore, in case of the used frequency $\nu_{opt} = 345\,\mathrm{GHz}$, a bandwidth of $\Delta\nu_{opt} = 40\,\mathrm{GHz}$ in the chosen optical window and a background temperature of $T_{bg} = 295\,\mathrm{K}$, the received background radiation is

$$P_{bg} \approx 1.3 \times 10^{-10}\,\mathrm{W} \tag{1.28}$$

with the corresponding maximum signal difference amounting to

$$(\Delta P_{sig})_{max} \approx 5.7 \times 10^{-12}\,\mathrm{W} \tag{1.29}$$

Different objects in the THz image are distinguished by their signal difference. Hence, the relevant measure to specify the sensitivity of a THz camera refers to the resolvable signal differences. The smallest power difference that can be resolved $(\Delta P_{sig})_{min}$ defines the maximum achievable bit depth b of resulting pictures:

$$b = log_2 \left[\frac{(\Delta P_{sig})_{max}}{(\Delta P_{sig})_{min}}\right] \tag{1.30}$$

This is oftentimes limited by the overall sensor noise, where $(\Delta P_{sig})_{min}$ equals the noise level P_{noise}. Accordingly, the maximum achievable resolution commonly is also given as the maximum signal to noise ratio (SNR), which in this case can be defined as

$$SNR \equiv SNR_{max} = \frac{(\Delta P_{sig})_{max}}{P_{noise}} \tag{1.31}$$

so in the noise limited case the relation between b and SNR is

$$SNR = 2^b \tag{1.32}$$

Therefore, the sensors used in a THz camera have to be able to detect significantly lower signal powers than $(\Delta P_{sig})_{max}$, depending on the aspired SNR.

Though promising developments in heterodyne detectors could be shown in the last years[24][25], the more simple implementation of thermal detectors combined with their good scalability and proven applicability for highly sensitive THz detection led to the decision of using thermal detectors for this thesis. This will be further discussed in chapter 2.

THz photons at the chosen frequency of 345 GHz have an energy of $h \cdot \nu_{opt} \approx 1.4\,\mathrm{meV}$. This is by a factor of approx. 18 smaller than the average thermal energy per degree of freedom of a particle at room temperature of 22 °C, which is $k_B \cdot T \approx 25\mathrm{meV}$. Thermally induced noise power (thermal fluctuation noise as well as Johnson-Nyquist noise) is proportional to $k_B \cdot T$, so a means for improving the sensitivity of a thermal sensor is to reduce its temperature T (see also section 2.1).

While cooling the sensor also constitutes an additional degree of complexity of the overall system, this is strongly alleviated by the development and improvement of commercial cryogen-free cooling systems. For an efficient and user-friendly cooling setup, fully automated two stage pulse tube coolers[26] that reach base temperatures of 4 K are commercially available[27]. However, sensitive setups in such cryocoolers may suffer from thermal oscillations and microphonic effects caused by the small vibrations due to the periodic gas pulses. Such distortions would reduce the sensitivity of cooled sensors. This effect can be significantly reduced by adding another cooling stage which is mechanically decoupled from the pulse tube. In the camera systems discussed in this thesis, a commercial closed system ^{3}He evaporation cooler [28] is used for that purpose which is also decoupled thermally from the cold stage of the pulse tube in operation mode. Another advantage of this combination is an additional drop in base temperature, which can be stabilized in a working point that can be chosen from 0.4 K to 1 K. Details of the specific setup of the particular systems will be given in the corresponding chapters, see sections 6.5 and 7.4.

2 Fundamentals of transition edge sensors

2.1 Requirements

The first decision while choosing an appropriate sensor type for a certain application is whether to use direct or heterodyne sensors. The higher spectral resolution of heterodyne sensors is especially favorable for applications like spectroscopy that aim for a small, possibly adaptable, signal bandwidth. Especially in the THz range, their scalability strongly depends on the availability of THz sources of adequate power to serve as the local oscillator for all sensors. Opposed to that, the use of the direct detection principle usually allows for wider optical bandwidths that improve the sensitivity of the sensors, which is advantageous for non-spectroscopic imaging applications where phase sensitivity does not play a role. The bandwidth of direct detectors usually is defined by radiation filters. The readout is simplified by the fact that no THz source is needed, however, to achieve high sensitivity, cooling is necessary. An extended discussion of this subject can be found in [24]. A fundamental limit of the achievable sensitivity of a direct sensor with wideband sensitivity is given by thermal radiation fluctuations from its environment. It depends on the effective blackbody temperature of it surrounding and the detector area[29]. The large wavelength in the THz range prevents detectors to become significantly smaller than of the order of a square millimeter, which makes cooling necessary down to 4 K and below to keep the the thermal fluctuation noise from the surrounding negligible[30]. Due to the serious improvements of automated and user-friendly cooling systems in the last years (see section 1.3) and the still limited power of THz sources especially in the range below 1 THz which is relevant for the targeted application in this work, the use of direct detectors was favored.

Based on the requirements from the previous sections, adequate sensors for the THz video camera concept have to fulfill several requirements: They should work at temperatures below 1 K, are sensitive enough to resolve signal differences of approx. 1×10^{-13} W under a constant background load of approx. 1×10^{-10} W (see section 1.3). Cooled low noise amplifiers should be available for low noise preamplification in the readout circuit. They have to be fabricable in thin film technology for high scalability, reproducibility and low production cost. This implies the use of low temperature bolometers[24], which proved to be highly scalable while achieving high sensitivity in the THz range[10].

2.2 Bolometers

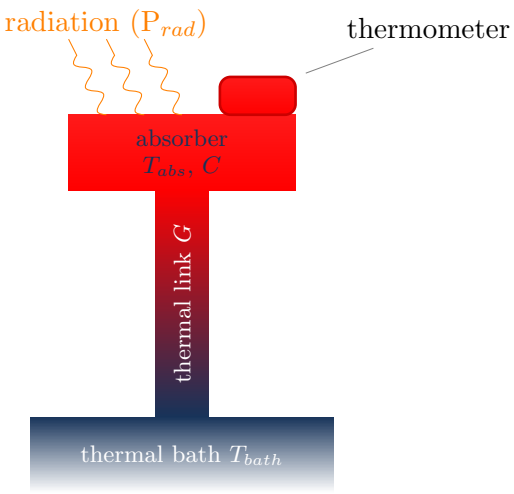

Figure 2.1: Sketch of a bolometer: An absorber material is heated up by incoming radiation and cooled by a link to a thermal bath at constant temperature T_{bath}. A connected electrical thermometer is used to measure the temperature of the absorber T_{abs}. The temperature difference $T_{abs} - T_{bath}$ is a function of the radiation power.

Bolometers (from Greek $\beta o\lambda\acute{\eta}$, and $\mu\acute{\epsilon}\tau\rho o\nu$ meaning 'tools to measure light') measure the power of electromagnetic radiation by converting it to heat which changes the temperature of an electrical thermometer. This principle was invented in 1878 by Samuel Langley, an American astronomer. Using this principle, he was able to detect the thermal radiation emitted by a cow from a distance of more than 400 m[31].

The principle setup of a bolometer is shown in figure 2.1: Incoming radiation is heating up an absorber material. An attached electrical thermometer measures its temperature T_{abs}. The absorber is thermally isolated except for a link to a thermal bath at constant temperature T_{bath}, which is cooling the absorber. In thermal equilibrium, incoming radiation power P_{rad} and the heat flow over said link P_{link} have to be equal:

$$P_{rad} = P_{link} \tag{2.1}$$

The thermal conductance G of the link and its average $\overline{G}$ are defined as

$$G \equiv G(T) = \frac{dP_{link}}{dT} \tag{2.2}$$

$$\overline{G} = \frac{1}{\Delta T} \int_{T_{bath}}^{T_{abs}} G(T')dT' \tag{2.3}$$

The ratio of P_{rad} and $\overline{G}$ defines the resulting temperature offset ΔT of the absorber:

$$\Delta T = T_{abs} - T_{bath} \tag{2.4}$$

$$\Rightarrow \Delta T = \frac{P_{rad}}{\overline{G}} \quad \text{(using equation 2.1)} \tag{2.5}$$

If a small signal $\delta P_{rad} \cdot e^{i\omega t}$ with the angular frequency ω is added with

$$P_{rad} = P_{rad,0} + \delta P_{rad} \cdot e^{i\omega t} \tag{2.6}$$

$$\delta P_{rad} \ll P_{rad} \tag{2.7}$$

the first order approximation results in

$$T_{abs} \approx T_0 + \delta T \cdot e^{i\omega t} \tag{2.8}$$

$$\delta T \equiv \frac{dT_{abs}}{dP_{rad}} \cdot \delta P_{rad} \tag{2.9}$$

$$\delta T \ll \Delta T \tag{2.10}$$

$$G(T_{abs}) \approx G(T_0) \equiv G = constant \tag{2.11}$$

and

$$P_{link} \approx P_{link,0} + \frac{dP_{link}}{dT} \cdot \delta T \cdot e^{i\omega t} \tag{2.12}$$

$$P_{link} \approx P_{link,0} + G \cdot \delta T \cdot e^{i\omega t} \tag{2.13}$$

The finite heat capacity of the absorber C (including attached elements, like the thermometer), causes a change of the corresponding thermal energy $U_{th} = C \cdot T$, which leads to a dissipated portion of the heat. This modifies equation 2.1 by adding another term,

describing the change of U_{th}:

$$P_{rad}(t) = P_{link}(t) + P_{th}(t) \tag{2.14}$$

$$P_{th} = \frac{dU_{th}}{dt} \tag{2.15}$$

$$C(T_{abs}) \approx C = constant \tag{2.16}$$

$$\Rightarrow P_{th} \approx i \cdot \omega \cdot C \cdot \delta T \cdot e^{i\omega t} \tag{2.17}$$

Equation 2.14 can be separated into an equilibrium term

$$P_{rad,0} = P_{link,0} \tag{2.18}$$

and a variing term

$$\delta P_{rad} \cdot e^{i\omega t} = (G + i \cdot \omega \cdot C) \cdot \delta T \cdot e^{i\omega t} \tag{2.19}$$

Therefore, the temperature responsivity S_T^{bolo} of the bolometer in the small signal case is given by

$$S_T^{bolo} \equiv \frac{\delta T}{\delta P_{rad}} \tag{2.20}$$

$$S_T^{bolo} = \frac{1}{G + i \cdot \omega \cdot C} \tag{2.21}$$

As the step response $h(t)$ of a system is given by the time integral over the inverse Laplace transform $\mathcal{L}^{-1}$ of its transfer function $G(\omega)$[32]

$$h(t) = \int_0^t \mathcal{L}^{-1}(G(\omega))dt' \tag{2.22}$$

the step response of the bolometer for a step ΔP_{rad}^{step} at $t = 0$ follows an exponential decay

$$\frac{\Delta T_{abs}^{step}}{\Delta P_{rad}^{step}} \equiv \frac{T_{abs}^{step} - T_0}{\Delta P_{rad}^{step}} = \int_0^t \mathcal{L}^{-1}(S_T^{bolo}(\omega))dt' \tag{2.23}$$

$$T_{abs}^{step}(t) = T_0 + \frac{\Delta P_{rad}^{step}}{G} \cdot \left(1 - e^{-t/\tau_0}\right) \tag{2.24}$$

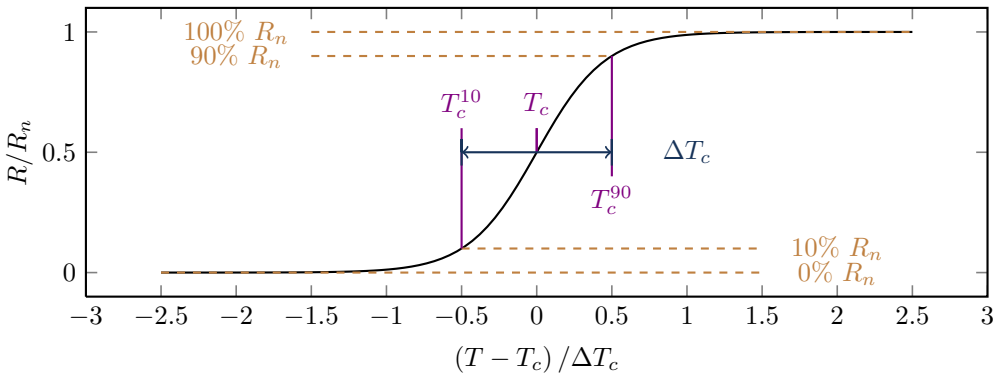

Figure 2.2: Sketch of the superconducting phase transition. Starting from the normal state resistance R_n at temperatures significantly above the critical temperature T_c, resistance drops down to zero around T_c. The temperatures at 90 % and 10 % of R_n, denoted by T_c^{90} and T_c^{10}, respectively, define the characteristic parameters of the transition: Their average is $T_c = \frac{T_c^{90}+T_c^{10}}{2}$, the difference the transition width $\Delta T_c = T_c^{90} - T_c^{10}$.

with the thermal time constant of the bolometer τ_0

$$\tau_0 = \frac{C}{G} \tag{2.25}$$

The bolometer is capable of measuring the absolute power of the absorbed radiation, when the thermal conductance of the link is known (equation 2.5). In the small signal case discussed above, the temperature offset to the bath is proportional to the radiation power (equation 2.11). For sufficiently slow signals, the sensitivity of this measurement only depends on the thermal conductance (equation 2.24) and the sensitivity of the used thermometer. As thermometer, any material with a temperature dependent resistance can be used, and the sensitivity is increasing with the strength of this dependency.

2.3 Transition edge sensor bolometers (TES)

As superconducting materials usually show a strong temperature dependence of their electrical resistance $R(T)$ in the superconducting transition (see figure 2.2), they are applicable as the thermometer of a bolometer. In 1942, this was demonstrated by Donald Hatch Andrews[33], an American chemist[34]. The fact that such bolometers work on the edge of the superconducting transition established the name "transition edge sensors" (TES). While a steep $R(T)$ curve is favorable as it causes a higher sensitivity, it is hard to stabilize such a working point. In addition, current biasing the thermometer to measure its resistance leads to a thermal runaway effect[35]. A solution to this problem was

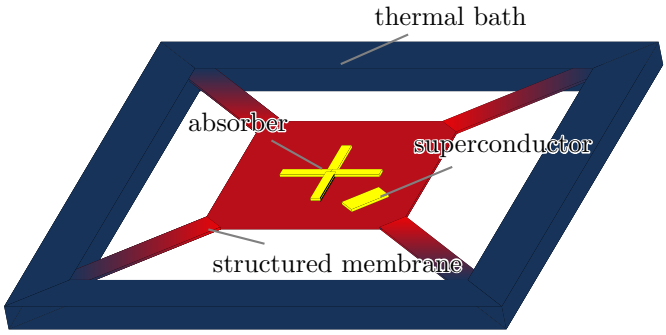

Figure 2.3: The absorber and the thermistor of a TES are located on a thin membrane. The membrane is structured to define the thermal conductivity to the thermal bath.

proposed and successfully performed by J. Clarke et al. in 1977[36]. They could stabilize the temperature of the superconductor with an external feedback loop including a heater. A further improvement was the integration of the feedback by voltage biasing the superconductor, leading to an internal feedback effect that drastically simplified the application of TES, as demonstrated by K. Irwin et al. in 1995[37]. This allows to keep the superconductor at a fixed temperature at varying radiation power and base temperature. Using the superconductor as a heater instead of a thermometer and measuring the necessary current to keep the temperature constant linearizes the bolometer response and can reduce its time constant significantly (see below). To avoid misunderstandings, such a superconductor in the following will be called thermistor. By now, TES in voltage biased mode are a common type of bolometers working at temperatures below 1 K for astronomical applications[38],[39],[40],[41].

In such bolometers, the absorber and the thermistor usually are placed together on a thin, self-supporting structured membrane[42]. The structuring of the membrane is used to properly adjust the thermal conductance to the bath (see figure 2.3).

As described above, incoming radiation with the power P_{rad} is transformed to heat in the absorbers and thereby heating the platform. In addition, the thermistor is biased with a constant voltage V_{th}, which adds an electrical heating power of

$$P_{el} = \frac{V_{th}^2}{R_{th}} \tag{2.26}$$

In the case of an evacuated cryostat and a thermal shield at the bath temperature with a highly reflective surface, other sources of energy transfer like gas coupling and thermal radiation from the surrounding to the platform usually can be neglected. Thus, the total

heating power P_{heat} is

$$P_{heat} = P_{rad} + P_{el} \tag{2.27}$$

In thermal equilibrium, the amounts of incoming and outgoing energy per time unit have to be the same:

$$P_{heat} = P_{out} \tag{2.28}$$

In an ideal bolometer, G is chosen to dominate the heat transfer from the platform

$$P_{out} \approx P_{link} \tag{2.29}$$

and the temperature on the platform, including absorber and thermistor, is homogeneous:

$$T \equiv T_{platform} \equiv T_{th} \equiv T_{abs} \tag{2.30}$$

These assumptions will be made for the following calculations.

2.3.1 Thermal response

Assuming a small signal $\delta P_{rad} \cdot e^{i\omega t}$ as in section 2.2, the TES can be described by

$$P_{rad}(t) + P_{el}(t) = P_{th}(t) + P_{link}(t) \tag{2.31}$$

$$P_{el} \approx P_{el,0} + \frac{dP_{el}}{dT} \cdot \delta T \cdot e^{i\omega t} \tag{2.32}$$

$$P_{el} \approx P_{el,0} + \left(\frac{1}{R_{th}} \cdot \frac{dV_{th}^2}{dR_{th}} - \frac{P_{el}}{R_{th}} \right) \cdot \frac{dR_{th}}{dT} \cdot \delta T \cdot e^{i\omega t} \tag{2.33}$$

$$P_{el} \approx P_{el,0} - \frac{P_{el}}{R_{th}} \cdot \frac{dR_{th}}{dT} \cdot \delta T \cdot e^{i\omega t} \quad (V_{th} = \text{constant}) \tag{2.34}$$

which can be separated in analogy to equations 2.18 and 2.19 into an equilibrium term

$$P_{rad,0} + P_{el,0} = P_{link,0} \tag{2.35}$$

and a variing term[43]

$$\delta P_{rad} \cdot e^{i\omega t} = \left(G + i \cdot \omega \cdot C + \frac{P_{el,0}}{T_0} \cdot \alpha(T_0) \right) \cdot \delta T \cdot e^{i\omega t} \tag{2.36}$$

introducing the commonly used transition parameter α[44]

$$\alpha(T_0) \equiv \alpha = \frac{T_0}{R_{th}} \cdot \frac{dR_{th}}{dT} \tag{2.37}$$

Thus, the temperature responsivity of the TES, S_T^{TES} in the small signal case is given by

$$S_T^{TES} \equiv \frac{\delta T}{\delta P_{rad}} \tag{2.38}$$

$$S_T^{TES} = \frac{1}{G + i \cdot \omega \cdot C + \frac{P_{el,0}}{T_0} \cdot \alpha(T_0)} \tag{2.39}$$

Defining an effective thermal conductance

$$G_{eff} = G + \frac{P_{el,0}}{T_0} \cdot \alpha(T_0) \tag{2.40}$$

$$S_T^{TES} = \frac{1}{G_{eff} + i \cdot \omega \cdot C} \tag{2.41}$$

allows to come to a similar representation as in equation 2.21. Thus, in analogy to equation 2.24, the step response of the TES in thermal equilibrium for a step ΔP_{rad}^{step} at $t = 0$, with an arbitrarily chosen zero point of the time scale, follows an exponential decay

$$T^{step}(t) = T_0 + \frac{\Delta P_{rad}^{step}}{G_{eff}} \cdot \left(1 - e^{-t/\tau}\right) \tag{2.42}$$

with the corresponding effective time constant

$$\tau = \frac{C}{G_{eff}} \tag{2.43}$$

2.3.2 Negative electrothermal feedback

In analogy to electrical amplifiers[45], the responsivity can be interpreted as an amplification factor. While the bolometer without electrical heating (chapter 2.2) is represented by an amplifier without feedback where the amplification A_{bolo} is equal to the temperature responsivity,

$$A_{bolo} = S_T^{bolo} \tag{2.44}$$

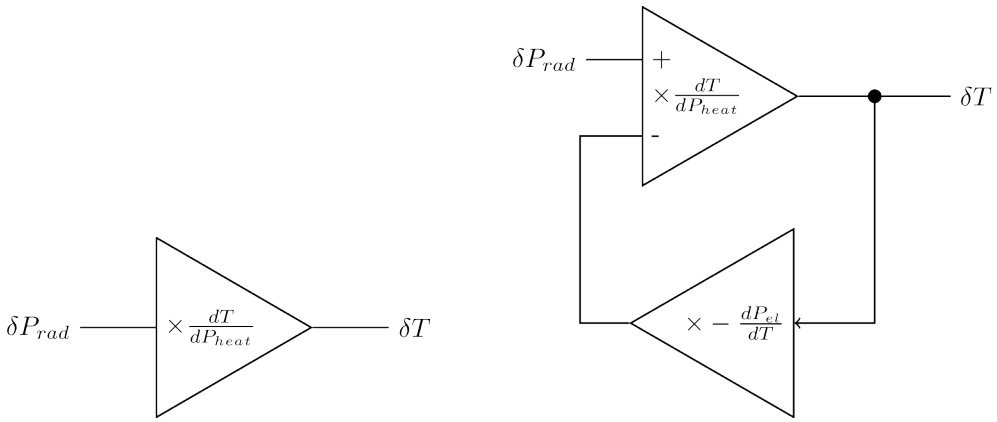

Figure 2.4: Left: Thermal response scheme without negative electrothermal feedback (nETF) in the small signal case (first order approximation): A change in radiation power δP_{rad} causes a change in temperature δT. Right: If nETF is applied, thermal response is reduced depending on the loop gain $\mathscr{L} = -\frac{dP_{el}}{dP_{heat}}$.

the TES behaves as an amplifier with amplification A_{TES}, negative feedback β and loop gain $\mathscr{L}$ (figure 2.4), where

$$A_{TES} = \frac{dT}{dP_{heat}} \tag{2.45}$$

$$\beta = -\frac{dP_{el}}{dT} > 0 \tag{2.46}$$

$$\mathscr{L} = A_{TES} \cdot \beta = -\frac{dP_{el}}{dP_{heat}} > 0 \tag{2.47}$$

$$\tag{2.48}$$

A_{TES} is the amplification without feedback, hence, it is identical to A_{bolo}.

The loop gain

$$\mathscr{L} = -\frac{\delta P_{el}}{\delta P_{link} + \delta P_{th}} \tag{2.49}$$

can be written as

$$\mathscr{L} = \frac{L}{1 + i\omega\tau_0} \tag{2.50}$$

$$L = \frac{P_{el,0} \cdot \alpha(T_0)}{G \cdot T_0} \tag{2.51}$$

L is the static loop gain. S_T^{TES} is reduced by the negative feedback compared to S_T^{bolo} by

$$\frac{S_T^{bolo}}{S_T^{TES}} = 1 + \mathscr{L} \tag{2.52}$$

In case of the TES, the feedback is caused by an electrothermal interaction and thus called negative electrothermal feedback (nETF). If the nETF is strong ($L \gg 1$), it significantly reduces the temperature variation of the platform and thereby stabilizes the working point. This also speeds up the reaction on signal changes, and a direct comparison to the bolometer without nETF (equation 2.25) shows that

$$\frac{\tau_0}{\tau} = \frac{G_{eff}}{G} \tag{2.53}$$

$$\frac{\tau_0}{\tau} - 1 = L \propto \alpha \tag{2.54}$$

Hence, the effective time constant τ is strongly influenced by α.

2.3.3 Current response

The read out measure of the TES is, as mentioned above, the current through the thermistor, I_{th}. For a constant bias voltage V_{bias}, it is proportional to the electrical heating power

$$I_{th} = \frac{P_{el}}{V_{th}} \tag{2.55}$$

which results in a current responsivity

$$S_I^{TES} = \frac{\delta I_{th}}{\delta P_{rad}} \tag{2.56}$$

$$S_I^{TES} = S_T^{TES} \cdot \frac{dI_{th}}{dT} \tag{2.57}$$

$$S_I^{TES} = S_T^{TES} \cdot \left(-\frac{I_{th,0}}{T_0}\right) \alpha \tag{2.58}$$

$$S_I^{TES} \propto S_T^{TES} \tag{2.59}$$

which is proportional to the temperature responsivity. Accordingly, the time constant of the current step response is identical to the one of the temperature step response:

$$I_{th}^{step}(t) = I_0 - \frac{I_0}{T_0} \cdot \alpha \cdot \frac{\Delta P_{rad}^{step}}{G_{eff}} \cdot \left(1 - e^{-t/\tau}\right) \tag{2.60}$$

$$I_{th}^{step}(t) = I_0 - \frac{\Delta P_{rad}^{step}}{V_{bias}} \cdot \frac{L}{L+1} \cdot \left(1 - e^{-t/\tau}\right) \tag{2.61}$$

Equation 2.61 shows that while measuring the current through the thermistor does not allow to determine the absolute value of the absorbed radiation power, it is possible for power differences ΔP_{rad}. A power difference is proportional to a difference in the measured current ΔI_{th}, and the factor of proportionality, S_I^{TES} is constant for a given working point. Rewriting it in terms of L and τ leads to

$$S_I^{TES} = -\frac{1}{V_{bias}} \cdot \frac{L}{L+1} \cdot \frac{1}{(1 + i\omega\tau)} \tag{2.62}$$

For large values of L, the equilibrium response of the electrical power to the radiation power will become independent on the working point

$$\frac{\delta P_{el}}{\delta P_{rad}} \equiv S_I^{TES} \cdot V_{bias} \tag{2.63}$$

$$\frac{\delta P_{el}}{\delta P_{rad}}(\omega \to 0) \to -\frac{L}{L+1} \tag{2.64}$$

2.4 Electrical setup and readout

In the sections above, an ideal model of the TES is described. For a more realistic representation, some additional aspects have to be taken into account: The bias voltage V_{bias} of the TES is implemented by a shunt resistor R_{sh} placed in parallel to the thermistor (see figure 2.5). This causes the voltage at the thermistor to be dependent of R_{th}, R_0 and R_L. R_0 denotes a parasitic resistance on the chip in series to the thermistor, while R_L represents a possibly non-zero resistance in the readout circuit in series to the thermistor. Different to R_L, a non-zero value of R_0 also increases P_{el}.

For possibly non-zero, but in the working range constant R_{sh}, R_L and R_0, the electrical heating power on the platform is given by

$$P_{el}^{eff} = \frac{V_{th}^2}{R_{th}} + \frac{V_{R_0}^2}{R_0} \tag{2.65}$$

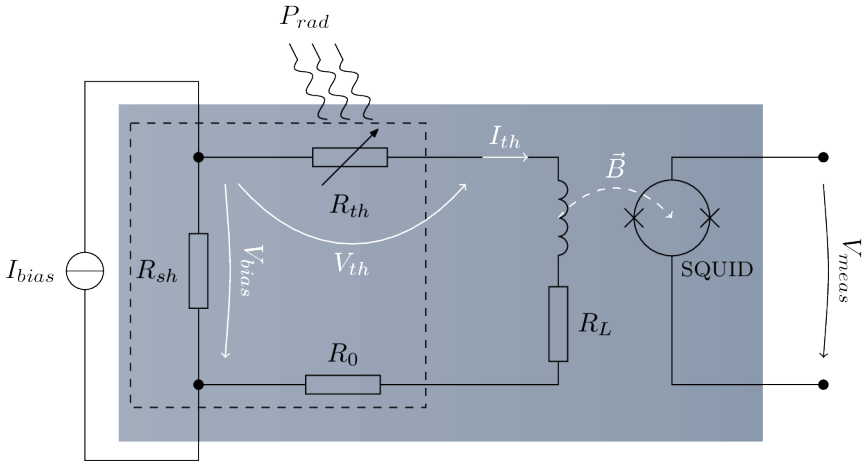

Figure 2.5: Schematic representation of the electrical setup of the TES and the readout. The shaded area represents the cooled electronics. On the TES chip, marked by the dashed rectangle, superconducting wiring is used to avoid parasitic resistances like R_0. R_L represents a possible parasitic resistance in the readout circuit. For voltage bias and strong nETF, $R_{sh}, R_L \ll R_{th}$ is necessary.

By introducing the effective thermistor resistance R_{th}^{eff} and voltage V_{th}^{eff} as

$$R_{th}^{eff} = R_{th} + R_0 \tag{2.66}$$

$$V_{th}^{eff} = V_{th} + V_{R_0} = \frac{V_{th}}{\eta} \tag{2.67}$$

$$\eta = \frac{R_{th}}{R_{th}^{eff}} \tag{2.68}$$

this can be simplified using $I_{th} = I_{R_0}$ to

$$P_{el}^{eff} = \frac{\left(V_{th}^{eff}\right)^2}{R_{th}^{eff}} \tag{2.69}$$

Using Kirchhoff's circuit laws, the exact form of V_{th}^{eff} for the general TES circuit shown in figure 2.5 is

$$V_{th}^{eff} = I_{bias} \cdot R_{sh} \cdot \frac{R_{th}^{eff}}{R_{th}^{eff} + R_L + R_{sh}} \tag{2.70}$$

In analogy to equation 2.32 we find

$$P_{el}^{eff} \approx P_{el,0}^{eff} + \frac{dP_{el}^{eff}}{dT} \cdot \delta T \cdot e^{i\omega t} \tag{2.71}$$

$$\alpha^{eff} = \frac{T}{R_{th}^{eff}} \cdot \frac{dR_{th}^{eff}}{dT} = \alpha \cdot \eta \tag{2.72}$$

$$-\beta^{eff} \equiv \frac{dP_{el}^{eff}}{dT} = -\frac{P_{el}^{eff}}{T} \cdot \alpha \cdot \xi \cdot \eta \tag{2.73}$$

with

$$\xi = \frac{R_{th}^{eff} - R_L - R_{sh}}{R_{th}^{eff} + R_L + R_{sh}} \leq 1 \tag{2.74}$$

The general form of equation 2.36 is

$$\delta P_{rad} \cdot e^{i\omega t} = \left(G + i \cdot \omega \cdot C - \frac{dP_{el}^{eff}}{dT} \right) \cdot \delta T \cdot e^{i\omega t} \tag{2.75}$$

This leads to the following general specific parameters of the TES, as the effective thermal conductance

$$G_{eff}^{eff} = G + \frac{P_{el}^{eff}}{T} \cdot \alpha \cdot \xi \cdot \eta = G \cdot (1 + L^{eff}) \tag{2.76}$$

and the feedback parameter

$$L^{eff} = -\frac{1}{G} \cdot \frac{dP_{el}^{eff}}{dT} = L \cdot \xi \cdot \eta \tag{2.77}$$

$$\mathscr{L}^{eff} = \frac{L^{eff}}{1 + i\omega\tau_0} = \mathscr{L} \cdot \xi \cdot \eta \tag{2.78}$$

Also, the temperature and current responsivities change to

$$S_T^{TES,eff} = \frac{1}{G_{eff}^{eff} + i \cdot \omega \cdot C} \tag{2.79}$$

$$\frac{S_T^{bolo}}{S_T^{TES,eff}} = 1 + \mathscr{L} \cdot \xi \cdot \eta \tag{2.80}$$

and

$$S_I^{TES,eff} = S_T^{TES,eff} \cdot \frac{dI_{th}}{dT} \tag{2.81}$$

$$S_I^{TES,eff} = S_I^{TES} \cdot \frac{R_{th}}{R_{th}^{eff} + R_L + R_{sh}} \tag{2.82}$$

leading to an effective time constant of

$$\tau^{eff} = \frac{\tau_0}{L^{eff} + 1} \tag{2.83}$$

$$\frac{\tau_0}{\tau_{eff}} - 1 = L \cdot \xi \cdot \eta \tag{2.84}$$

For any working point with

$$\xi \approx 1 \tag{2.85}$$

$$\eta \approx 1 \tag{2.86}$$

equation 2.70 shows that the V_{th} is nearly independent on variations of R_{th} that do not affect the conditions above:

$$V_{th}^{eff} = I_{bias} \cdot R_{sh} \cdot \frac{R_{th}^{eff}}{R_{th}^{eff} + R_L + R_{sh}} = \frac{V_{th}}{\eta} \tag{2.87}$$

$$V_{th} = I_{bias} \cdot R_{sh} \cdot \frac{R_{th}^{eff}}{R_{th}^{eff} + R_L + R_{sh}} \cdot \eta \tag{2.88}$$

$$V_{th} = I_{bias} \cdot R_{sh} \cdot \frac{\xi + 1}{2} \cdot \eta \tag{2.89}$$

From equation 2.82 it is obvious that the current responsivity of the TES will be reduced, if R_{th} is not much larger than R_{sh}, R_L and R_0. In this case, also the effective time constant will be larger (equation 2.83). By placing the shunt on chip with the thermistor and using superconducting wiring, extremely low values of R_{sh} can be realized, and R_0 can be neglected. As this is the case for all designs discussed in this thesis, R_0 will not be included in the formulas from this point on, leading to a model as discussed in [46]. For perfect voltage biasing, an infinitely small shunt resistance R_{sh} would be necessary; However, the lower R_{sh}, the higher the necessary bias current I_{bias} for a given working point with R_{th} and the necessary V_{th}. In particular, the resulting joule heating

power of the shunt rises, which imposes an additional thermal load to the cooling stage:

$$I_{bias} = V_{th} \cdot \frac{R_{th} + R_L + R_{sh}}{R_{th} \cdot R_{sh}} \tag{2.90}$$

$$R_{sh} \to 0 \Rightarrow I_{bias} \to V_{th} \cdot \frac{R_{th} + R_L}{R_{th}} \cdot \frac{1}{R_{sh}} \propto \frac{1}{R_{sh}} \tag{2.91}$$

$$P_{sh,joule} = \frac{V_{bias}^2}{R_{sh}} = \frac{V_{th}^2}{R_{sh}} \cdot \left(\frac{R_{th} + R_L}{R_{th}}\right)^2 \tag{2.92}$$

$$\Rightarrow P_{sh,joule} \propto \frac{1}{R_{sh}} \tag{2.93}$$

Hence, a good compromise is to chose $R_{sh} \approx \frac{R_{th}}{10}$ for the (lowest) targeted R_{th}.

The output signal I_{th} of the TES is measured, because of the low impedance of the circuit, using superconducting quantum interference device (SQUID) current sensors[47]. SQUIDs are highly sensitive magnetic flux meters[48]. Combined with a superconducting coil, located in a close, fixed position to the SQUID which transforms the input current to a measurable flux, they can be used to precisely measure the current flowing through this coil by determining the resulting magnetic flux. As the SQUIDs are working at low temperatures, they can be located close to the sensors and be used as low noise preamplifiers. However, the output voltage of the SQUID is nonlinear and periodic. The flux-voltage characteristic of the SQUID and thus the current-voltage characteristic of the current sensor has a periodic and sinusoidal shape. To linearize the transfer function, a negative feedback is applied. To achieve this, a current proportional to the output voltage of the SQUID is fed into a feedback coil attached to the SQUID. By applying this flux in opposed polarity compared to the signal from the input coil, changes in the input signal are compensated, and the SQUID is kept in a fixed working point. A voltage proportional to the feedback current of this flux locked loop (FLL) is used as the output value. This gives a linearized output voltage proportional to the input current with an unknown offset, which is due to the periodicity of the SQUID transfer function. The use of superconducting input coils and wiring allows to limit R_L to the resistance of connectors which can be significantly below $1\,\Omega$.

3 Fabrication and stability

3.1 Initial TES design

3.1.1 Overview

TES have been fabricated at IPHT for more than ten years now. The application focus was put on bolometric systems for astrophysical observations in the THz band[49], as the Submillimetre APEX Bolometer Camera at the APEX telescope in Chile[50]. Adapted from these developments, a SuperCOnducting Terahertz Imager (SCOTI) was set up to demonstrate the applicability of this technology for a security camera. The setup is shown in figure 3.1. A small cryostat, cooled with liquid ^4He and equipped with a ^3He evaporation cooler stage was used as refrigerator. The base temperature was approximately 300 mK. Using a single TES as the sensor, it was capable to demonstrate the basic functionality of a THz camera for security purposes at moderate frame rates of several seconds per image[51]. After implementing a fast optical scanner, it was able to produce circular pictures of 40 cm diameter with 1.5 cm spatial resolution from a distance of 5 m at a maximum frame rate of nearly 1 Hz, still using a single TES bolometer[52]. However, as figure 3.1 shows, the field of view and the optical resolution were reduced at the higher frame rates due to the limited bandwidth of the sensor.

The TES design of SCOTI was used as a basis of the TES developments in this thesis. Its characteristic parameters will be described in the following. Due to its characteristic number of 16 absorbers, it will be called “16A”.

The general concept of a voltage biased TES as described in chapter 2.3 was realized in a pure thin film system. A free standing 1 µm thin silicon nitride (Si_3N_4) membrane was structured to define a platform with weak thermal links to a thermal bath (figure 3.2). The bath is defined by the used crystalline silicon substrate. On top of the platform, absorbers and thermistor are placed. the thermistor is electrically connected to superconducting wiring made of niobium (Nb).

3.1.2 The membrane

A silicon substrate covered with a 1 µm thick layer of Si_3N_4 is used as the substrate and thermal bath. By removing the silicon below the Si_3N_4 in a wet etching process, a free standing membrane is created[53]. The significantly reduced heat capacity of the membrane compared to the substrate combined with the reduced thermal conductance result in a higher sensitivity at a lower time constant. Patterning this membrane is used

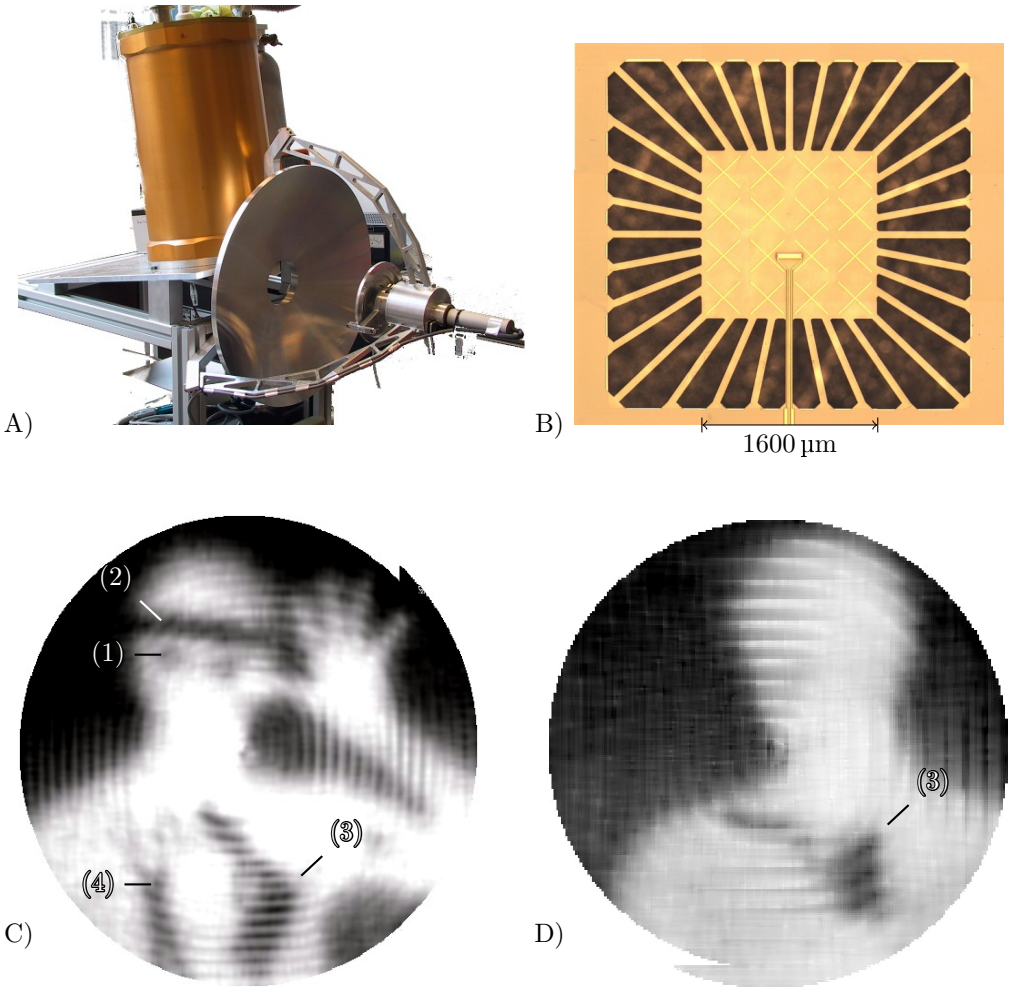

Figure 3.1: Upper Left: The SuperCOnducting Terahertz Imager (SCOTI). Right: Micrograph of a single TES as used in SCOTI. Below: THz images of a person. Left: 0.5Hz frame rate (2s). Right:0.8Hz frame rate (1.25s) with a reduced field of view (upscaled). Visible objects: Glasses (1), a stripe of aluminum tape (2). Hidden under a T-shirt: Aluminum dummy handgun (3), scissors (4).

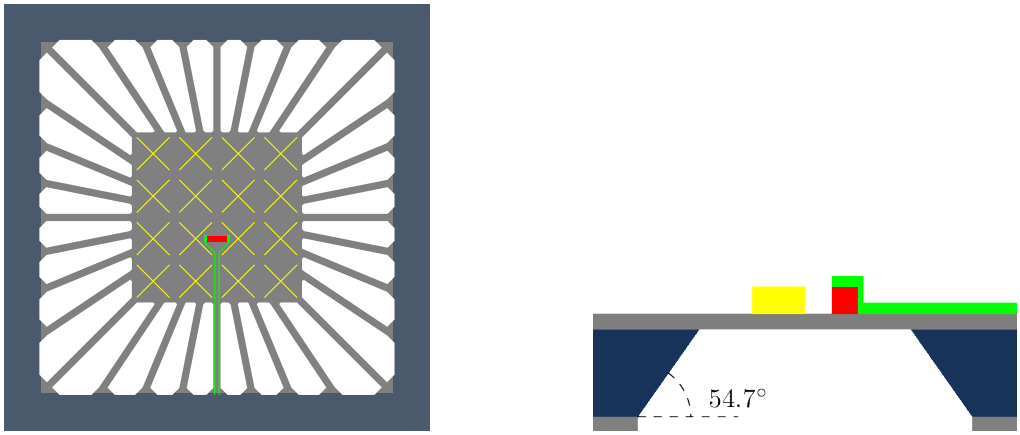

Figure 3.2: Top view (left) and schematic sectional view (right) of the 16A TES design: A set of 16 dipole absorber pairs (yellow) and the thermistor (red) are placed on top of the silicon nitride membrane (gray), that spans the opening of the silicon substrate (blue). The thermistor is electrically connected to superconducting niobium wires (green).

to further reduce the thermal conductivity of the TES and to adjust it to the desired value that is adequate concerning sensitivity and background load. This technology allows to use the same production process for security and astronomical applications, only changes in the lateral geometry are necessary[41].

In the case of 16A, the square shaped membrane has an edge length of 3.3 mm and 32 radially arranged legs that connect the bath to a platform with 1.6 mm edge length. The legs have a width of 68 µm and vary in length from 850 µm to 1200 µm. On the platform, the thermistor and the absorbers are located.

3.1.3 The thermistor

As the thermistor of the TES, a thin film superconductor-metal bilayer is used. In such a system, the quasi-particles as well as the cooper pairs have a finite probability to exist in the superconductor and metal, respectively (figure 3.3). This causes the (superconducting) proximity effect[54], which was first discovered in 1932[55] by the Swedish and German physicists R. Holm[56] and W. Meißner[57]. The critical superconducting temperature T_c is tunable over a wide range below the T_c of the superconductor as a single layer.

Such thin film bilayers with molybdenum (Mo) as the superconducting layer are suitable for TES working in the sub-kelvin range[58]. E.g, they are used in several astronomical applications[59][60].

At IPHT, a gold-palladium (AuPd) alloy of 50 atomic percent (at%) each is used as the

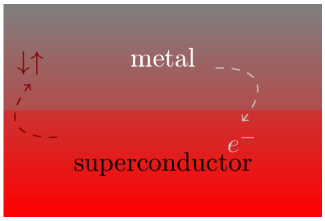

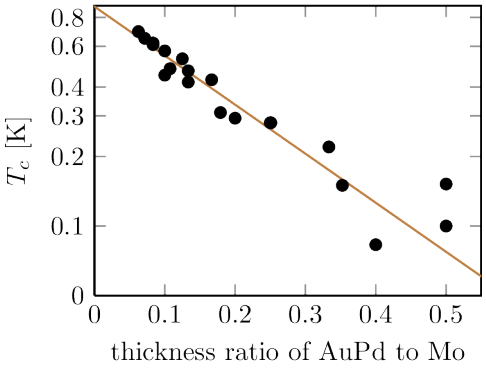

Figure 3.3: Left: Proximity system consisting of a stack of superconductor and a normal conducting metal. Charge carriers as quasi particles and cooper pairs have a non-zero propability to exist in both layers which causes the bilayer as a whole to act as a superconductor with a reduced T_c compared to the single superconducting layer. Right: Proximity effect in Mo/AuPd bilayers produced and measured at IPHT: The transition temperature is tunable from ≈800 mK down to ≈100 mK by adjusting the thickness ratio of the layers. Varying the Mo thickness from 60 to 140 nm at a constant thickness ratio does not affect the resulting T_c. Each point in the graph corresponds to a reference sample of a long term (seven years) series of wafer runs. Layer thicknesses are calculated from deposition times determined from regular calibration measurements. The resulting long term scatter is proportional to the AuPd:Mo thickness ratio.

normal metal, in order to cover the full temperature range of usual TES applications with a single fabrication process (≈100 mK up to several hundred mK, see figure 3.3)[61],[62]. Compared to Mo/Cu or Mo/Au bilayers, the stronger suppression of T_c by the AuPd allows for thinner layers and thus easier production especially in the range of a few hundred mK[63].

In the original SCOTI design, the bilayer was shaped rectangularly, with a base area of 220 µm × 50 µm and a thickness of approx. 100 nm. The 16A samples analyzed in this chapter were produced on the same wafer as those discussed in chapter 6 and had a width of 58 µm for better comparability. The exact geometrical parameters which are also used as the basis of the presented calculations in the following chapters are given in table 3.1.

3.1.4 The absorber

The used absorbers consist of $\lambda/2$ dipole antennas. Each dipole is designed to match the desired wavelength. In case of 345 GHz radiation, corresponding to $\lambda = 870$ µm, the dipole length is 435 µm. The dipoles are placed in a periodic grid structure, covering approx. 2.65% of the area A_{unit} of a unit cell of this grid. This leads to an average

Table 3.1: Geometry parameters of the 16A design.

component	number	height [m]	length [m]	width [m]	total volume [m^3]
platform	1	$1{\cdot}10^{-6}$	$1.6{\cdot}10^{-3}$	$1.6{\cdot}10^{-3}$	$2.56{\cdot}10^{-12}$
thermistor	1	$1.08{\cdot}10^{-7}$	$2.2{\cdot}10^{-4}$	$5.8{\cdot}10^{-5}$	$1.38{\cdot}10^{-15}$
dipole	32	$2.1{\cdot}10^{-8}$	$4.3{\cdot}10^{-4}$	$1{\cdot}10^{-5}$	$2.89{\cdot}10^{-15}$
wiring	2	$1.5{\cdot}10^{-7}$	$7.26{\cdot}10^{-4}$	$1{\cdot}10^{-5}$	$2.18{\cdot}10^{-15}$

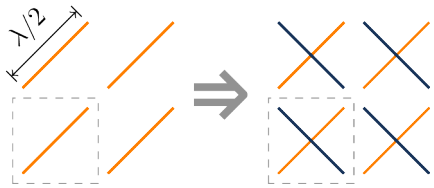

Figure 3.4: Left: Sketch of the dipole absorber structure. The absorbers are located in a periodic grid. The unit cell (marked by a dashed square) contains one $\lambda/2$ dipole absorber. Right: To achieve polarisation independent absorption, two grids with orthogonal orientation of the dipoles are superposed.

square impedance $\overline{Z^{\square}}$ of

$$\overline{Z^{\square}} = \frac{A_{unit}}{A_{abs}} \cdot Z^{\square}_{abs} \tag{3.1}$$

The $\overline{Z^{\square}}$ is matched to the impedance of free space $Z_0 \approx 377\,\Omega$:

$$\overline{Z^{\square}} = Z_0 \tag{3.2}$$

$$Z^{\square}_{abs} = 0.0265 \cdot Z_0 \approx 10\,\Omega \tag{3.3}$$

Such a grid matches one linear polarization. As any polarization can be formally described by a separation into two orthogonal linear components, an orthogonal superposition of two of such grids can be used to achieve polarisation independent absorption. A possible solution are crossed dipole antennas, as they are used in this case (see figure 3.4). As analyzed by [64], a combination of such absorbers with a feedhorn antenna and a backshort reflector can achieve high absorptances.

The 16A design contains 16 absorbers made of AuPd in a grid with 400 µm base length. The dipoles are 435 µm long, 10 µm wide and 21 nm thick. An overview of the geometric parameters of the different components of the 16A design is given in table 3.1.

3.2 Fabrication

Samples were fabricated by the standard IPHT TES process on 4 inch silicon wafers. As substrates low-resistive ⟨110⟩ cut Si was used, covered with a Si_3N_4 layer with a thickness of 1 µm. Reactive ion etching (RIE) was used to open windows at the back side of the wafer. Later in the process, these windows define the membrane sizes of the bolometers. Before deposition of the bilayer for the thermistors, the wafers were cleaned for 2 min in Ar plasma. During deposition, the temperature stayed below 30 °C. The bilayer was magnetron sputtered in situ with a substrate-source distance of about 100 mm. The deposition rates for Mo and AuPd were $14\,\mathrm{nm\,min^{-1}}$ and $7\,\mathrm{nm\,min^{-1}}$, respectively. The base chamber pressure was below 6×10^{-8} mbar, the working pressure was 1×10^{-3} mbar for Mo and 4×10^{-3} mbar for AuPd. The thermistors were structured in a lift-off process.

Further sputtering steps with subsequent lift-off were used to deposit and pattern the Nb wiring, the absorbers and the bond pads, respectively. The shunt resistors were deposited in an electron beam evaporation and lift-off process. After finishing the thin film deposition, the front side of the wafer was protected with a wax cover. Then, the Si behind the Si_3N_4 membranes was completely removed in a sodium hydroxide solution ($NaOH_{aq}$) wet etching process. Because of the anisotropic nature of the $NaOH_{aq}$ etching, which is slower on ⟨111⟩ planes compared to the other directions in the crystal, the resulting windows are defined by ⟨111⟩ oriented walls at 54.7°. A final RIE step defines the spider leg structure of the Si_3N_4 membranes.

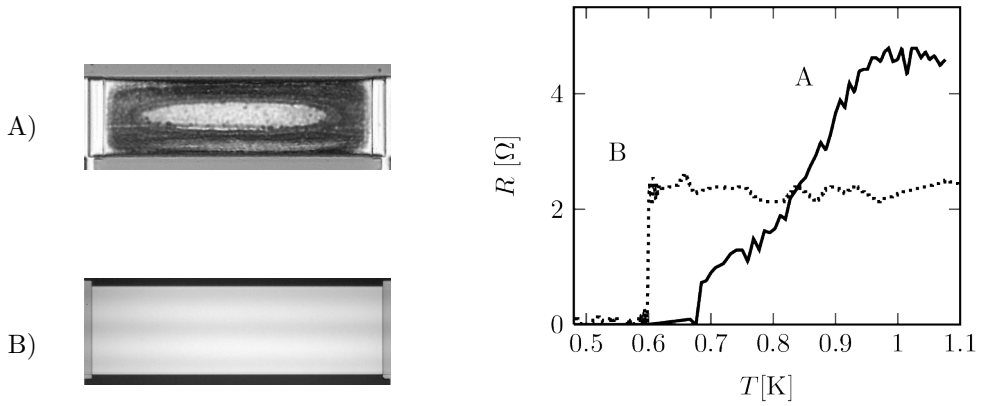

Figure 3.5: A) VIS micrograph of a visibly degraded thermistor. The usually homogeneous surface of the bilayer in between the electrical contacts (white) looks roughened, seemingly caused by a process starting from the edges, as the center is less affected. B) A faultless thermistor is shown for comparison. Right: A) Corresponding R-T curve of the degraded sample, revealing substantial increase of R_n from initially approximately $2\,\Omega$ and drastic widening of the transition width to several hundred millikelvin. B) shows an unaffected steep transition.

3.3 Parameter stability

TES based on the 16A design as described above sometimes showed broadened transition widths ΔT_c and a local T_c variation between different thermistors (see table 3.2) that is higher than expected from the known production parameters and partly not reproducible. In addition, degradation effects could be observed that led to declining T_c values and variations of ΔT_c in time and sometimes even destroyed the TES physically, as shown in figure 3.5). According to equation 2.83, the former weakens the feedback strength and thus is expected to cause higher time constants of the TES. The latter aggravates the implementation of arrays of TES, because varying T_c values in an array cause the working points to vary from TES to TES. This makes common biasing hard to realize and would lead to reduced performance as non-ideal working points have to be accepted. Thus, low, well defined and long term stable ΔT_c values are necessary for arrays of fast TES bolometers. Especially for large arrays, a low scatter in T_c is essential.

These parameters can be influenced by oxidation of the molybdenum as part of the bilayer which is forming the thermistor of the TES. Therefore, chemical degradation, for example by condensed water, can be expected to significantly contribute to the observed effects. To understand the underlying processes and the relevance concerning the deteriorated parameters of the TES, different analyses of single Mo layers and Mo/AuPd bilayers have been performed. Starting with the degradation process of pure thin film

Table 3.2: T_c and ΔT_c variation, measured at 3.5 µA of different thermistors on two different sample chips of type EL.

chip	TES	T_c [mK]	ΔT_c [mK]	R_n [Ω]
1	1	689	16.2	2.32
1	2	701	18.0	2.31
1	3	694	14.6	2.21
2	1	690	9.2	2.31
2	2	690	13.8	2.35
2	3	697	19.6	2.31

Table 3.3: X-ray diffraction results of Mo-layers for different substrates. The crystallite size was estimated using the Scherrer equation.

substrate	FWHM Mo (110) [°]	crystallite size [nm]	rocking curve FWHM Mo (110) [°]
Si	0.3	33	9.5
Si	0.34	27	
Si_3N_4	0.4	24	9

Mo (section 3.3.3) to judge its sensitivity under exposure to water, the found results were compared to the effects on Mo/AuPd bilayers (section 3.3.4) under the same conditions. The relation of the observed degradation to the superconductivity parameters of the bilayer is discussed in section 3.3.5. The results of these analyses were published in [65].

3.3.1 Samples

Samples were produced as described in section 3.2. However, for samples analyzed in energy dispersive electron probe micro-analyzer (EPMA) measurements as in sections 3.3.3 and 3.3.4, substrates without Si_3N_4 coating were used. This type of substrate is advantageous for EPMA measurements, as will be explained in section 3.3.2. X-ray diffraction analysis showed that the Mo layer has the same structural characteristics with and without the Si_3N_4 layer on the substrate. In particular, all Mo layers are polycrystalline, grow in the (110) direction, have a similar lattice constant variation and rocking curves (see table 3.3). For the measurements in section 3.3.3, an unstructured

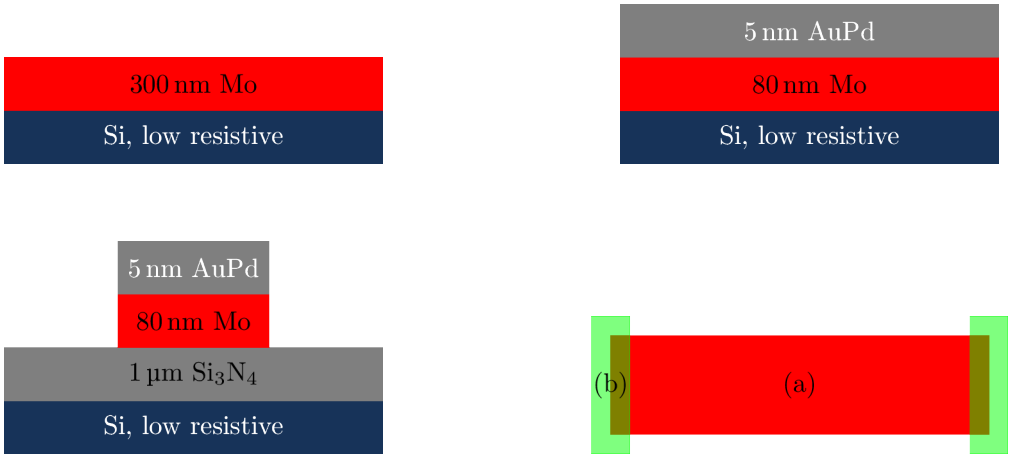

Figure 3.6: Sectional view of samples of type *SL* (upper left), *BL* (upper right) and *EL*. Bottom right: Top view of Mo/AuPd bilayer (a) with niobium wiring connectors (b). The uncovered area of the bilayer is 200 µm × 58 µm.

single Mo layer (*SL*) of 300 nm thickness was used (figure 3.6), as the quantitative EPMA is improved by using a thick layer. To come close to the worst case of bilayers, samples with thinner AuPd layers than used in the camera systems were prepared for the bilayer experiments. Therefore, an unstructured bilayer (*BL*) of (80 ± 3) nm Mo and (5 ± 1) nm AuPd is analyzed in section 3.3.4. A second wafer with a bilayer with the same parameters was produced for electrical measurements. Following the 16A TES design (see section 3.1), it was deposited on a Si_3N_4 covered substrate and structured with 200 µm × 58 µm wide elements of which seven were arranged on a chip with niobium wiring, following the standard test sample design shown in figure 4.2. On half of the sample chips, the silicon was not removed under the nitride membrane, as the free standing membrane would not allow for fast drying of the sample after the different immersion steps, which is necessary to ensure defined immersion times. We call these samples *EL-n*, where *n* denotes the position index of the thermistor on the chip. They were used for the experiments described in section 3.3.5.

3.3.2 Methods

To achieve meaningful results, a defined oxidation of the samples was necessary. This was achieved by first cleaning and then immersing them in deionized water at room temperature for a given time. Afterward, they were immediately dried with pure nitrogen gas.

To determine the oxidation level in the Mo layers of both *SL* and *BL* samples, EPMA measurements were performed[66]. This method allows to quantitatively analyze the

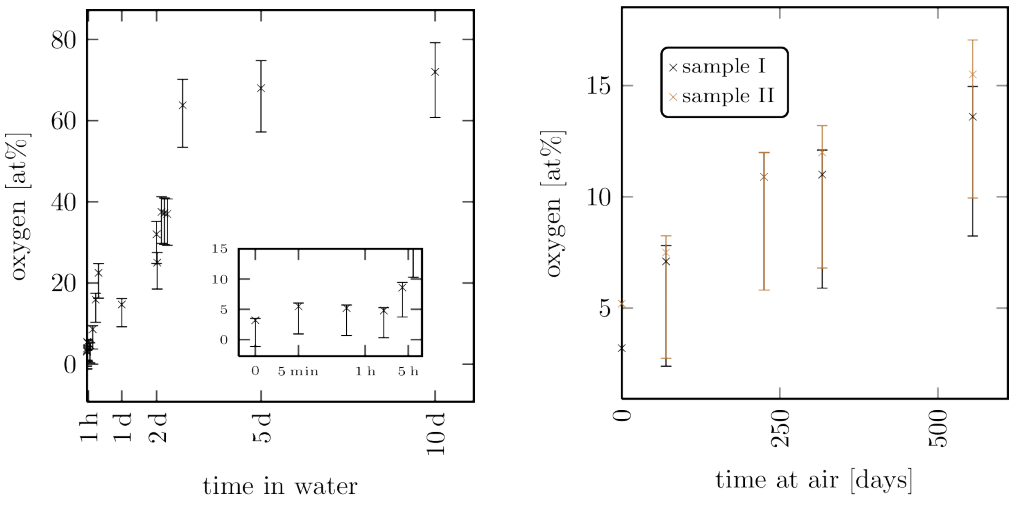

Figure 3.7: Left: The relative amount of oxygen in the excited volume of samples of type *SL* found by EPMA analysis vs. exposure time. Within the first few hours oxidation is slow (inset). The excited volume extends in depth from ≈100 nm to ≈200 nm with increasing oxidation, because of the higher penetration depth in MoO_x compared to Mo. Right: Oxidation process of samples stored outside the desiccator in an air-conditioned room. The rel. humidity was measured as (40 ± 5) % for 5 days a week, and up to 50 % for two days a week. Initially, sample I was immersed for 30 s, sample II for 30 min.

chemical composition of a sample. This is achieved by focusing an electron beam on it. As a result, characteristic X-rays are emitted. By analyzing the spectra of these emissions, the proportions of the chemical components of the sample can be found. The usual method to avoid misleading charging effects during these measurements is to cover the sample with a thin conductive layer. This would have influenced the results and the following immersion steps. Therefore, the electrically conducting substrates in both the *SL* and *BL* were used to minimize the performance degrading charge buildup in the sample.

The temperature dependence of the resistance of the *EL-n* samples at low temperatures was measured in the DC regime as described in section 4.3.2 with a constant bias current of 3.5 µA. While on samples with free standing Si_3N_4 membranes a reduced transition width was measured due to self-heating effects, on those samples where the silicon behind the Si_3N_4 was not removed, this current was low enough to ensure self-heating effects were negligible (see also figure 3.12 in section 3.3.6).

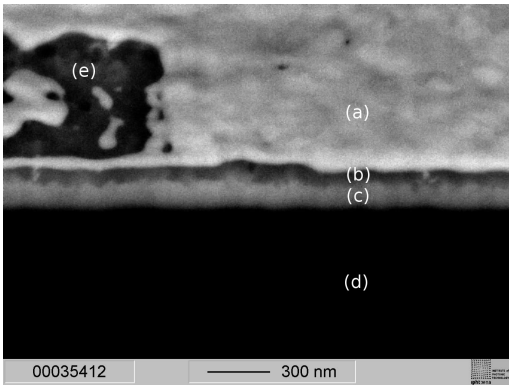

Figure 3.8: SEM BSE image at 45° tilt of a FIB cut through a sample of type *SL* after 66 h in water. A protective Pt layer (a) was sputtered on the sample just before the cut. It was locally removed by the ion beam (e). An oxide layer (b) of ≈ 100 nm thickness can be clearly separated from the pure Mo (c) and the substrate (d). This suggests exhaustive oxidation in (b), separated from pure metal by a negligible intermediate transition zone.

3.3.3 Oxidation of molybdenum

Bulk Mo is rather insensitive to water and oxygen at room temperature. Surface oxidation will form an oxide barrier of MoO_3 strongly reducing further oxidation up to temperatures of 790 °C, which is the melting temperature of MoO_3[67]. Similar behavior is reported for thin films exposed to pure water in [68], while a continuous oxidation by water and moisture in e-beam deposited Mo films is observed by [69]. The *SL* samples produced at IPHT with thin Mo films sputtered at room temperature, showed significant oxidation when in contact with water. As can be seen from figure 3.7, the oxygen concentration did rise slowly within the first few hours, probably due do the formation of a dense MoO_x layer (figure 3.7, inset). This could be confirmed by the analysis of focused ion beam (FIB) cuts on partly oxidized samples, which showed a clear border between pure and oxidized Mo (figure 3.8). An increase in oxidation rate was followed by the formation of visible cracks (figure 3.9). They can be explained by the integration of oxygen which increases the volume, causing internal stress of the layer. Resulting cracks increase the surface area. With increasing depth, they permit the water to come in direct contact to the inner regions leading to faster oxidation. After 66 h, the formation of an oxide layer of approx. 100 nm could be observed (figure 3.8). After 10 days, cracks in the 300 nm film had reached the substrate and the film separated into pieces which detached from the substrate surface (figure 3.9, bottom right).

The Mo (110)-peak, that was clearly visible in X-ray diffraction measurements of unoxidized samples, reduced in amplitude with increasing oxidation and finally was no longer measurable after 10 days, meaning exhaustive oxidation of the Mo. Since no

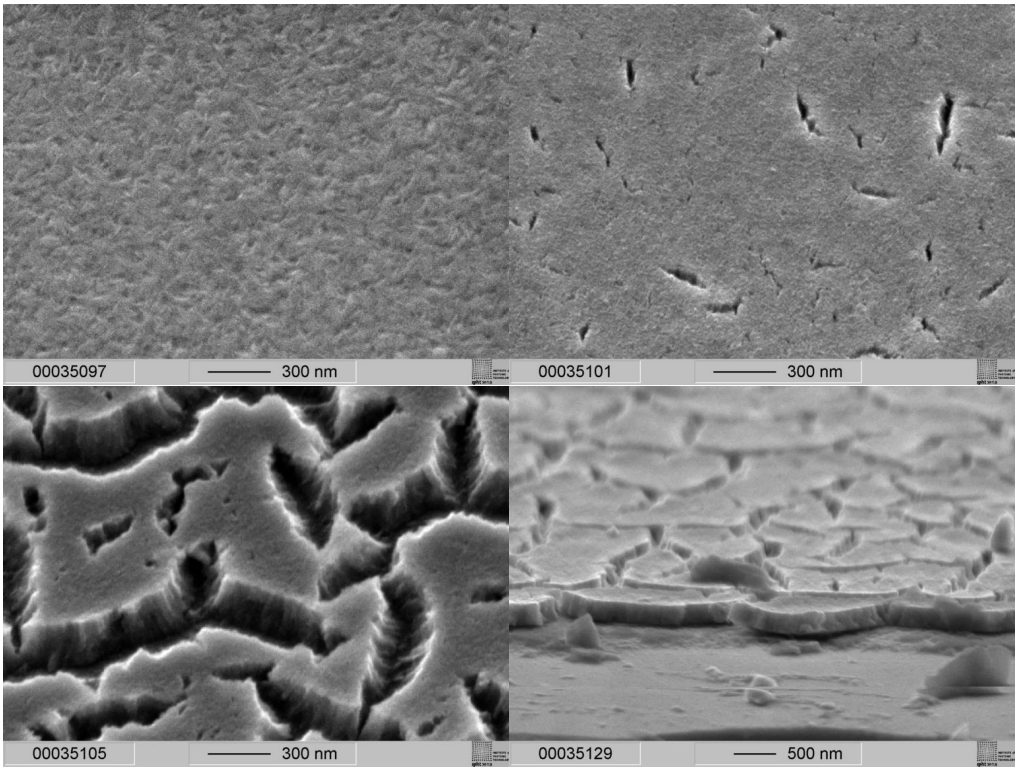

Figure 3.9: SEM micrographs at 40° tilt of samples of type *SL* stored in a desiccator (upper left), 66 h (upper right) and ten days in water (bottom). The cracks in the latter sample reach the substrate and the film separates into partly detached pieces (bottom right, 60° tilt).

MoO_x peaks could be measured, the formed oxide was amorphous. EPMA measurements resulted in (74 ± 8) at% of oxygen in this state, making MoO_3 (75 at%) the most probable oxide formed. However, MoO_2 (66 at%) would also fit the error margins.

Unoxidized samples left in ambient conditions for one week showed no significant changes in comparison to the reference samples stored in a desiccator, confirming the findings in[70]. Furthermore, partly oxidized samples showed similar stability. This confirms the protective properties of the formed surficial oxide layer. Thus, the oxidation in air is much slower compared to the effect of water and is independent of the initial oxidation state, as can be seen from the right side of figure 3.7 that shows the results of a long term evaluation. The corresponding samples were stored for more than one year at ambient conditions outside the desiccator in a room equipped with an air-conditioning system. The relative humidity was measured as (40 ± 5) % for 5 days a week, and up to 50 % for two days a week (on weekends). EPMA measurements showed that they reached a comparable oxidation level within this time as samples immersed for a few hours. Thus, oxidation at humid air has to be taken into account for long term stability; Condensed water is able to extremely accelerate this process.

3.3.4 Bilayers

In the following, the results from above will be compared to the effect of oxidation on bilayers. The directional growth of the oxide layer normal to the surface in contact with water observed in the *SL* samples suggests higher resistance to oxidation for *BL*, as the only uncovered surfaces of the Mo are the edges of the samples. As expected, EPMA analysis on a *BL* sample showed no significant oxidation after 50 h of immersion, compared to several 10 at% of oxygen in *SL* samples. However, this does not apply in cases of structural defects of the AuPd layer. After 1 min of immersion single local spots of circular shape and a few micrometer in diameter could be found on some samples, which grew in size and number with increasing immersion time (see figure 3.10). Their convex surface in earlier states and the nearly perfect circular shape strongly indicates point-shaped openings in the AuPd layer, through which oxidation of the Mo can happen locally. Resulting stress between the layers seemingly has a very destructive effect since the bilayer is strongly degraded or even removed in areas of serveral hundred µm diameter after 50 h (figure 3.10, D), whereas pure Mo did not show such effects. EPMA analysis shows that while in regions outside of such spots (figure 3.10 region (a)) no oxidation effect can be seen, due to the protection by the AuPd layer, (b) shows a strong oxygen peak. This means while the AuPd layer is still there, the Mo layer is oxidized and transformed to a porous material, which can be seen once the AuPd is ruptured and lifted. In doing so it is partly ripping off the Mo from the substrate (figure 3.10 (c)), laying the latter open.

Degradation effects could also be observed in several Mo/AuPd bilayers used as TES after some time of exposure to air (figure 3.10 E), where the time varies strongly, but tends

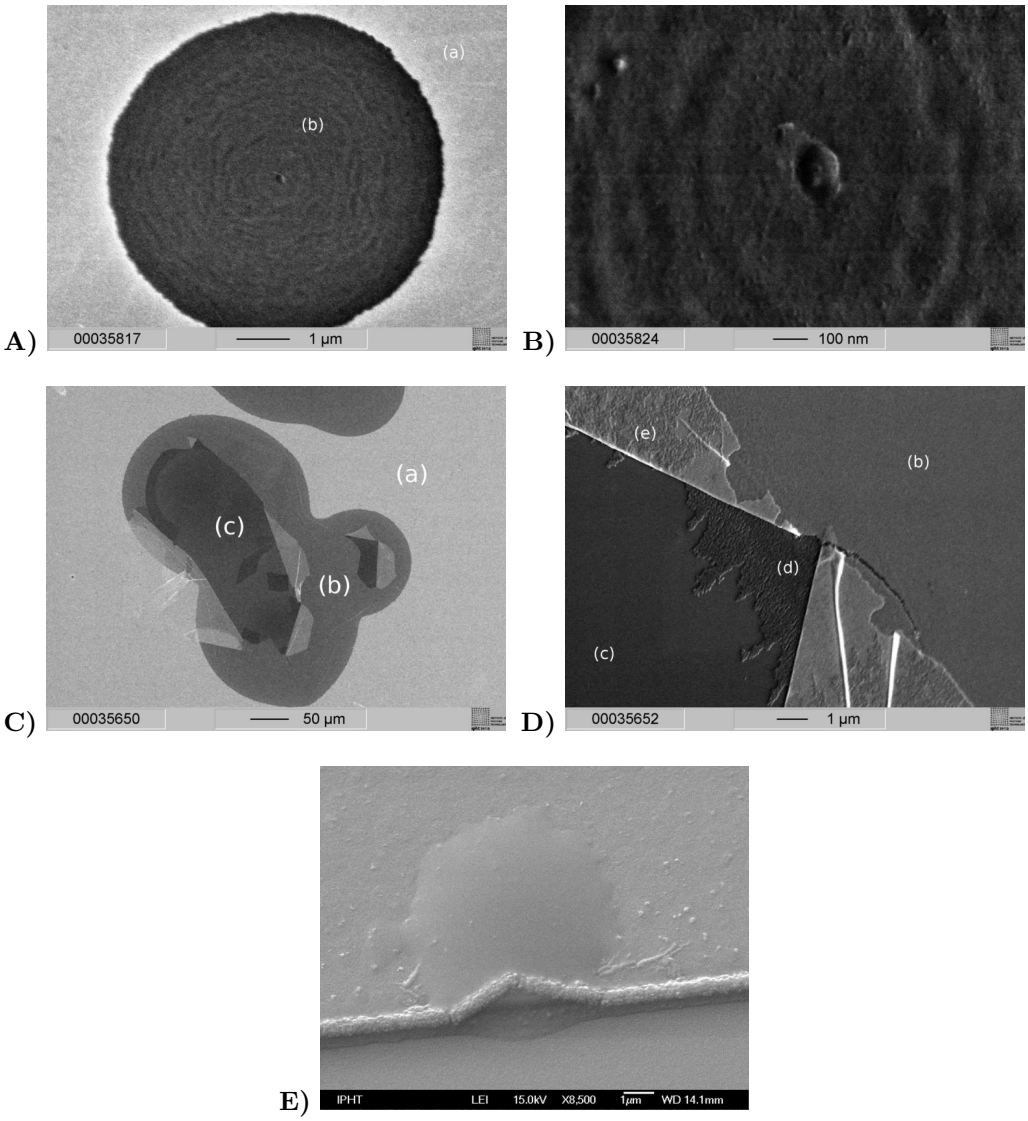

Figure 3.10: A) A Circular oxidation spot on a sample of type *BL* immersed for 30 min. B) In the center of all such spots, a small structure can be observed.
C) and D) *BL* immersed for 50 h. EPMA analysis shows that while in region (a) no oxidation effect can be seen, (b) is strongly degraded. In region (c), the substrate is laid open. In the transition from (b) to (c), the AuPd layer is lifted (e), sometimes with Mo attached, in other regions leaving uncovered Mo (d). E) Structured Mo/AuPd bilayer (type *BL*) degraded at the outer edge after several weeks of contact to air.

Table 3.4: Electrical parameters after different immersion times for samples of type *EL*.

		T_c [mK]				ΔT_c [mK]				R_n [Ω]	
immersion time		0	30 min	4.5 h	17 h	0	30 min	4.5 h	17 h	0	66 h
w/o SP	*EL*-1	689	664	651	635	16	25	20	20	2.3	448
	EL-3	701	694	680	665	18	22	20	30	2.4	521
	EL-6	694	664	631	613	15	69	26	12	2.3	565
average		*695*	*674*	*654*	*638*	*16*	*39*	*22*	*21*	*2.3*	*511*

to be smaller for thinner AuPd layers. Based on the measurements described above, two effects have to be considered: Oxidation from uncovered sides of the structured bilayer (see section 3.3.1) and oxidation through defects in the AuPd layer. In a given area, the rate of oxidation strongly depends on the local defect density.

3.3.5 Electrical measurements

For the analysis of the effect on the usability of these bilayers as sensors, the electrical behavior of samples of type *EL* was measured. Table 3.4 shows the influence of immersion in water on several superconductivity parameters. After 30 min the T_c of the bilayers was already reduced significantly, and decreased further for longer immersion times. ΔT_c of these samples varied strongly without a general tendency. From the continuous reduction of T_c it can be deduced that no significant oxidation through the top AuPd layer happened within the first 17 h. Such oxidation would first affect parts of the Mo close to the AuPd, reducing the coupling and the proximity effect[54] and thus resulting in an increased T_c[71, 72]. It is known that changes in stress of the bilayer can affect T_c[73], thus a possible conclusion is that oxidation from the sides and resulting stress to the bilayer is a likely cause of the reduction in T_c. In this case, ΔT_c will be dominated by local inhomogeneities in oxidation of the bilayer at the edges. The reducing rate of T_c change again is a sign of the forming of an oxide barrier slowing down further oxidation. Assuming the speed of growth of the oxide layer to be comparable to the case of pure Mo (samples *SL*) where an oxide layer of 100 nm is formed within several days, full oxidation would take weeks as the width of the bilayer is approx. 60 µm.

Relevant changes in R_n could be observed for the first time after several days of immersion, when large scale degradation was also visible on the AuPd layer. Based on these results it can be assumed that for several hours, only small portions of the bilayer are changed by oxidation, stressing the high sensitivity of superconductivity to even slight oxidation.

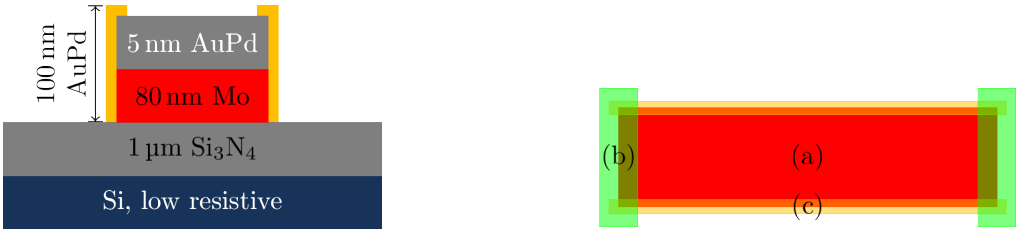

Figure 3.11: Left: Sectional view of samples of type *EL* with SP. Right: Top view of Mo/AuPd bilayer (a) with niobium wiring connectors (b) and AuPd SP (c). The uncovered area of the bilayer is 200 µm × 50 µm.

3.3.6 Sidewall passivation (SP)

Samples

For the following experiments, samples of type *EL-n* as described in section 3.3.1 were used. Sidewall passivation (SP) was added at the otherwise unprotected edges of the superconductors (see figure 3.11). This was applied to four of these elements per chip, as to leave 3 elements without SP for direct comparison. The AuPd film used as SP was chosen to be 100 nm thick and 8 µm wide, laterally overlapping the bilayer by 4 µm. It was structured with lift-off, to avoid etching on top of the fragile bilayer. The combination of bilayers with and without SP on the same chip ensures identical production and later treatment of the compared bilayers.

Effects of SP

To further compare the significance of oxidation from the top and the edges, we compared samples with and without SP as described in section 3.3.6. For samples with SP, oxidation will mainly happen through defects in the thin AuPd top layer, as the 100 nm thick and 4 µm wide AuPd SP will prevent oxidation from the previously unprotected edges of the Mo layer and constitute a much stronger barrier to water than the thin AuPd top layer.

As table 3.5 shows, the SP ensures low initial values of the transition width. Results for a larger number of samples are presented in figure 3.12. Also a reduction of the scatter of T_c can be observed in agreement with results for Mo/Cu bilayers found in[74]. This can be explained by avoiding any early oxidation, resulting in a more homogeneous coupling of the two layers at the edges and thus a lower local T_c variation. This low parameter variation is highly reproducible, as the table shows. Furthermore, T_c itself is reduced reproducibly by adding SP on these samples. This could not be observed on samples with target values of T_c below 600 mK. An increasing number of structural defects for thinner AuPd layers would be reasonable. It could cause a reduction of the

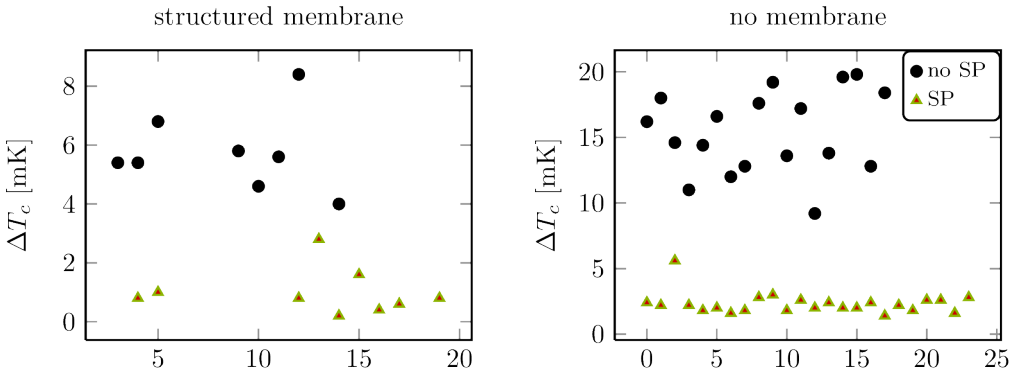

Figure 3.12: Transition width of a series of samples of type *EL* without and with SP. The abscissae denote arbitrary sample numbers. Left: Because of the low thermal conductance, self heating of the thermistor leads to seemingly lower transition widths. Right: This can be avoided by not removing the silicon substrate below the silicon nitride. In this case, the transition width is independent on the measurement current, thus representing the actual value. Both graphs show a strong reduction in ΔT_c and its variation.

adhesion of the AuPd cover to the Mo layer, especially towards the edges, and thus lead to a weakened proximity effect. This might explain increased T_cs as well as high initial transition widths. The covering of the edges with SP might improve the definedness of the layer contact at the edges and thus avoid these effects. However, for a clear explanation of this behavior, extensive experiments are necessary which go beyond the scope of this thesis.

Throughout the first 17 h of immersion, no significant change in T_c could be observed for samples with a SP, and the variation of ΔT_c remained low. This confirms that the changes in the samples without SP were caused by oxidation from the edges. Hence, even in the case of higher T_c and thus thin AuPd layers, SP can drastically reduce the sensitivity to degradation.

After immersing the samples with a SP for 66 h, surficial changes were visible in large areas similar to those observed on samples of type *BL*. Their R_n increased, and only some regions of the samples were superconducting, shown by a non-zero residual resistance. These effects can be attributed to slow oxidation through the top AuPd layer. Even in this state, the samples without SP showed stronger degradation. Therefore, edge oxidation will probably support oxidation from top by affecting the structure of the AuPd layer.

Table 3.5: Electrical parameters after different immersion times for samples of type *EL* with and without SP. Sample *EL*-5 shows a local distortion on the surface, probably causing the higher ΔT_c.

		T_c [mK]				ΔT_c [mK]				R_n [Ω]	
immersion time		0	30 min	4.5h	17h	0	30min	4.5h	17h	0	66h
w/o SP	*EL*-1	689	664	651	635	16	25	20	20	2.3	448
	EL-3	701	694	680	665	18	22	20	30	2.4	521
	EL-6	694	664	631	613	15	69	26	12	2.3	565
average		*695*	*674*	*654*	*638*	*16*	*39*	*22*	*21*	*2.3*	*511*
with SP	*EL*-2	609	608	606	610	2.4	2.4	4.7	2.0	2.1	19
	EL-4	613	613	609	611	2.2	2.0	2.5	2.0	2.0	241
	EL-5	607	606	608	607	5.6	5.0	5.2	4.8	2.1	27
	EL-7	607	608	604	606	2.2	2.2	2.6	1.6	2.0	16
average		*609*	*609*	*607*	*609*	*3.1*	*2.9*	*3.8*	*2.6*	*2.1*	*76*

Table 3.6: Geometry parameters of the 16A design with SP.

component	number	height [m]	length [m]	width [m]	total volume [m^3]
platform	1	$1{\cdot}10^{-6}$	$1.6{\cdot}10^{-3}$	$1.6{\cdot}10^{-3}$	$2.56{\cdot}10^{-12}$
thermistor	1	$1.08{\cdot}10^{-7}$	$2.2{\cdot}10^{-4}$	$5.8{\cdot}10^{-5}$	$1.38{\cdot}10^{-15}$
dipole	32	$2.1{\cdot}10^{-8}$	$4.3{\cdot}10^{-4}$	$1{\cdot}10^{-5}$	$2.89{\cdot}10^{-15}$
wiring	2	$1.5{\cdot}10^{-7}$	$7.26{\cdot}10^{-4}$	$1{\cdot}10^{-5}$	$2.18{\cdot}10^{-15}$
SP	2	$1{\cdot}10^{-7}$	$2.28{\cdot}10^{-4}$	$8{\cdot}10^{-6}$	$3.65{\cdot}10^{-16}$

3.3.7 Applicability

Low scatter of T_c and ΔT_c as well as long term stability are important requirements on Mo/AuPd bilayers for TES applications. The found strong and continuous reduction of T_c as well as the increased values and variation of ΔT_c in such bilayers was caused by oxidation of the Mo, even by only a few percent by volume. Contact for a few minutes only to e.g. condensed water can degrade such bilayers measurably. It was possible to reduce this significantly by adding SP at the uncovered edges of the bilayer, leaving only oxidation through defects in the covering AuPd layer. Even in the investigated case of higher T_c and thus very thin AuPd layers, the transition width could be reduced by this measure and kept low even in direct contact to water for several hours. No significant T_c change was measured in this case. No negative side effects of SP could be observed. The geometry parameters of the 16A design including SP are given in table 3.6.

4 Characteristics of the initial TES design

The 16A TES design as used in SCOTI was taken as a basis for the development of appropriate sensors for a THz video camera for security applications. The results of SCOTI showed, that for the primary requirements, a larger field of view and higher frame rates, faster TES implemented in multi-sensor arrays were necessary. To define the precise steps of adjustment, the characteristics of this TES design was determined in the following sections. The development of an appropriate computer model as a basis for optimizations is described in section 5.2.3.

4.1 Testbed cryostat setup

For the different measurements on TES, a dedicated multi-purpose cryostat was designed for series measurements on test samples. The cryostat is evacuated to 1×10^{-7} mbar to limit the heat transfer by gas particles to a negligible level. Liquid nitrogen is used to supply a precooling stage at 77 K. All wires are thermally anchored on the different temperature levels to limit the heat load to the next temperature stage, as cooling power and heat capacities decrease with temperature. For the same reason, all wiring is limited to a diameter of 100 µm, and has a minimum length of 1 m. Finally, manganin wiring with low thermal conductivity and an electrical resistance of approximately $50\,\Omega\,\mathrm{m}^{-1}$ is used for all lines except those for which a lower resistance is necessary. In the latter case, copper wiring is used.

The inner surface of the outer shell of the cryostat is equipped with a highly reflective surface to reduce the thermal load by radiation on the 77 K stage. The load is proportional to the emissivity ϵ of the surface, which is given by $1 - r$ with the reflectivity r (Kirchhoff's law of thermal radiation). Similarly, a cooled and highly reflective radiation shield at the 77 K stage further reduces the radiative load on the lower temperature levels. As the load is proportional to the fourth power of the temperature according to the Stefan–Boltzmann law, this causes a reduction by a factor of more than 200.

The intermediate thermal stage is cooled with liquid helium-4 (l^4He). Reducing the vapor pressure of the l^4He to approximately 1.5 mbar results in a temperature of 1.3 K. This allows to condense helium-3 (^{3}He) which has a critical temperature of ≈ 3.3 K in the last temperature stage, a helium-3 (^{3}He) evaporation refrigerator. Again, a thermal shield is limiting the radiative load from the l^4He stage to the last stage, where in a closed

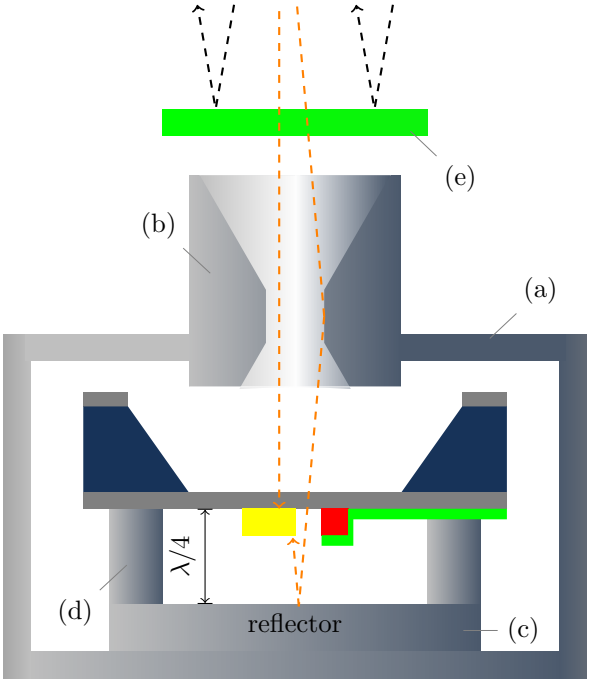

Figure 4.1: The bolometer is surrounded by a superconducting aluminum shield (a) cooled down to T_{bath} to protect it from thermal radiation of the setup and electromagnetic and magnetic distortions. The signal is coupled into this casing through feedhorn antennas (b). To increase the absorption efficiency, a backshort reflector (c) is located behind the membrane at a distance of $\lambda/4$, which is defined using spacers (d). A set of optical filters (e) defines the bandwidth of the received radiation that is coupled to the feedhorn antenna.

cycle system ^{3}He can be liquified inside a small container attached to the experimental platform. A temperature controlled sorption pump reduces the vapor pressure of the ^{3}He to values in the range from 10 mbar to 10 µbar, giving a continuously controllable temperature range from 1 K to 350 mK, which is used as the base temperature for experiments. Two different measurement chambers as described below are attached to this stage. They are connected to the SQUID readout (see section 2.4) which is located at the intermediate stage at 1.3 K with superconducting wiring to avoid ohmic resistance and limit the thermal load.

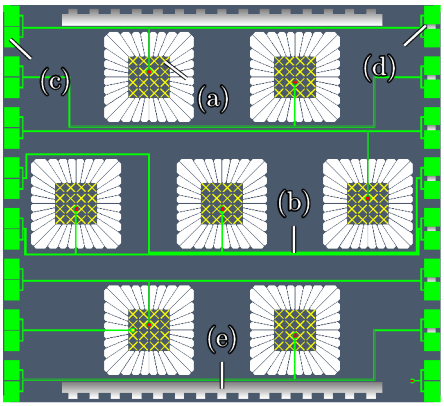

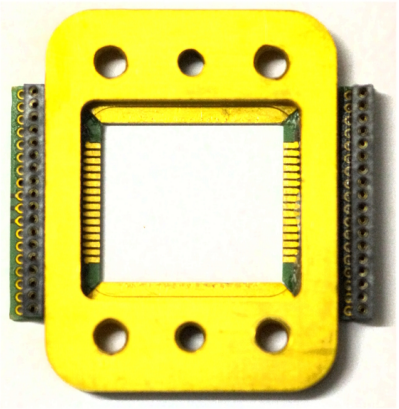

Figure 4.2: Left: Layout of the standard test sample design used throughout this thesis. It contains seven TES (a) arranged in a regular hexagonal structure. Superconducting wiring (b) made of niobium connects the TES and the bond pads (c). The shunt resistor (d) is included on the chip to realize small resistances. Additional bond pads (e) along the electrically unused edges of the chip are used to thermally couple the chip to its carrier. Right: Photograph of a carrier for TES sample chips as shown on the left. It is made of electrolytic copper plated with gold to ensure good thermalization of the chip and the PCBs. Along two sides of the sample chip, it provides gold plated surfaces in 0.2 mm distance, which are thermally coupled to the chip using short gold bonds. On the other two sides, the PCBs are glued to the carrier. The asymmetric placement of the connecting plugs referring to the center of the carrier allows to provide two different connection modes.

4.2 System integration

Figure 4.1 shows how the TES is integrated into the system. The setup concept is the same for the testbed cryostat as well as for the camera systems: A set of optical filters limits the bandwidth of the incoming radiation. For each sensor, a feedhorn antenna defines the angular field of view of the TES and transfers the radiation into a closed casing made of aluminum, which contains a chip with several TES. This casing is cooled down to T_{bath} and is superconducting at that temperature. Thus, it serves as a magnetic and electromagnetic shield for the contained sensors, removing external noise influences and thermal radiation. Opposed to the output cone of the feedhorn antenna, at a distance of $\lambda/4$ behind the membrane of the TES, an aluminum backshort enforces a maximum of the electric field component of the radiation in the plane containing the absorber, improving the absorption efficiency[64].

All sample chips analyzed in the testbed cryostat were produced with a fixed arrangement of TES, electrical wiring and bond pads to allow for simple sample changing and backwards compatibility. The general layout of such a chip is shown in figure 4.2: Seven TES are arranged in a regular hexagonal structure with fixed center coordinates to pro-

vide the possibility to measure different chips without the need to change the surrounding system, providing better comparability. Evenly distributed pairs of bond pads along opposed edges of the chip allow for short bonding distances to the carriers PCB, while the strip lines of the PCB can be short and wide to minimize parasitic resistances.

The carrier used in the testbed cryostat itself is shown on the right side of figure 4.2. It is made of gold plated electrolytic copper. Along two sides of the sample chip, it provides gold plated surfaces in 0.2 mm distance, which are thermally coupled to the chip using short gold bonds. On the other two sides, the PCBs are glued to the carrier, each with a distance of 0.2 mm to the chip. Each bond pad is connected by two aluminum bond wires to a wide, gold-plated strip line. The connection between PCB and carrier is realized using a thin film of stycast epoxy directly attaching the wired surface of the PCB to the carrier to thermalize the wiring. Two connecting plugs attached to the outer edges of the carrier and soldered to the PCB allow for fast sample changing. The asymmetric placement of the connecting plugs referring to the center of the carrier allows to provide two different connection modes in the cryostat by plugging it to the measurement chamber either unrotated or rotated by 180°. These two connection modes are used to provide the capability to subsequently measure the voltage-temperature characteristic of the thermistor as described in section 4.3.2 and the current-current characteristic of the TES (section 4.3.4) without the need for changes of the bonding.

4.3 Characteristic of the 16A TES

4.3.1 Heat capacities

The heat capacity of an ideal crystalline and infinitely large solid at low temperatures can be described mainly by the sum of the contributions of phonons and electrons. At low temperatures, the difference between the values for constant volume C_V and constant pressure C_P is negligible [76]. Therefore, it will just be called heat capacity in this thesis and denoted by C for absolute values and c for the specific heat capacity. In materials without conduction electrons like isolators and superconductors significantly below their transition temperature, electrons do not the contribute to the heat capacity. Other processes like magnetism can add terms to the heat capacity which are usually small and negligible for a consideration of total values. In real materials, deviations from the ideal crystal structure, boundaries, defects and impurities can lead to significant differences from the ideal values. However, as measurements of the heat capacities especially in small volumes, thin films and at temperatures below 1 K are complex in implementation, the use of experimentally found bulk values is a common means for estimations of the heat capacity of thin film structures [76].

The phonon contribution c_{ph} to the specific heat capacity c can be described by the

Table 4.1: Literature values of relevant properties of the used materials. These are bulk values, which can significantly differ from thin film properties. The values in this table are taken from or calculated based on values from [75–79]. The values for AuPd are deduced from averages of the per particle values of Au and Pd. The value for k of Si_3N_4 is derived from measurement data given by [80] for thin film low stress Si_3N_4 in the range from 0.2 K to 1 K. "WFL" marks values that are estimated as needed from the particular electrical conductivity using the Wiedemann-Franz law (eqn. 4.14).

material	β $[\mathrm{J\,K^{-4}\,m^{-3}}]$	γ $[\mathrm{J\,K^{-2}\,m^{-3}}]$	θ_D [K]	k $[\mathrm{W\,m^{-1}\,K^{-1}}]$
Mo	2.27	224	450	WFL
AuPd	29.4	540	-	WFL
Si_3N_4	0.58	0	-	$0.0129 \cdot T^{2.2}$
Nb	8.39	0	277	-
Au	44.8	67.5	162	-
Pd	11	1,100	274	-

Debye model, which gives (cf. [75]):

$$c_{ph} \approx \frac{12}{5} \cdot \frac{\pi^4 \cdot N_A \cdot k_B}{\theta_D^3} \cdot T^3 \tag{4.1}$$

Here, N_A denotes the Avogadro constant, k_B the Boltzmann constant, and θ_D the Debye temperature, a characteristic value for a given material. A common writing is

$$c_{ph} \approx \beta \cdot T^3 \tag{4.2}$$

$$\beta \approx \frac{1943.8\,\mathrm{J\,mol^{-1}\,K^{-1}}}{\theta_D^3} \tag{4.3}$$

introducing the material constant β.

This approximation gives a proportionality of the heat capacity to the third power of the temperature, and is valid in the case of $T \ll \theta_D$. Temperatures below 1 K comply to this condition (cf. table 4.1).

While phonons contribute to the heat capacity for all materials, electrons only play a role when they can move freely as conduction electrons. In metals at low temperatures, the contribution of the electrons is proportional to the ratio of the temperature and the

so called Fermi temperature T_F derived from the Fermi energy E_F, and is given by[75]

$$c_{el} \approx \frac{m_{eff}}{m} \cdot \frac{\pi^2 N_A \cdot k_B}{2} \cdot \frac{T}{T_F} = \gamma \cdot T \tag{4.4}$$

$$T_F = \frac{E_F}{k_B} \tag{4.5}$$

In real metals, due to different interaction processes of the electrons with each other and their surrounding, the effective electron mass m_{eff} usually differs from the free electron mass m. The first factor of equation 4.4 accounts for this correction, usually based on experimentally found values of the material constant γ. This approximation works well for $T \ll T_F$, which is highly maintained by temperatures below 1 K, as T_F of metals amounts to the range from 1×10^4 K to 1×10^5 K[81].

The total specific heat capacity can be written in good approximation as

$$c = c_{ph} + c_{el} = \beta \cdot T^3 + \gamma \cdot T \tag{4.6}$$

In the special case of a metal with a superconducting transition, the heat capacity will change when it enters the superconducting state. Because of the new degree of freedom, a discontinuous jump happens at the upper edge of the transition, which is given by $\Delta c_{el} = 1.43 \cdot c_{el}$ for superconductors following the BCS theory[82]. To lower temperatures, c_{el} drops exponentially due to the decreasing number of conduction electrons[76]. Far below T_c ($T \lesssim 0.1 \cdot T_c$), the electron contribution to the heat capacity becomes negligible, as it drops exponentially with respect to $\frac{T_c}{T}$[83].

Based on the values given in table 4.1, the heat capacities of the different components of the thermal platform of the 16A design have been estimated using the geometric parameters shown in table 3.1. The results for $T = 0.56$ K are shown in table 4.2. For the thermistor, the electron component is assumed to be equal to the one of the normal state multiplied by a factor of 2.43.

While table 4.2 clearly shows that the wiring does not affect the heat capacity of the TES significantly, the contributions from the absorber dipoles, the thermistor and the platform itself are all of the same order of magnitude. Keeping in mind possible significant deviations from these literature values, all of them will be considered in further calculations. As the original SCOTI TES was produced without SP, for the following analysis, a 16A TES without SP was used, which was selected not to show effects of degradation. For comparison, the heat capacity for the 16A TES with SP is shown in table 4.3. It predicts an acceptably small increase of $\approx 7\,\%$ of the total heat capacity compared to the TES without SP.

Table 4.2: Heat capacities of the 16A design at 0.56 K based on the values given in table 4.1 and the geometry shown in table 3.1. The electron contribution of Mo in the thermistor is multiplied by 2.43 to reflect the effect of the superconducting transition.

component	C_{AuPd} $[\mathrm{J\,K^{-1}}]$	C_{Mo} $[\mathrm{J\,K^{-1}}]$	$C_{\mathrm{Si_3N_4}}$ $[\mathrm{J\,K^{-1}}]$	C_{Nb} $[\mathrm{J\,K^{-1}}]$	C_{total} $[\mathrm{J\,K^{-1}}]$
platform	0	0	$2.61 \cdot 10^{-13}$	0	$2.61 \cdot 10^{-13}$
thermistor	$2.97 \cdot 10^{-14}$	$3.91 \cdot 10^{-13}$	0	0	$4.21 \cdot 10^{-13}$
dipole	$8 \cdot 10^{-13}$	$8.82 \cdot 10^{-14}$	0	0	$8.88 \cdot 10^{-13}$
wiring	0	0	0	$3.21 \cdot 10^{-15}$	$3.21 \cdot 10^{-15}$
sum	$8.3 \cdot 10^{-13}$	$4.79 \cdot 10^{-13}$	$2.61 \cdot 10^{-13}$	$3.21 \cdot 10^{-15}$	$1.57 \cdot 10^{-12}$

Table 4.3: Heat capacities of the 16A design including SP at 0.56 K based on the values given in table 4.1 and the geometry shown in table 3.6. The direct comparison to table 4.2 results in an expected increase of the heat capacity of $\approx 7\,\%$ by adding SP to the thermistor.

component	C_{AuPd} $[\mathrm{J\,K^{-1}}]$	C_{Mo} $[\mathrm{J\,K^{-1}}]$	$C_{\mathrm{Si_3N_4}}$ $[\mathrm{J\,K^{-1}}]$	C_{Nb} $[\mathrm{J\,K^{-1}}]$	C_{total} $[\mathrm{J\,K^{-1}}]$
platform	0	0	$2.61 \cdot 10^{-13}$	0	$2.61 \cdot 10^{-13}$
thermistor	$2.97 \cdot 10^{-14}$	$3.91 \cdot 10^{-13}$	0	0	$4.21 \cdot 10^{-13}$
dipole	$8 \cdot 10^{-13}$	$8.82 \cdot 10^{-14}$	0	0	$8.88 \cdot 10^{-13}$
wiring	0	0	0	$3.21 \cdot 10^{-15}$	$3.21 \cdot 10^{-15}$
SP	$1.12 \cdot 10^{-13}$	0	0	0	$1.12 \cdot 10^{-13}$
sum	$9.42 \cdot 10^{-13}$	$4.79 \cdot 10^{-13}$	$2.61 \cdot 10^{-13}$	$3.21 \cdot 10^{-15}$	$1.69 \cdot 10^{-12}$

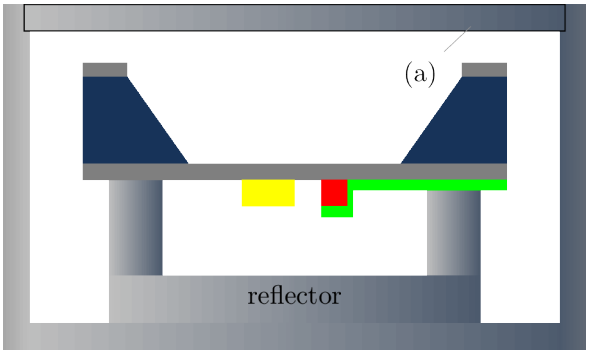

Figure 4.3: The bolometer is surrounded by a superconducting aluminum shield which is closed by an aluminum blind flange (a). Cooled down to T_{bath}, this casing protects the TES from thermal radiation of the setup and electromagnetic and magnetic distortions and thus allows for measurements of the bolometer behavior for $P_{heat} = P_{el}$.

4.3.2 Voltage-temperature characteristic of the thermistor

The voltage-temperature characteristic (V-T curve) of the thermistor was used to define fundamental properties of the thermistor, like T_c, ΔT_c and the normal state resistance R_n, which are necessary for further analysis of the TES properties. The V-T curve was measured in a dedicated setup as described in section 4.1). A sample chip with seven TES, following the structure shown in figure 4.2, was placed in a closed aluminum chamber cooled down to T_{bath}, as sketched in figure 4.3. The cold, highly reflecting surface of this casing avoids significant influence of radiation on the temperature of the superconductor. While sweeping T_{bath}, V_{th} was measured at a fixed DC current I_{th} in a four point measurement setup, as shown in figure 4.4. All thermistors were measured in the same sweep to ensure comparability of the results. The current was supplied by a battery and a tunable series resistance R_{var} and measured with a multimeter. The voltages were read with a Prema 6001 digital multimeter with multiplexed inputs.

Temperature measurements were made with a calibrated RuO_2 thermometer with a precision of $\pm 10\,\%$. From repeated measurements of T_c we found a reproducibility of $\leq 1\,\mathrm{mK}$ within a cooldown cycle and $\leq \pm 1\,\%$ for different cool down cycles. ΔT_c was defined as the temperature difference between $90\,\%$ R_n and $10\,\%$ R_n (see figure 2.2), resulting in an uncertainty of values for ΔT_c of $\pm 10\,\%$, but not less than $\pm 1\,\mathrm{mK}$. For R_n, the uncertainty is $\pm 5\,\%$.

Using the results from the V-T measurements, the resistance-temperature characteristic (R-T curve) can be determined. Figure 4.5 A) shows the R-T curve of a thermistor in the 16A design, measured with a current of $3.5\,\mu\mathrm{A}$. The transition was measured once with increasing and decreasing temperature, respectively. The bent arrows mark the measurement direction for the two curves. For the second curve, the current polarity

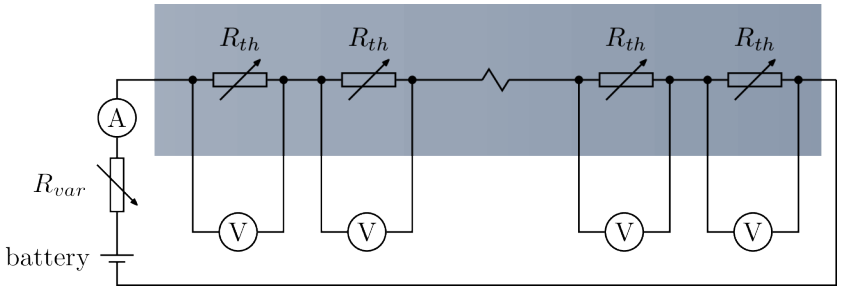

Figure 4.4: Setup for measuring the V-T curve of several thermistors. V_{th} is measured at a fixed current I_{th} defined by a battery and a tunable series resistance R_{var} and measured with a multimeter. All seven thermistors on a chip are measured at the same time to ensure comparability of the results. The shaded area represents the cooled components.

was flipped. Consequently, the offset in the superconducting state did change by less than 40 mΩ, while the offset itself was about 200 mΩ in both cases. This means that the offset is mainly due to the multimeter itself. As a slow time drift in this value could be watched, it can be attributed to a thermal drift. Thus, R_n can be determined as the difference of the $\frac{V_{th}}{I_{th}}$ values in the normal conducting state and the superconducting state. T_c, ΔT_c and R_n were determined by least-squares fits of the data with a piecewise linear function, $R_{segm}(T)$ consisting of five linear segments:

$$R_{segm}(T) = R_{offset} + R_n \cdot \begin{cases} 0 & ,T < T_c^0 \\ 0.1 \cdot \frac{T-T_c^0}{T_c^{10}-T_c^0} & ,T_c^0 \leq T < T_c^{10} \\ 0.1 + 0.8 \cdot \frac{T-T_c^{10}}{\Delta T_c} & ,T_c^{10} \leq T \leq T_c^{90} \\ 0.9 + 0.1 \cdot \frac{T-T_c^{90}}{T_c^{100}-T_c^{90}} & ,T_c^{90} < T \leq T_c^{100} \\ 1 & ,T > T_c^{100} \end{cases} \tag{4.7}$$

The adjustable parameters of the fit are the resistance offset R_{offset}, the normal state resistance R_n, $T_c = \frac{T_c^{10}+T_c^{90}}{2}$, $\Delta T_c = T_c^{90} - T_c^{10}$, T_c^0 and T_c^{100}. This fit method allows to precisely determine T_c and ΔT_c independent of the actual transition shape. An example of such a fit is given in figure 4.5 B).

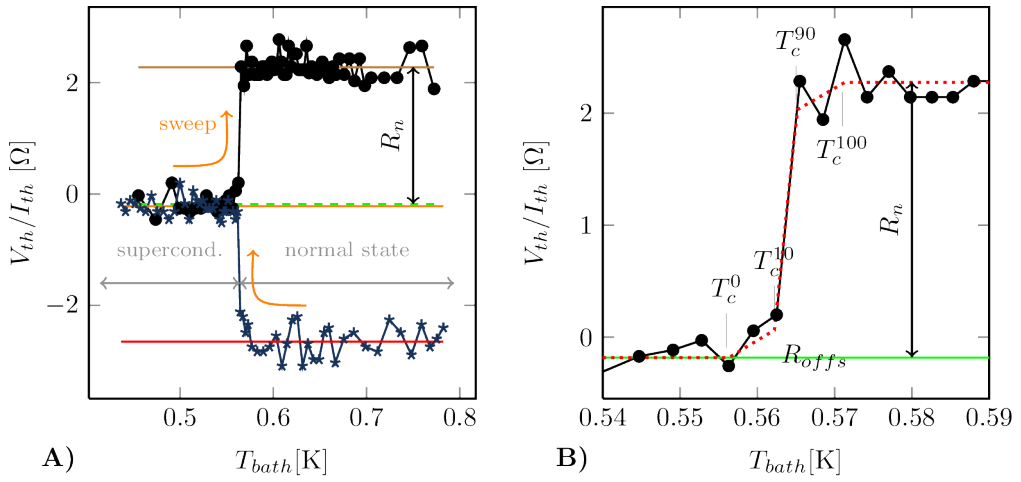

Figure 4.5: Measured R-T curve of a thermistor in the 16A design ($I_{th} = 3.5\,\mu A$). A) The transition was measured once with increasing and decreasing temperature, respectively. The bent arrows mark the measurement direction. For the second curve, the current polarity was flipped. The values for T_c differ by 100 µK which confirms that the measurement was slow enough to be in thermal equilibrium. B) Least squares fit with $R_{segm}(T)$ (see eqn. 4.7).

4.3.3 Thermal conductance

A temperature gradient in a material of length l and cross section A causes a heat flow P_{flow} in the direction of the gradient. Along this gradient, a thermal conductance

$$G(T) = \frac{dP}{dT} \tag{4.8}$$

can be observed. While for temperatures of around 100 mK and below ballistic transport mechanisms in thin Si_3N_4 membranes were found[84][85], the diffuse phonon transport model as described in [80] reproduces the behavior of the samples discussed in this thesis at temperatures above 300 mK. Hence, only diffuse heat transport will be discussed in the following. In this case, the geometry independent thermal conductivity k is defined as

$$k(T) = G(T) \cdot \frac{l}{A} \tag{4.9}$$

for infinitesimal A and l.

The process of thermal conductance can be generalized as the transport of heat carriers with a certain heat capacity C and an effective average transport velocity, where the latter

depends on the particle velocity and their mean free path λ[76]. In dielectric materials, heat transported by phonons defines the thermal conductivity: $k = k_{ph}$ with

$$k_{ph} \propto C_{ph} \cdot \lambda_{ph}(T) \tag{4.10}$$

The Debye model predicts a proportionality of $C_{ph} \propto T^3$ (equation 4.1) for temperatures significantly below the Debye-temperature. This leads to

$$k_{ph} = \lambda_{ph}(T) \cdot T^3 \tag{4.11}$$

At temperatures far below the Debye temperature, the small number of excited phonons

makes phonon-phonon-interactions negligible and causes defects, dislocations and crystallite boundaries to dominate λ_{ph}[76]. Varying numbers of defects can have strong influence on the low temperature thermal conductivity. In case of grain-boundary scattering, λ_{ph} is expected to be temperature independent[76], while randomly distributed dislocations cause a proportionality of $k \propto T^2$ [86]. This would equal a thermal conductivity proportional to T^3 and T^2, respectively.

Applying this to the Si_3N_4 membrane of the TES, the thermal conductance can be written as

$$G(T) = G_0 \cdot T^n \tag{4.12}$$

resulting in the heat transfer along the thermal link

$$P_{link} = \frac{G_0}{n+1} \cdot \left(T_{th}^{n+1} - T_{bath}^{n+1}\right) \tag{4.13}$$

where G_0 is independent of the temperature and a constant for a given material and geometry. For Si_3N_4 membranes similar to the ones used here, [80] found a proportionality close to T^2 below 1 K.

In addition to the thermal conductivity of the Si_3N_4 membrane (table 4.1), values of the intrinsic thermal conductivity of the thermistor and the absorber are needed for later modeling of the TES (see chapter 6). Measuring the thermal conductivity of a metal at low temperatures is difficult[87]; however, as electrons dominate the thermal conductivity in such a case, it can be approximated using the Wiedemann-Franz law (WFL) that describes the proportionality of the thermal conductivity to the electrical conductivity. It is applicable in cases of $T \ll \theta_D$, which is the case here[87]:

$$k = \sigma \cdot L_0 \cdot T \tag{4.14}$$

$$L_0 = 2.443 \times 10^{-8}\,\mathrm{V^2\,K^{-2}} \tag{4.15}$$

σ denotes the electrical conductivity, L_0 is the Lorentz constant. Thus, for the absorber,

of which the electrical conductivity is known from the impedance adjustment, the WFL is used to approximate the thermal conductivity for calculations and simulations.

Based on the geometry parameters given in table 3.1, for the thermal conductivity of the absorber this results in $\approx 0.12\,\mathrm{W\,m^{-1}\,K^{-2}} \cdot T$ which is significantly higher than the thermal conductivity of the membrane. At 0.6 K, the ratio is approx. 17:1. However, due to the thickness ratio of $\approx 1:48$ between absorber and membrane, the thermal conductance ratio per cross section is $\approx 1:3$. Hence, the absorbers do not strongly affect the thermal conductance on the membrane.

The thermistor is operated close to T_c where a large number of electrons is not bound in cooper-pairs which makes the WFL still applicable. Thus, it is also used, taking R_n as a reference. The resulting thermal conductivity for $R_n \approx 2.5\,\Omega$ is $0.31\,\mathrm{W\,m^{-1}\,K^{-2}} \cdot T$. At 0.6 K, it is 45 times as high as the thermal conductivity of the membrane. Again, the ratio is reduced because of the thickness ratio of $\approx 1:9$ when the thermal conductance per cross section is considered. But different to the absorber, it is still 5 times as high as the one of the membrane, increasing the temperature homogeneity locally at the thermistor.

4.3.4 Current-current characteristic of the TES

Different to the V-T curve described in section 4.3.2, the current-current characteristic (I-I curve) of the TES is measured in the normal TES biasing and readout setup as described in figure 2.5.

Using the relation between P_{el} and I_{th},

$$P_{el} = P_{link} - P_{rad} = R_{th} \cdot I_{th}^2 \tag{4.16}$$

I_{th} (assumed to be positive) can be expressed as a function of T:

$$I_{th}(T) = \sqrt{\frac{P_{link}(T) - P_{rad}}{R_{th}(T)}} \tag{4.17}$$

Combining equations 4.13 and 4.17 gives

$$I_{th}(T) = \sqrt{\frac{\frac{G_0}{n+1} \cdot (T^{n+1} - T_{bath}^{n+1}) - P_{rad}}{R_{th}(T)}} \tag{4.18}$$

The relation between I_{bias} and I_{th} resulting from equation 2.90 allows to do the same for I_{bias}:

$$I_{bias}(T) = I_{th}(T) \cdot \left(1 + \frac{R_{th}(T) + R_L}{R_{sh}}\right) \tag{4.19}$$

The negative electrothermal feedback (see section 2.3.2) turns into a positive feedback

for $\beta^{eff} < 0$, as shown by equation 2.73. The critical resistance for this is given by

$$\beta^{eff}(R_{th}^{min}) = \frac{P_{el}}{T} \cdot \alpha \cdot \frac{R_{th}^{min} - R_L - R_{sh}}{R_{th}^{min} + R_L + R_{sh}} \stackrel{!}{=} 0 \tag{4.20}$$

$$\beta^{eff}(R_{th} < R_{th}^{min}) \stackrel{!}{<} 0 \tag{4.21}$$

as

$$R_{th}^{min} = R_L + R_{sh} \tag{4.22}$$

This is the minimum resistance of stable operation that can be theoretically reached in the transition, as for lower values the positive feedback will cause the thermistor to switch to the superconducting state or back to the stable states, as soon as a small signal fluctuation occurs. For the *R-I* curve this means a minimum of $I_{bias}(R_{th})$ at R_{th}^{min}, and as in good approximation $I_{th} \propto \frac{1}{\sqrt{R_{th}}}$, the *I-I* curve shows a local minimum of $I_{bias}(I_{th})$.

The quotient of I_{bias} and I_{th},

$$Q \equiv Q(R_{th}) = \frac{I_{bias}}{I_{th}} = \left(1 + \frac{R_{th} + R_L}{R_{sh}}\right) \tag{4.23}$$

in different regions of the *I-I* curve can be expressed as

$$Q_n = Q(R_{th} = R_n) = \left.\frac{dI_{bias}}{dI_{th}}\right|_{R_{th}=R_n} \tag{4.24}$$

$$Q_s = Q(R_{th} = 0) = \left.\frac{dI_{bias}}{dI_{th}}\right|_{R_{th}=0} \tag{4.25}$$

Using equation 4.19, the characteristic resistances of the setup can be expressed using these quotients and R_{sh} as

$$R_L = (Q_s - 1) \cdot R_{sh} \tag{4.26}$$

$$R_n = (Q_n - Q_s) \cdot R_{sh} \tag{4.27}$$

Thereby, R_L and R_n can be precisely determined if R_{sh} is known. We found no significant difference in R_{sh} at 4.2 K and 300 mK, and the value is stable throughout a four inch wafer with a variation smaller than $\pm 1\,\mathrm{m\Omega}$. Thus, it can be easily measured using a simple helium dip stick at 4.2 K and be used to calculate said parameters.

As a model for $R_{th}(T)$ in the transition, a smoothed step function can be used, as it is shown in figure 2.2:

$$R_{th}(T) = \frac{R_n}{1 + e^{-\frac{2.2 \cdot (T - T_c)}{\Delta T_c}}} \tag{4.28}$$

The resulting calculated *I-I* curve is shown in figure 4.6. for a fixed base temperature, the bias current is varied. Starting from the superconducting state of the thermistor, the measured current will vary along the steep blue line described by

$$I_{th}^{s} = \frac{I_{bias}}{Q_s} \tag{4.29}$$

$$R_{th}^{s} = 0 \tag{4.30}$$

Once the critical current is exceeded, I_{th} jumps to the black curve. The region coincident with the straight red dotted line marks the normal conducting state with

$$I_{th}^{n} = \frac{I_{bias}}{Q_n} \tag{4.31}$$

$$R_{th}^{s} = R_n \tag{4.32}$$

where Joule heating of the thermistor occurs.

Reducing I_{bias} from a point in the normal conducting range causes T to fall. When the superconducting transition is entered, the curve starts turning with a local minimum marked by the arrow in figure 4.6. Further reducing I_{bias} causes R_{th} to fall and I_{th} to rise, which slows down the temperature reduction until the negative electrothermal feedback turns into a positive feedback at $R_{th} = R_{th}^{min}$. While theoretically the curve would follow along the thin black dotted line, due to the positive feedback these states are not stable. The thermistor will enter the superconducting state, leading to a jump of I_{th} to the blue line. As the readout usually does not follow this sudden change in current, I_{th} seemingly runs down on a shifted path which is represented by the green dashed line. By using its differential definition in equation 4.25, Q_s still can be determined by a least squares fit using a linear function.

In a measurement, the same is necessary for Q_n due to the fact that the SQUID readout circuit produces an unknown current offset ΔI_{th} (see section 2.4). Thus, the curve has to be shifted accordingly. This is done by using the offset parameter $I_{th,offs}$ of the least squares fit of a linear function to the measured values I_{th}^{meas} in the normal resistive range:

$$I_{th}^{meas} = I_{th} + \Delta I_{th} = Q_n \cdot I_{bias} + I_{th,offs} \tag{4.33}$$

Because of the fact that the real current I_{th} has to be zero at $I_{bias} = 0$, the offset has to be

$$\Delta I_{th} \stackrel{!}{=} I_{th,offs} \tag{4.34}$$

and thus can be canceled out by shifting the data by $I_{th,offs}$.

The measured *I-I* curve in figure 4.7 shows discontinuous regions, caused by distortions of the signal that cause changes in the offset of the readout signal. In the *I-I* curves of the discussed TES, irregularly distributed regions of such distortions have been observed.

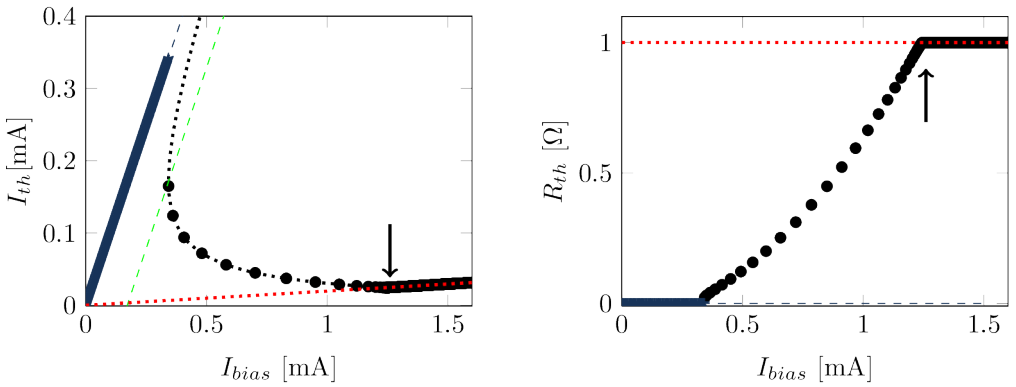

Figure 4.6: Calculated *I-I* curve (left) and the corresponding *R-I* curve (right) of a TES with $T_c = 0.6\,\mathrm{K} \pm 1 \times 10^{-3}\,\mathrm{K}$, $T_{bath} = 0.4\,\mathrm{K}$, $R_n = 1.0\,\Omega$, $R_{sh} = Rn/50.0$, $R_L = 0\,\Omega$, $G = 9.5 \times 10^{-9} \cdot T^{1.7}\mathrm{W\,K^{-1}}$, $P_{rad} = 0.0\,\mathrm{W}$. The dotted line represents a constant resistance as it is in the normal conducting region, the dashed blue line equals the superconducting state. As the readout usually does not follow the jump from the normal to the superconducting state, the green dashed line instead will be measured.

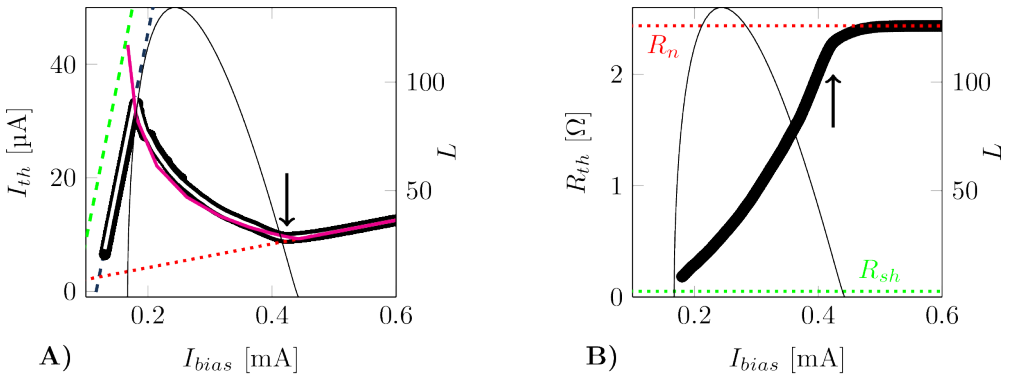

Figure 4.7: A) Measured *I-I* curve (bold black line) and corrected curve (white line). The lower limit of stable operation is slightly higher than suggested from the calculated ideal curve (dashed magenta line), thus the straight line representing the superconducting range is shifted from the dashed green to the dashed blue line. $R_L \approx (44 \pm 1)\,\mathrm{m\Omega}$ was determined from Q_s, with $R_{sh} = (52.9 \pm 0.5)\,\mathrm{m\Omega}$ as measured at 4.2 K. The calculated feedback factor L is shown as a straight thin black line. B) Corresponding *R-I* curve.

This is discussed in detail in section 7. By eliminating non-monotonic jumps, a corrected curve can be calculated. As can be seen, it fits the calculated ideal curve well. Slight differences within the transition range are due to slight temperature variations throughout the measurement which are limited to ±2 mK and deviations of the real transition shape from the assumed one for the calculated model (equation 4.28). The lower limit of stable operation is shifted to higher resistance of the thermistor compared to the modeled value. As the negative feedback gets weaker towards lower resistance within this region as shown in figure 4.7, this is most likely due to uncompensated fluctuations that cause a premature jump to the superconducting state.

Thermal conductance measurements

To find G_0 and n of the membrane from measurements, the TES is located in a completely closed case of aluminum at T_{bath} (figure 4.3), as it is also used for the V-T curve measurements. Its highly reflective surface results in a negligible net radiation power P_{rad}. This means in terms of chapter 2.3

$$P_{heat} \approx P_{el} \tag{4.35}$$

$$P_{link} \approx P_{el} \tag{4.36}$$

and with equations 4.18 and 4.19, G_0 can be expressed in terms of the currents I_{th} and I_{bias}:

$$G_0 \approx \frac{n+1}{T^{n+1} - T_{bath}^{n+1}} \cdot I_{th} \cdot (I_{bias} \cdot R_{sh} - I_{th} \cdot (R_{sh} + R_L)) \tag{4.37}$$

By measuring the I-I-curve (see figure 4.7, left), G_0 can be calculated using eqn. 4.37 from the superconducting transition range, where the temperature of the thermistor is known to be in very good approximation $T \approx T_c$. While close to the normal conducting range the current offset is precisely defined by the offset calibration as described in section 4.3.4, the above mentioned distortions cause an increasing uncertainty of the current offset towards lower resistance. Thus, it is advantageous to use a point close to the upper edge of the superconducting transition for determining G_0.

The local minimum of the curve, marked by the arrow in figure 4.7, can be used as such a reference point. Though the related resistance depends on the precise transition shape and thus can vary from sample to sample, it is always clearly located within and in the uppermost part of the transition, as for example in the right graph in figure 4.7. In this case, T can be assumed to be in the range from T_c to $T_c + \Delta T_c$.

Figure 4.8 shows a set of I-I-curves of the 16A design measured at different base temperatures. The curves are plotted after a correction for single non-monotonic jumps as described above in section 4.3.4. The fit results for R_n and R_L for the different curves deduced from equations 4.26 and 4.27 are listed in table 4.4. These values are reproduced with a precision of approx. 1 % at the different base temperatures. While

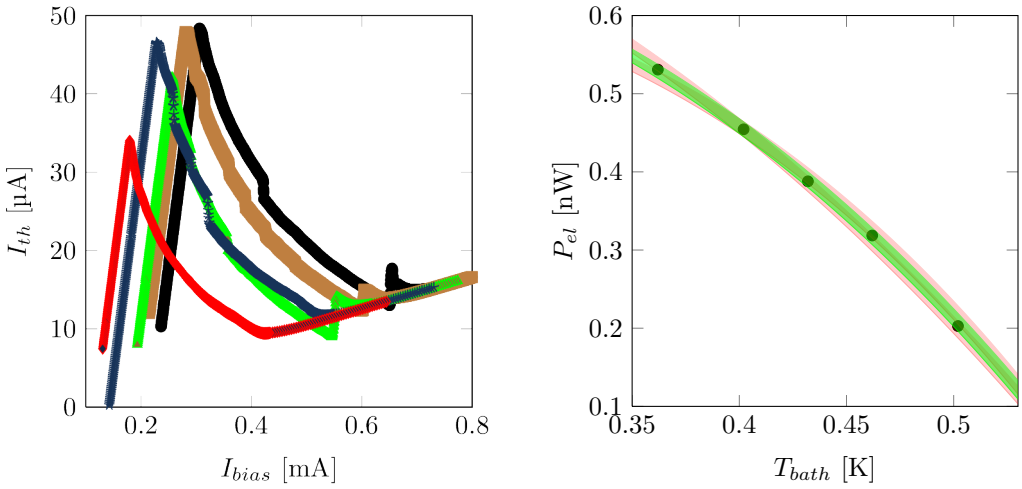

Figure 4.8: *I-I* curves of a TES with the 16A design. The curves were taken at different base temperatures to determine the temperature dependence of the thermal conductance. Visible discontinuities arise from distorted states of the TES as discussed in the text. Right: The symbols denote the determined electrical heating powers from the curves on the left. The data can be approximated using equation 4.38 with $n = 1.7 \pm 0.5$. The green shaded region marks the error margins resulting from the precision limits of the temperatures for $n = 1.7$, the purple shades mark the range from $n = 1.2$ to $n = 2.2$.

Table 4.4: Fit parameters derived from the curves shown in figure 4.8.

T_{bath}	R_n	R_L
0.362	2.452	0.044
0.402	2.449	0.044
0.432	2.441	0.044
0.462	2.428	0.044
0.502	2.435	0.044
average	2.441	0.044
(max-min)/av	0.01	0.011

they confirm that the upper region of the transition is precisely defined by the Q_n fit, significant variation in current offset of the superconducting range occurs. It can be attributed to the remaining discontinuities of the curves after the correction of jumps. These discontinuities are reproducible areas in which distortions occur that cause the linearization of the SQUID readout to fail and produce arbitrary offset changes. This phenomenon will be discussed in section 7.

By using the above mentioned local minimum as a reference point in these curves, several values for P_{el} can be determined for the different bath temperatures (figure 4.8, right). These values can be approximated by

$$P_{el} = \frac{G_0}{n+1} \cdot \left(T^{n+1} - T_{bath}^{n+1}\right) \tag{4.38}$$

$$T \approx T_c + \Delta T_c \tag{4.39}$$

resulting in $n = 1.7 \pm 0.5$. For $n = 1.7$, the least squares fit results in

$$G_0 = (9.5 \pm 0.7)\,\mathrm{nW\,K^{-2.7}}. \tag{4.40}$$

The error margins are dominated by the temperature fluctuations of the bath temperature of $\Delta T_{bath} = \pm 2\,\mathrm{mK}$ while measuring and the exact temperature of the thermistor, which is located in the interval from T_c to $T_c + \Delta T_c$. The result for n fits the literature value given in table 4.1. As discussed in section 4.3.3, a value of n close to two suggests that the thermal conductance is dominated by phonon-dislocation scattering.

4.3.5 Time constants

Combining the results from sections 4.3.1 and 4.3.4, the thermal time constant τ_0 can be estimated from G and C. This results in

$$\tau_0 = \frac{C}{G} \approx \frac{1.7 \times 10^{-12}\,\mathrm{J\,K^{-1}}}{4.0 \times 10^{-9}\,\mathrm{W\,K^{-1}}} \approx 430\,\mu\mathrm{s} \tag{4.41}$$

for $T_c = 0.6\,\mathrm{K}$ and

$$\tau_0 = \frac{C}{G} \approx \frac{1.6 \times 10^{-12}\,\mathrm{J\,K^{-1}}}{3.6 \times 10^{-9}\,\mathrm{W\,K^{-1}}} \approx 440\,\mu\mathrm{s} \tag{4.42}$$

for $T_c = 0.56\,\mathrm{K}$. The similarity of these values which is due to the fact that both C and G rise and fall with rising and falling temperature, respectively, though with different exponents, shows that a variation of the critical temperature of some 10 mK does not strongly affect the time constant. This allows to apply findings at one temperature to a temperature range of several 10 mK.

For time constant measurements, a setup as sketched in figure 4.9 was used. The

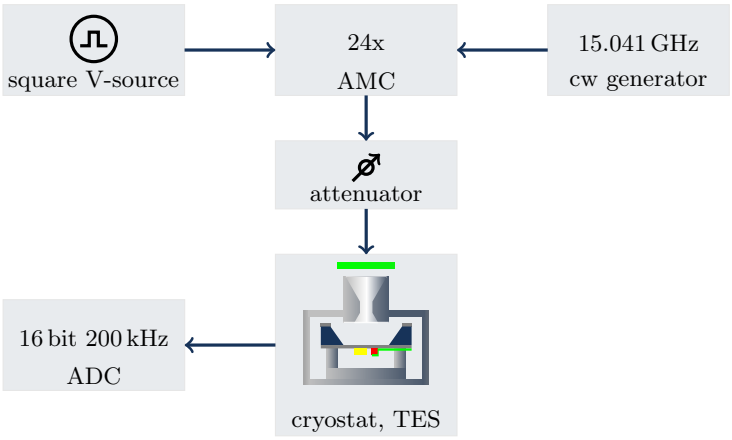

Figure 4.9: Time constant measurement setup.

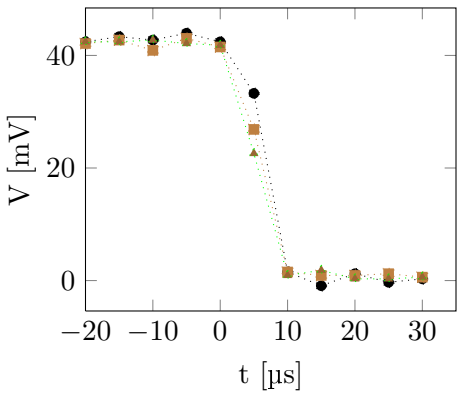

Figure 4.10: Step response of the time constant measurement setup, including the data aquisition system. It is measured using a zero bias detector, replacing the cryostat with the TES.

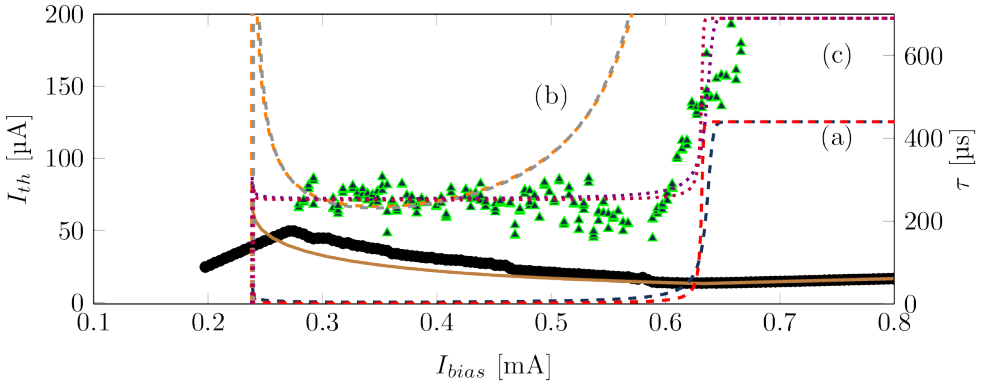

Figure 4.11: Measured $\tau\,(I_{bias})$ (symbols) and I-I curve (thick black line) for the 16A design. A calculated curve (brown line) was used to determine the lumped model time constant levels (a) based on the measured parameters of the curve and the thermal time constant (eqn. 4.42) for $\Delta T_c = 1\,\mathrm{mK}$ and $\Delta T_c = 3\,\mathrm{mK}$, respectively. Upscaling the heat capacity by factors of 147 ($\Delta T_c = 1\,\mathrm{mK}$) and 50 ($\Delta T_c = 3\,\mathrm{mK}$) leads to a similar minimum τ as the measured data, but considerable differences in the shape of the curves (b). Much better fitting curves (c) result from adding an offset of 250 µs to the curves (a) without heat capacity scaling (see text).

TES was placed inside a superconducting aluminum chamber as shown in figure 4.1. Microwaves at a constant power level of 10 mW and a frequency of 15.041 GHz from an HP 83650L[88] continuous wave generator were fed into an amplifier/multiplier chain (AMC) S145 from virgina diodes (VDI)[89] with a total frequency multiplication factor of 24, resulting in an output frequency of 361 GHz. This signal was modulated using a rectangular voltage from a Tektronix AFG 3022B[90] function generator using the attenuation control input of the AMC. The output feedhorn of the AMC emits a linearly polarized signal.

The resulting time domain signal shape was measured with a VDI zero bias detector "ZBD". The signal includes the characteristic of the source as well as of the used analog-to-digital converter (ADC), a Ni DAQPad-6015 from national instruments[91], with a maximum sampling rate of $f_{sampling} = 200\,\mathrm{kHz}$ and 16 bit resolution. Figure 4.10 shows the resulting shape of the falling edge of the signal, with three consecutive measurements. On the rising edge of the AMC, a severe overshoot with a damped oscillation can be observed. Thus, only the clean falling edge was used. At a sampling frequency of 200 kHz, it contains in all measured cases only one single sampling point, meaning the total step is not wider than 10 µs. Thus, time constants significantly above this time can reliably be identified with this system. From the Nyquist-Shannon sampling theorem, the sampling

rate of 2×10^5 samples/s would allow to reproduce a minimum time constant τ_{min} of

$$\tau_{min} > \frac{1}{2\pi f_{max}} \tag{4.43}$$

and

$$f_{max} = \frac{f_{sampling}}{2} \tag{4.44}$$

thus $\tau_{min} \approx 16\,\mu s$. In real measurements, due to the small signals and the strong dependence of the fit precision on the number of samples within the edge of the signal, this limit is shifted to approx. 30 µs.

By feeding the signal into the cryostat with the TES as shown in figure 4.9, the step response of the TES was measured. To ensure a comparable signal as it would occur in a THz camera, the signal amplitude was reduced. As a reference, the signal difference of the room temperature background radiation to the emission of the human body was used (see figure 1.4). For this, a hand was slowly passed in front of the entry window of the cryostat. The corresponding current response ("hand response") of the TES in an arbitrarily chosen working point was measured. An adjustable optical attenuator consisting of a set of fiberglass plates with variing thickness was placed in between the output feedhorn of the AMC and the entry window of the cryostat. This was used to adjust the THz signal to cause a current response of the TES that was of the same order of magnitude as the "hand response".

To find the bias dependent current step response of the TES, the *I-I* curve was sampled starting from the normal resistive range down to the lowest stable working point in steps of the bias current of 4 µA. For each resulting working point, a time domain sample of I_{th} containing the response to three periods of the input signal was recorded. The period of the signal was chosen to be significantly longer, at least by a factor of 20, than the highest time constant of the TES. This allows the TES to fully reach the equilibrium state after each signal change. For each of these samples, the rising edge of the current response (which corresponds to the falling edge of the THz signal) was approximated with a least squares fit of an exponential decay function

$$I(t) = I_0 + A \cdot \left(1 - e^{-(t-t_0)/\tau}\right) \tag{4.45}$$

to find the time constant τ.

Figure 4.11 shows the result of this process for a TES with the 16A design at a base temperature of 400 mK. The thick black line represents the corresponding measured *I-I* curve, which again includes distorted regions that lead to a jump in the measured current offset. A calculated *I-I* curve based on the measured parameters is plotted as a brown line. Based on this and the thermal time constant of $\tau_0 = 440\,\mu s$ calculated in equation 4.42, the predicted dependency of the time constant on the bias current was

calculated as described in section 2.3. Corresponding to the measured transition width of $\Delta T_c = (2 \pm 1)\,\mathrm{mK}$, the results are plotted for $\Delta T_c = 1\,\mathrm{mK}$ and $\Delta T_c = 3\,\mathrm{mK}$ as a red and a blue dashed line, respectively.

In its lowest range, the curve for $\Delta T_c = 1\,\mathrm{mK}$ goes down to $\approx 3.4\,\mu\mathrm{s}$. For $\Delta T_c = 3\,\mathrm{mK}$, the minimum time constant is $\approx 10\,\mu\mathrm{s}$. As can be seen, the measured time constants significantly differ from these predictions. Throughout the working range, they show a significantly higher minimum level of

$$\tau_{min} \approx (250 \pm 50)\,\mu\mathrm{s} \tag{4.46}$$

which is nearly constant throughout the working range.

A possible cause for this is the approximation of the heat capacities with values of bulk crystalline materials. Amorphous materials like the used sputtered thin films oftentimes show significantly increased heat capacity below 1 K compared to the crystalline material due to localized excitations[87]. However, a simple upscaling of the heat capacity to fit the minimum of the calculated time constants to the measured ones does not fit the measured results. The orange dashed curve shows the results for $\Delta T_c = 3\,\mathrm{mK}$ and $\tau_0 = 11\,\mathrm{ms}$ which is 50 times the calculated value. The accordant curve for $\Delta T_c = 1\,\mathrm{mK}$ and $\tau_0 = 32\,\mathrm{ms}$, corresponding to a factor of 147, is given as a dashed gray line. Different to the measured data, a steep increase of the time constant in the upper half of the transition range can be observed in the calculated curves. Thus, the heat capacity scaling can not be assumed to be the only cause for the difference. Instead, adding an offset of $250\,\mu\mathrm{s}$ to the curves for $\tau_0 = 440\,\mu\mathrm{s}$ results in a qualitatively much better fitting trend of the time constant. This is visualized in figure 4.11 as the dotted purple ($\Delta T_c = 1\,\mathrm{mK}$) and violet ($\Delta T_c = 3\,\mathrm{mK}$) curves. Such an additional time constant can result from coupled elements with different time constants. Hence, it is presumably due to the distributed structure of the bolometer, which causes the simple TES model that assumes lumped structures to fail[92]. A modeling of the extended geometry and its effect on the time constant will be given in chapter 6.

4.3.6 Sensitivity

A crucial parameter of the TES is the sensitivity to signal differences in the incoming radiation power. It is given by formula 2.56 as S_I^{TES}. However, this refers to the power differences at the thermistor and does not account for any type of losses throughout the way of the radiation from its source in the object plane to the TES. Signal reduction caused by the optical system, like shadowing effects in the imaging optics, unavoidable losses in the optical filter sets and the coupling of the radiation to the TES is not avoidable. As the overall efficiency of the system can vary from setup to setup as the optical system design varies for different applications, it is necessary to estimate the real background load and referred to the sensor noise the achievable bit depth of the system, as given in equation 1.30. For the comparison of different TES designs, the coupling

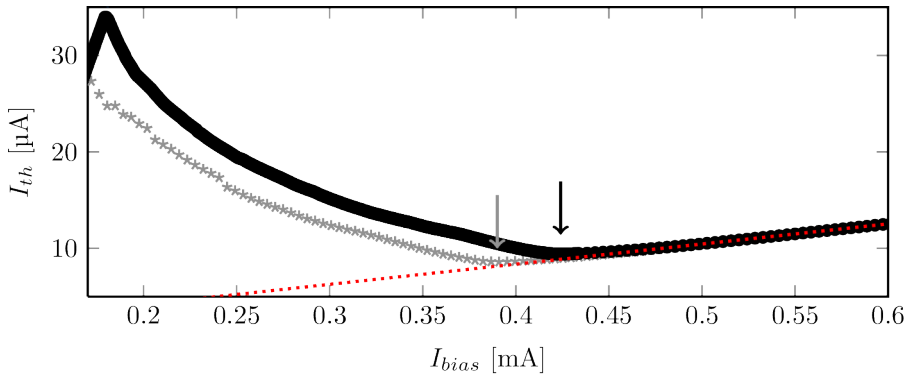

Figure 4.12: *I-I*-curves for the 16A design with (gray curve) and without (black curve) the load from room temperature radiation. The radiation power can be determined from the shift of the marked turning points. The resulting effective radiation power is $P_{rad} \approx 3.2 \times 10^{-11}\,\mathrm{W}$.

efficiency of the TES to the horn antenna is a key parameter which is independent of the optical system. It will be discussed in detail in chapter 6.

By measuring the *I-I*-curve of the TES without optical load as described in section 4.3.4 and comparing the determined electrical heating power P_{el}^{0} to the one under the load from room temperature background radiation, P_{el}^{RT}, the effective radiation power can be determined from equation 4.16 as

$$P_{rad} = P_{el}^{0} - P_{el}^{RT} \tag{4.47}$$

Figure 4.12 shows the *I-I*-curves for the 16A design, with and without the load from room temperature radiation. The radiation power results in a shift of the transition range of the curve towards the origin of the graph, as the electrical heating power is reduced by the same value (equation 4.47). The resulting absorbed radiation power is

$$P_{rad} \approx 3.2 \times 10^{-11}\,\mathrm{W} \tag{4.48}$$

Compared to the electrical heating power of the thermistor of approx. $4.2 \times 10^{-10}\,\mathrm{W}$ at a bath temperature of $T_{bath} = 400\,\mathrm{mK}$, this results in a ratio of

$$\frac{P_{rad}}{P_{el}} \approx 8\,\% \tag{4.49}$$

For $T_{bath} = 500\,\mathrm{mK}$, $P_{el} \approx 1.7 \times 10^{-10}\,\mathrm{W}$, hence the ratio rises to about 19 %.

Transforming equation 2.77 for the static loop gain L to

$$L = \frac{P_{el} \cdot \alpha}{G \cdot T} \cdot \xi \tag{4.50}$$

$$\Rightarrow L = \left(1 - \left(\frac{T_{bath}}{T}\right)^{n+1}\right) \cdot \frac{P_{el}}{P_{flow}} \cdot \frac{\alpha}{n+1} \cdot \xi \tag{4.51}$$

shows that for a given thermistor characteristic and bath temperature, the ratio of P_{el} to P_{flow} will influence the strength of the negative electrothermal feedback. Using the relationship given in equation 4.16 leads to the condition

$$\frac{P_{el}}{P_{el} + P_{rad}} \approx 1 \tag{4.52}$$

which means that

$$P_{el} \ll P_{rad} \tag{4.53}$$

is necessary to avoid a reduction of the feedback strength. The results listed above maintain this demand. Hence, the thermal conductance is not limiting the feedback strength for this design.

Compared to the calculated value of the background radiation received by the system of $1.3 \times 10^{-10}\,\mathrm{W}$ as given in section 1.3, this results in an optical system efficiency of approx. $\eta_{opt} \approx 24\,\%$ and a maximum signal difference of

$$(\Delta P_{sig})_{max} = 1.4 \times 10^{-12}\,\mathrm{W} \tag{4.54}$$

In combination with the noise level, $(\Delta P_{sig})_{max}$ can be used to determine the achievable SNR and the corresponding bit depth as given in equation 1.30. Noise in TES is hard to describe precisely, as there are many sources of so called excess noise and high frequency terms, that are only partly understood[93–96]. However, the fundamental noise components to compare to as an ideal reference are caused by the fluctuations of the carriers of electric charge, heat and light. These are Johnson noise, phonon noise and photon noise. To be able to compare to the signal amplitude, noise usually is given as the electrical noise equivalent power (NEP), that represents the smallest signal power difference at the thermistor that can be measured. Thus, it represents the characteristic noise of the TES.

For the Johnson noise, the NEP of a TES is given by[44]

$$NEP_{johnson} = \frac{1}{\left|S_I^{TES}\right|} \cdot \sqrt{\frac{4 \cdot k_B \cdot T}{R}} \cdot \frac{\tau}{\tau_0} \cdot \sqrt{\frac{1 + \omega_{el}^2 \cdot \tau_0^2}{1 + \omega_{el}^2 \cdot \tau^2}} \tag{4.55}$$

To distinguish between optical and electrical signal frequency, the electrical frequency

ν_{el} and the corresponding angular frequency $\omega_{el} = 2\pi\nu_{el}$ are denoted with a subscript 'el', while the optical frequency is marked with an 'opt'.

Phonon noise, oftentimes also called thermal fluctuation noise, contributes as [44]

$$NEP_{phonon} = \sqrt{\gamma \cdot 4 \cdot k_B \cdot T^2 \cdot G} \tag{4.56}$$

$$\gamma < 1 \tag{4.57}$$

$$\gamma = \frac{n+1}{2n+3} \cdot \frac{1 - \left(\frac{T_{bath}}{T}\right)^{2n+3}}{1 - \left(\frac{T_{bath}}{T}\right)^{n+1}} \tag{4.58}$$

γ is a correction factor that compensates for the temperature gradient along the thermal link[97].

The radio case of optical noise is defined by the condition

$$\frac{k_B \cdot T_{source}}{h \cdot \nu_{opt}} \gg 1 \tag{4.59}$$

where T_{source} is the effective blackbody temperature of the source. For $T_{source} \approx 300\,\mathrm{K}$ and $\nu \approx 350\,\mathrm{GHz}$ the left hand side results in approximately eighteen, therefore the approximation is suitable in the case of the considered TES.

In the radio case, the photon component of the noise can be written as[98]

$$NEP_{photon} \approx \eta_{opt} \cdot k_B \cdot T_{source} \cdot \sqrt{2 \cdot \Delta\nu_{opt}} \tag{4.60}$$

It is scaled by the optical efficiency η_{opt} of the system, as the NEPs in the given forms refer to the power at the thermistor.

As the different noise components are uncorrelated, the Johnson noise, phonon noise and photon noise result in a combined NEP_{comb} of

$$NEP_{comb} = \sqrt{NEP^2_{johnson} + NEP^2_{phonon} + NEP^2_{photon}} \tag{4.61}$$

It is plotted as dashed lines in the graphs of figure 4.13.

A common way to present noise is to plot the noise current which is achieved by multiplying the NEP with S_I^{TES}. However, this is strongly dependent on the TES working point and does not allow to directly compare to the optical signal level ΔP_{sig} without a working point dependent correction factor of the latter. Plotting of the NEP instead allows to compare to the power spectral density S_{sig} referring to the square root of the electrical bandwidth $\Delta\nu_{el}$

$$S_{sig} = \frac{\Delta P_{sig}}{\sqrt{\Delta\nu_{el}}} \tag{4.62}$$

The measured time constant of the TES of $\tau \approx 250\,\mu s$ as given in equation 4.46 corresponds to an electrical bandwidth of

$$\Delta\nu_{el} = \nu_l = \frac{1}{2\pi\tau} \tag{4.63}$$

with $\Delta\nu_{el} \approx 640\,\mathrm{Hz}$, where ν_l denotes the cutoff frequency of the TES.

Noise measurements were performed with a HP 35670A dynamic signal analyzer[88]. They resulted in the spectral density of the root mean square of the noise current, δI_{rms}^{noise}, given in $\mathrm{A\,Hz^{-1/2}}$. To deduce the achievable bit depth, the noise was transformed to the NEP, representing the smallest signal power difference at the TES that can be measured. This was realized using the current responsivity S_I^{TES} as defined in equation 2.56

$$NEP = \frac{\delta I_{rms}^{noise}}{\left|S_I^{TES}\right|} \tag{4.64}$$

$$S_I^{TES} = \frac{\delta I_{th}}{\delta P_{rad}} \tag{4.65}$$

Referring to equation 2.62, we find

$$NEP = \delta I_{rms}^{noise} \cdot V_{th} \cdot \frac{L+1}{L} \cdot \sqrt{1+\omega_{el}^2 \cdot \tau^2} \tag{4.66}$$

which can be approximated for working points with $L \gg 1$ to

$$NEP \approx \delta I_{rms}^{noise} \cdot V_{th} \cdot \sqrt{1+\omega_{el}^2 \cdot \tau^2} \tag{4.67}$$

The frequency dependency of S_I^{TES} represents the limited capability of the TES to follow signals faster than its cutoff frequency. This leads to a strong rise in the Johnson noise NEP for higher frequencies, corresponding to the reduction of the SNR with increasing frequency. This results in plots like shown on the left graph of figure 4.13. It is clearly visible that this representation suppresses the visibility of high frequency features of the noise. Thus, an advantageous alternative is to scale the graphs by

$$\kappa \equiv \kappa(\omega_{el}) = \frac{1}{\sqrt{1+\omega_{el}^2 \cdot \tau^2}} \tag{4.68}$$

which preserves the SNR while high frequency features are shown in a more prominent way. This is realized on the right side of figure 4.13. In this case, the general characteristics of the noise levels equal those of the noise current as measured in the system. The resulting frequency dependency of the optical signal, which is represented by a dotted line in the graphs, is proportional to the measured signal amplitude and accounts for the ceasing sensitivity to fast signals.

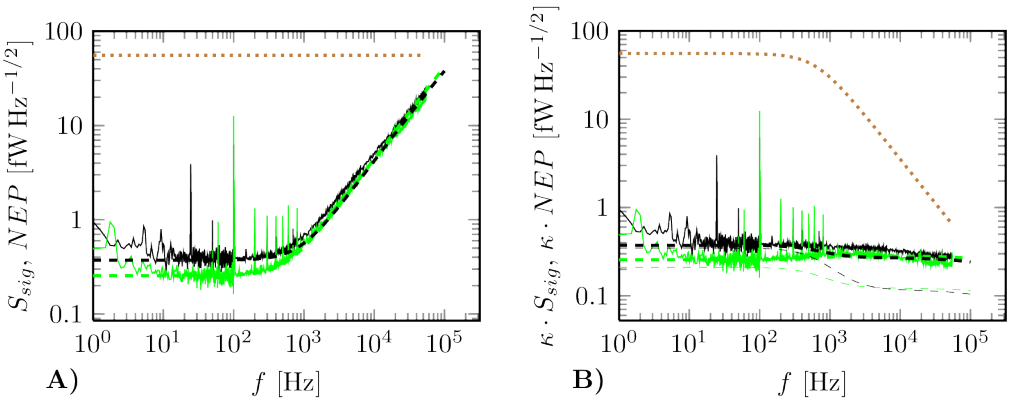

Figure 4.13: A) Measured NEP of the TES and S_{sig}^{max} (dotted line) are compared. The noise under background radiation load from 295 K (black) and T_{bath} (green) is shown. The dashed lines correspond to the calculated NEP_{comb} (eqn. 4.61). B) all graphs are scaled by $\kappa(\omega_{el})$. While NEP_{comb} fits the noise level within the electrical bandwidth of the TES fairly well, towards higher frequencies excess noise can be observed. In addition to the theoretical noise levels with a feedback strength corresponding to the found time constants, the theoretical levels for strong feedback ($L >> 1$) are shown as thin dashed lines.

The plotted signal is given as the signal power spectral density S_{sig}^{max} derived from the maximum signal difference $(\Delta P_{sig})_{max}$ in equation 4.54, hence

$$S_{sig}^{max} = \frac{(\Delta P_{sig})_{max}}{\sqrt{\Delta\nu_{el}}} \tag{4.69}$$

Within the bandwidth $\Delta\nu_{el}$ of the TES, the measured NEP for the 16A design is approximately $4 \times 10^{-16}\,\mathrm{W\,Hz^{-1/2}}$ for room temperature background radiation load. This is only slightly higher than the calculated NEP_{comb} of $3.8 \times 10^{-16}\,\mathrm{W\,Hz^{-1/2}}$.

This allows for a SNR of

$$SNR = \frac{(\Delta P_{sig})_{max}}{NEP \cdot \sqrt{\Delta\nu_{el}}} \tag{4.70}$$

$$SNR_{16A} \approx 135 \tag{4.71}$$

and according to equation 1.30 equals an achievable bit depth of ≈ 7 bit.

Below 10 Hz, an increase of the measured noise level can be observed which is varying from measurement to measurement and mainly due to temperature fluctuations of the bath temperature caused by the temperature stabilization. As this is below the targeted frame rate for a THz video camera, these contributions do not cause differences within

one frame and thus are of minor importance. Further, the usual offset calibration in the image processing will compensate for resulting differences between consecutive pictures.

Towards higher frequencies, significant excess noise can be observed compared to the theoretical noise level. Similar behavior has been observed oftentimes in TES, and several correlations have been identified. [95] was able to assign effects of excess noise to the distributed heat capacity in the spider leg structure. [93] described an excess noise hump at higher frequencies which was proportional to the inverse transition width of the thermistor. [94] described excess noise due to the high frequency thermal decoupling of normal state and superconducting areas within the thermistor. Suggestions to limit excess noise, which can not be fully avoided[96], oftentimes try to reduce the feedback strength or increase the heat capacity and thus the effective time constant of the TES[93]. This works for astronomical applications which do not need fast sensors[99] or systems for short wavelengths that can compensate reduced feedback by strong reduction of the heat capacity of the TES. For TES for security applications using wavelengths in the order of millimeters, the possibility for heat capacity reduction, as described in chapter 6 is limited, and reduced feedback strength therefore not acceptable. With the assumed weak feedback deduced from the calculated thermal time constant in equation 4.42 and the measured time constants, which results in $L \lesssim 2$, the theoretical noise levels exceed the measured data towards the high frequency limit of the right graph of figure 4.13. For comparison, the theoretical noise levels for the strong feedback limit $L \gg 1$ are plotted as thin dashed lines, suggesting a stronger feedback combined with an excess noise hump as in [93]. An explanation of a possibly higher feedback will be suggested in chapter 6.

As mentioned above, there is different working points that show significant distortions of the readout electronics. This goes along with increased excess noise. While in cases of strong distortions this can not be measured as the readout circuit does not work, in moderately distorted regions increased noise can be observed as shown in figure 4.14. The noise level is increased throughout the whole measured frequency range; However, it is most significant above the cutoff frequency of the TES. This will be further analyzed in chapter 7. As long as sufficient anti alias filtering is applied, the excess noise above the bandwidth is not affecting the operation. Otherwise, it will add to the noise in the working band.

4.4 Summary

A detailed analysis of the properties of TES following the 16A design has been performed. Concerning sensitivity and characteristics of the chosen optical window, they are suitable for THz imaging for security applications. The images provided by the single pixel demonstrator SCOTI showed, that hidden objects under clothing could be visualized. However, for a THz video camera, higher frame rates and a larger field of view (FOV) are necessary. The time constant of the TES limits the applicability of the TES in

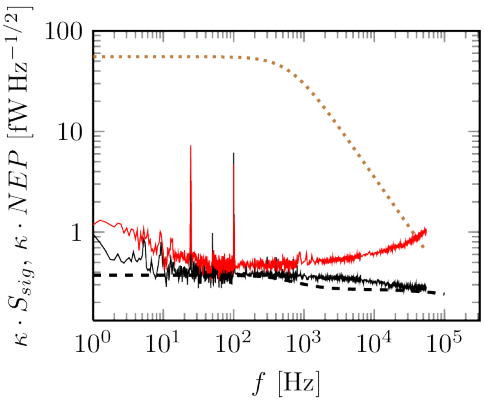

Figure 4.14: Measured NEP of the TES under room temperature background radiation load (black). In a moderately distorted working point (red line), where the readout electronics was still working, excess noise could be observed throughout the full frequency range with a strong rise above the cutoff frequency of the TES. The dotted line marks S_{sig}^{max}, the dashed line corresponds to the calculated NEP_{comb} (see eqn. 4.61). All graphs are scaled by $\kappa(\omega_{el})$.

two ways: First, the reduction of the SNR at frequencies close to and above the cutoff frequency of the TES causes fast signals, for example small objects in a scanning camera system to result in smaller system response amplitudes, which is the usual cause for the limit of their visibility. At the same time, the suppression of frequency components above ν_l smears signal steps. In a scanning system, this limits the lateral optical resolution. Therefore, for higher frame rates as well as a larger FOV, reduced time constants of the TES are necessary. Also the use of an array of several sensors is reasonable to limit the demands on the single TES. For a feasible operation of such arrays, the relevant properties of the thermistor have to be reproducible. For practical applications, also long-term stability has to be ensured. Finally, the appearance of unusable working points gains in importance for larger numbers of TES, to find common working points. Solutions for these demands will be addressed in the following chapters.

5 FEM Models

5.1 Motivation

The results of chapter 4 stress that the main necessities for a faster THz camera are the improvement of the sampling speed and a larger FOV. Both correlate to the number of sensors and the time constant of the TES. While the improvements that result from chapter 3.3 facilitate the use of larger TES arrays, the complexity as well as the production cost of a system increase with the number of sensors. In contrast, the design of the single TES itself has a much smaller influence on both. Accordingly, ways to reduce the time constant by redesigning the TES are a necessary step towards a THz camera achieving frames at video rate. As the time constants of the TES discussed in section 4.3.5 showed significant deviations from the predictions of the lumped model given in section 2.3, a more realistic model was necessary to allow for better understanding of the TES behavior. Based on this, improved designs could be developed. Thus, a finite element simulations model was developed based on the 16A design, which will be presented in section 5.2.3. It takes into account the geometrical distribution of the different components and the heat capacities of the TES. Its predictions are compared to the measurement results from above to verify the significance of the model as well as its limitations. Based on this, the effects of the geometrical composition of the TES on the time domain behavior will be discussed. To include the influence of the sensor design on the coupling efficiency into this model, the sensor has to be considered as a whole, including the coupling components. Therefore, a model of the feedhorn antenna, the absorber structure and the backshort reflector was implemented to simulate the electro-magnetic interaction (section 5.2.1).

5.2 Finite element simulations

5.2.1 Model for electro-magnetic simulations

For a precise model of a TES with an extended geometry, the influence of its geometrical setup on the radiation coupling is of fundamental importance. In addition, as for any sensor, the influential parameters of the design on the coupling efficiency have to be identified and optimized for each setup. To achieve this, three dimensional electromagnetic field simulations were performed. As a basis for the electro-thermal modeling discussed in section 5.2.3 and as a reference for further designs, the relevant components of the 16A design were simulated. Figure 5.1 gives an overview of the involved components.

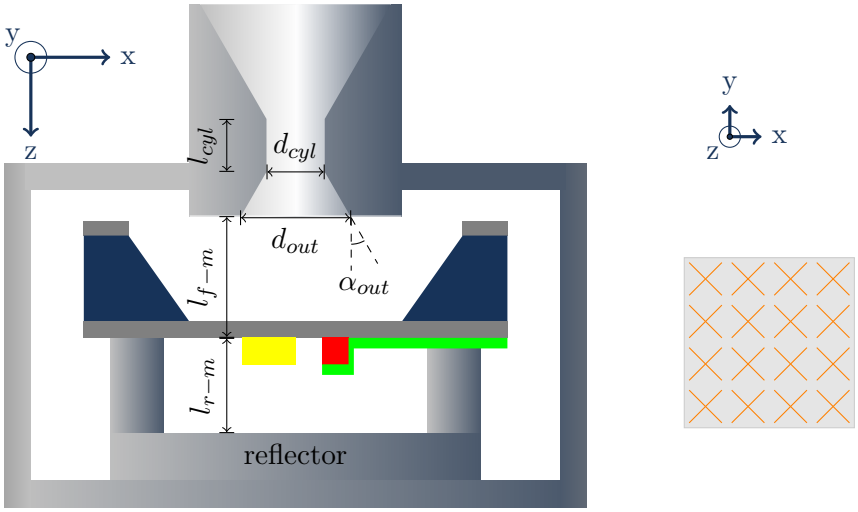

Figure 5.1: For the analysis of the absorptance, several geometric parameters are of importance: Here, d_{out} and α_{out} denote output diameter and the opening angle of the output cone of the feedhorn. l_{f-m} is the distance between output cone opening and the averted Si_3N_4 membrane surface, l_{r-m} the distance between membrane and reflector. l_{cyl} and d_{cyl} define the length and diameter of cylindric wave guide, respectively. Right: Absorber structure used in the EM model to simulate the 16A design.

Table 5.1: Geometrical parameters of the radiation coupling components for the 16A setup.

parameter	value	unit
d_{cyl}	0.54	mm
l_{cyl}	1	mm
d_{out}	1	mm
l_{f-m}	0.2	mm
l_{r-m}	0.22	mm
α_{out}	22.5	°

This includes, in addition to the alignment of the dipole absorbers on the TES, the adjacent guiding elements for the electro-magnetic field. The latter is coupled into the sensor chamber by the feedhorn antenna, which defines a lower frequency limit by the diameter of the cylindrical waveguide d_{cyl}, which has a length of l_{cyl}. The opening of the connected output cone, referred to by its diameter d_{out} defines the output lobe in combination with the opposed reflector. The distances between feedhorn cone and membrane is denoted by l_{f-m}, the distance between reflector and membrane by l_{r-m}. The latter is fixed to approx. a quarter of the center wavelength in the used optical window. The relevant parameters of the 16A design are shown in table 5.1.

A simplified model of this structure was implemented with the simulation software "CST microwave studio" (CST) [100], which uses the finite integration technique (FIT) to solve Maxwell's equations for this setup. As sketched in figure 5.2, it is independent of external components like radiation filters or optical elements and thus focuses on the actual sensor setup to be as general as possible. Several idealizations have been carried out to exclude external influences: The incoming radiation is represented by an ideal source at the averted end of the cylindrical waveguide of the feedhorn regarding the TES. Consequently, the input cone of the feedhorn is not included, and the model refers to the power reaching the waveguide, excluding reflections at the input of the feedhorn antenna. The source, implemented as a so called "port" in CST, emits electromagnetic radiation at a constant power level within the analyzed bandwidth. It creates the dominant mode (H11) with the electric field vector polarized in parallel to the x-axis in the cylindrical waveguide which limits the maximum wavelength to approx. 923 µm corresponding to a minimum frequency of approx. 325 GHz [101]. The waveguide walls are defined as a lossless material. While in the real superconducting material losses will occur, for the short length taken into account within the model of only a few wavelengths, these are negligible. Additionally, the length of the feedhorn antennas is not significantly changed for all designs discussed in this thesis, therefore, all results will be directly comparable. At the output of the cylinder, the radiation is guided through the emitting cone with the opening angle α_{out} and the opening diameter d_{out} to the absorbers. The Si_3N_4 membrane is ignored, as a dielectric material with a thickness below of 1 % of

the radiation wavelength does not significantly interact with the radiation. Hence, the absorbers are defined as freely floating bodies with the appropriate square impedance of $Z_{abs}^{\square} = 10\,\Omega$ as required in equation 3.3. The backshort behind the absorbers is implemented as a lossless reflector. The defined border constraints allow the radiation to travel in directions in the x-y-plane away from the absorbers but not to be reflected. This ensured a defined environment and avoids reflections while allowing the model have a compact geometry.

5.2.2 Radiation coupling

Using this model, the frequency dependent absorptance $A(\nu_{opt})$ of the TES was simulated for the frequency range from 300 GHz to 450 GHz. This was achieved by recording the sum of the absorbed powers

$$P_{abs}^{sum} = \sum_i P_{abs}^i \tag{5.1}$$

in the dipoles and dividing it by the source power P_{source}:

$$A(\nu_{opt}) = \frac{P_{abs}^{sum}}{P_{source}} \tag{5.2}$$

In addition, the lateral power distribution which has to be taken into account for the setup of the electro-thermal simulations in section 5.2.3 could be determined by analyzing the absorbers individually and considering the absorbed power within each dipole P_{abs}^i relative to the total absorbed power P_{abs}^{sum}. Accordingly, about 60 % of P_{abs}^{sum} are absorbed by the four cross dipole pairs closest to the center of the TES while the other 40 % are distributed over the outer dipoles.

Figure 5.3 shows a plot of the simulated overall absorptance of the 16A model. Above the cutoff frequency of the cylindrical waveguide at approx. 325 GHz, the absorptance rises strongly. This rise is accompanied by a resonant overshoot on the rising edge of the absorptance, which is an artifact of the simulation without a real counterpart. Towards higher frequencies, the absorptance rises fast up to a maximum of nearly 80 % at 364 GHz. Afterwards, it continuously sinks again at a much lower rate compared to the initial rise, being still at 70 % at 450 GHz. This is only slightly below the average of 71 % within the frequency window from 328 GHz to 368 GHz marked in the graph as a shaded rectangle. Based on the average absorptance $\bar{A}$ in the frequency range from ν_{opt}^{min} to ν_{opt}^{max}, given as

$$\bar{A}\left(\nu_{opt}^{min}, \nu_{opt}^{max}\right) = \frac{1}{\nu_{opt}^{max} - \nu_{opt}^{min}} \cdot \int_{\nu_{opt}^{min}}^{\nu_{opt}^{max}} A(\nu) d\nu \tag{5.3}$$

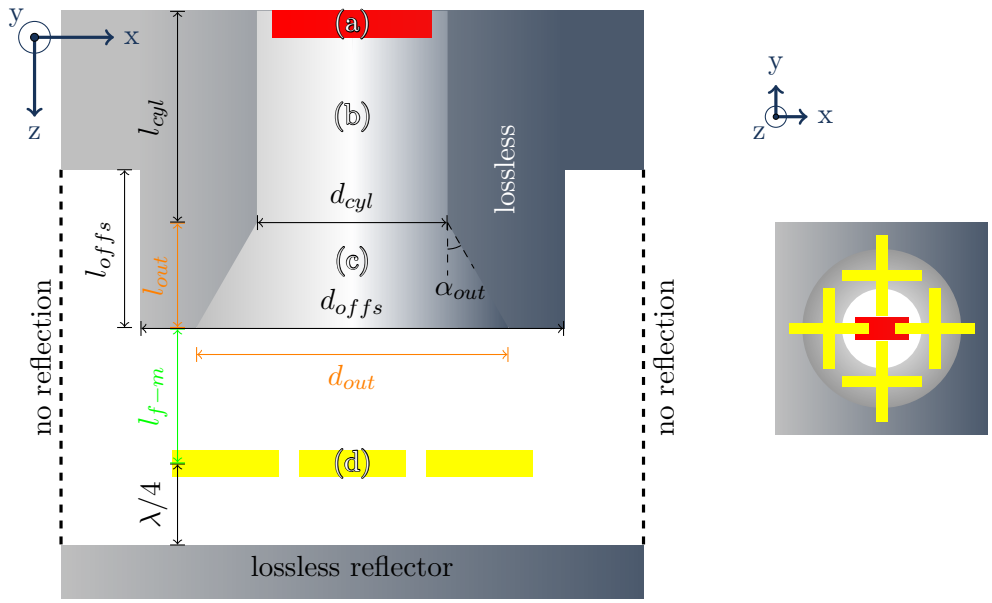

Figure 5.2: The setup for electro-magnetic coupling simulations: A source ("port") emits electro-magnetic radiation at a constant power level within the analyzed bandwidth. It creates the dominant mode (H11) with the electric field vector polarized in parallel to the x-axis in a cylindrical waveguide (b) with fixed length $l_{cyl} = 1\,\text{mm}$ and diameter $d_{cyl} = 0.54\,\text{mm}$ which limits the maximum wavelength to approx. $923\,\mu\text{m}$ corresponding to a minimum frequency of approx. $325\,\text{GHz}$ [101]. The waveguide walls are defined as lossless material. They guide the radiation into the emitting cone (c) with a fixed opening angle α_{out} towards the absorbers (d). The opening diameter d_{out} and the distance to the absorbers l_{f-m} can be varied independently. The backshort behind the absorbers is implemented as a lossless reflector. Border constraints allow radiation traveling in directions in the x-y-plane away from the absorbers but not to be reflected. For better visualization, objects are rescaled in the drawing and a reduced number of absorbers is plotted.

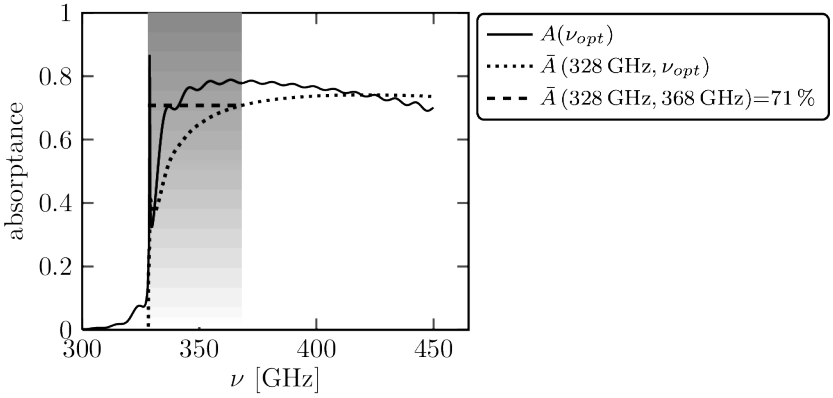

Figure 5.3: Electro-magnetic simulation of the absorptance A of the 16A model with the parameters of table 5.1. The dashed line marks the average absorptance $\bar{A}$ for the window from 328 GHz to 368 GHz. The dotted line represents the average $\bar{A}$ starting from 328 GHz to the particular frequency.

the electro-magnetic coupling efficiency η_{EM} can be defined as

$$\eta_{EM} = \bar{A}\left(\nu_{opt}^{min}, \nu_{opt}^{min} + \Delta\nu_{opt}\right) = \frac{1}{\Delta\nu_{opt}} \cdot \int_{\nu_{opt}^{min}}^{\nu_{opt}^{max}} A(\nu) d\nu \tag{5.4}$$

$$\Delta\nu_{opt} = \nu_{opt}^{max} - \nu_{opt}^{min} \tag{5.5}$$

For the shaded window with $\nu_{opt}^{min} = 328\,\text{GHz}$ and $\Delta\nu_{opt} = 40\,\text{GHz}$ this results in

$$\eta_{EM} \approx 71\,\% \tag{5.6}$$

The average absorptance $\bar{A}\,(328\,\text{GHz}, \nu_{opt})$ starting from 328 GHz up to the respective frequency ν_{opt} is plotted as a dotted line in the graph. It reaches its maximum of 74 % at approximately 420 GHz, corresponding to the maximum coupling efficiency

$$\eta_{EM}^{max} \approx 74\,\% \tag{5.7}$$

This would allow for the use of a wider frequency window for moderate distances, for which the attenuation of air plays a minor role.

5.2.3 Model for electro-thermal simulations

As a basis for the development of improved designs, the results of the measurements presented above were used to create a virtual model of the 16A design TES.

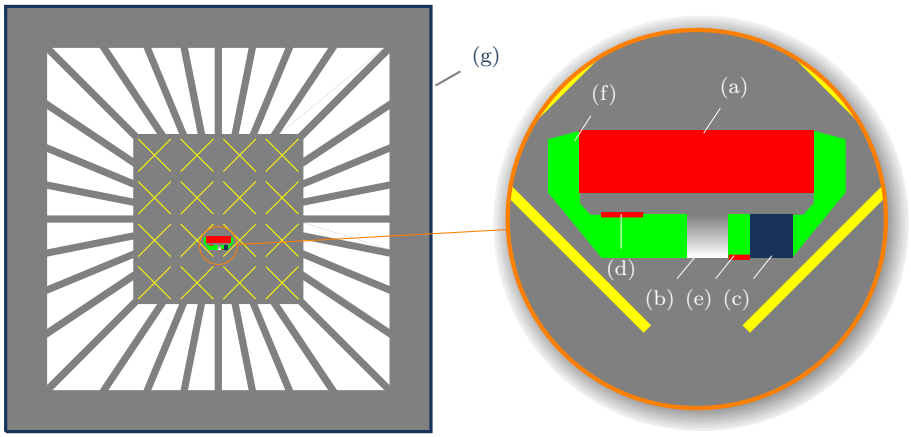

Figure 5.4: Geometry of the 16A TES FEM model. Compared to the structure of the fabricated TES (fig. 3.2), the spider leg structure is slightly simplified. SP and superconducting wiring are omitted as they do not significantly contribute to the total heat capacity (cf. table 4.3). The magnification shows the electrical circuit that allows for a realistic modeling. It includes the thermistor (a), the shunt resistor (b), R_L (c) and the current nodes (d) and (e) on the wiring (f). The blue frame (g) marks the fixed thermal bath at T_{bath}.

Because of the numerous interactions within this model, an analytical description of the contribution of each component is extremely complicated. Even if the distributed heat capacity of the membrane would be ignored, 18 separated elements (the thermal bath, the absorbers and the thermistor) would have to be taken into account. Utilizing the symmetry, this can be reduced to 10. However, each of these components interacts with all others, resulting in 45 different time dependent coupled heat flow equations. As shown in [92], the quantitative analysis of only 3 elements already results in a complex set of equations. Therefore, to achieve realistic representation of the extended geometries, a modeling system based on the finite element method (FEM) was chosen. The necessity to take into account the different physical processes and their interactions led to the choice of the finite element analysis (FEA) software "comsol multiphysics"[102] as the basis of the model. It is capable to combine the thermal properties, heat distribution and thermal conductance as well as electrical behavior, resistance modeling, current flow and Joule heating including their interactions into one model and describe the time dependent development of these properties. This allows to describe the temperature distribution on the membrane of the TES as well as to simulate its I-I curves and signal step responses.

Using this system, a simplified model of the 16A TES was set up. It consists of a set of two-dimensional adjacent elements in the x-y plane, as shown in figure 5.4. Each element has a defined virtual thickness to represent the three dimensional character of the real TES. The corresponding values were taken from table 3.1, to adequately fit the

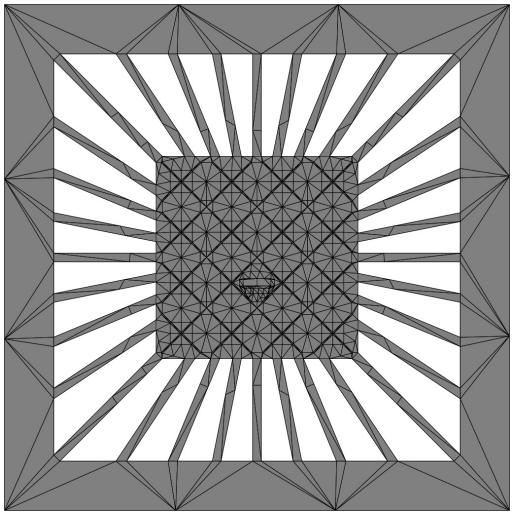

Figure 5.5: Mesh structure of the FEM model of the 16A design.

real geometry. To avoid this flat modeling to cause unnatural results, boundary effects like thermal boundary resistances in between these elements are set to zero. Also no equivalents of the real three-dimensional boundary effects were introduced to focus on unavoidable fundamental effects resulting from the geometry itself, keeping the model as general as possible. For the same reason, an ideal thermal bath is assumed and simulated by fixing the outer edges of the model geometry, as marked in figure 5.4, to the bath temperature T_{bath}. The results presented in the following will confirm that despite these limitations still a good matching to measurement data can be achieved, confirming the fundamental influence of the geometrical properties of the TES.

Because of their negligible contribution to the total heat capacity (see table 4.3), superconducting wiring and SP were not included into the model. Instead, a simplified electrical circuit containing all the relevant components was included directly on the membrane. It consists of the thermistor itself, the bias circuit including the shunt resistor R_{sh} and the series resistance R_L connected by low resistive strip lines and nodes for the current bias, as marked on the right side of figure 5.4. The parasitic resistance R_0 is included into the thermistor without a geometric representation.

To not distort the thermal properties of the model, all electrical components except the thermistor were set as thermally identical to the membrane: Heat capacity, thermal conductance and thicknesses are the same as for the membrane. In addition, these components can not cause Joule heating. This limits their effect to the electrical domain and causes the thermal behavior of the TES to be exactly the same as if these components were located outside of the membrane.

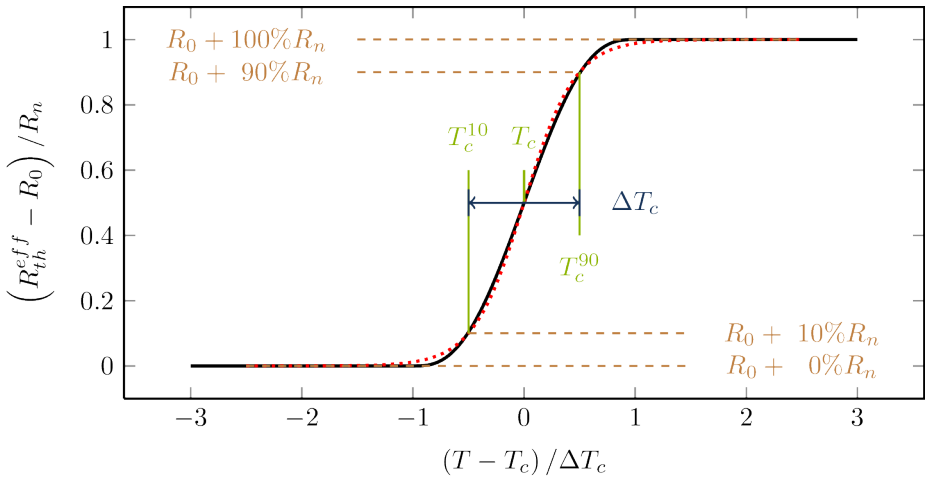

Figure 5.6: *R-T* curve used in the comsol FEM models (black line). It is nearly identical to the *R-T* curve given in figure 2.2, here plotted as a red dotted line which is used in the calculated curves. For comparable results, the levels at T_c^{10} and T_c^{90} and consequently the transition width are identical for both curves. Slight differences occur at the edges of the transition resulting from the faster convergence of the comsol curve to the constant asymptotic levels in the fully superconducting and normal conducting ranges. This only causes small changes in the shape of the resulting *I-I* curves but is advantageous for the stability of the FEM model.

For the calculation of the time dependent properties of the model, its geometry is separated into a set of small subdomains. This fragmentation is represented by a mesh of nodes and their interconnections that covers the model. For each node, the necessary differential equations, as the heat equation, Ohm's law and Joule's law, are numerically solved with regard to its neighbors, and the results are interpolated to get a full solution for the whole model. Figure 5.5 shows the used mesh for the 16A model.

In analogy to the analytical lumped model used in section 4.3.4, the temperature dependence of the electrical resistance of the thermistor in the comsol model is given by a smoothed step function, defined by the normal state resistance R_n, critical temperature T_c and transition width ΔT_c, defining the 10 % and 90 % limits of the resistance drop (see figure 5.6). For practical reasons, the used functions are not fully identical: For the analytical description of the lumped model, the use of an invertible function is advantageous. The chosen function as given by equation 4.28 converges to constant resistance levels in the fully superconducting and normalconducting states, respectively, but never actually reaches a constant state. Opposed to that, the stability of the FEM simulations is improved if extremely small differences from the asymptotic levels can be avoided. Thus, in the latter case, a function is used that converges faster and returns constant

levels for both cases. This is achieved by the internal "flc2hs" comsol function [103].

However, as can be seen from figure 5.6, the *R-T* curve of the FEM model is nearly identical to the analytical *R-T* curve given in equation 4.28 which is used for calculated curves based on the model in section 4.3.4. Slight deviations can be seen at the edges of the transition. This is caused by the required faster convergence of the comsol curve to the constant asymptotic levels in the fully superconducting and normal conducting ranges. As these slight differences only cause small changes in the shape of the resulting *I-I* curves but do not significantly affect the results, these minor differences are justified by their practical advantages.

Another difference between the numerical and analytical models is also caused by the difficulty to handle extremly small or large quantities correctly in the numerical models without affecting the stability of the simulations. In the superconducting state, the electrical resistance becomes zero. However, the corresponding infinitely large electric conductivity causes the simulations to diverge and thus become non-solvable. Thus, a small parasitic resistance R_0 is introduced to ensure a non-zero minimum resistance. It is kept low enough to be fully negligible for the behavior of the thermistor and thus of the TES throughout its working range and to reproduce the behavior in the superconducting state, which is the case for

$$R_0 \ll R_{sh} \tag{5.8}$$

$$R_0 \ll R_{th}^{min} \tag{5.9}$$

$$R_0 \ll R_L \tag{5.10}$$

as discussed in section 4.3.4. In this and the following simulations, it is set to

$$R_0 = 1\,\mathrm{m\Omega} \tag{5.11}$$

which fulfills the conditions given above.

For the same reason, the superconducting wiring is represented by a electrical conductivity which is not infinitely large but 1000 times as high as the conductivity of the shunt resistor. Due to the compact geometry used in the model with wide and extremely short wiring (see figure 5.4), the model approaches the case of superconductivity fairly well and differences resulting from this slight deviation are negligible.

Material properties, especially specific heat capacities and thermal conductivities were defined by temperature dependent functions for each element as discussed in section 4.3.1:

$$c_{th} = \beta_{th} \cdot T^3 + \gamma_{th} \cdot T \tag{5.12}$$

$$c_{abs} = \beta_{abs} \cdot T^3 + \gamma_{abs} \cdot T \tag{5.13}$$

$$c_{mem} = \beta_{mem} \cdot T^3 \tag{5.14}$$

and

$$k_{th} = \sigma_{th}^{NC} \cdot L_0 \cdot T \tag{5.15}$$

$$k_{abs} = \sigma_{abs} \cdot L_0 \cdot T \tag{5.16}$$

$$k_{mem} = k_{mem}^0 \cdot T^{1.7} \tag{5.17}$$

where the indizes "th", "abs" and "mem" denote the properties of the thermistor, the absorber and the membrane, respectively. σ is the electrical conductivity and L_0 the Lorentz constant (see equation 4.14). σ_{th}^{NC} refers to the value in the normal conducting state conductivity of the thermistor.

For the definition of the specific heat capacities and thermal conductivities of the different components, the values given in table 4.1 were used. However, due to the two-dimensional character of the model, the thermistor and the dipoles replace the membrane at these locations, while in the real TES, they are located on top of it. To accommodate these structural differences, effective values for the thermal conductivities for the thermistor and the dipoles were used to represent the membrane at these locations. Thus, the used values are

$$k_{th}^{eff} = \sigma_{th}^{NC} \cdot L_0 \cdot T + k_{mem} \cdot \frac{d_{mem}}{d_{th}} \tag{5.18}$$

$$k_{abs}^{eff} = \sigma_{abs} \cdot L_0 \cdot T + k_{mem} \cdot \frac{d_{mem}}{d_{abs}} \tag{5.19}$$

The values of d_{mem}, d_{th} and d_{abs} represent the thicknesses of the membrane, the thermistor and the absorber. The last factors are used to compensate the differences of the thicknesses of the modeled elements and the membrane. For the heat capacities no adjustments of the values were used as table 3.1 shows that the total mismatch of the heat capacity of the platform is below 6 %, so it would have only minor effects on the behavior of the TES as a whole. Locally, the additional heat capacity would be approx. 0.3 % at the thermistor and 1.6 % at the absorbers, referring to table 4.2. Thus, also local effects can be neglected.

The thermal conductivity of the membrane as given in equation 5.17 was determined using the findings of section 4.3.4. Due to the non-trivial geometrical influences on the ratio between G_0 and k_{mem}^0, simulated I-I curves were used to find the corresponding value of k_{mem}^0.

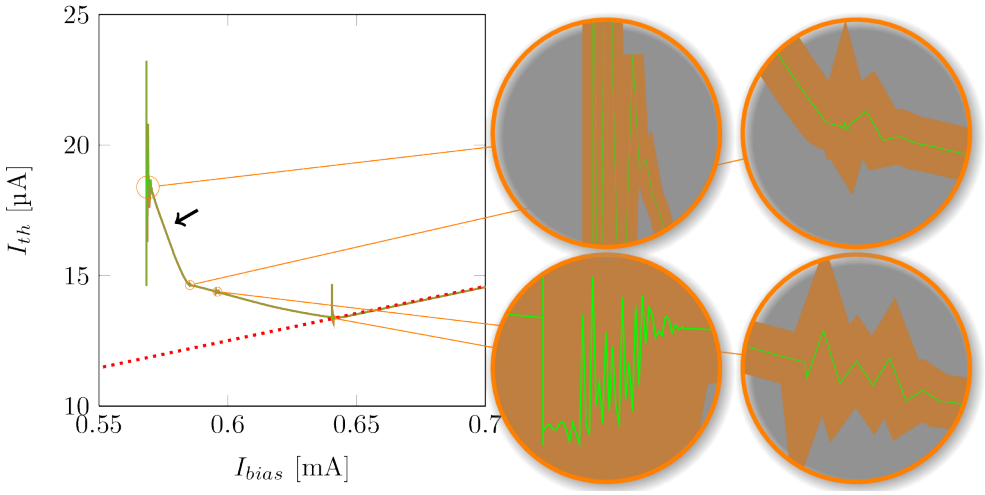

Figure 5.7: *I-I* curve simulated using the comsol FEM model with k_{th} as calculated from the WFL. For improved visibility of details, it is plotted twice: As a thicker brown line to guide the eye in the overview on the left and a thinner green line reflecting fine details of the curves. The initial bias current was set to the normal conducting range (red dotted line) and continuously reduced. Throughout the transition range, for certain bias current ranges the solution is very sensitive to smallest current changes or even diverging, as can be seen in the magnifications on the right. In some regions, the local trend of the curve drastically changes as in the section marked by the black arrow.

5.2.4 current-current characteristic

By virtually feeding a decreasing current bias ramp $I_{bias}(t)$ into the current nodes of the bias circuit of the FEM model, the *I-I* characteristic of the TES can be simulated.

Figure 5.7 shows such an *I-I* curve using k_{th} as calculated from the WFL (equation 4.14). Starting from a bias current value in the normal conducting range and consecutively reducing it, the typical curve shape as described in section 4.3.4 can be reproduced. However, as the magnifications on the right side of the graph show, the curve contains several sections of increased sensitivity to changes in the bias current. While normally moderate changes of I_{bias} lead to a fast convergence to the corresponding new working point, in these sections even small steps can cause inappropriate results like discontinuous jumps. The resulting local distortions of the curve can be reduced by running the simulation with extremely small current step sizes. However, in several bias ranges, resonant-like oscillations of the current through the thermistor could be observed which also result in divergent solutions. These resonances become stronger the closer a certain bias region is sampled and can fully break the simulation. Thus, in these regions the bias step size must be increased. As both types of these regions occurred throughout the

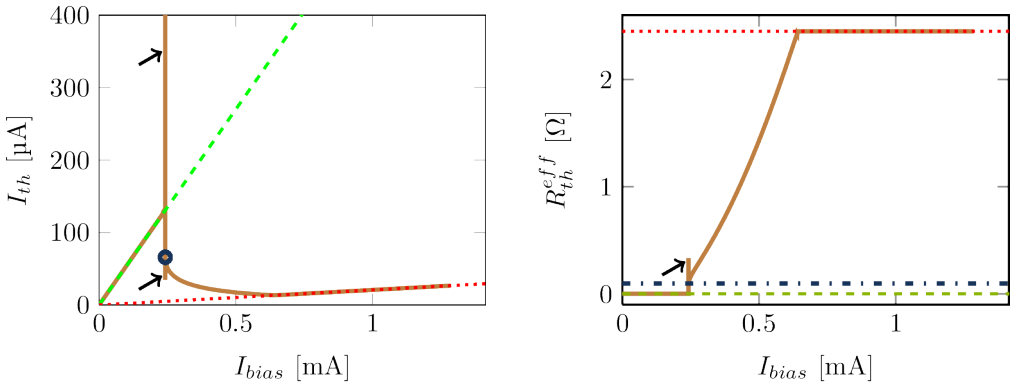

Figure 5.8: *I-I* curve (left) and the corresponding *R-I* curve (right) simulated using the comsol FEM model. The initial bias current was set to the normal conducting range (red dotted line) and continuously reduced. Close to the superconducting range, the simulated curves show an overshooting oscillation (black arrows) due to the transition to the positive electrothermal feedback at $R_{th,eff}^{min}$ which is marked by a blue circle on the left and a blue dash-dotted line in the right graph. The overshoot is a non-realistic effect and due to a local divergence of the solution of the simulation. For lower currents, the curve converges to the superconducting state (green dashed line).

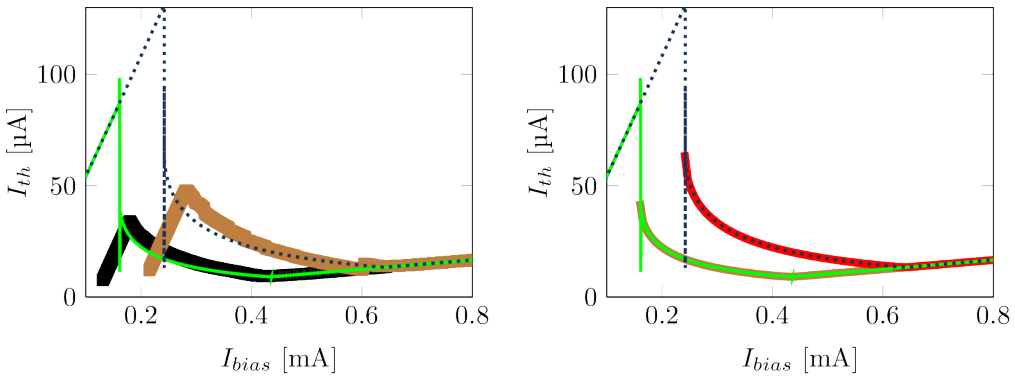

Figure 5.9: Left: Measured *I-I* curves of the 16A model without background radiation (square symbols) at $T_{bath} = 402\,\mathrm{mK}$ (brown) and $T_{bath} = 502\,\mathrm{mK}$ (black) and the corresponding simulated curves of the comsol model (thin lines). The local minimum at the upper end of the transition range was used to adjust the value of k_{mem}^{0} by fitting the simulated curves to the measured data.
Right: The simulated curves match the analytically calculated curves of the lumped model (thick lines) very well throughout the transition range.

whole transition range and their location could not be predicted, an empirically found set of strongly varying sampling step widths must be used to find a stable solution for a curve. For a given set of parameters for the model, this set of steps reproducibly leads to a stable solution. However, the process to find such a set is extremely time consuming. Furthermore, even with these parameters, in some regions of the curve the local trend changed, causing the curve to bend. An example of such a behavior is marked by the black arrow in figure 5.7. This effect could be observed for various mesh sizes and different temperature levels. However, in these critical regions, oftentimes a clear separation of the thermistor into segments with different temperatures and thus resistive states could be observed. A substantial increase of the thermal conductivity k_{th} within the thermistor could significantly reduce these effects. Therefore, a scaling factor ψ_{th} for k_{th} was introduced. This extends equation 5.15 to

$$k_{th}^{eff} = \sigma_{th}^{NC} \cdot L_0 \cdot T \cdot \psi_{th} + k_{mem} \cdot \frac{d_{mem}}{d_{th}} \tag{5.20}$$

Based on the discussed in section 4.3.3 it is possible to conclude that increasing k_{th} by choosing values of ψ_{th} larger than one should not affect the characteristic behavior of the TES as a whole, as even for $\psi_{th} = 1$ the local thermal conductance at the thermistor is dominated by the thermistor itself. Thus, as long as the thermal conductivity of the membrane is not significantly larger as the value given in table 4.1, only intrinsic effects on the thermistor are to be expected for $\psi_{th} \gg 1$, like influences on the distortions. In particular, the determination of k_{mem}^0 would not be affected. Consequently, $\psi_{th} = 100$ was used in the following to find k_{mem}^0.

The left graph of figure 5.8 shows a typical curve with $\psi_{th} = 100$: By starting with an initial bias current in the normal conducting range and continuously decreasing it in the following, a full I-I curve from the normal conducting range to the superconducting state as discussed in section 4.3.4 can be achieved. The very good matching of the analytically calculated and the simulated curves shown in figure 5.9 stresses that the FEM model despite its distributed geometry maintains the properties of the analytical model for lumped TES for the I-I characteristic.

As for the analytically calculated curves but different to the measured ones, the absolute current values show no variable offset, and the jump to the superconducting range is clearly visible. As can be seen in the figure, this jump happens exactly at the predicted minimum resistance R_{th}^{min} marked by a blue circle as defined in equation 4.22. Including the parasitic resistance R_0, it is given by

$$R_{th,eff}^{min} = R_L + R_{sh} \tag{5.21}$$

However, in the immediate vicinity of this jump coming from higher bias currents, due to the transition from negative to positive electrothermal feedback, an oscillation and overshoot of the simulated resistance and thus the current through the thermistor I_{th}

can be observed, which leads to non-realistic values, like values of I_{th} exceeding I_{bias}. But different to the distortions described above for $\psi_{th} = 1$ this is a strongly localized effect in the curve which immediately converges as soon as the superconducting range is reached.

Simulated *I-I* curves were used to adjust the thermal conductivity to a value that results in the same thermal conductance as found in section 4.3.4. For the temperature exponent, the value of 1.7 based on the above mentioned measurements was used. While the measurements resulted in a value for G_0, the constant factor of the thermal conductance, a direct calculation of the corresponding thermal conductivity is challenging due to the extended and complex geometry. Instead, for a set of simulations, the value of k^0_{mem} was adjusted to result in *I-I* curves fitting the measured data as shown in figure 5.9. Thus, by combining FEM simulations and measurements, the material parameter k^0_{mem} could be estimated. The resulting value is

$$k^0_{mem} = 7.5 \times 10^{-3}\,\mathrm{W\,m^{-1}\,K^{-1}\,K^{-1.7}} \tag{5.22}$$

which results in a relative difference to the literature value given in table 4.1 of

$$\frac{k^{lit}_{mem} - k^{comsol}_{mem}}{k^{lit}_{mem}} \approx 1 - \frac{0.58}{\sqrt{T}} \tag{5.23}$$

This yields 8 % to 25 % for the temperature range from 0.4 K to 0.6 K. Therefore, the derived value is very close to the found value in [80]. In particular, it is not significantly larger than k^{lit}_{mem} for temperatures above 0.35 K, which is the lowest temperature discussed in this thesis. Therefore, the conditions of section 4.3.3 are fulfilled: k^0_{mem} it does not affect the local thermal conductance at the thermistor and thus justifies the use of $\psi_{th} > 1$ as discussed above.

5.2.5 Temperature distribution and efficiency

By applying a bias current within the transition range, the thermistor is heated up to a temperature close to T_c. The resulting temperature distribution for $T_{bath} = 402\,\mathrm{mK}$ is shown on the left in figure 5.10. A significant thermal gradient across the platform of the membrane can be observed which is due to the not negligible thermal resistance from the thermistor to the edges of the platform. This distribution does not change significantly throughout the whole working range, as the temperature changes in the thermistor are limited to ΔT_c, which is much smaller than the observed temperature differences throughout the platform.

To include the effect of radiation into the FEM model, the radiation power was simulated as heat sources in the dipole absorbers. To keep the simulation conditions as close as possible at the measured results, the total radiation power was matched to the absorbed background power as measured for the 16A TES of $P_{rad} = 3.2 \times 10^{-11}\,\mathrm{W}$, which is given in equation 4.48. As this value was determined as the difference in the joule

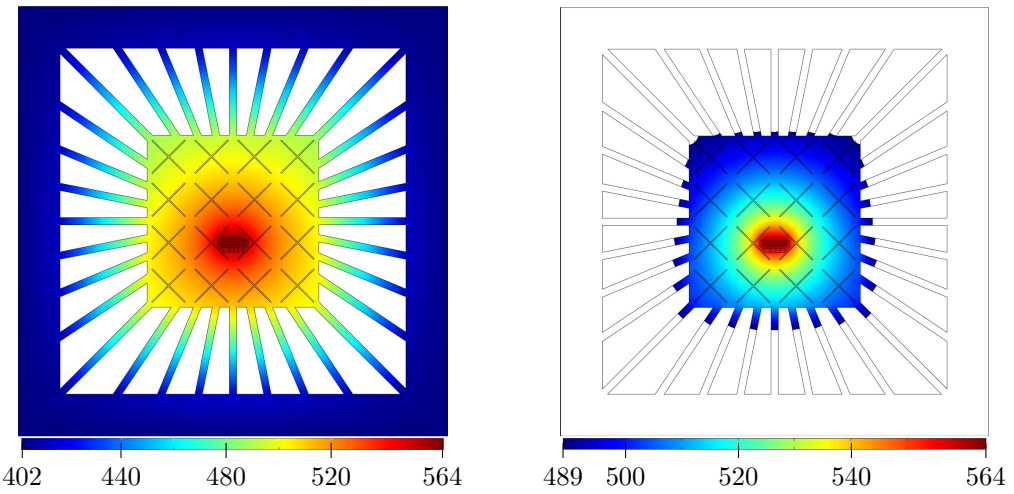

Figure 5.10: Left: Temperature distribution of the 16A comsol model in the transition range for $T_{bath} = 402\,\mathrm{mK}$ and $T_c = 564\,\mathrm{mK}$ without radiation load. The color scale marks the temperature levels in mK.
Right: The simulated total background radiation power was $P_{rad} = 48\,\mathrm{pW}$. A limited temperature range was used to visualize the gradient on the platform.

heating power ΔP_{el} of the thermistor caused by the additional radiation (see section 4.3.6), ΔP_{el} had to be matched to the measurements. Due to the thermal gradient on the platform, the effect of the radiation load on the thermistor is reduced. This can be expressed by an efficiency factor η_{abs} between the power at the absorbers P_{rad}^{abs} and the power difference at the thermistor $P_{rad}^{th} \equiv P_{rad} = \Delta P_{el}$ below one. It can be defined as

$$\eta_{abs} = \frac{\Delta P_{el}}{P_{rad}^{abs}} \tag{5.24}$$

To take into account the lateral intensity distribution across the platform, the found parameters from section 5.2.2 were applied, resulting in 60 % of the total power absorbed in the four dipole absorber pairs closest to the center of the membrane, while the remaining 40 % were evenly distributed over the outer absorbers.

By simulating the I-I curves with varied values of P_{rad}^{abs} and calculating the corresponding ΔP_{el}, η_{abs} was determined as

$$\eta_{abs} \approx 67\,\% \tag{5.25}$$

with the resulting radiation power at the absorbers of

$$P_{rad}^{abs} = \frac{\Delta P_{el}}{\eta_{abs}} = 4.76 \times 10^{-11}\,\mathrm{W} \tag{5.26}$$

This efficiency can be combined with the coupling efficiency found in section 5.2.2 to a bandwidth dependent overall efficiency for the TES including the feedhorn antenna of

$$\eta_{TES} = \eta_{EM} \cdot \eta_{abs} \tag{5.27}$$

which evaluates for the 16A model to

$$\eta_{TES}^{16A} \approx 48\,\% \tag{5.28}$$

for the optical frequency range from 328 GHz to 368 GHz.

The temperature distribution on the thermal platform with radiation load is shown on the right side of figure 5.10. As can be seen from the figure, the Joule heating in the thermistor dominates the temperature distribution as required by equation 4.53 for a strong negative electrothermal feedback. As for the case without background load, the thermalization is strongly inhomogeneous. The temperature difference between the outer edges of the platform and the thermistor is approx. 70 mK, thus far beyond the temperature variation caused by a signal in the working range of the TES, which has to be significantly smaller than ΔT_c. Therefore, the different components on the platform have to be considered individually, and significant deviations from the lumped geometry modeling which predicts $\eta_{abs} = 1$ can be caused by the different interactions of these components, even in case of less complex structures[92].

5.2.6 Time constants

To determine the time constants of the comsol model, a concept based on the experimental setup described in section 4.3.5 was used to avoid systematical differences to the measurements. Thus, under a background load as described in section 5.2.5, a rectangular signal δP_{rad} was applied to the TES. It was added to the background Power P_{rad} and thus directly applied to the absorbers. For the amplitude of the total signal, $(\Delta P_{sig})_{max} = 1.4 \times 10^{-12}\,\mathrm{W}$ as given in equation 4.54 was used. To accommodate the internal efficiency of the TES, it was scaled by η_{abs} as

$$\delta P_{rad} = \frac{(\Delta P_{sig})_{max}}{\eta_{abs}} \approx 2.0 \times 10^{-12}\,\mathrm{W} \tag{5.29}$$

δP_{rad} was distributed in the same ratio over the absorbers as the background radiation. As a reference for the following simulations, the *I-I* curve with background load was simulated to exactly locate the working range referred to the bias current. It is shown in the left graph of figure 5.12. For the actual simulation of the signal response a set

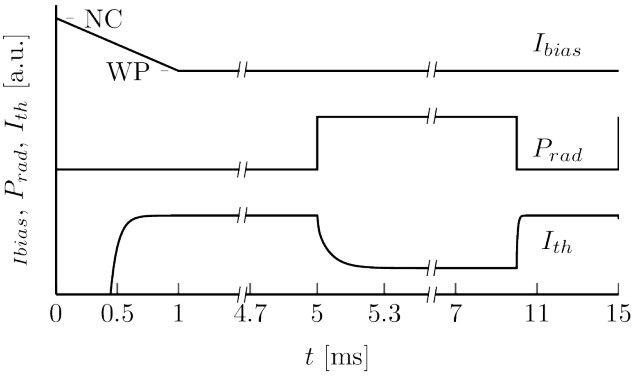

Figure 5.11: Time flow diagram of the time constant simulation. At $t = 0$, I_{bias} is set to the normal conducting state (denoted as "NC") of the thermistor, and the radiation is set to the background power level P_{rad}. Within the first millisecond, it is linearly reduced to the working point value (marked as "WP"). Starting at $t = 5\,\text{ms}$, the signal is switched on for 5 ms every 10 ms. The current through the thermistor I_{th} is reduced accordingly with its characteristic time constant. The curves are scaled and shifted arbitrarily for a better visualization. For values of K_C^{FEM} different from 1, all timing values are scaled accordingly (see text and equation 5.33).

of working points was chosen for individual evaluation. To achieve a stable model for each of them, a defined initial state was created by setting the bias current to a value in the normal resistive state and linearly reducing it within 1 ms to the actual working point, where it was kept constant until the end of the simulation run. The background radiation was applied from the beginning, while a settling time of 5 ms was used to fully stabilize the simulation before the signal was switched on for another 5 ms. Within this time span, the TES could fully reach the new state of equilibrium even for the largest time constants measured. Afterward, the signal was switched off again. A periodic signal was used, but as the step responses proved to be very reproducible, only one period was evaluated. A time flow diagram of this simulation procedure is presented in figure 5.11.

Three examples of the step responses resulting from this procedure are shown in figure 5.12. The used working points are marked in the I-I curve. As can be seen from the figure, the simulated curves can not fully be matched by single exponential functions. Thus, for comparison, the effective time constants were determined using the $1/e$ drop criterion. For this purpose, the time difference between the start of the step to the drop to 1/e of the level differences was compared to the time constants resulting from the exponential curve fits. The differences in the time constants for both methods were found to be only a few percent of the value, oftentimes smaller than one percent. Thus, both methods result in comparable time constants. However, for the best reproducibility, the results from the $1/e$ drop were used in the following evaluation.

As the current response δI_{th} of the TES depends on the first derivative of the resistance

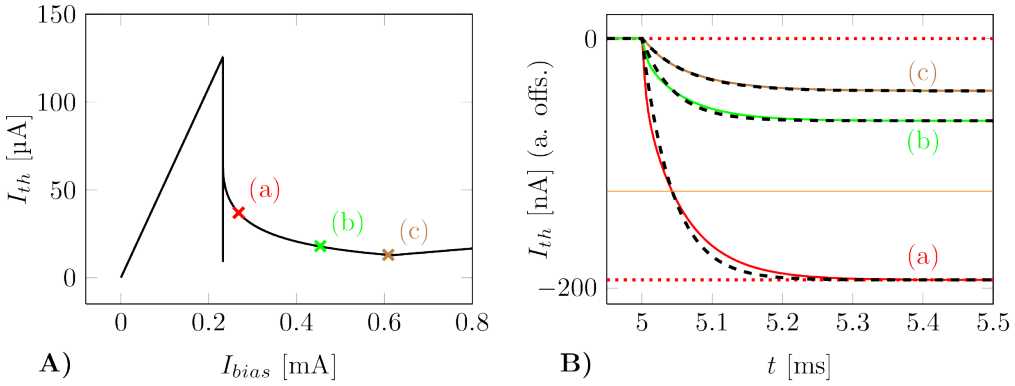

Figure 5.12: A) Simulated *I-I* curve with background load of 48 pW. For the marked working points denoted as (a), (b) and (c), the corresponding step responses of the TES are shown in B). The step response curves (continuous lines) are shifted to have a common upper level for easier comparison. They can not be fully matched by single exponential functions (dashed lines). Thus, time constants were also determined as the time difference between the start of the step to the drop to 1/e (marked as straight orange line for the red curve) of the level differences (dotted lines). However, the differences in the time constants for both methods were found to be only a few percent of the value, oftentimes smaller than one percent.

of the thermistor with respect to its temperature (cf. equation 2.58), the closer a working point comes to the normal conducting range, the smaller is δI_{th}. Above a certain bias value, the response becomes too small to be evaluated. While in measurements this is limited by the SNR, in the FEM simulations dR_{th}/dT becomes exactly zero (see figure 5.6). Hence, to still be able to evaluate working points close to and in the normal conducting range to define a thermal time constant τ_0, using δI_{th} is not suitable. Instead, for these working points the thermal response δT was used. For R_{th} close to R_n, the thermistor voltage can be assumed to be constant for sufficiently small signals (see section 2.4), with a direct proportionality of the resistance response δR_{th} to the current response:

$$\delta I_{th} = -\frac{V_{th}}{R_{th}^2} \cdot \delta R_{th} \propto \delta R_{th}, \qquad \delta R_{th} \ll R_{th}, V_{th} \approx const. \tag{5.30}$$

In this case, due to the strictly monotonic character of the *R-T* curve within the transition range, the resulting temperature response can be assumed to be proportional to the current response for small enough signals to keep dR_{th}/dT constant.

While the latter condition is hard to match in the strongly nonlinear range of the *R-T* curve close to R_n, it can be extrapolated to temperatures close to the transition with $dR_{th}/dT = 0$. The thermal response found there by evaluating $\delta T(t)$ can be expected to be very close to the thermal time constant of the TES without electrothermal feedback.

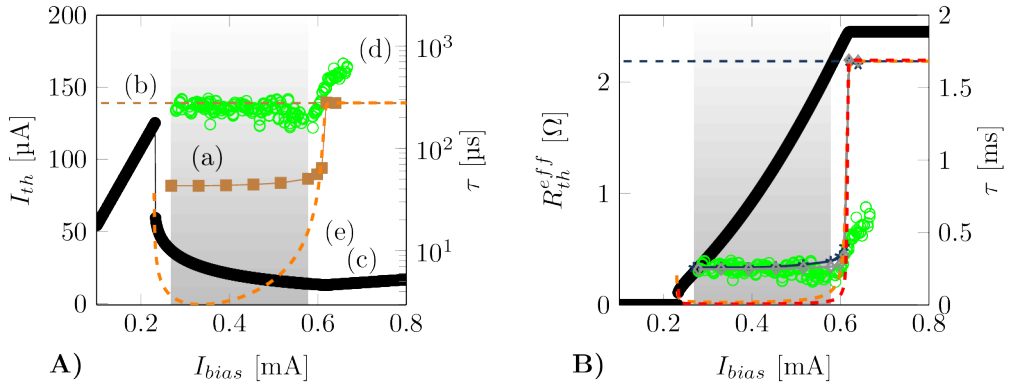

Figure 5.13: A) shows the FEM simulation results for $\Delta T_c = 3\,\mathrm{mK}$ of $\tau\,(I_{bias})$ (a), τ_0 (b) and the I-I curve (c). While the course of the simulated τ is similar to the measured time constants (d) throughout the usable working range (shaded), it significantly differs from the lumped model results (e). B) Scaling the heat capacities by $K_C^{FEM} = 6$ results in an also quantitatively good matching of the simulated and the measured τ throughout the shaded range for $\Delta T_c = 3\,\mathrm{mK}$ (blue stars) as well as for $\Delta T_c = 1\,\mathrm{mK}$ (gray rhombi) while both strongly deviate from the lumped model results (orange dashed line: $\Delta T_c = 3\,\mathrm{mK}$, red dashed line: $\Delta T_c = 1\,\mathrm{mK}$). For comparison, R_{th}^{eff} is plotted (black line).

Therefore, in addition the current based evaluation of the time constants throughout the transition range, a value for the thermal time constant was determined by using the temperature response for each set of simulations.

The symbols in the left graph of figure 5.13 show the resulting time constants plotted versus the bias current of the corresponding working points. The determined thermal time constant level is marked by a horizontal dashed line.

Though the heat capacities and thermal conductance used in the model are the same as those used for the lumped model thermal time constant $\tau_0^{lumped} \approx 440\,\mu\mathrm{s}$ in equation 4.42, the FEM model results in a significantly smaller value of

$$\tau_0^{FEM} = 277\,\mu\mathrm{s} \tag{5.31}$$

Thus, the ratio of these thermal time constants η_{τ_0} of

$$\eta_{\tau_0} = \frac{\tau_0^{FEM}}{\tau_0^{lumped}} \approx 63\,\% \tag{5.32}$$

is another result of the distributed structure as the TES. It confirms that the found internal efficiency η_{abs} of the radiation power in the TES is not just due to an effective reduction of the signal amplitude but results in changed effective total heat capacities

and thermal conductances, which constitute the thermal time constant. This stresses the limitations of the lumped model for such structures, in which the different components of the TES interact with each other, resulting in a distinct signal course and corresponding time constant for each pair of components. At the thermistor, an effective signal response and time constant result from the combination of all of these signals. Therefore, η_{τ_0} and η_{abs} can be interpreted as if a significant part of the TES would not interact with the thermistor, resulting in an effectively reduced total heat capacity by η_{τ_0} compared to the physical value. The fact that only a part of the incoming radiation power is effectively transferred to the thermistor reduces its power efficiency, and at the same time lowers the reaction time as a smaller amount of heat has to be compensated for per time interval. In the extreme case of a nearly fully decoupled thermistor, this would result in η_{τ_0} and η_{abs} both being close to zero, which obviously corresponds to a very small, but fast response.

For comparison to the simulated data shown in figure 5.13, the measured time constants are given. In addition, the analytically calculated time constant course for the lumped model based on the *I-I* curve and the thermal time constant resulting from the FEM simulation τ_0^{FEM} is plotted for $\Delta T_c = 3\,\mathrm{mK}$. As discussed in section 4.3.5, the course of the time constants resulting from the lumped model varies much stronger with the bias current throughout the working range than the measured time constants, which show a fast drop at the upper end of the transition range and are nearly constant throughout the rest of the working range.

The resulting values of the comsol simulation reproduce the general tendency of the measurement: They vary by less than $\pm 10\,\%$ throughout nearly the whole transition range, with a sharp jump close to the normal resistance range. Within the shaded area of the graph, the simulated time constants rise by approx. $17\,\%$ referred to the minimum value, while in the same range the lumped model values show a rise by approx $420\,\%$. As the model uses idealized components, this effect again has to be attributed to the geometrical separation of the different components of the TES.

However, the absolute levels of the simulated time constants significantly differ from the measured values. In the working range marked in the graph, the simulation resulted in time constants in the range from $43\,\mu\mathrm{s}$ to $50\,\mu\mathrm{s}$, which is by a factor of 6 lower than the measured values. To accommodate the difference in the absolute levels of the time constant plateau of measured and simulated data, the total heat capacity of the comsol model was scaled by a factor K_C^{FEM}. The timing parameters of the simulation as described in figure 5.11 were scaled accordingly by the same factor. By applying it to the specific heat of every component in the model, a new set of time constants was determined. As the right side of figure 5.13 shows, a good matching to the measured data was achieved within the range of low τ for

$$K_C^{FEM} = 6 \tag{5.33}$$

which resulted in time constants from $259\,\mu\mathrm{s}$ to $302\,\mu\mathrm{s}$ and from $246\,\mu\mathrm{s}$ to $264\,\mu\mathrm{s}$ for $\Delta T_c = 3\,\mathrm{mK}$ and $\Delta T_c = 1\,\mathrm{mK}$, respectively, in the shaded area. The resulting thermal

time constant is

$$\tau_0^{FEM,C\times 6} \approx 1.66\,\mathrm{ms} \tag{5.34}$$

which is in accordance with the expected value resulting from upscaling the value for $K_C^{FEM} = 1$ by a factor of 6:

$$\tau_0^{FEM,C\times 6} \approx 6 \cdot \tau_0^{FEM} \approx 1.66\,\mathrm{ms} \tag{5.35}$$

This and the good accordance in the working range confirms that also in this model the time constants are proportional to the total heat capacity of the TES, as it is the case in the lumped model. However, the good matching can be observed for $\Delta T_c = 3\,\mathrm{mK}$ as well as for $\Delta T_c = 1\,\mathrm{mK}$. For both simulated transition widths, the minimum time constant is at the same level, and the ratio of $\frac{tau0}{\tau}$ does not exceed 6.4 and 6.7, respectively, while the theoretical values are 93 and 278. Also the course of the values is very similar. A slightly stronger rise of the time constants towards higher resistance values can be observed. However, even in the case of $\Delta T_c = 3\,\mathrm{mK}$ in the shaded area the rise is only 16 %, for $\Delta T_c = 1\,\mathrm{mK}$ it is only 7 %. This is significantly lower than the calculated values from the lumped model, which show an increase of 419 % and 380 %, respectively, in the same range.

In the uppermost part of the transition, the measured data show a stronger deviation from the simulated and calculated data, as well. This is mainly due to the deviation of the real transition curve from the simplified curves used in the models. However, as this range is not in a practically useable range because of its very low current response as discussed above, it is not in the main focus of optimizations. Thus, this mismatch was accepted in the optimization process.

The observed effects lead to the conclusion, that the time constants for this design are limited by effects caused by the extended geometric structure and can not be correctly predicted by the lumped model. Therefore, a supplementary FEM model was used to analyze the effect of the absorbers more closely. By fixing the temperature of the thermistor to $T_{th} = T_c$ and thereby making it independent of its surrounding, a situation was created in which the thermistor acts as a second thermal bath. This assures that the time dependent temperature response of the absorbers was not influenced by the response of the thermistor and can be analyzed separately. Thus, for a given set of material parameters, it did only depend on the interaction of the absorbers among themselves and their location with respect to the two thermal baths. All other parameters were chosen to be identical to the settings in the time constant analysis of the thermistor described above.

The results of a simulation in this configuration are shown in figure 5.14: For each pair of dipole absorbers, the temperature response to the step in radiation power was determined. As the figure shows, significant differences in the amplitudes can be observed. According to equation 2.5, for each absorber j the equilibrium level of the response

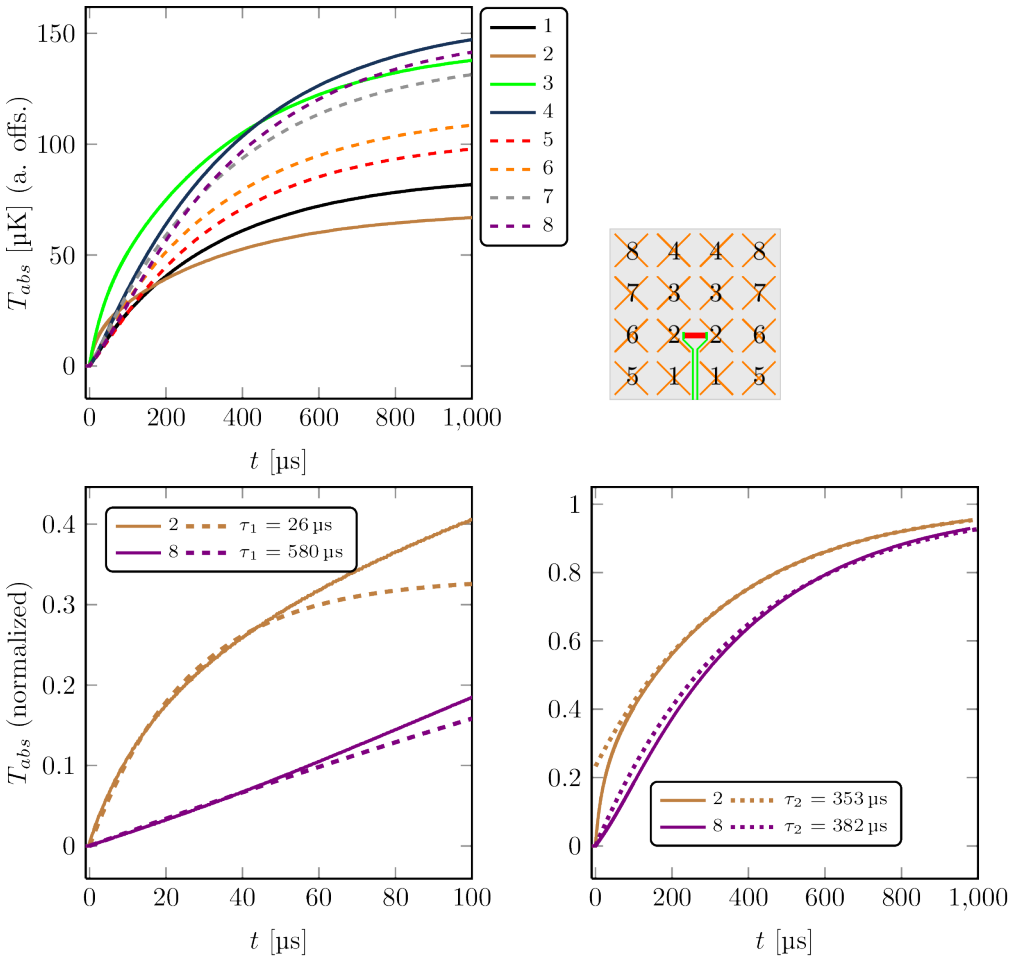

Figure 5.14: Time dependent temperature response T_{abs} at the absorbers to a signal step in the applied radiation power (upper left). For this simulation, a modified model with fixed T_{th} was used to separate the interaction of the absorbers with each other from effects of the ETF at the thermistor. The absorbers are numbered as shown in the upper right sketch. T_{abs} can not be approximated by a simple exponential function. Least square fit results of the initial range up to 50 µs (denoted as τ_1, lower left) deviate significantly from the results for the upper range starting from 400 µs (τ_2, lower right).

amplitude depends on the thermal conductance in between it and the heat sinks and sources in the system, which in this case are the fixed thermal bath, the thermistor and the other absorbers i. As the signals are small enough to comply with

$$\delta T \ll T \tag{5.36}$$

constant average thermal conductances $\overline{G^j_{th}}$ to the thermistor, $\overline{G^j_{bath}}$ to the bath and $\overline{G^j_{abs,i}}$ to the other absorbers can be assumed for an approximation with

$$P^j_{toth} \approx \overline{G^j_{th}} \cdot \left(T^j_{abs} - T_{th}\right) \tag{5.37}$$

$$P^j_{tobath} \approx \overline{G^j_{bath}} \cdot \left(T^j_{abs} - T_{bath}\right) \tag{5.38}$$

$$P^j_{toabs,i} \approx \overline{G^j_{abs,i}} \cdot \left(T^j_{abs} - T^i_{abs}\right), \qquad i \neq j \tag{5.39}$$

where P^j_{toth}, P^j_{tobath} and P^j_{toabs} are the effective energy flows per time unit from the absorber to the thermistor, to the bath, and to the absorber i, respectively. Due to the conservation of energy, the difference between received radiation power P^j_{rad} and the transferred powers has to be equal to the change in thermal energy $U^j_{th} = C^j_{abs} \cdot T^j_{abs}$:

$$\frac{d}{dt}(C^j_{abs} \cdot T^j_{abs}) = P^j_{rad} - P^j_{toth} - P^j_{tobath} - \sum_{i \neq j} P^j_{toabs,i} \tag{5.40}$$

In the equilibrium state, T^j_{abs} is constant. Thus, in this case the term on the left hand side becomes zero and equation 5.40 can be written as

$$\begin{aligned} P^j_{rad} \approx & T^j_{abs} \cdot \left(\overline{G^j_{th}} + \overline{G^j_{bath}} + \sum_{i \neq j} \overline{G^j_{abs,i}}\right) - T_{th} \cdot \overline{G^j_{th}} - T_{bath} \cdot \overline{G^j_{bath}} \\ & - \sum_{i \neq j} \overline{G^j_{abs,i}} \cdot T^i_{abs} \end{aligned} \tag{5.41}$$

The resulting equation for T^j_{abs}

$$T^j_{abs} \approx \frac{P^j_{rad} + T_{th} \cdot \overline{G^j_{th}} + T_{bath} \cdot \overline{G^j_{bath}} + \sum_{i \neq j} \overline{G}^j_{abs,i} \cdot T^i_{abs}}{\overline{G^j_{th}} + \overline{G^j_{bath}} + \sum_{i \neq j} \overline{G^j_{abs,i}}} \tag{5.42}$$

Table 5.2: Time constants of the different absorbers in the 16A FEM model. The assignment of the absorber numbers is visualized in figure 5.14, as well as the definition of τ_1 and τ_2. τ_{eff} corresponds to the effective time constant determined as the 1/e drop of the response.

absorber no.	τ_1	τ_2	τ_{eff}
1	330µs	351µs	323µs
2	26µs	353µs	263µs
3	53µs	356µs	302µs
4	574µs	376µs	375µs
5	416µs	351µs	358µs
6	570µs	354µs	345µs
7	421µs	363µs	365µs
8	580µs	382µs	395µs

leads to the equilibrium small signal step response of

$$\delta T^j_{abs} \approx \frac{\delta P^j_{rad} + \sum_{i \neq j} \overline{G}^j_{abs,i} \cdot \delta T^i_{abs}}{\overline{G^j_{th}} + \overline{G^j_{bath}} + \sum_{i \neq j} \overline{G^j_{abs,i}}} \tag{5.43}$$

According to equation 5.43, a higher thermal coupling of the absorber j to the bath leads to a lower equilibrium step response of this absorber. In addition, the temperature responses of the other absorbers δT^i_{abs} increase the temperature response, scaled by their individual thermal coupling to j relative to the total thermal coupling of the latter to its surrounding. Thus, the influence of two absorbers on each other will decrease with increasing distance between them.

The absorbers marked as number "2" in figure 5.14 are considerably closer to the thermistor than the other absorbers, leading to a relatively large value of $\overline{G^j_{th}}$. Even though the power signal received by this absorber is 4.5 times as high as the power signal on the outer absorbers (numbers 1 and 4 to 8) due to the radiation distribution, the effect is overcompensated by the large $\overline{G^j_{th}}$. The resulting δT^j_{abs} for these absorbers is the smallest of all, as can be seen in the graph. In general, the variation of the thermal response levels by more than a factor of two stresses the individual influence of each absorber on the behavior of the TES as a whole.

As an effect of the different temperature levels in the initial and the final equilibrium state, respectively, the thermal energy U^j_{th} changes in the transition between these states. The resulting non-zero differential term in equation 5.40 causes the temperature change not to happen immediately but to need a certain time. In the most simple case, it will follow an exponential function with a fixed time constant τ as described in section 2.2. In general, as the effect of one absorber on another scales with δT^i_{abs}, it is increasing with time after the step until all absorbers have reached the new equilibrium state.

Thus, the non-equilibrium results show a strong interaction in between the absorbers: The step response can not be approximated by a single exponential function as it would be the case for a single element with only one source of heat as described in equation 2.24, but shows a changing time constant throughout the course of the step response. By approximating the ranges from $t = 0\,\mu s$ to $50\,\mu s$ and from $t = 400\,\mu s$ to the equilibrium state with exponential functions as least square fits, significantly different time constants were determined, as shown in figure 5.14. They are denoted as τ_1 and τ_2 for these ranges, respectively. In addition, the effective time τ_{eff} constant was determined as the time needed for the level difference to drop to $1/e$ as described above. The results are listed in table 5.2. The absorber number "2" which is located closely at the thermistor, shows the strongest change in time constant throughout the response curve, as illustrated in the lower part of the figure: In the beginning of the course the reaction is fast, τ_1 is $26\,\mu s$. Closer to the equilibrium state, the response slows down. τ_2 is $353\,\mu s$, which is an increase of the time constant by a factor of approx. 14. In contrast, absorber number "8", which has the farthest location with respect to the thermistor, even shows a reduction from $\tau_1 = 580\,\mu s$ to $\tau_2 = 382\,\mu s$ by 34 %. This is caused by the interaction of the absorbers: While the initial effect of the other absorbers is small and thus can be neglected, with increasing amplitude the interaction is intensified. Absorber "2" initially is dominated by its high thermal conductance to the thermistor and a sharp rise in amplitude can be observed while the other absorbers still show a lower amplitude. However, once δT^i_{abs} rise in amplitude its step response is slowed down. Hence, τ_2 of absorber "2" has a similar value as for the other absorbers. Similarly, absorber "8" starts with a slow rise, but later adapts to the other absorbers, once the coupling gets stronger. In summary, the time constants in the working range are strongly influenced by geometrical effects and limited by the coupling of the absorbers to the thermistor. Hence, to improve the design, these interactions have to be taken into account.

6 Time constant reduction

6.1 Motivation

As discussed above, one of the main demands of a video rate THz camera is a fast TES, as the number of sensors is limited by the acceptable complexity and production cost of the system. The FEM simulations in chapter 5 proved to be able to model the time domain behavior of the 16A TES appropriately, which could not be achieved with the lumped model in section 2.3. Hence, the FEM model was used as a basis for further improvements. The findings based on the model presented above suggest the possibility to reduce the TES time constant by adjusting the geometrical design. Hence, the TES geometry was revised with respect to sensitivity and speed using adapted models. Again, also the coupling components were included into the modeling, to take into account the electro-magnetic interaction between TES, feedhorn antenna and resonator. The predictions of these models for the redesign were compared to the results of the 16A TES. Additionally, the model was compared to the predictions of the lumped model. Finally, a direct comparison to measured data from the new TES design was performed to verify the models results.

For a TES following the lumped model, according to equation 2.83 the time constant is given as

$$\tau = \frac{\tau_0}{L \cdot \xi \cdot \eta + 1} \tag{6.1}$$

$$\tau_0 = \frac{C}{G} \tag{6.2}$$

which can be rewritten using equation 4.51 as

$$\frac{\tau_0}{\tau} = 1 + \frac{\alpha \cdot \xi \cdot \eta}{n+1} \cdot \left(1 - \left(\frac{T_{bath}}{T}\right)^{n+1}\right) \cdot \frac{P_{el}}{P_{rad} + P_{el}} \tag{6.3}$$

However, the previous findings showed that the extended geometry of the thermal platform limits the minimum time constants that can be achieved. Hence, predictions should not simply base on the lumped model but need the affirmation of FEM simulations. In particular, an increase of α does not necessarily reduce the time constant. According to the FEM simulations, the time constant is still proportional to the thermal time constant

τ_0, and the latter is proportional to the total heat capacity of the TES, in agreement with the lumped model. However, the proportionality factor depends on the structural details. Thus, for a given set of working parameters, optimizations have to focus on the reduction of the heat capacity as well as on the reduction of the structural complexity. While an increased thermal conductance would also reduce the time constants, this has several disadvantageous side effects: Thermal fluctuation noise power is proportional to the square root of G (cf. equation 4.56) and the current response is reduced by increased thermal conductance (cf. equation 2.60). A local increase of the thermal conductance on the thermal platform would increase the coupling between absorbers and the thermistor and thus result in a properties more close to the lumped model. This again would be possible in different ways: Either by a local increase of the cross section area of the platform, which is hard to realize, or by adding conductive material to the platform. However, both methods increase the heat capacity, which is counterproductive as the thermal time constant will be increased by this method. Hence, a third way is to be preferred: The reduction of the lateral distances on the platform, which combines a reduction of heat capacity with a local increase of the thermal conductance.

As a consequence of these considerations, a simplified TES design with reduced heat capacitance and a smaller thermal platform was developed. Periodic absorber structures with finite extensions deviate in efficiency from the ideal infinite structure, and this deviation usually increases with decreasing number of periods. However, [64] showed that an appropriate adjustment of the setup geometry based on simulations can considerably improve the absorptance. Hence, the electro-magnetic coupling and the resulting efficiency were estimated by FIT simulations which will be presented in section 6.2. FEM simulations were used to analyze the temperature distribution, the intrinsic efficiency and the time constants. The results and a comparison to the lumped model are given in section 6.3. To verify the simulations, this design was used to fabricate TES. The corresponding measurements are discussed and compared to the simulation results in section 6.4. Finally, demonstrator of a terahertz video camera was set up equipped with these TES. This system and the achieved results are described in section 6.5.

6.2 Radiation coupling

Based on the aforementioned criteria, a design with a reduced platform size was created. As the size of the absorbers depends on the optical wavelength, it was not changed. This results in a reduced number of absorbers. Thus, to preserve the general structure while reducing distances and the heat capacity, the number of the absorbers was reduced by a factor of four, removing the farthest located absorbers with reference to the thermistor. The platform was scaled appropriately.

The resulting structure equals an extract of the platform of the 16A design in its center with one quarter of its total size. This is illustrated on the left side of figure 6.1. The initial structure is given for comparison. Referring to the number of absorbers, the new

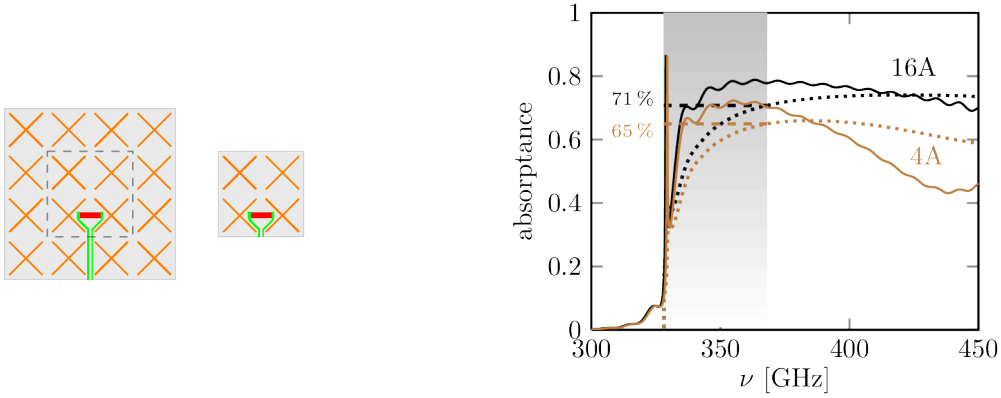

Figure 6.1: Left: absorber structure on the thermal platform for the 16A model (leftmost sketch) and the 4A model with a reduced platform size, which can be interpreted as an extract of the 16A platform within the dashed square. Right: Absorptances $A(\nu)$ (solid lines) and averages $\bar{A}(328\,\mathrm{GHz}, \nu)$ (dotted lines) resulting from simulations for the 16A and 4A design both using the original parameters of 16A as given in table 5.1. In particular, $d_{out} = 1000\,\mu\mathrm{m}$ and $l_{f-m} = 200\,\mu\mathrm{m}$.

design will be called '4A' in the following. As the effective reduction of the absorbing area is expected to considerably influence the coupling of the TES to the feedhorn antenna, a three-dimensional electromagnetic field simulation with this geometry was performed to analyze the coupling behavior. This model was set up with a simplified structure as described in section 5.2.1, to be directly comparable to the results found for the 16A design.

The graph in figure 6.1 shows a direct comparison of the results of this simulation for the 4A design with the original 16A design results. In both simulations, the same feedhorn and resonator geometry as listed in table 5.1 was used. As can be seen from the figure, the absorptance of the 4A design is reduced compared to the 16A design throughout the whole analyzed frequency range. Within the window from 328 GHz to 368 GHz, the average absorptance exhibits a reduction by approx. 8 % from 71 % to 65 %. Thus, the absorbed power is significantly higher than the power absorber in the inner 4 absorber pairs of the 16A model, which would equal a reduction by 40 % (see section 5.2.2). This discrepancy can be attributed to the fact that the absorbing structures themselves influence the field pattern within the resonator. However, significant differences can be observed between the compared designs: The maximum absorptance of 72 % at 355 GHz is lowered and shifted to lower frequencies compared to the 16A design, where it was located at 364 GHz, amounting to 80 %. For higher frequencies, the absorptance of the 4A design drops significantly faster than in the 16A design, reaching approx. 44 % at 440 GHz, while the 16A design is still at 71 % at the same frequency. This reduces the

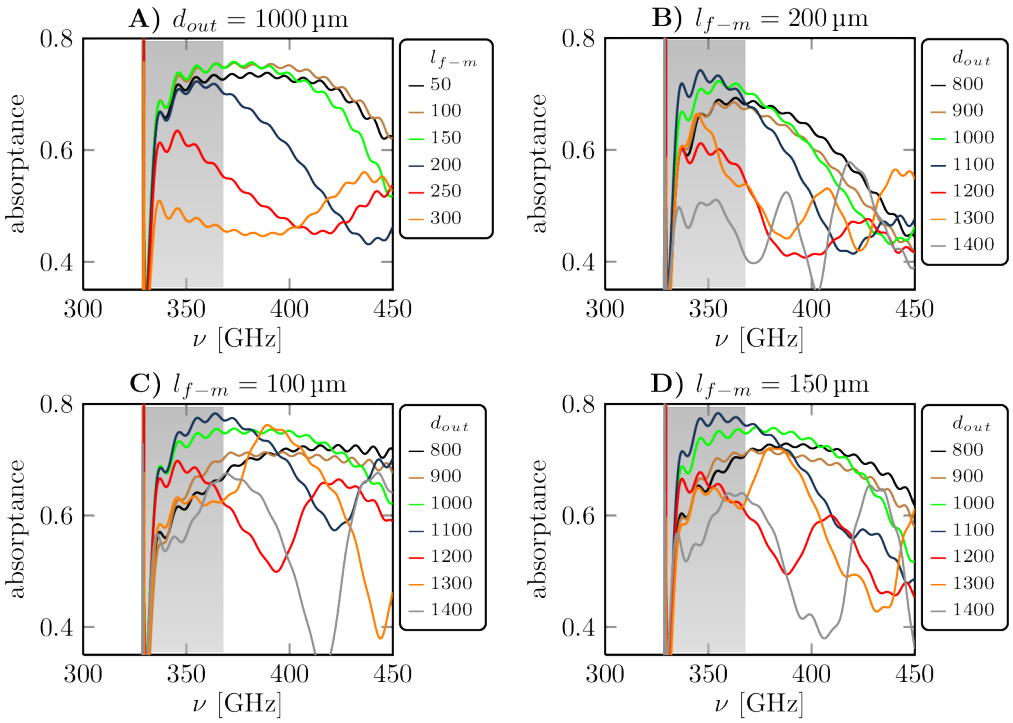

Figure 6.2: Absorptance vs. frequency resulting from electro-magnetic simulations of the 4A model. The distance between opening of the feedhorn and the averted Si_3N_4 membrane surface, l_{f-m} and the diameter d_{out} of the output cone of the feedhorn antenna are varied (see figure 5.1). All values of l_{f-m} and d_{out} are given in micrometers. A) d_{out} is fixed at 1000 µm, l_{f-m} is varied. B) l_{f-m} is fixed at 200 µm, d_{out} is varied. C) l_{f-m} is fixed at 100 µm, d_{out} is varied. D) l_{f-m} is fixed at 150 µm, d_{out} is varied.

usability for wider bandwidths, as the average absorptance has its maximum already at 385 GHz at 66 %, while for the 16A design it it at 419 GHz with 74 %.

As discussed in [64], for absorber structures of finite extents, the optimal geometrical parameter sets of the resonator differ from those for infinite absorber structures. Hence, when changing the extents of the absorber, changes in these parameters have to be expected. Therefore, a parameter variation was performed to find settings with higher absorption results. As variation parameters, the distance between output cone opening and the averted Si_3N_4 membrane surface, l_{f-m} as well as the output diameter of the output cone of the feedhorn d_{out} were chosen, as these parameters strongly influence the field pattern in the plane of the absorbers.

A chosen set of results is presented in figure 6.2. Sub-figure A contains a variation of

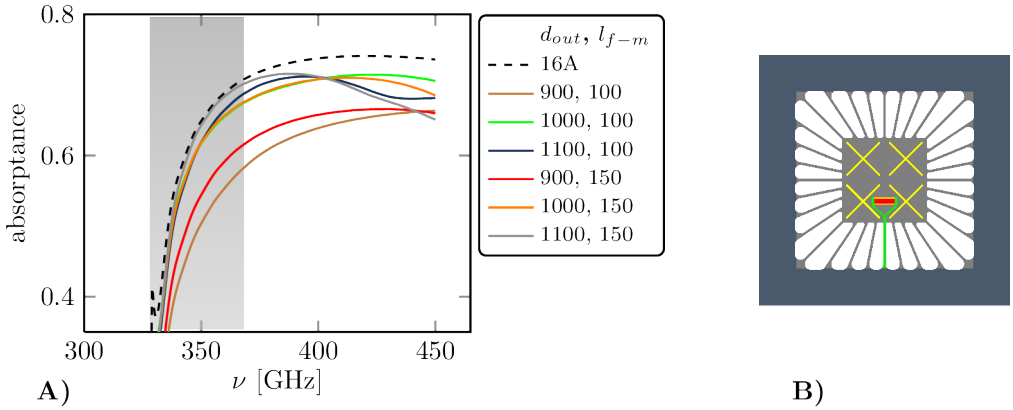

Figure 6.3: A) Electro-magnetic simulation of the 4A-model. The average absorptance $\bar{A}(328\,\mathrm{GHz}, \nu)$ is plotted versus ν. Selected values with high absorptances are selected for the diameter of the output cone of the feedhorn d_{out} and l_{f-m} in µm (see figure 5.1). B) Top view of the 4A design: Four absorber pairs (yellow) and the thermistor (red) with SP (yellow) are placed on top of the silicon nitride membrane (gray), that spans the opening of the silicon substrate (blue). The thermistor is electrically connected to superconducting niobium wires (green).

l_{f-m}, while d_{out} is kept constant at 1000 µm. Compared to the initially used $l_{f-m} = 200$ µm, the absorptance can be significantly improved by reducing l_{f-m}. Especially, a nearly constant absorptance can be achieved for a significantly larger bandwidth. The maximum absorptance is increased to 76 % for $l_{f-m} = 100$ µm and $l_{f-m} = 150$ µm compared to 72 % for $l_{f-m} = 200$ µm. Additionally, it is shifted from 355 GHz to 373 GHz for both distances. Values of l_{f-m} larger than 200 µm cause a strong reduction within the marked frequency range and a fast drop down to approx. 45 % in a local minimum which is shifted to lower frequencies for higher distances. Towards still higher frequencies, a slight increase of the absorptance within the analyzed range up to 55 % can be observed. A variation of d_{out} as presented in sub-figure B with fixed l_{f-m} showed only a small potential for improvements. Increasing d_{out} by 10 % to 1100 µm results in a slight rise of the absorptance within the atmospheric window from 328 GHz to 368 GHz. However, for higher frequencies, it drops significantly faster than the absorptance for 1000 µm. Still larger as well as smaller values of d_{out} resulted in worse results compared to 1000 µm.

Hence, d_{out} was varied again for lower values of l_{f-m}. The best results were achieved for 100 µm and 150 µm, which are presented in sub-figures C and D, respectively. They both show the same tendencies and similar results: The highest absorptance within the atmospheric window is achieved at $d_{out} = 1100$ µm, with a maximum of 78 % for both distances. Towards higher frequencies, the absorptance drops faster than for $d_{out} = 1000$, which gives the second best results within the atmospheric window.

To evaluate the effective absorptance for a given bandwidth, the average values of

Table 6.1: Geometry parameters of the 4A design with SP.

component	number	height [m]	length [m]	width [m]	total volume [m^3]
platform	1	$1{\cdot}10^{-6}$	$8{\cdot}10^{-4}$	$8{\cdot}10^{-4}$	$6.4{\cdot}10^{-13}$
thermistor	1	$1.08{\cdot}10^{-7}$	$2.2{\cdot}10^{-4}$	$5.8{\cdot}10^{-5}$	$1.38{\cdot}10^{-15}$
dipole	8	$2.1{\cdot}10^{-8}$	$4.3{\cdot}10^{-4}$	$1{\cdot}10^{-5}$	$7.22{\cdot}10^{-16}$
wiring	2	$1.5{\cdot}10^{-7}$	$4.41{\cdot}10^{-4}$	$6{\cdot}10^{-6}$	$7.94{\cdot}10^{-16}$
SP	2	$1{\cdot}10^{-7}$	$2.28{\cdot}10^{-4}$	$8{\cdot}10^{-6}$	$3.65{\cdot}10^{-16}$

the range from 328 GHz to ν was calculated for each value of ν for direct comparison. The results are shown in figure 6.3 A) for the parameter sets with the best results. As can be seen from the figure, within the atmospheric window, nearly the same average absorptance can be achieved as for the 16A design. For $l_{f-m} = 150\,\mu m$ and $d_{out} = 1100\,\mu m$, the difference is below 1 %. With a reduced l_{f-m} of 100 µm, the difference rises to approx. 3 %. With $d_{out} = 1000\,\mu m$, it amounts 5 %. The results for $d_{out} = 1000\,\mu m$ have their maximum shifted to higher frequencies. Above 403 GHz, the corresponding average value for $l_{f-m} = 100\,\mu m$ outnumbers the other configurations and reaches a value of 71 %. Accordingly, a smaller value of l_{f-m} compared to the 16A setup leads to improved absorptances. Depending on the bandwidth, the best results are achieved for values from 100 µm to 150 µm. For d_{out}, the corresponding values are 1000 µm and 1100 µm. Within the atmospheric window, a coupling efficiency of

$$\eta_{EM}^{4A} \approx 70\,\% \tag{6.4}$$

can be achieved, which is less than 1 % below the corresponding value for the 16A design, as given in equation 5.6.

Also the maximum value of

$$\eta_{EM}^{4A,max} \approx 72\,\% \tag{6.5}$$

is only slightly below the result of the 16A design of 74 % (see equation 5.7), and throughout the analyzed frequency range up to 450 GHz, the difference between the 16A results and the results of the 4A design with the best parameter set in each case is at most 3 %.

6.3 Electro-thermal simulations

The considerations above showed that a TES with a platform in the 4A design can achieve good electro-magnetic coupling. A constraint resulting from the discussion above was to keep the total thermal conductance at the same level as in the 16A design to avoid

Table 6.2: Heat capacities of the 4A design with SP at 0.56 K based on the values given in table 4.1 and the geometry shown in table 6.1. The electron contribution of Mo is multiplied by 2.43 to reflect the effect of the superconducting transition. For better comparability to the tables 4.2 and 4.3, unscaled values are listed (assuming $K_C^{FEM} = 1$).

component	C_{AuPd} $[\mathrm{J\,K^{-1}}]$	C_{Mo} $[\mathrm{J\,K^{-1}}]$	$C_{\mathrm{Si_3N_4}}$ $[\mathrm{J\,K^{-1}}]$	C_{Nb} $[\mathrm{J\,K^{-1}}]$	C_{total} $[\mathrm{J\,K^{-1}}]$
platform	0	0	$6.52 \cdot 10^{-14}$	0	$6.52 \cdot 10^{-14}$
thermistor	$2.97 \cdot 10^{-14}$	$3.91 \cdot 10^{-13}$	0	0	$4.21 \cdot 10^{-13}$
dipole	$2 \cdot 10^{-13}$	$2.2 \cdot 10^{-14}$	0	0	$2.22 \cdot 10^{-13}$
wiring	0	0	0	$1.17 \cdot 10^{-15}$	$1.17 \cdot 10^{-15}$
SP	$1.12 \cdot 10^{-13}$	0	0	0	$1.12 \cdot 10^{-13}$
sum	$3.42 \cdot 10^{-13}$	$4.13 \cdot 10^{-13}$	$6.52 \cdot 10^{-14}$	$1.17 \cdot 10^{-15}$	$8.21 \cdot 10^{-13}$

negative effects on noise and sensitivity. Hence, the spider leg structure of the membrane was defined by downscaling the original structure shown in figure 3.2 appropriately. The resulting TES design is presented in figure 6.3 B). It was equipped with SP to reduce the risk of degradation and provide long term stability, as suggested by the results of section 3.3). The used geometry parameters are listed in table 6.1. Based on these, the heat capacities of the different components of the design were calculated using the literature values given in table 4.1. Parameters as base temperature, critical temperature and transition width were assumed to be identical to ensure a maximum of comparability and to isolate effects of the geometrical differences of the models. Though the measurements presented in section 4.3 and the simulations in section 5.2.6 revealed significant deviations from the predicted time constants based on these values and suggested a general scaling factor of $K_C^{FEM} = 6$ (cf. equation 5.33), a relative comparison based on these values is still possible to estimate the significance of each value. Furthermore, the general scaling does not affect these considerations and allows for a prediction of the relative thermal time constant scaling referred to the 16A design. Hence, the resulting values for $K_C^{FEM} = 1$ are listed in table 6.2.

The total heat capacity predicted by these calculations for the 4A design can be used to estimate the thermal time constant. A simulated *I-I* curve without background load was used to determine the Joule heating power. By combining equations 4.12, 4.38 and 4.39 to

$$G = G_0 \cdot T^n = \frac{n+1}{T} \cdot \frac{P_{el}}{1 - \left(\frac{T_{bath}}{T}\right)^{n+1}} \tag{6.6}$$

$$T = T_c + \Delta T_c \tag{6.7}$$

the thermal conductance G was calculated, resulting in

$$G \approx 3.9 \times 10^{-9}\,\mathrm{W\,K^{-1}} \tag{6.8}$$

which is slightly higher compared to the 16A TES by 10 % due to the smaller platform dimensions. The resulting calculated thermal time constant is

$$\tau_0^{lumped} = 209\,\mu\mathrm{s} \tag{6.9}$$

which is approx. 48 % of the corresponding 16A value. If the scaling of the heat capacity is taken into account as $K_C^{FEM} = 6$, the thermal time constant increases to

$$\tau_0^{lumped,C\times 6} = 1.26\,\mathrm{ms} \tag{6.10}$$

However, the thermal time constant found from the FEM simulations τ_0^{FEM} for the 16A design presented in equation 5.31 amounted to only 63 % of the theoretical value. Due to this significant deviation caused by the geometrical extensiveness of the design, a different value of the thermal time constant of the 4A design can be predicted by scaling τ_0^{FEM} by the ratio of the total heat capacities of both designs. The total heat capacity given in table 6.2 is reduced by approx. 49 % referred to the 16A design, which should be reflected in the expected thermal time constant:

$$\tau_0^{S,4A} \approx 0.49 \cdot \tau_0^{FEM,16A} \approx 814\,\mu\mathrm{s} \tag{6.11}$$

Due to the diminution of the platform and the dipoles both by 75 %, the heat capacity of the thermistor becomes more dominant. Hence, the 4A design provides a reduced heat capacity scatter and therefore is closer to the lumped model, where the whole heat capacity is concentrated within a single point. As a consequence, a reduction of the time constants in the working range can be expected, that exceeds the reduction of the thermal time constant. However, as still about 50 % of the heat capacity are distributed over an area that is approx. 50 times as large as the thermistor, still considerable deviations from the lumped model have to be expected. Thus, for more precise predictions, the extended geometry again has to be taken into account. To further analyze the temperature distribution, the intrinsic efficiency and the time constants, a 4A comsol FEM model was created, following the design shown in figure 6.3 and considering the principles described in section 5.2.3.

As the contribution of the wiring to the total heat capacity of the thermal platform is only approximately 0.1 % (see table 6.2), it is ignored in the simulation. However, different to the 16A model, the SP are taken into account as they provide about 14 % of the total heat capacity. Again, a simplified electrical circuit containing all the relevant components was included directly on the membrane, as shown in figure 6.4. This circuit

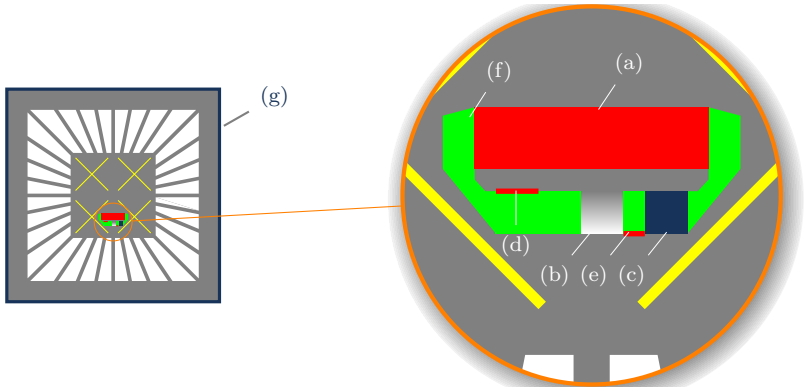

Figure 6.4: Geometry of the FEM model used to simulate the electro-thermal behavior of the 4A TES. The superconducting wiring is omitted as it does not significantly contribute to the total heat capacity (cf. table 6.2). The magnification on the right shows the electrical circuit that allows for a realistic modeling. It consists of the thermistor (a), that incorporates the parasitic resistance R_0 as well as the heat capacity of the SP. Further elements are the shunt resistor (b), R_L (c) and the current nodes (d), (e) on the wiring (f). The blue frame (g) at the outer edge of the TES marks the thermal bath which is kept at the fixed temperature T_{bath}.

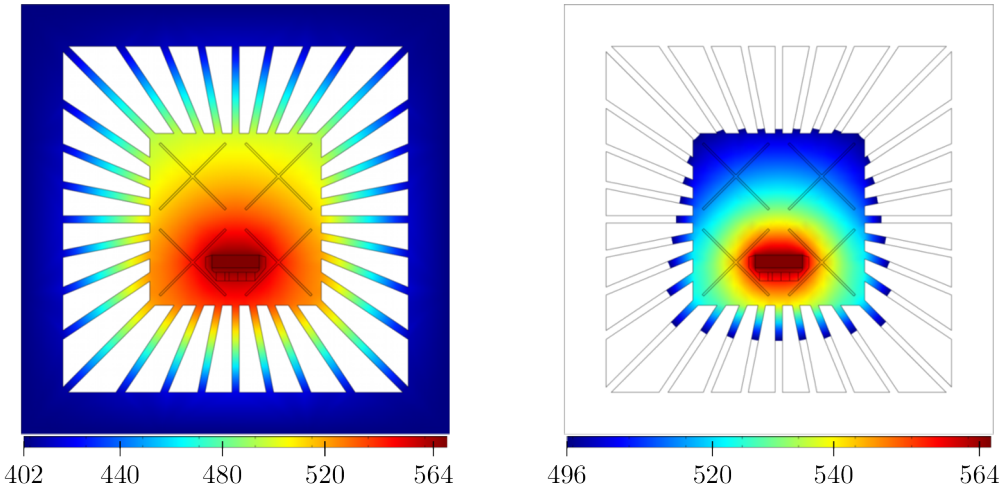

Figure 6.5: Left: Temperature distribution of the 4A comsol model in the transition range for $T_{bath} = 402\,\mathrm{mK}$ and $T_c = 564\,\mathrm{mK}$ without radiation load. The color scale marks the temperature levels in mK.
Right: The simulated total background radiation power was $P_{rad} \approx 46\,\mathrm{pW}$. A limited temperature range was used to visualize the gradient on the platform.

is identical to the one used for the 16A model to ensure the comparability and does not contribute to joule heating, heat capacity and thermal conductance except from the thermistor. The additional SP was included into the heat capacity of the thermistor without a geometric representation, as its close location to the thermistor and the small structures otherwise would increase the simulation computing time, while no difference in the resulting TES behavior could be expected.

6.3.1 Temperature distribution and efficiency

To acquire the temperature distribution on the platform, a simulation with the thermistor being biased to a working point in the transition range was performed. The resulting temperature distribution for $T_{bath} = 402\,\mathrm{mK}$ is presented on the left in figure 6.5. As for the 16A model, a significant temperature gradient across the platform can be observed. As the nitride membrane of 4A compared to the 16A membrane is scaled, but has the same shape, the distribution for both models is very similar. For simulations including background radiation, the radiation power was distributed equally over the four absorbers, as they are placed symmetrically around the optical axis of the incoming radiation. The Joule heating power difference ΔP_{el} between simulations with and without background radiation, respectively, was adjusted to match the same value as for the 16A model of $\Delta P_{el} = 3.2 \times 10^{-11}\,\mathrm{W}$, to use comparable conditions for both models. This was done by adjusting the total radiation power appropriately. This resulted in a value of

$$P_{rad}^{abs} \approx 4.6 \times 10^{-11}\,\mathrm{W} \tag{6.12}$$

corresponding to the intrinsic power efficiency of the 4A model of

$$\eta_{abs}^{4A} = \frac{\Delta P_{el}}{P_{rad}^{abs}} \approx 70\,\% \tag{6.13}$$

which is only slightly higher than the value for the 16A design of 67 %, in accordance with the similar temperature gradient.

By combining this efficiency with the coupling efficiency found in section 6.2, the bandwidth dependent overall efficiency of the 4A TES within the atmospheric window from 328 GHz to 368 GHz is

$$\eta_{TES}^{4A} = \eta_{EM}^{4A} \cdot \eta_{abs}^{4A} \approx 49\,\% \tag{6.14}$$

which is very close to the results of the 16A TES at 48 %. Hence, with the reduced number of absorbers in the 4A design the same efficiency can be achieved as for the 16A design.

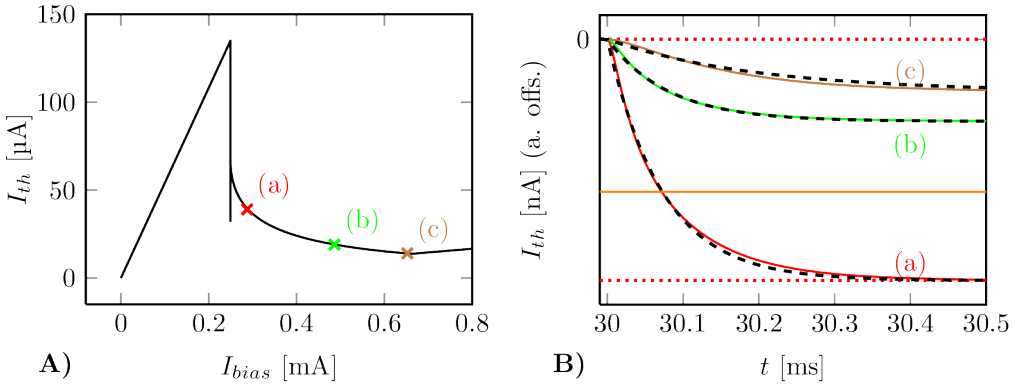

Figure 6.6: A) Simulated I-I curve with background load of 46 pW. For the marked working points (a), (b) and (c), the corresponding TES step responses are shown in B) (solid lines, shifted to a common upper level for comparison). They can not be fully matched by single exponential functions (dashed lines). Thus, τ was also determined as the time difference between the start of the step to the drop to $1/e$ (solid orange line for (a)) of the level differences (dotted lines). The differences for both methods were only a few percent of τ within the usable working range (e.g. for (a) and (b)). Due to the strong nonlinearity of the R-T curve close to R_n, in this range the deviations increase to above 10 % (e.g. 17 % for (c)).

6.3.2 Time constants

For the analysis of the time dependent behavior of the TES, the same simulation setup as described in section 5.2.6 was used. A rectangular signal was added to the background radiation power. To determine the amplitude, the same maximum signal difference at the thermistor as used for the 16A model, $(\Delta P_{sig})_{max} = 1.4 \times 10^{-12}$ W, was chosen to achieve comparable results. By applying the internal efficiency of the 4A TES given in equation 6.13, the resulting amplitude at the absorbers was

$$\delta P_{rad} = \frac{(\Delta P_{sig})_{max}}{\eta_{abs}^{4A}} \approx 2.0 \times 10^{-12}\,\mathrm{W} \tag{6.15}$$

For the exact location of the used working points with respect to the bias current, the I-I curve with background load was simulated. It is shown in the left graph of figure 6.6. A selection of working points is marked with crosses. For these working points, in the right graph the current response δI_{th} is shown together with exponential least square fits. Similar to the 16A model, the curves can not be fully matched by exponential functions, as predicted by the lumped TES model. However, the differences in the resulting time constants to those determined from the 1/e drop of the curves amount to a few percent only except from the range close to the normal resistive state, where deviations of more

Table 6.3: Amplitudes of the temperature response δT_{abs} of the absorbers for the 16A and the 4A model, denoted as in figure 6.7. The scaling factor s cancels the effect of the different radiation power levels per absorber.

absorber no.	$1/s$	$s \cdot \delta T_{abs}$	$s \cdot \delta T_{abs}/\delta T_{abs}^{N}$
N	1	66	1
F	1	156	2.4
2	0.6	117	1.8
3	0.6	242	3.7
1	0.13	648	9.8
4	0.13	1,180	18
5	0.13	779	12
6	0.13	864	13
7	0.13	1,050	16
8	0.13	1,140	17

than 10 % can be observed. This can be attributed to the strong non-linearity of the R-T characteristic and the weak feedback, resulting in a stronger thermal component of the signal.

The 16A model showed a strong variation of the different absorber time constants that result in the limitation of the TES time constant. Hence, the time constants of the absorbers were analyzed for the 4A model. To eliminate the influence of the ETF at the thermistor, its temperature was fixed to T_c as described in section 5.2.6, causing the thermistor to act as a second thermal bath. In this setup, the temperature responses of the thermistors were simulated. The results are shown in figure 6.7. For direct comparison, also the results of the equivalent simulation of the 16A model are included. Again, significant differences in the amplitude between the absorbers near to the thermistor of the 4A model, denoted as N, and the farther located ones, marked by an F, can be observed. The difference is comparable to the maximum level difference for the 16A absorbers, which can be attributed to the similar temperature gradients across the platforms. However, as the radiation power is evenly distributed in the 4A model while in the 16A model the inner absorbers receive a 4.5 times higher radiation power than the absorbers at the edge of the platform, the radiation power levels have to be taken into account to compare the total thermal conductance of the different absorbers, as equation 5.43 shows. Therefore, the amplitudes were scaled relative to the inverse of the input radiation power. The resulting curves are plotted in the upper right graph of figure 6.7. The scaled amplitudes for N and 2 are the lowest, stressing the strong influence of the thermistor on these absorbers compared to the thermal bath. The still by a factor of 1.8 lower scaled amplitude for N compared to 2 stresses the larger coupling to the bath of N due to their closer location to the edge of the platform.

Also the scaled equilibrium level for F is located between results of 2 and 3, meaning

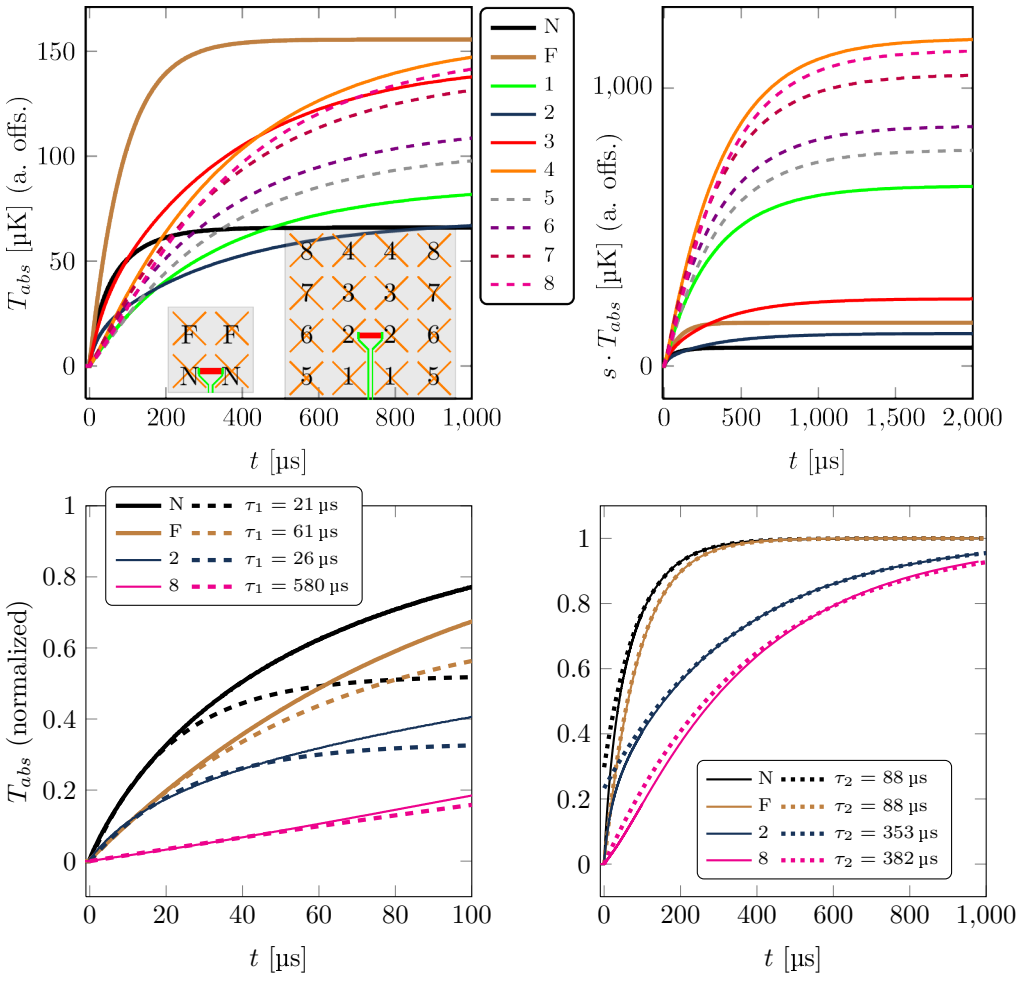

Figure 6.7: Upper left: Absorber Temperature response to a signal step in the radiation power with T_{th} fixed to T_c. The results for the 16A and the 4A model are shown for comparison. The denotation of the absorbers is marked in the inset sketches. Upper right: To characterize the total thermal conductance of the absorbers, the curves are scaled relative to the inverse of the radiation power. Lower left: Least square fit results of the initial range up to 20 µs and 50 µs for the 4A and the 16A model, respectively, denoted as τ_1. They deviate significantly from the results for the upper range (τ_2) starting from 150 µs and 400 µs (lower right).

Table 6.4: Time constants of the different absorbers in the 4A FEM model. For reference, results for the 16A model are included. The definition of τ_1 and τ_2 as well as the assignment of the absorber names is visualized in figure 6.7. τ_{eff} corresponds to the effective time constant determined as the 1/e drop of the response.

absorber name	τ_1	τ_2	τ_{eff}
N	21µs	88µs	61µs
F	61µs	88µs	90µs
2	26µs	353µs	263µs
3	53µs	356µs	302µs

a significantly higher thermal conductance for F than for the outer absorbers of the 16A model, as the listed equilibrium levels in table 6.3 show.

For both designs, the curves could not be matched by a single exponential function as it would be the case for a single heat capacity (see section 2.2). As the influence of the other absorbers on each absorber increases with the amplitude of their response signal, the initial range of the response curve is close to the unaffected case, while towards the new equilibrium state significant interaction takes place , as can be seen from equation 5.43. Hence, individual least squares fits with exponential functions to the first 20 µs were performed, resulting in the time constant τ_1. The same was done for the range starting from 150 µs, which lead to the second time constant τ_2. The results are shown in figure 6.7. For F as also for the absorbers 2 of the 16A design, the differences between τ_1 and τ_2 were the most pronounced, as these absorbers have a significantly smaller initial time constant than the others due to the close location to the thermistor. The dominating influence of the thermistor also causes very similar values for both models of τ_1 for these absorbers (cf. table 6.4). This is also the case for F and the absorber 3, while the other absorbers of the 16A model exhibit substantially higher values. Hence, the individual time constants of the 4A absorbers are very similar to the inner 4 absorber pairs of the 16A model which are marked in figure 6.1. Consequently, the lack of the slowest absorbers in the 4A model results in significantly lower values of τ_2, which are reduced by a factor of approximately 4 compared to absorbers 2 and 3. Therefore, also the corresponding values of τ_{eff}, the effective time constants determined from the 1/e drop of the thermal response, are reduced by a factor of at least 3. Accordingly, a reduction of the lower time constant limit of the 4A TES caused by the absorbers and therefore a decrease of the minimum time constants achieved with this design can be expected.

A series of simulations was used to determine the effective time constant of the 4A TES, without fixing the temperature as it was used to analyze the absorbers. The left graph of figure 6.8 shows the resulting time constants referred to the bias current, and the I-I curve as reference. While in general the current response δI_{th} was used to determine the time constants, for values of I_{bias} close to or in the normal conducting range, the

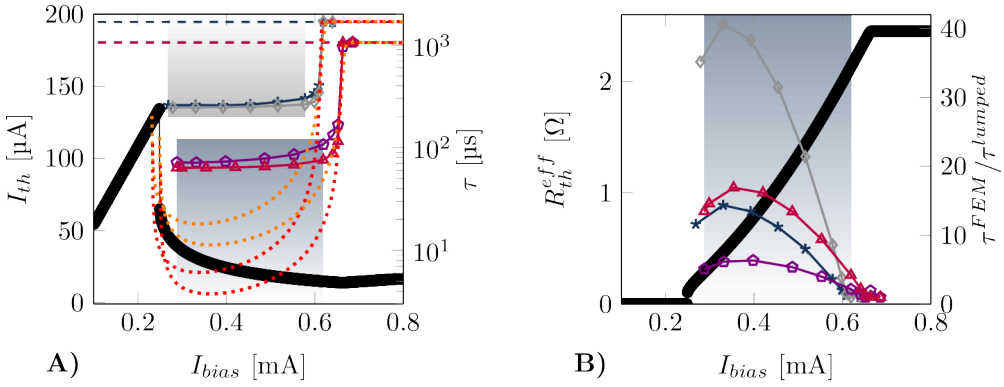

Figure 6.8: A) $\tau\,(I_{bias})$. The symbols mark the FEM results, pentagon ($\Delta T_c = 3\,\mathrm{mK}$) and triangle ($\Delta T_c = 1\,\mathrm{mK}$) for the 4A design, star and diamond shape for 16A. The τ_0 levels are marked by dashed horizontal lines. The dotted lines represent the lumped model predictions. The shaded blue and gray areas mark equal working ranges with respect to the *I-I* curve of 4A and 16A, respectively. For reference, the 4A *I-I* curve is plotted as a thick black line. B) The time constant ratio of the FEM results and the lumped model predictions is plotted versus the bias current. The assignment of the symbols and the shading is identical to A). For reference, the *R-I* curve is given as a thick black line.

temperature response δT_{th} was used to approximate the time constants instead, as δI_{th} becomes very small in this range and finally fully vanishes once the normal resistance is reached, as discussed in detail in section 5.2.6.

The found thermal time constant is marked in the figure by a dashed horizontal line. It amounts to

$$\tau_0^{FEM} = 1.06\,\mathrm{ms} \tag{6.16}$$

and thus is located nearly centrally in between the predicted value derived from the total heat capacity and the thermal conductance given in equation 6.10 as $\tau_0^{lumped,C\times 6}$ and the value resulting from scaling the result of the 16A model FEM simulations accordingly by the heat capacity change between both models, shown in equation 6.11 as $\tau_0^{S,4A}$. As the difference between the latter values results from the deviation of the model from the ideal lumped structure, the decreased difference of τ_0^{FEM} to $\tau_0^{lumped,C\times 6}$ confirms the improved compliance of 4A with the lumped model. This is also reflected by the corresponding value of η_{τ_0},

$$\eta_{\tau_0}^{4A} = \frac{\tau_0^{FEM}}{\tau_0^{lumped,C\times 6}} \approx 84\,\% \tag{6.17}$$

Table 6.5: Comparison of the time constant characteristic of the 4A and the 16A model based on simulations ("FEM") and lumped model calculations ("lumped"). The used symbols are defined in the text.

design	ΔT_c	τ_{min}^{FEM}	$\frac{\tau_0^{FEM}}{\tau_{min}^{FEM}}$	ϱ^{FEM}	τ_{min}^{lumped}	ϱ^{lumped}	$\frac{\varrho^{lumped}}{\varrho^{FEM}}$	$\frac{\tau_{min}^{FEM}}{\tau_{min}^{lumped}}$
4A	3 mK	71 µs	15	50 %	11 µs	340 %	6.8	6.3
4A	1 mK	64 µs	17	19 %	3.8 µs	380 %	20	17
16A	3 mK	259 µs	6.4	16 %	18 µs	420 %	26	14
16A	1 mK	246 µs	6.7	7.3 %	6.1 µs	380 %	52	41

compared to

$$\eta_{\tau_0}^{16A} \approx 63\,\% \tag{6.18}$$

Nevertheless, the fact that the deviation is reduced only by 55 % stresses that it is still not negligible and the design can not be described sufficiently with the lumped model.

Similar to the 16A design, within most of the transition range, the course of the simulated effective time constants of the TES shows significantly smaller variations than predicted by the lumped model. In the shaded area of figure 6.8, the simulated time constants vary from 71 µs to 107 µs for $\Delta T_c = 3\,\mathrm{mK}$, which corresponds to a rise by 50 % with respect to the minimum value. In the same range, the lumped model predicts a rise by 340 % from 11.3 µs to 50 µs. For $\Delta T_c = 1\,\mathrm{mK}$ the variation of the simulation results is still smaller: The values range from 64 µs to 76 µs, which corresponds to an increase by 19.3 % referred to the minimum value. The associated lumped model predicts a rise by 379 % from 3.8 µs to 18 µs. Obviously, there is a strong mismatch of the absolute values of the minima between lumped model and simulation (cf. table 6.5). Further, while the predicted minimum values differ by a factor of 3 for the used transition widths, the simulation results in a ratio of 1.1. Hence, a limitation of the lower limit of the time constants is obvious, which can not be explained by the lumped model. Instead, comparing these values to the effective time constants of the absorbers shows that they are of the same order of magnitude as the minimum TES time constants. Therefore, the dominant influence of the extended geometry as assumed in section 5.2.6 from the results of the 16A model is confirmed by these observations and still valid for the 4A design.

However, the above found approach by the 4A design to the ideal structure is also clearly visible: The ratio of the time constant values of the lumped model and the simulation, respectively, is visualized in the right graph of figure 6.8. For each transition width, the time constants of the 4A model are closer to the predictions of lumped model than the 16A values. Also the general course of the time constants affirms this improve-

ment: While the predicted relative rise of the time constants

$$\varrho^{lumped} = \frac{\tau_{max}^{lumped} - \tau_{min}^{lumped}}{\tau_{min}^{lumped}} \tag{6.19}$$

in the marked area results in similar values for both designs and both transition widths as can be seen from column ϱ^{lumped} in table 6.5, the corresponding rise in the simulated data, represented by

$$\varrho^{FEM} = \frac{\tau_{max}^{FEM} - \tau_{min}^{FEM}}{\tau_{min}^{FEM}} \tag{6.20}$$

shows a substantial variation, which is also reflected by the ratio of ϱ^{lumped} to ϱ^{FEM} (column $\frac{\varrho^{lumped}}{\varrho^{FEM}}$). In general, this ratio is significantly smaller for the 4A model, confirming the smaller deviation from the lumped model. In addition, the difference between $\Delta T_c = 3\,\mathrm{mK}$ and $\Delta T_c = 1\,\mathrm{mK}$ is larger for the 4A design. As the structural effects define a lower limit for the time constants, their influence increases with increasing feedback strength, if the theoretical time constants approach this limit. If the feedback, e.g. by larger transition widths, is weak enough, the TES will again behave in accordance with the lumped model. Accordingly, a higher sensitivity to feedback changes for a given feedback strength is a sign of reduced influence of the geometrical structure. Hence, the increased sensitivity of the time constants to the transition width change for the 4A design compared to the 16A design is another affirmation of the approach to the ideal behavior.

6.4 Measurements

To verify the simulations, 4A TES were fabricated as described in section 3.1.1. In the simulations discussed above, the same parameters were assumed as for the 16A design. Hence, for best comparability and to exclude effects resulting from different production conditions, the compared TES were fabricated on the same wafer. The corresponding measurements are discussed and compared to the simulation results in this section.

V-*T* measurements as described in section 4.3.2 were used to determine the *R*-*T* characteristic of the 4A TES. This resulted in $T_c = 565\,\mathrm{mK}$. With respect to the found reproducibility of approx. $\pm 1\,\mathrm{mK}$ within the same cool down cycle for each T_c value, this matches the result of the 16A TES. Similarly, the found transition width of $\Delta T_c = (2.5 \pm 1.0)\,\mathrm{mK}$ matches the value of $(2 \pm 1)\,\mathrm{mK}$. The found value for $R_n = (2.26 \pm 0.10)\,\Omega$ was verified by the more precise results of an *I*-*I* curve measurement as discussed in section 4.3.4 without background load. The least squares fits of Q_n and Q_s resulted in $R_n = (2.25 \pm 0.01)\,\Omega$ and $R_L = (0.048 \pm 0.001)\,\Omega$.

As already observed from the 16A TES, also the 4A TES *I*-*I* curves exhibit distorted

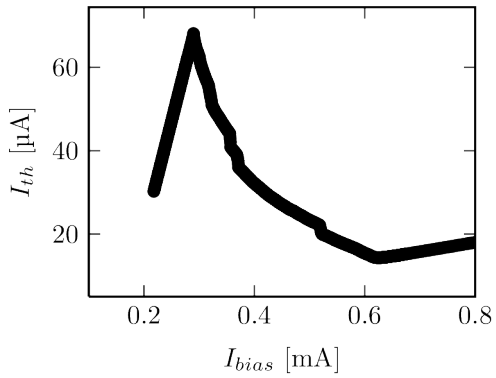

Figure 6.9: Measured *I-I* curve of the 4A design without background load. As for the 16A design, discontinuous regions can be observed (see text).

regions in the transition range, which can be seen in figure 6.9. As they result in arbitrary offset changes of the measured curve, the same method as described in section 4.3.4 is used to determine the Joule heating power

$$P_{el} = I_{th}^{min} \cdot \left(I_{bias}^{min} \cdot R_{sh} - I_{th}^{min} \cdot (R_{sh} + R_L) \right) \tag{6.21}$$

of the thermistor in the local minimum of the above mentioned *I-I* curve and a second measurement with room temperature radiation background load. I_{bias}^{min} marks the bias current in said minimum, and I_{th}^{min} the corresponding current through the thermistor. After equation 4.47, the difference between these values equals the effective background radiation load power at the thermistor

$$P_{rad} = \Delta P_{el} = (3.2 \pm 0.2) \times 10^{-11}\,\mathrm{W} \tag{6.22}$$

Hence, the measured overall efficiencies of 16A and 4A model are nearly the same, which is in good agreement with the predictions by the simulations in sections 5.2.5 and 6.3.1 and hence affirms that the 4A design can be used without a loss in signal efficiency.

Measurements with a rectangular radiation signal were performed to determine the step response of the TES. The same setup and evaluation method as described in section 4.3.5 was used to identify the time constants to ensure comparability of the results for the different designs. The results are presented in figure 6.10. The measured time constants affirm the findings of the simulation results above: Throughout most of the transition range, the time constants are nearly constant, hence following the same trend as the simulation. Also the absolute values are in good agreement with the simulation data, as can be seen from the right graph of figure 6.10. In the marked area of the graph, the

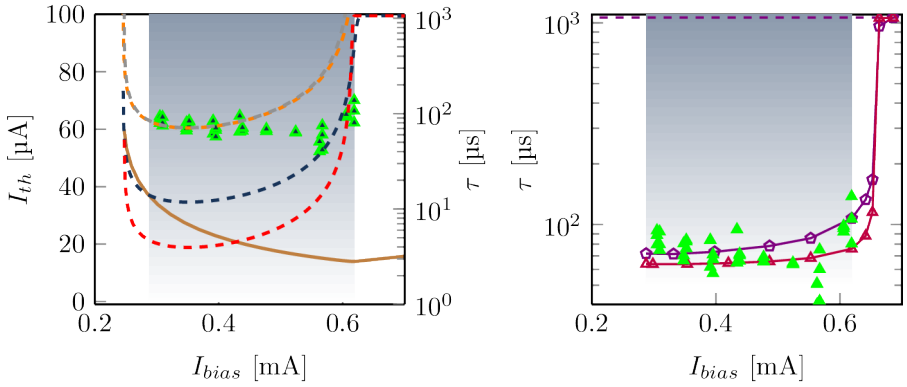

Figure 6.10: Time constants versus bias current. The shaded area marks the same region as in figure 6.8. Left: The symbols mark measured data, while the red ($\Delta T_c = 1\,\mathrm{mK}$) and blue ($\Delta T_c = 3\,\mathrm{mK}$) dashed lines represent the calculated time constant course based on the calculated I-I curve (straight brown line). By upscaling the heat capacity to a value where the calculated minimum time constants match the measured data, the general course mismatch can not be solved (gray and orange dashed lines). Right: The measured data (isolated symbols) is matched by the simulation results (connected symbols) for $\Delta T_c = 3\,\mathrm{mK}$ (violet) as well as for $\Delta T_c = 1\,\mathrm{mK}$ (purple).

measured time constants lie in the range of

$$\tau^{meas} = (70 \pm 20)\,\mu\mathrm{s} \tag{6.23}$$

which is close to the simulation results of $(70 \pm 6)\,\mu\mathrm{s}$ and $(89 \pm 19)\,\mu\mathrm{s}$ for $\Delta T_c = 1\,\mathrm{mK}$ and $\Delta T_c = 3\,\mathrm{mK}$, respectively. As the simulation model was only adjusted with respect to the geometry, but all used material parameters and the general setup was unchanged compared to the 16A model, this agreement certifies the predictive potential of the model. Hence, it should be possible to make qualitative predictions concerning new geometries, and even quantitative data can be gained. However, due to the strongly simplified physics no perfect matching can be expected.

The direct comparison of the time constants to the results for the 16A TES shown in equation 4.46 reveals a scaling factor of

$$\chi_{16A}^{4A} = \frac{\tau^{16A}}{\tau^{4A}} \approx 3.6 \tag{6.24}$$

Hence, the time constants could be improved significantly by the 4A design. For a comparison of the sensitivity, the found parameters presented above were used to model the expected noise using equation 4.61 and to compare it to measurements. As thermal time constant in the calculations, the value given in equation 6.16 was used. The results

are shown in figure 6.11. As can be seen, within the bandwidth

$$\Delta\nu_{el}^{4A} = \frac{1}{2\pi\tau} \approx 2270\,\mathrm{Hz} \tag{6.25}$$

of the TES, which is defined as in equation 4.63, the measured noise level is

$$NEP^{4A} = 4.5 \times 10^{-16}\,\mathrm{W\,Hz^{-1/2}} \tag{6.26}$$

which is approx. 30 % higher than the theoretically calculated value. It is also by 18 % larger than the 16A noise level. The increased noise level could be verified from the noise level without radiation background load, which is by approximately 60 % above the theoretical level, while the photon noise found from the noise levels with and without background radiation load is in accordance with the theoretical value. Above the bandwidth limit of the TES, an excess noise hump can be observed which is much more pronounced than for the 16A TES (see figure 4.13). In a model with additional heat capacities, increased in-band noise as well as a high frequency hump is predicted by [92] for the case of average coupling of these heat capacities to the TES. This effect gains significance with increasing feedback and has a maximum for medium coupling strength between TES and additional heat capacities. Therefore, a possible explanation of the higher noise in the 4A model compared to the 16A model is the improved coupling of the absorbers as a whole to the TES, while still maintaining a significant decoupling. However, also various types of excess noise could be observed in the vicinity of distorted working points, as shown in the right graph of figure 4.13. General noise level increase could be observed to different scales as well as rather localized peaks. In either case the usability of such working points was reduced due to the degraded SNR. Still, as the location of these distortions were well defined referring to the *I-I* curve for a given base temperature level, stable working points with low noise levels could be chosen.

Based on the noise level in these points, the effective maximum radiation power difference and the electrical bandwidth $\Delta\nu_{el}^{4A}$ the SNR could be calculated using equation 4.70 as

$$SNR^{4A} = \frac{(\Delta P_{sig})_{max}}{NEP^{4A} \cdot \sqrt{\Delta\nu_{el}^{4A}}} \tag{6.27}$$

resulting in

$$SNR^{4A} = \frac{1.4 \times 10^{-12}\,\mathrm{W}}{4.5 \times 10^{-16}\,\mathrm{W\,Hz^{-1/2}} \cdot \sqrt{2270\,\mathrm{Hz}}} \approx 65 \tag{6.28}$$

According to equation 1.30, this equals an achievable bit depth of ≈ 6 bit. Compared to the 16A TES, this is a reduction of the SNR by 50 % (see equation 4.71) which is mainly

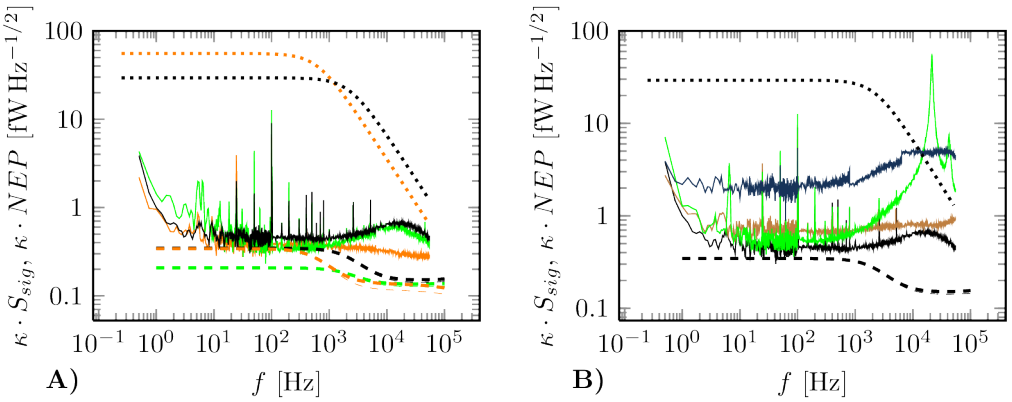

Figure 6.11: Measured NEP and S_{sig}^{max} (dotted lines) scaled by $\kappa(\omega_{el})$. A) NEP under room temperature background radiation of the 4A (black) and the 16A TES (orange) and with a background load from 0.4 K for 4A (green). τ_0^{FEM} was used to calculate NEP_{comb} (eqn. 4.61, dashed lines; thin dashed lines: strong feedback limit). B) Examples of distorted working points with different levels of excess noise. Both wide-band and strongly frequency dependent excess noise could be observed. Discontinuities in the blue curve are due to a strong dependency of the noise level on small temperature differences between consecutively measured frequency intervals.

due to the electrical bandwidth increase of

$$\frac{\Delta\nu_{el}^{4A}}{\Delta\nu_{el}^{16A}} = \sqrt{\chi_{16A}^{4A}} \approx 1.9 \tag{6.29}$$

However, the simulations in section 6.2 suggested an increase of the optical bandwidth for application distances with low atmospheric attenuation. Within the range of nearly constant efficiency, a scaling factor n of the bandwidth would roughly rise the signal by a factor of n. As the phonon noise scales with $\sqrt{n}$ while the other noise terms are not affected by the scaling, a minimum improvement of the SNR of $\sqrt{n}$ can be achieved.

6.5 Demonstrator for 10 frames per second

6.5.1 Requirements

A demonstrator of a THz camera that is capable of producing moving pictures in real time was planned as an improved successor of SCOTI (see section 3.1.1). To demonstrate an intermediate step from single frame images to 25 frames per second (fps) video with a full body length FOV, the defined general requirements for this new demonstrator were a larger field of view (FOV) with a diameter of 1 m and frame rates of up to 10 fps. Also

the object distance requirement was increased to the range from 7 m to 10 m. Even at a slightly reduced optical resolution compared to SCOTI of 2 cm, equaling 1 cm/line and sample, this FOV consists of a number of nearly 8000 pixels in a rectangular grid.

Hence, to fulfill these requirements with a full sensor array, several thousand sensors would be necessary, including the corresponding readout. This would lead to inacceptably high production and operation costs. Even for much slower readout requirements like in astronomical applications where price plays a minor role currently large arrays are limited to a few thousand sensor elements[40],[42],[104]. In addition, efficiently shielded sensors use feedhorn antennas as described in section 4.2. In this case, for all array geometries to fully sample a given FOV, scanning is unavoidable[105][106].

To prevent smearing effects e.g. caused by moving persons in the object plane, the integration time per frame t_{int} must be limited. The condition to keep the shift

$$d_{shift} = v_{person} \cdot t_{int} \tag{6.30}$$

of a person moving perpendicular to the optical axis significantly below the width of one pixel per frame, the maximum integration time within this frame is given by

$$t_{int} \ll \frac{r_{min}}{2} \cdot \frac{1}{v_{person}} \tag{6.31}$$

For a line width of $\frac{r_{min}}{2} = 1\,\text{cm}$ and a typical velocity of the person of $v_{person} = 1\,\text{m}\,\text{s}^{-1}$, a limitation to 10 % of the pixel width results in

$$t_{int} \leq 1\,\text{ms} \tag{6.32}$$

If the frame rate falls below $\frac{1}{t_{int}} = 1\,\text{kHz}$, dead times will occur. Alternatively, the sensors can be used more efficiently by scanning the FOV. This has to be taken into account for systems with high cost per sensor. While geometrical deformations in the resulting images can be caused by moving persons using this method, smearing effects are strongly limited while maintaining continuous signal integration at each sensor[107].

Therefore, for this system, an upper limit of 20 sensors was defined, with 20 parallel readout channels. To acquire the full FOV, it is scanned using an optical scanner. In the following the choice of the used scanning mechanism, the parameters of the scanner and the adaption of the sensor array geometry to it will be explained.

6.5.2 Scanning the field of view

In principle, several scanning methods can be used to sample a given field of view with a certain number of sensors. A small selection of such methods will be discussed in this section concerning their advantages and disadvantages with respect to the above-mentioned application.

The most simple way to acquire a rectangular image is to perform a line scan, with a

linear array of sensors being virtually moved along a line perpendicular to the orientation of the array. This allows for fast scanning as only one turning point of the scanning mechanism per frame is necessary, keeping the occurring mechanical forces on a low level. No redundancy will occur, as the scan traces of the single sensors will not overlap. This allows to take full advantage of all sampling points, which can be evenly distributed over the FOV. However, This method is limited in the lateral resolution achieved parallel to the line array. To resolve a given number of lines along this direction, an equaling number of sampling points is necessary. This number is directly defined by the number of used sensors in the array. To be able to separate for example two bright lines, at least one dark line is necessary in between. Hence, the resolution usually is defined in as a spatial frequency ν_{spat} in line pairs (e.g. one bright and one dark line) per distance, equaling the smallest period of the spatial grid that can be resolved[108]. It is limited to

$$\nu_{spat}^{line} = \frac{N_{sensors}}{2} \cdot \frac{1}{d_{FOV}} \tag{6.33}$$

which can be achieved for evenly distributed sensors along an array with the length d_{FOV}, where d_{FOV} represents the width of the targeted field of view in parallel to the linear sensor array and $N_{sensors}$ denotes the number of sensors. For $d_{FOV} = 1\,\mathrm{m}$ and $N_{sensors} = 20$ as defined above for this demonstrator system, this would lead to a minimum resolution of

$$r_{min}^{line} = \left(\nu_{spat}^{line}\right)^{-1} = 10\,\mathrm{cm} \tag{6.34}$$

which is unacceptably large for the aspired detection capabilities. A common alternative for scanning with single sensors or small arrays is to use a meander scanner with two orthogonal axes. Its advantage over the line scanner is the possibility to freely chose the sampling density in both directions, theoretically allowing for any chosen value. Hence, the achievable spatial resolution is not limited by the scanning. However, to scan a field of $N_c \times N_r$ samples consisting of N_c columns and N_r rows, a single sensor needs to be moved consecutively along the rows (or columns). Regarding the mechanical load, this results in the need for a large number N_{turn} of changes in direction of the deflection unit, where N_{turn} in the best case is chosen as the minimum of N_c and N_r. As the scanning is slowed down in the turning point and the time consumed for the turns has to be significantly lower than the scanning time per line, large forces on the deflection unit will occur. In most cases of scanning, a constant angular velocity ω is used along the scanned FOV, represented by the total scanning angle θ. In this case, the time used for changing the direction of the deflection unit has to be limited to a small fraction Υ of the total time per frame Δt_{frame}. The resulting time for a single turn t_{turn} is given by

$$\Delta t_{turn} = \frac{\Upsilon \cdot \Delta t_{frame}}{N_{turn}} \propto \frac{1}{N_{turn}} \tag{6.35}$$

and hence inversely proportional to the number of turns. Additionally, the angular velocity ω itself is proportional to N_{turn}, as it results directly from the time per frame:

$$\omega = \frac{\theta}{(1-\Upsilon)\cdot\frac{\Delta t_{frame}}{N_{turn}}} \tag{6.36}$$

and in the aspired case of $\Upsilon \ll 1$

$$\omega \approx \frac{\theta}{\Delta t_{frame}} \cdot N_{turn} \propto N_{turn} \tag{6.37}$$

Therefore, the minimum angular acceleration in each turning point is given by

$$\alpha = \frac{d\omega}{dt} \geq \frac{2\omega}{\Delta t_{turn}} \propto N_{turn}^2 \tag{6.38}$$

and therefore rises as the square of the number of turning points.

This is especially significant in the case of large apertures, as the moments of inertia increase with the lateral dimension of the aperture. For optical elements, a common case is a thin disc. for a given density ρ_m, its moment of inertia with respect to an axis through its diameter is proportional to the radius R to the power of four[109]:

$$I_{dia} = \frac{mR^2}{4} = \frac{\rho_m \cdot \pi \cdot d \cdot R^4}{4} \tag{6.39}$$

This strongly limits the achievable maximum frame rate of the scanning mechanism. The use of an array of several sensors for a meander scan does not reduce the forces if the possibility to freely chose the sampling density for both dimensions of the FOV is maintained. A compromise, as scanning with a short line of evenly distributed sensors along paths of a distance that is equal to the length of this line, would result in the need for at least

$$N_{turn} = \frac{N_c}{N_{sensors}} \tag{6.40}$$

turns, assuming without loss of generality that $N_c < N_r$. The achievable spatial resolution along this line array therefore is given by

$$r_{min}^{meander,line} = 2 \cdot \frac{d_{FOV}}{N_c} \tag{6.41}$$

and hence connected to the number of necessary turns per frame as

$$r_{min}^{meander,line} = 2 \cdot \frac{d_{FOV}}{N_{turn} \cdot N_{sensors}} \propto \frac{1}{N_{turn}} \tag{6.42}$$

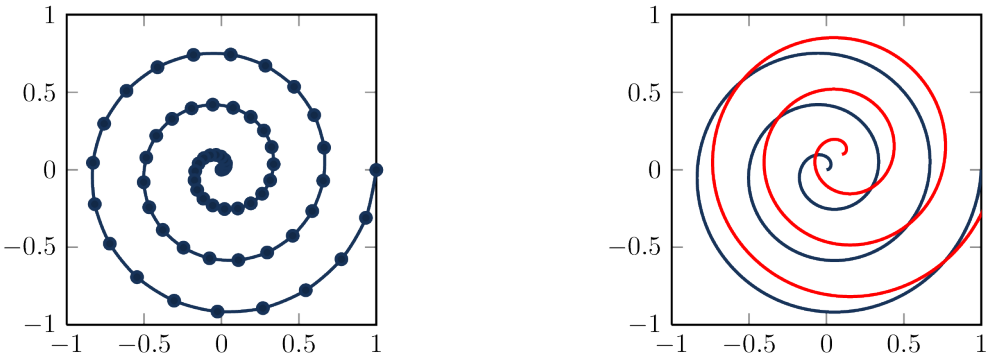

Figure 6.12: Left: Simulated trace of a sensor for spiral scanning with sampling points at equidistant time steps. Right: The traces of different sensors overlap at several positions in the image, hence allowing for direct calibration.

To achieve a resolution of $r_{min} = 2\,\text{cm}$ with $d_{FOV} = 1\,\text{m}$ with 20 sensors, still a minimum number of

$$N_{turn}^{meander,line} = 2 \cdot \frac{d_{FOV}}{N_{sensors} \cdot r_{min}} = 5 \tag{6.43}$$

would be necessary, which have to be accompanied by the same number of fast shifts of the scan path.

In contrast, a spiral scanner allows to reduce the number of turning points to as low as 0.5 per frame. In this case, a two-dimensional scanning is achieved by separating the polar coordinates ϕ and r. These coordinates define the FOV in the range of $\phi \in [0; 2\pi]$ and $r \in [0; r_{max}]$. While ϕ is being scanned by rotating a deflection mirror, r is varied by tilting this mirror in a range of $\pm\frac{\theta}{2}$. As a full tilt from $-\frac{\theta}{2}$ to $\frac{\theta}{2}$ requires only one turning point, but results in scanning twice the range from $r = 0$ to $r = r_{max}$ which corresponds to two full frames, only 0.5 turning points per frame are necessary. By this mechanism, the sensor array is virtually moved on spiral traces across the circular FOV. The number of traces N_{traces} is defined by the rotations per frame. Constant sampling and rotation frequencies lead to a decreasing sampling density along the ϕ direction (see figure 6.12) and hence a decreasing maximum recoverable spatial frequency ν_{spat}^{spiral} with increasing r, which for a given sampling frequency ν_{sample} is given by

$$\nu_{spat}^{spiral} = \frac{1}{2} \cdot \frac{\nu_{sample}}{\nu_{frame} \cdot N_{traces} \cdot 2 \cdot \pi \cdot r} \tag{6.44}$$

Hence, to achieve a certain lateral resolution at the outer edges of the FOV, sampling parameters have to be chosen that cause significant oversampling in the inner range of

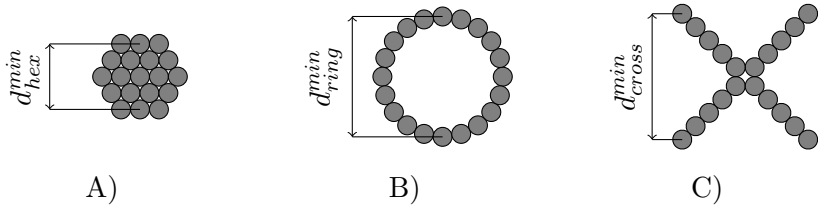

Figure 6.13: Different array configurations for an array limited to 20 pixels: A) Hexagonal structure (19 pixels), B) ring structure (20 pixels), C) cross geometry (20 pixels). The ratios of the minimum diameters are $d_{hex}^{min} \approx 0.54 \cdot d_{ring}^{min}$ and $d_{cross}^{min} \approx 1.05 \cdot d_{ring}^{min}$.

the FOV. This results in redundant sampling points which reduces the effective number of distinct samples. In addition, the scan traces overlap at different positions in the picture. This causes additional redundancy. However, this redundant information also results in a great advantage, as it allows for direct calibration of the different sensors in commonly sampled positions of the image, as illustrated in figure 6.12. By this, the separate sub-images from the single sensors can be smoothly matched into a combined image in real time. Another advantage of this scanning mechanism comes from the independent adjustability of the coordinate parameters r and ϕ. Similar to the freely sampled meander scan, the minimum resolution limit caused by the sampling density can be tuned by varying these parameters. This also allows for full image sampling with a decreased number of sensors at reduced sampling speed. Hence, sensor outages can be compensated for without having to accept unsampled regions. In addition, the possibility to independently tune frame rate and number of traces allows for different combinations of speed and resolution with varying numbers of activated sensors. Due to these advantages especially for a demonstrator with a small number of sensors as demanded in this case, spiral scanning was chosen to be the favorable technique for this system.

An on-axis telescope was used as the objective of the camera. It was designed as a Cassegrain reflector, consisting of a large concave primary mirror and a smaller convex secondary mirror. In this arrangement, the main mirror with a diameter of 0.5 m directs the received radiation on the secondary mirror, from where it is led towards the sensors. The secondary mirror was equipped with a tilting mechanism which again was mounted rotatable around the axis of symmetry of the telescope. This setup allows for spiral scanning with frame rates up to 10 Hz. The secondary mirror mount allows for varying the distance of the mirrors, and hence for adjusting the focal distance of the system in the range from 7 m to 10 m. According to equation 1.1, this results in a diffraction limited resolution of 1.5 cm to 2.1 cm depending on the chosen distance.

6.5.3 Sensor array and system integration

To fit the special demands of the spiral scanner, the 20 TES were arranged in an array that allows for small numbers of scan traces N_{traces}, because N_{traces} defines the forces that act on the scanner for a given frame rate. As the scan traces at least have to have a width w_{trace} equal to their radial distance to avoid unsampled regions in the image, the width of the array should be as large as possible. Due to the rotation symmetry of the scanning movement, the minimum width d^{min} of the array is deciding when watched from different directions, which is equal to the minimum linear projection of the array. At the same time, the sensors have to be placed as close as possible to avoid sampling gaps. The maximum density in case of the used TES is defined by the feedhorn antennas, as their input cone is larger than the extents of the TES itself. As discussed in [110], power-efficient feedhorns need to be scanned for full sampling independent of the arrangement, even in a close-packed configuration. Because of the small diameter of a densely packed hexagonal array as shown in figure 6.13 A), it increases the number of necessary scanning traces. Hence, a good compromise was to use a ring structure, formed by circularly arranged sensors with densely packed feedhorns. This geometry exhibits a large diameter independent on the lateral angle of view, which can be seen in figure 6.13 B). It is given by

$$d_{ring}^{min} = 2 \cdot r_{horn} \cdot \frac{20}{\pi} \tag{6.45}$$

with r_{horn} being the diameter of the feedhorn opening. Compared to the corresponding minimum diameter of the hexagonal arrangement,

$$d_{hex}^{min} = 4\sqrt{3} \cdot r_{horn} \tag{6.46}$$

the ring structure exhibits a considerably larger minimum diameter with a relative scaling factor of

$$\frac{d_{ring}^{min}}{d_{hex}^{min}} = \frac{10}{\sqrt{3}\pi} \approx 1.84 \tag{6.47}$$

The continuous radial shift while scanning combined with the non-equal spacing of the sensors projected on the diameter of the array leads to a superior homogeneity of the sampling pattern compared to a cross-type arrangement, which also exhibits a large minimum diameter (figure 6.13 C)). The latter is given by

$$d_{cross}^{min} = 2r_{horn} \cdot \left(1 + \frac{8}{\sqrt{2}}\right) \tag{6.48}$$

and thus nearly identical to the diameter of the ring arrangement:

$$\frac{d_{cross}^{min}}{d_{ring}^{min}} = \frac{\pi \cdot \left(1 + \frac{8}{\sqrt{2}}\right)}{20} \approx 1.05 \tag{6.49}$$

A direct comparison of the sampling patterns of the ring and the cross array geometry is shown in figure 6.14. They are calculated for the same parameters for direct comparability. The frame rate was chosen as $\nu_{frame} = 10\,\text{fps}$, as this was the maximum aspired frame rate for this demonstrator and hence the most demanding case of operation. The sampling rate of 4.5 kHz corresponds to twice the electrical bandwidth of the TES as given in equation 6.25 due to the sampling theorem.

While an optical system that maps the airy disc to the feedhorn diameter avoids losses in radiation power, it requires at least 16 sampling steps per feedhorn for full sampling in the case of densely packed feedhorns, independent of the array geometry[110]. For close packed feedhorns along certain direction, this equals three additional sampling steps in between two feedhorns for each lateral dimension of the sampled FOV.

These additional steps can be avoided by mapping a quarter of the airy disc diameter to the feedhorn diameter and the use of close packed feedhorns. However, less than 24 % of the signal are received from the watched airy disc in this case. Hence, more than 75 % of the signal result from locations outside of this ary disc, leading to a significantly degraded SNR. As a compromise, for this demonstrator a mapping of half of the airy disc diameter to the feed horn diameter was chosen. This limits the necessary samples in between two feedhorns to one. The received power from the airy disc is still approx. 70 %, which limits the SNR reduction to a moderate level. In this case, already 3 traces result in a good sampling of the FOV. This is shown in the figure for a FOV of 1 m diameter recorded from a distance of 8.5 m which corresponds to a diffraction limited resolution of approx. 2.1 cm. The black spots in the figure have a diameter equal to the projection of the feedhorn entry. Hence, they mark the area of the FOV that is sampled. The brown spots have a diameter of half the airy disc radius and hence represent the area that is sampled at full resolution. Hence, Gaps in between these spots represent regions of reduced resolution.

As can be seen from the figure, both array types result in gapless sampling throughout most of the FOV. For single frames as shown in sub-figures A and B, a larger contiguous unsampled area can be observed. As they are sampled in the next frame which can be seen in sub-figures A and B, these regions are not affected by a reduced resolution but exhibit a reduced effective frame rate. Both array types also show smaller regions in the FOV with reduced sampling depth within a single frame. This can not be fully avoided for still efficient scanning parameters. However, its effect is strongly mitigated by the fact that these gaps are shifted for successive frames. Sub-figures C and D show the results for two consecutive frames. These show a strong reduction of the sampling gaps compared to the single frame results. Hence, these gaps are not permanent in the

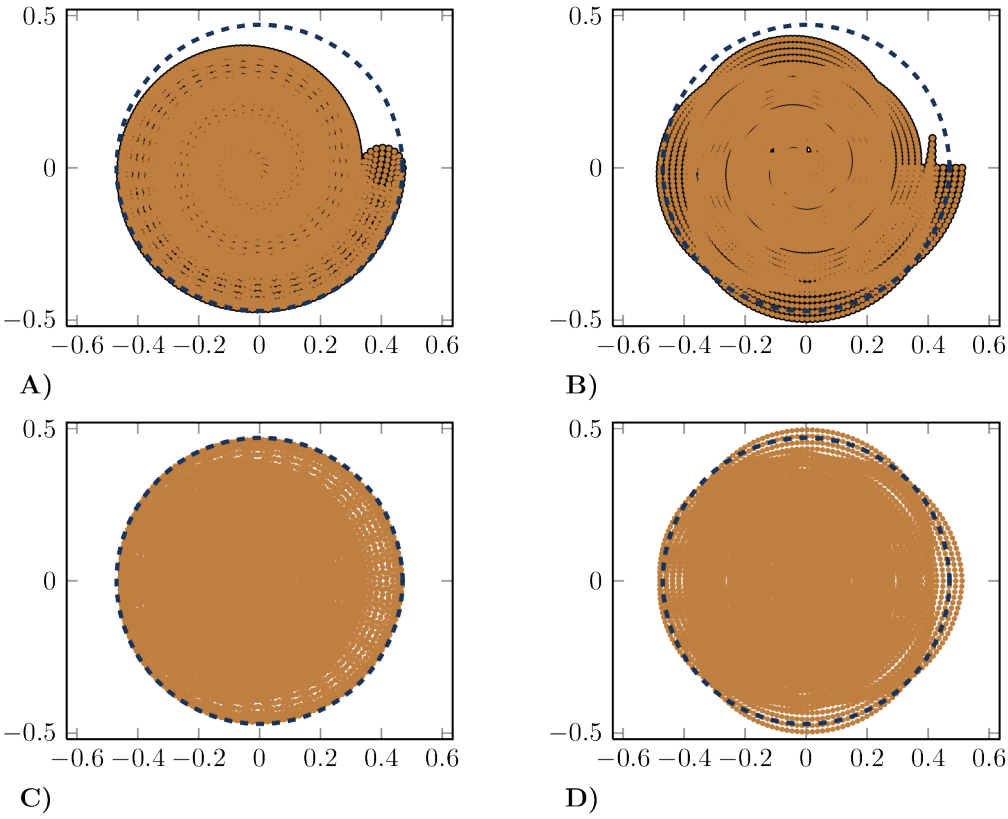

Figure 6.14: Sampling pattern for the ring structure (A, C) and the cross geometry (B, D) for 3 scan traces sampled at 4.5 kHz and for 10 fps. The diameter of the black spots in A and B equals the projected feedhorn entry diameter, while the brown spots have half of this diameter. A) and B) show the results for a single frame, C) and D) for two consecutive frames. The dashed line marks a FOV of 1 m diameter.

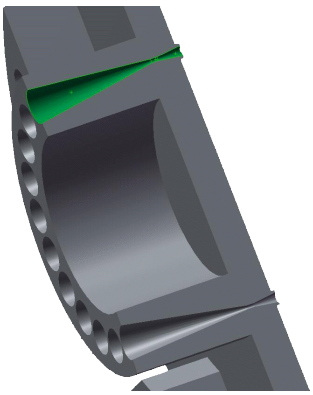

Figure 6.15: Left: Sectional view of the circular feedhorn arrangement. The openings of the large cones are located on the surface of a sphere centered on the middle of the secondary mirror to optimize its necessary size and to simplify the optical design constraints. Right: Aluminum casing used as thermal, magnetic and electro-magnetic shielding.

video stream, but rather lead to flickering effects, which can be minimized by adequately choosing the number of traces for a given frame rate. For the ring arrangement, the sampling gaps are smaller and distributed in a more homogeneous way compared to the cross geometry, which improves the stability of the image stream.

Another advantage of the ring geometry results from practical reasons: To reduce the demands on the optical components, the input openings of the feedhorn antennas were arranged on a spherical shell. This allows their optical axes to intersect in the center of the scanning mirror, resulting in a completely rotation-symmetric arrangement. Hence, all feedhorns receive radiation from a centered area of this mirror, which allows this mirror to be much smaller compared to the case of parallel optical axes. This leads to a significant reduction of the moments of inertia and therefore allows for faster scanning (see section 6.5.2). In case of the ring arrangement, the constant angle of the feedhorns referred to the axis of symmetry of the array simplifies the production process and thus enhances the precision, which leads to reduced production costs while increasing the reproducibility. The circular arrangement of tilted feedhorns is shown in figure 6.15.

Therefore, the 20 TES were arranged as a ring on a chip consisting of twenty sensors as shown in figure 6.16. These are connected using superconducting thin film Nb wiring to avoid parasitic electrical resistances on the chip. The inner area of the chip was kept clear for a clamping mechanism fixing the chip location with a beryllium copper spring. This ensures the exact chip distance to the feedhorns and avoids sensitivity due to vibrational effects.

The wiring leads to bond pads aligned along two opposed edges of the chip to connect

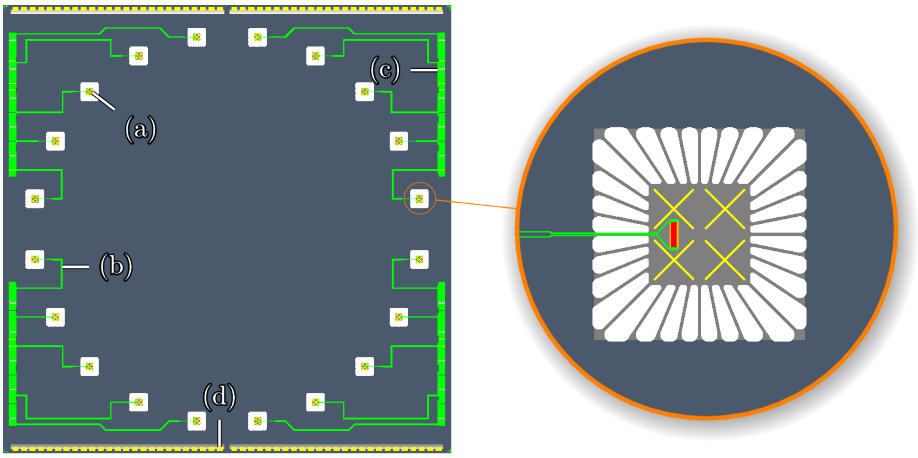

Figure 6.16: Top view on a sensor array consisting of 20 4A TES arranged equally spaced on a ring (a). They are connected using thin film Nb wiring (b), connected to gold plated bond pads (c) including the shunt resistance. For effective thermal coupling to the cooling stage, two edges are covered with a gold film that is thermally connected to the chip carrier using gold bonds (d).

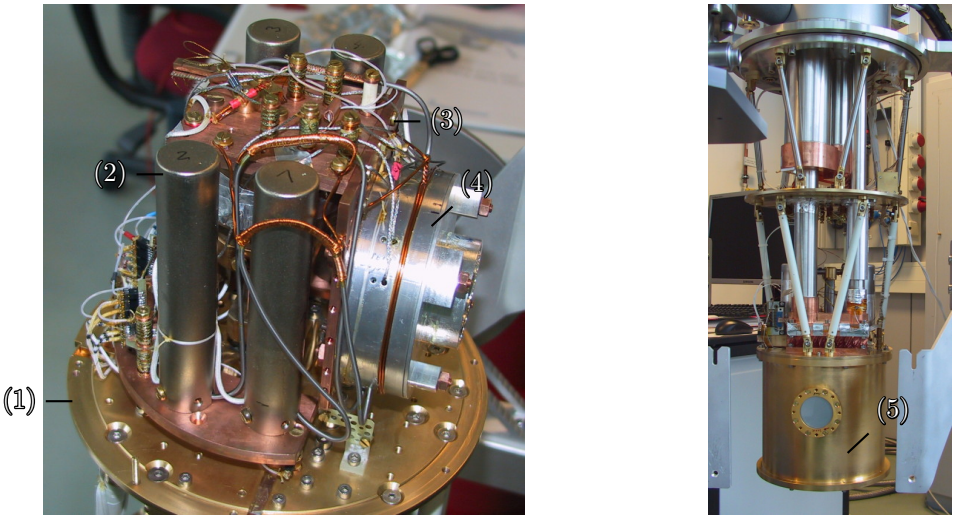

Figure 6.17: Left: 3 K cold stage (1) with SQUID readout amplifiers (2) and 350 mK stage (3) with sensor casing (4) attached. Right: Pulse tube cooler with thermal shield (5) mounted on the 3 K stage.

the TES electrically. These bond pads are arranged in 4 groups of 5 TES for symmetric connection. Accordingly, the electrical contacts of the chip are attached by superconducting aluminum bond wires to four PCBs with wide gold plated strip lines. The PCBs are are glued to the chip carrier. This connection is realized using a thin film of stycast epoxy, attaching the wired surface of the PCB to the carrier, which provides the thermalization of the wiring to avoid additional heat load on the chip. To also achieve a good thermal contact of the chip to the cooling stage, its remaining edges are plated with gold pads, which are connected to the chip carrier using gold bonds. The carrier itself consists of gold plated electrolytic copper and is directly connected to the cooling stage by copper bolts.

A superconducting aluminum casing containing the chip and the carrier serves as thermal, magnetic and electromagnetic shielding. It is shown in figure 6.15. The carrier is connected via low resistive multi-pin connectors on the four attached PCBs to PCBs fixed inside the casing. This allows for simple replacement of the loaded chip carrier. From inside the casing, superconducting wiring is fed through thin cylindric holes to maintain the shielding, and led to the SQUID readout amplifiers, as can be seen in figure 6.17. The THz radiation is coupled into the casing by the above-mentioned twenty feedhorn antennas which are integrated in the removable front cover.

In this demonstrator system, the sensor chamber was placed on a temperature controlled ^{3}He evaporation cooler with a minimum base temperature of 350 mK. This cold stage was precooled and thermally shielded by two temperature stages at approx. 3 K and 50 K, respectively. These stages are cooled by pulse tubes, which produce unavoidable microphonic effects. Hence, the thermal coupling between the temperature stages and the pulse tubes was established by flexible copper wire, which allows to achieve a good thermal conductance and a weak mechanical coupling at the same time. Figure 6.17 shows the inner cryostat setup.

For a maximum distance of 10 m, the atmospheric attenuation allows for an extension of the optical bandwidth, as can be seen from figure 6.18. Therefore, The demonstrator was equipped with optical filters with a bandpass from approx. 328 GHz to 408 GHz, which results in a slightly reduced average transmission of at least 94 % compared to the 328 GHz to 368 GHz window (98 %) for the aspired distance of up to 10 m. Due to the resulting higher radiation power, the signal is increased by a factor of 2. As the corresponding noise increase is below a factor of $\sqrt{2}$, This adjustment increases the maximum achievable SNR to

$$SNR^{4A}_{80\,\mathrm{GHz}} = 92 \tag{6.50}$$

which equals a bit depth of 6.5 bit.

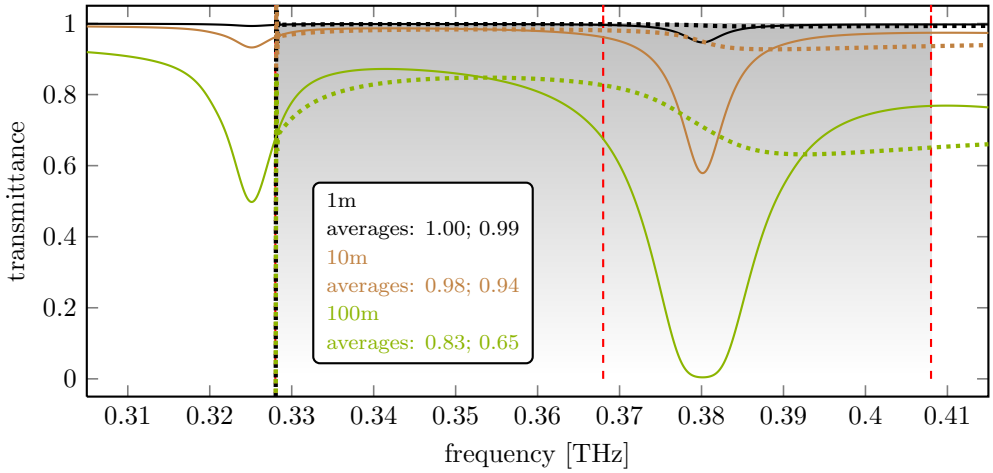

Figure 6.18: Transmittance of air at 295 K, 1013 mbar and 30 % relative humidity for different object distances. The shown data was calculated using [22]. The range from 328 GHz to 408 GHz is shaded. The dotted lines mark the average transmittance from 328 GHz to the current frequency. The average values for 368 GHz and 408 GHz are shown in the legend.

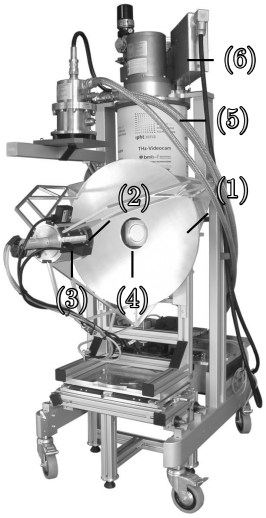

Figure 6.19: THz video camera demonstrator for 10 fps. Marked are the primary mirror (1), the secondary mirror including the scanning mechanism (2), the objective framework for adjusting the focal length (3), the radiation entrance window (4) to the cryostat containing the sensors (5), and the readout electronics (6).

6.5.4 Results and discussion

The demonstrator is shown in figure 6.19. Initially, it was equipped with 16A TES, for direct comparison of the system performance to the SCOTI system. The results are discussed in[111]. It could be shown that the system is able to achieve real time imaging at 10 fps. However, above 3 fps, the spatial resolution was visibly degraded due to the large time constants of the 16A TES. Hence, the later setup with 4A TES resulted in significant improvements, as predicted by the previous sections. Figure 6.20 shows single frames of a video taken at 10 fps from 8.5 m distance using the 4A detectors. It shows the front and rear view of a person wearing a T-shirt and a jacket. The body becomes apparent as a white silhouette without revealing intimate anatomic details. This is an inherent advantage of the passive detection, which occurs in optical frequency ranges with low reflectivity of the skin (see section 1.2). With increasing optical wavelength and hence increasing reflectivity[16][20] the formation of shades by reflected radiation gains weight. This again causes the impression of nudity in the resulting images, which can not be observed in the presented images in figure 6.20. Different hidden objects can be seen, represented by dark shades in front of the body. As a demonstration of the versatile detection capabilities of the camera, a dummy handgun made of aluminum, a cell phone and a plastic tube filled with screws to simulate a pipe bomb are were hidden and can be clearly located. To demonstrate the capability to detect non-metallic objects, also a gel pack and a plastic tube filled with sugar were used, as equivalents of explosives in liquid and solid powder form, which both could also be detected. While the diffraction limited resolution of 2.1 cm at this distance could not fully be achieved at the maximum frame rate, the images show a sufficient detection capability even of small objects. As the figure shows, even the zipper of the jacket with a width of less than 1 cm can be clearly seen. At a frame rate of 10 Hz also the advantage of a video could be observed compared to the slower frame rates, as it was possible to watch a moving person. This improves the possibility to detect objects that are temporarily hidden e.g. by the hands of the screened person.

This also stressed the focus of the next development steps, as moderate movements could be imaged properly, but faster motion still caused significant blurring. Hence, a further improvement of the time constants of the TES accompanied by a higher frame rate would improve the performance. In continuous measurements, temperature fluctuations lead to shifts of the working points. This could lead to a temporary shift of the TES into a working point with significant distortions as discussed above, causing the sensor channel to become unstable. While this could be compensated for by dynamic adjustment of the working point or deactivation of the channel, this effect in general causes unpredictable distortions of the images. Therefore, the reduction of these distortions will be addressed in the following.

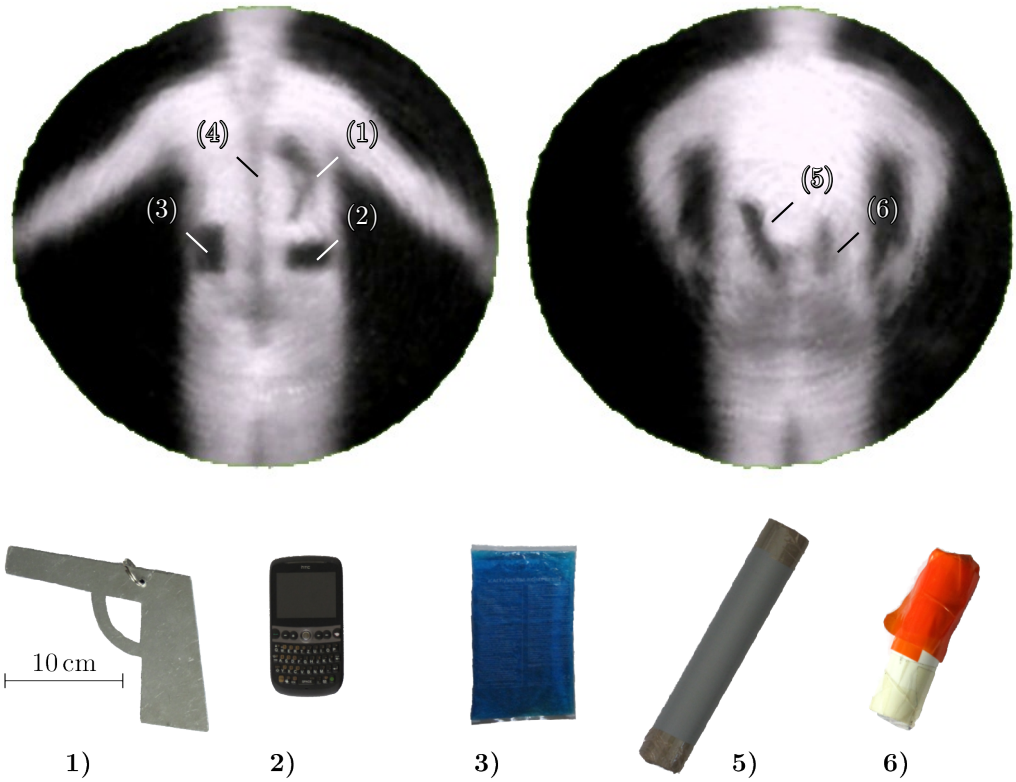

Figure 6.20: Above: THz images taken from 8.5 m distance, taken at 10 fps. A dummy handgun (aluminum) (1), a cell phone (2) and a gel pack (3) hidden under the jacket as well as the zipper (4) show up as dark silhouettes in the front view (left). In the rear view, two plastic tubes can be detected, the larger filled with sugar (5) and the smaller filled with screws (6). Below: dummy handgun (aluminum), plastic tube filled with screws to imitate a pipe bomb.

7 Distorted operating ranges

7.1 Motivation

The different TES analyzed in the previous chapters all show distortions in the I-I curves. These correspond to working point intervals in the superconducting transition that show excess noise and, depending on the strength of the effect, also affect the modulation amplitude of the current sensor SQUID. The modulation amplitude is reduced, which decreases the dynamic range of the FLL. This again leads to a larger number of jumps in the output voltage, causing discontinuities in the I-I-curves as described above. In addition, the instability of such working points makes them inappropriate for the camera operation.

The strength of this effect varies from slight modulation reduction to total loss of visible modulation. In the latter case the readout does not work at all. These distorted operating ranges (DORs) in general are distributed over the whole range of the superconducting transition, and no simple pattern to predict them can be observed. However, the probability of such DORs increases with a decreasing working point resistance as well as with an increasing temperature gradient $T_c - T_{bath}$.

While it is possible for all TES discussed in this thesis to chose working points which do not show such effects, several facts limit the applicability of TES with this property: The choice of a working point is limited to regions which are far enough away from DORs to avoid slight thermal drifts to shift the working point into a DOR. Especially for larger numbers of TES where groups with common bias are necessary, this can cause significant disadvantages up to the impossibility to activate all TES at the same time, which will result in failure of sensors in a camera system. While for a fixed bath temperature the location of the DORs for a certain TES does not vary, for different TES of the same type they are not identical. In combination with their unpredictability this significantly limits the range of common working points for lager numbers of pixels. Hence, In the worst case, individual pixels can not be used. For a camera system with high redundancy as described in section 6.5, this is an acceptable limitation as it only slightly affects the maximum frame rate or the lateral resolution of the achieved images, while no gaps in the image are caused. However, the spiral scanner used in the aforementioned system is not suitable for a larger angular field of view and frame rates above 10 Hz. Additionally, a larger number of TES is necessary. To limit the production cost and effort, a system design with low redundancy was favored. Hence, to achieve these goals, a line scanner was implemented. Of course, the total lack of redundancy in such a scanner drastically reduces the number of TES and readout channels; However, it also causes one of the

fundamental disadvantages of such a system. If any of the TES does not have a usable common working point with the other TES e.g. due to disadvantageous location of DORs, it has to be deactivated. This causes a gap to occur throughout the whole image of the width of one sampling pixel. This is usually filled by interpolating in between the neighboring pixels. Still, it causes a reduction by a factor of two of the local spatial resolution perpendicular to the path of this gap through the image. Therefore, the DORs were analyzed to find a way to eliminate or at least reduce them in number and strength.

7.2 Measurement method

To obtain a comparable measure of the DOR distribution and intensity, a systematic analysis of their occurrence depending on the bias current was performed. While excess noise was found to be the most sensitive indicator of a DOR, due to its diverse location in the frequency domain (see figure 6.11) and the time consuming measurement it was not feasible for a routine analysis method covering the whole transition range. All but very weak DORs did also affect the modulation depth ΔV_{mod} of the V-ϕ characteristic of the readout SQUID at least in their center region. [112] described a strong effect of radio frequency signals coupled into a SQUID on ΔV_{mod}. Also [113] demonstrated a correlation of wideband flux noise and reduced ΔV_{mod}. Hence, the observed effect in the DORs might be due to the high frequency component of the TES noise in the DORs observed in our samples (see above) and commonly found in different TES designs (see e.g. [92]).

The transfer function of the SQUID is given by [48]

$$V_{SQUID}(\phi) = \Delta V_{mod} \cdot sin\left(2\pi \cdot \frac{\phi}{\phi_0}\right) \tag{7.1}$$

as its voltage response V_{SQUID} to a magnetic flux ϕ with

$$\phi_0 = \frac{h}{2e} \approx 2.07 \times 10^{-15}\,\mathrm{Wb} \tag{7.2}$$

where h is Planck's constant and e the elementary electric charge.

The corresponding amplitude $\Delta V_{mod}\,(I_{bias})$ as a function of the TES bias current I_{bias} can be measured with the same setup as the I-I curves, which is described in section 2.4. Additionally, it can be determined significantly faster than the noise. Hence, its reduction was taken as an indicator of the occurrence and as a measure of the intensity of a DOR. To measure the actual SQUID modulation amplitude, the FLL, the linearizing feedback loop of the SQUID (see section 2.4) was deactivated. By feeding a sinusoidal signal at 15 Hz to a superconducting coil attached to the SQUID, a modulated flux was applied to the SQUID. As the TES was still connected to the SQUID to observe the DORs, the total flux through the SQUID was also affected by current through the thermistor, causing a

phase shift of the modulation. However, as the amplitude of the modulation flux was chosen to be larger than ϕ_0, this did not affect the measured modulation amplitude. The TES bias current was swept from the normal conducting range of the thermistor down to zero, while the response to several modulation periods was acquired, as shown in figure 7.1 A). This resulted in the V_{SQUID}-I characteristic of this TES (sub-figure B). By determining the peak-peak amplitude ΔV_{mod} of these samples and plotting it versus the bias current, the modulation-current characteristic (M-I curve) could be determined.

7.3 Distribution of DORs

An example measurement for the 4A design is presented together with the corresponding I-I curve in figure 7.1 C). A reduction of the M-I level corresponds to a DOR. If V_{mod} reaches zero, no modulation of the SQUID can be observed. In the normal conducting range as well as in the superconducting range of the thermistor, ΔV_{mod} is on a constant level. Throughout the whole transition range, DORs of different intensity occur without showing a simple pattern. However, it is clearly visible that their number and density increases with reduced bias current. This was the case for all measurements made, independent on TES design, measurement setup or used SQUIDs. Therefore, the reason for the occurrence of DORs can be clearly attributed to the TES thermistor state.

As the M-I and the I-I curve could not be measured at the same time, a small offset in the bias current due to temperature fluctuations was compensated in sub-figure C) by shifting the M-I curve accordingly. It was possible to match the strong DORs with the discontinuities in the I-I curve by applying a constant shift to the whole M-I curve, revealing a direct correlation between both effects. This could be reproduced by all M-I measurements for the different designs. Hence, a causal connection is highly probable meaning the DORs increase the risk of instability of the readout circuit and therefore are responsible for the discontinuous areas of the I-I curve. This can be ascribed to two effects: In general, the linearization by the FLL is sensitive to high noise levels. The linearized voltage output of the FLL is given by

$$V_{FLL}\left(I_{th}\right) = c_{FLL} \cdot \left(c_{I\rightarrow\phi} \cdot I_{th} + \phi_{off}\right) \tag{7.3}$$

where $c_{I\rightarrow\phi}$ denotes the current to flux transfer factor of the SQUID current sensor. ϕ_{off} is a generally non-zero flux offset that includes all magnetic flux at the SQUID which is not caused by the input coil. c_{FLL} represents the flux to voltage transfer factor of the FLL.

A noise spike $\Delta\phi_{noise}$ exceeding the slew rate of the FLL can cause the stabilized working point to be shifted by an integral number of periods in the V-ϕ curve of the SQUID and thereby shifting the output level of the readout electronics. If this coincides with a change $\Delta\phi_{signal}$ in the input signal flux level, the reproduced signal change at the

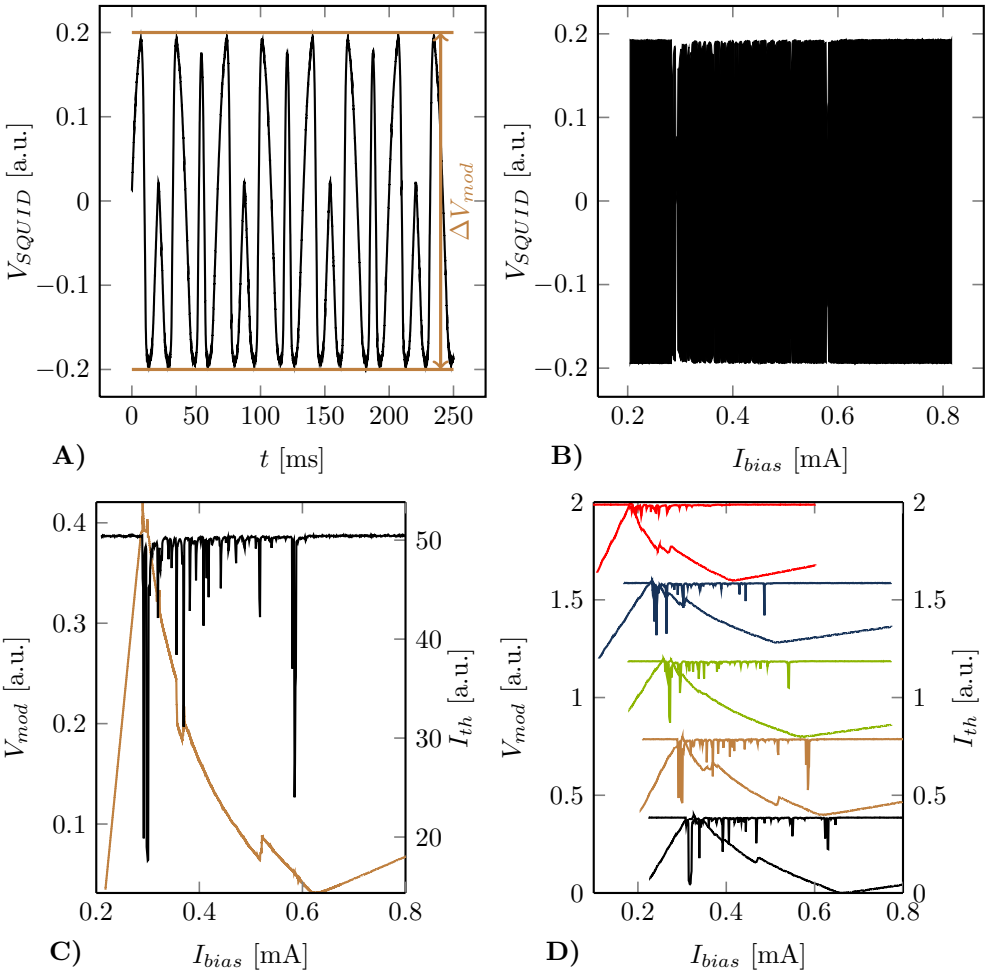

Figure 7.1: A) SQUID voltage response to a modulation signal at constant TES bias current. B) V_{SQUID}-I characteristic of the TES determined by sweeping the bias while measuring the SQUID voltage response on each bias level. C) M-I and I-I curve of a 4A TES. D) M-I curves combined with the corresponding I-I curves for the same TES at different bath temperatures (from top to bottom: 89 %, 82 %, 76 %, 71 % and 64 % of T_c. The curves are shifted in y direction for better visualization.

output is given by

$$\Delta V_{FLL} = c_{FLL} \cdot (\Delta\phi_{signal} + \Delta\phi_{noise} + m \cdot \phi_0)\,, \qquad m \in \mathbb{Z} \tag{7.4}$$

Hence, in a DOR with excess noise, this can cause jumps of the measured current level. The second effect is caused by the reduction of ΔV_{mod}. As the achievable slew rate scales with ΔV_{mod}[48], This will increase the chance of the previously described discontinuities up to a level of total signal loss when ΔV_{mod} falls below a level where the FLL can not stabilize the working point any more. In case of single jumps of the signal, this can be compensated for by software, as long as the noise is small compared to ϕ_0. However, an accumulation of such jumps due in a stronger DOR combined with the occurring high excess noise peaks can lead to arbitrary level changes that can not be correctly reconstructed, as shown in the *I-I* curves in the previous chapters.

Figure 7.1 D) shows a series of measurements on the same 4A TES for different base temperatures. As the temperature ratio $\frac{T_{bath}}{T_c}$ is a relevant figure for the theoretical feedback strength in the lumped TES model (see equation 4.51), the relative values are given for these measurements, which range from approx. 64 % to 89 %. A general tendency of the DORs to show a stronger effect for lower temperature ratios can be observed. Hence, a correlation between the effect DORs and the theoretical feedback strength is suggested, as the latter rises with decreasing ratios. However, for a chosen DOR, no exact prediction can be made concerning its intensity at a certain temperature. This might also be due to the limited bias sampling density of the measurements, as some of the DORs showed very sharp lines in the curves, with significant changes in strength for bias current changes of less than 1 µA. Still, the average reduction of the effect at temperatures closer to T_c, which was 565 mK for this sample, is clearly visible. A reduction in number of the DORs could not be distinctly observed, considering the fact that weak DORs might fall below the sensitivity of this measurement method. However, the density of the DORs increases at all temperatures towards lower bias current, which corresponds to a rising value of α (see equation 2.37). Therefore, and due to the direct proportionality of the static loop gain L to α as given in equation 4.51, this observation is also in agreement with the assumption that the DORs are correlated to the theoretical feedback strength.

A set of *M-I* curves for the 16A design TES at the same relative bath temperatures as used in figure 7.1 is plotted in figure 7.2 A). The general tendencies are the same as for the 4A TES: For lower bias currents, more and stronger DORs can be observed. Also for higher temperature gradients, the average strength of the DORs increases. However, compared to the 4A TES the 16A TES shows a larger number of strong distortions. As can be seen from sub-figure B), a modified 16A TES with additional SP shows even stronger distortions than the one without SP, but the same tendencies. The influence of the SP is confirmed by measurements on a 4A TES without SP, that again shows less significant DORs than the 4A TES with SP (sub-figure C). [114], [115] and [93] found a correlation between excess noise and the feedback strength as well as the transition

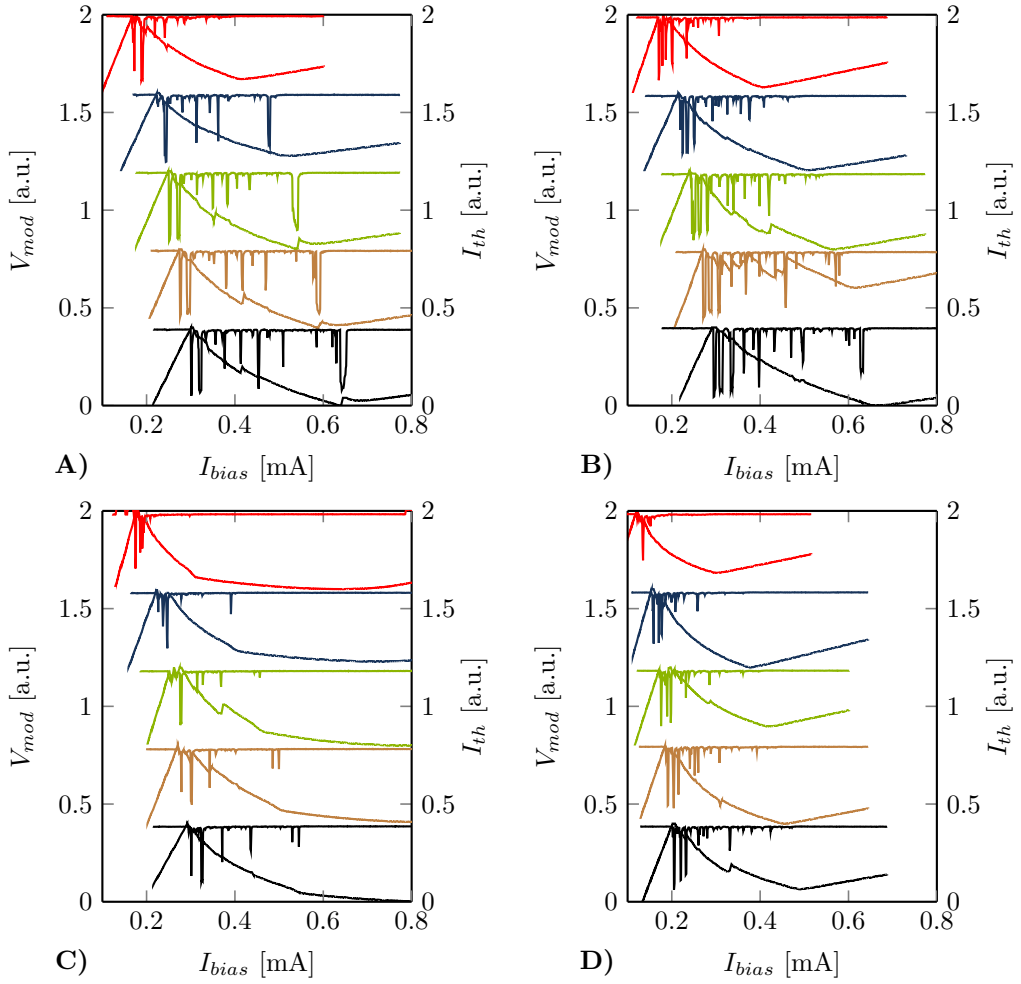

Figure 7.2: A) M-I curves combined with the corresponding I-I curves for the 16A design at different bath temperatures (from top to bottom: 89 %, 82 %, 77 %, 71 % and 64 % of T_c). The curves are shifted in y direction for better visualization. B) 16A TES with additional SP at the same relative temperatures. C) 4A TES without SP at 80 %, 74 %, 69 %, 64 % and 58 % of T_c. D) 4A TES with reduced thermal conductance at 89 %, 82 %, 77 %, 71 % and 64 % of T_c.

width of the thermistor for TES as x-ray calorimeters, where the noise increased for lower thermistor resistances as well as for lower transition widths. They could reduce the excess noise effects by methods to increase the transition width and reduce the feedback strength. The demands for bolometers in the THz band are substantially different to those of such x-ray calorimeters in terms of time constants, as they are limited by their extents due to the large wavelengths. The necessity to reduce the time constants to the desired level demands for the use of the electro-thermal feedback as a means that ideally neither increases of noise and loss of sensitivity, as it would be caused by increasing the thermal conductance (see section 4.3.6). Hence, an intentional broadening of the transition width is not acceptable in this case. However, recent models of non-lumped TES suggest general additional noise from the interaction of the different components of a multi-body TES[92]. These effects have been discussed in [94] for different TES geometries. It was found that reasons for such non-ideal behavior can result from various types of thermal separation of the components of the TES, e.g. thermal separation of superconducting and normal conducting phases inside the thermistor. In case of the THz bolometers discussed here, the geometrical separation as discussed in section 5.2 above is the most obvious type of such a possible source of additional noise. This would explain the stronger DORs of the 16A TES compared to the 4A model, as the absorbers show stronger decoupling from the thermistor (see section 6.3.2). This assumption is also supported by measurement results on a modified 4A model with reduced thermal conductance of the platform to the bath by reducing the total cross-section area of the spider leg structure, while on the platform itself it was kept constant. The analysis showed a decreased number of DORs compared to the original 4A model (figure 7.2 D).

In another experiment, a general strong increase of the excess noise was found for working points with higher feedback strength[99]. As a solution, additional metallic structures were added to the TES and coupled to the thermistor. This increased the heat capacity and the sensitivity of the TES and reduced the noise significantly. While this reduced the feedback strength and hence the time constant of the TES, in the calorimeter case, the achieved time constants at weak electro-thermal feedback oftentimes are sufficient for the aspired applications[99]. As a reason for the additional noise, the decoupling of the thermistor from the thermal membrane was suggested. Hence, as an alternative solution, improved coupling between these layers was suggested to reduce the noise. Different to slowing down the TES which is not acceptable for the pursued aims in this work, the adjustment of said coupling does not disagree with the goal of a fast THz sensor.

Therefore, as a straight forward means of examining the effect of the thermal coupling between membrane and thermistor, a variation of the thermistor size was performed. To be able to vary the thermistor size without affecting other parameters, a redesign of the 4A TES platform was necessary. As the extents of the thermistor at the original location was limited by the adjacent absorbers, the thermistor was shifted to the outer edge of the thermal platform. The platform was slightly enlarged, to allow for a thermistor size of up to 400 µm times 100 µm. To emphasize effects of the coupling between thermistor and membrane, an increased critical temperature was chosen to increase the thermal conduc-

tance of the thermal platform. To compensate for the higher total thermal conductance, the number of spider legs was reduced to 16. The resulting design can be seen in figure 7.3. It will be called 4AE in the following.

Three different thermistor geometries, each scaled by a factor of 2 per dimension, were analyzed. In addition to the thermistor size used for 4A, which consisted of an uncovered thermistor area of 200 µm times 50 µm, two TES variants were created, one with an upscaled, the other with a downscaled thermistor. Their uncovered thermistor areas were 400 µm times 100 µm and 100 µm times 25 µm, respectively. The location of the center of the thermistor was kept constant for the different variants, as can be seen in figure 7.3. The resulting M-I curves are shown in figure 7.3. A strong correlation between the strength of the DORs and the size of the thermistor can be observed: The smaller the thermistor, the stronger the DORs.

To evaluate whether this is an effect of slowing down the thermistor by increasing its heat capacity similar to the method described in [99] or rather an effect of the coupling of the thermistor to the substrate, the time constants of these TES were evaluated following the setup and evaluation method described in section 4.3.5. The measured time constants are plotted versus the corresponding bias current in figure 7.4. If the above mentioned effect of reducing the strength of DORs by increasing the size of the thermistor would result from the additional heat capacity, a corresponding slowdown of the TES would have to be expected. Hence, with increasing size of the thermistor, the time constants would rise. However, the measured data show an opposed behavior: The larger the thermistor, the faster the TES. This gives clear evidence of a different source of the reduction of the DORs. Decoupling of the thermistor from the membrane would explain the slowdown due to the weaker coupling to the absorbers. A clear sign of a working-point dependence of this effect is given by the course of the time constants: They increase towards lower bias currents, which strongly conflicts with the predictions of the lumped model, as the loop gain increases with lower thermistor resistance. The relative increase of the time constants is much stronger for the larger thermistor, suggesting a stronger variation of the coupling. For any given working point in the superconducting transition, the thermistor can separate into superconducting and normal conducting areas. Independent of their distribution, the relative fraction of the thermistor that is superconducting will increase towards lower bias currents and hence lower resistances. While the electrical heating power is nearly constant throughout the transition range, it is only created in non-superconducting segments of the thermistor. As this can also involve a reduced effective cross section of the thermal contact area to the membrane, the thermal coupling is reduced. As cooper pairs do not contribute to the thermal conductance[76], the latter is reduced for the superconducting part of the thermistor with decreasing temperature below T_c. Therefore, the observed behavior suggests the decoupling of the superconducting regions of the thermistor from the membrane. In this case, lower time constants of the large thermistor at working points with higher bias current result from the larger area of normal conducting material compared to the smaller thermistors and the corresponding stronger coupling to the membrane. Comparing these results to the occurrence of DORs,

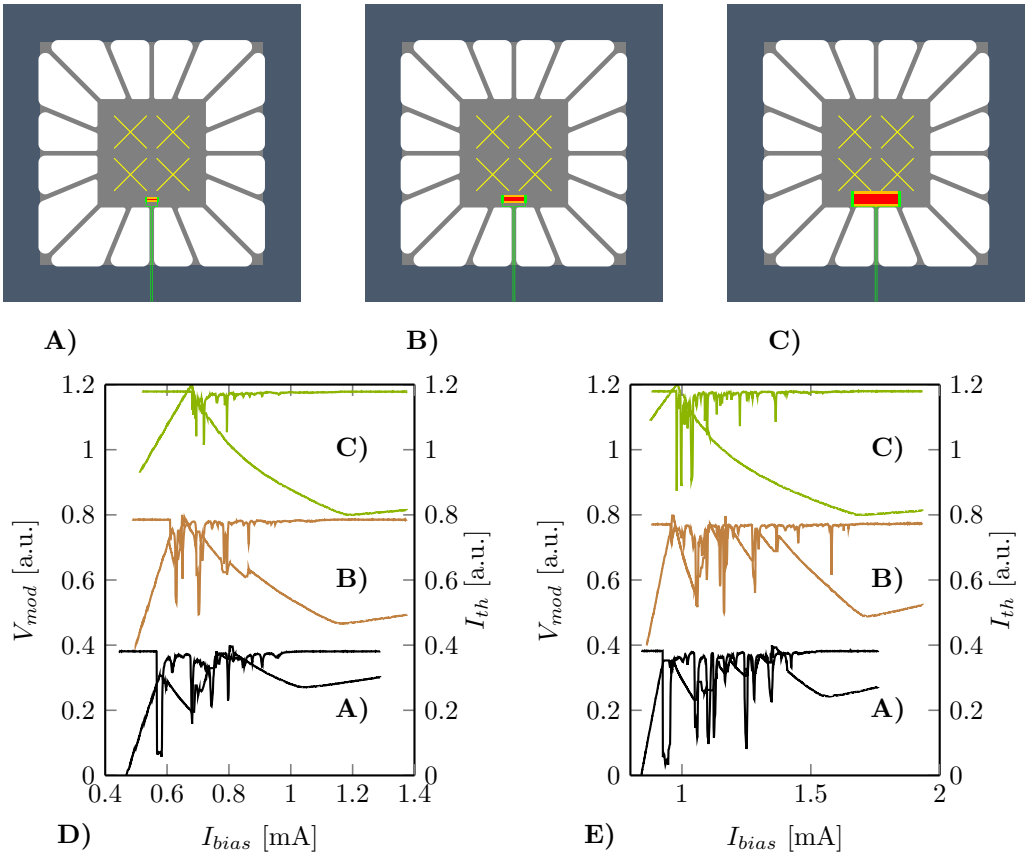

Figure 7.3: Geometry of the 4AE design with uncovered thermistor areas of $100 \times 25\,\mu m^2$ (A), $200 \times 50\,\mu m^2$ (B) and $400 \times 100\,\mu m^2$ (C). Below: Measured M-I curves combined with the corresponding I-I curves for these TES are shown for $\frac{T_{bath}}{T_c} = 93\,\%$ (D) and $82\,\%$ (E) (vertically shifted for better visualization).

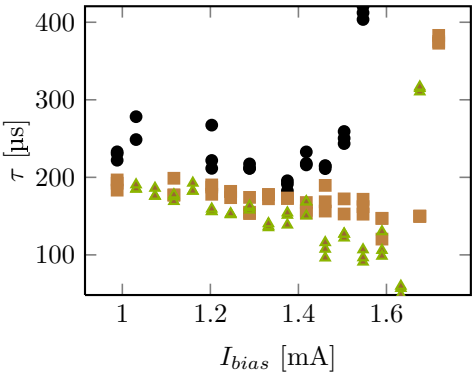

Figure 7.4: Measured time constants for the 4AE TES with different thermistor sizes: 100 µm times 25 µm (black symbols), 200 µm times 50 µm (brown symbols) and 400 µm times 100 µm (green symbols).

we find that for the smallest thermistor, strong DORs occur nearly throughout the whole working range, corresponding to high time constants throughout this range. In contrast, the largest thermistor shows a clear tendency of rising strength of the DORs towards lower bias currents, which correlates to the increasing time constants. As suggested by [92], such decoupled components of the TES can introduce additional noise components. Due to the limited thermal conductance within the thermistor, a separation of the thermistor into normal conducting and superconducting regions is probable. Depending on the degree of this separation this noise will vary and might even induce oscillations of the normal to superconducting border in between such sections[116]. Structural properties of the thermistor could be responsible for the irregular, but for a given thermistor reproducible dependency of the location of the DORs within the I-I curve for a given base temperature.

7.4 Demonstrator for 25 frames per second

7.4.1 Requirements

To overcome the limitations of the THz camera demonstrator presented in section 6.5, an improved demonstrator was setup. The main goals were to enlarge the FOV while achieving smooth video data with frame rates up to 25 Hz. Scanning the FOV on spiral paths as used for the previous system causes increasing redundancy as the number of used sensors increases. Additionally, the redundancy as well as the demands on the sensor time constants increase with rising radius of the FOV, as the scanning speed scales with the distance from the center of the FOV. Finally, the circular shape of the resulting images is not ideal for the visualization of the human body, which rather demands for

a rectangular FOV. Hence, the system was designed to use a horizontal line of sensors which is vertically scanned by a tilting mirror. In this case, the number of used sensors directly defines the achievable resolution. For w being the width of the FOV and N_s the number of sensors along the line, the distance between horizontal samples d_h is given as

$$d_h = \frac{w}{N_s} \tag{7.5}$$

corresponding to a horizontal resolution of

$$r_{min,h} = 2 \cdot d_h \tag{7.6}$$

where $r_{min,h}$ is the lateral resolution per line pair which is inversely proportional to the number of sensors. For an aspired FOV of 1 m, 64 sensors were implemented to achieve a resolution of approximately 3 cm, which will be extended to 128 sensors in the final state to achieve 1.6 cm. While the lack of redundancy allows for an efficient use of all sensors, this also demands for full availability of all TES, as each outage of a sensor causes a reduction by a factor of two of the local spatial resolution perpendicular to the path of this gap through the image, as said gap can only be filled by interpolating the image data of the neighboring sensors. Hence, the TES were chosen to have only few and weak DORs.

The vertical resolution is defined by the vertical sampling distance d_v and hence depends on the number of horizontal rows N_r the FOV is separated into, assuming an even distribution. N_r is equivalent to the number of samples per frame taken for each sensor. A vertical resolution of

$$r_{min,v} = 1.6\,\text{cm} \tag{7.7}$$

was aspired, which is equal to the horizontal resolution in the final setup. The resulting number of rows is given by the height h of the FOV as

$$N_r = \frac{h}{d_v} = 2 \cdot \frac{h}{r_{min,v}} \tag{7.8}$$

resulting in

$$N_r = 256 \tag{7.9}$$

for a FOV of $h = 2\,\text{m}$ height.

From N_r, the necessary sampling frequency ν_{sample} can be determined as

$$\nu_{sample} = N_r \cdot \nu_{frame} \tag{7.10}$$

depending on the frame rate ν_{frame}. The corresponding bandwidth $\Delta\nu$ and the time

constant τ of a sensor required to achieve the full resolution can be calculated using the Nyquist–Shannon sampling theorem[117] as

$$\Delta\nu = \frac{\nu_{sample}}{2} \tag{7.11}$$

and

$$\tau = \frac{1}{2\pi \cdot \Delta\nu} = \frac{1}{\pi \cdot N_r \cdot \nu_{frame}} \tag{7.12}$$

Accordingly, at a frame rate of 10 Hz, a time constant of 124 µs is necessary to achieve the full resolution, for 25 Hz, 50 µs are needed. For higher time constants, the vertical resolution will degrade, causing a vertical smearing effect in the resulting pictures.

7.4.2 Sensor properties

The findings concerning the DORs discussed in section 7.3 were used to create an adjusted TES design based on 4A with reduced DORs. The found improvement by increasing the thermistor size was combined with a stronger thermal coupling on the membrane, realized by a reduced thermal conductance from the platform to the thermal bath, while it was kept constant on the platform itself, as the results above showed a reduction of the DORs by this adaption. It was achieved by reducing the spider legs in number as well as in width. The resulting design is shown in figure 7.5 A). It will be called 4AEL in the following. The thermistor was chosen to have an uncovered area of 400 µm times 100 µm. The thermal platform was slightly enlarged to fit this thermistor. However, the platform was scaled to the minimum possible extents to limit the slowdown of the TES by the distributed heat capacity. The resulting platform has a rectangular shape with an area of 800 µm times 920 µm, which is only by 15 % larger than the platform of the 4A TES.

Figure 7.5 B) shows the results of M-I curve measurements. The measured TES was located on the same chip as the 4A and the 16A TES presented in figures 7.1 and 7.2 for direct comparison. Additionally, the presented M-I curves were taken at the same bath temperatures as the data shown in said figures. As also the critical temperature of the measured TES of 567 mK was very close to the 4A and 16A TES (the maximum difference was less than 0.5 %) differences can be clearly attributed to the different geometrical designs. For the 16A TES strong DORs could be found throughout the whole transition range for lower $\frac{T_{bath}}{T_c}$, and even for higher temperatures still strong DORs could be observed in the working points at lower bias current. While the average strength of these effects was reduced for the 4A TES, the general behavior was the same. In contrast, the 4AEL TES shows only weak DORs even at the lowest base temperature measured, and only for low bias currents.

However, the measured time constants as presented in figure 7.5 C) show a strong variation throughout the superconducting transition range of the thermistor, as observed on the 4AE TES with the largest thermistor: While for high bias currents time constants

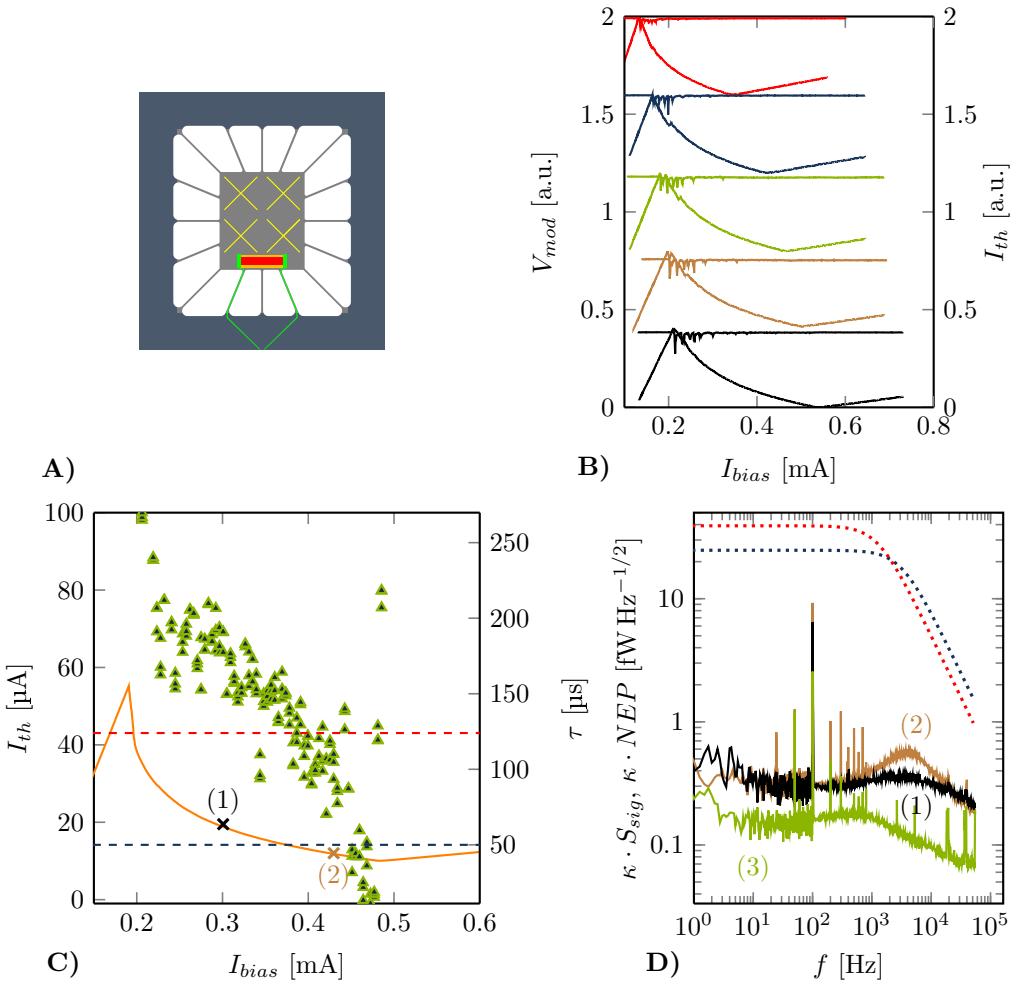

Figure 7.5: A) 4AEL design with a 400 µm × 100 µm thermistor. B) M-I curves combined with the corresponding I-I curves for different $\frac{T_{bath}}{T_c}$ (from top to bottom: 89 %, 82 %, 76 %, 71 % and 64 %). C) Measured time constants (symbols). The dashed lines mark the 50 µs and 124 µs levels, respectively. NEP measured under room temperature radiation load in the marked working points on the I-I curve and the NEP for 0.4 K background (3) are presented in D) together with the optical signal power spectral density S_{sig}^{max} (dotted lines for 10 Hz (red) and 25 Hz (blue) frame rate), both scaled by $\kappa(\omega_{el})$.

of as low as 20 µs were achieved, towards lower bias the time constants rose up to 250 µs. As discussed above, this can be attributed to the increasing decoupling of the thermistor from the membrane, resulting in a slowdown of the TES. This means that the system requirements of $\tau = 50\,\mu s$ for a lateral resolution of 1.6 cm along the vertical axis, which is affected by the time constant of the TES, are achieved even for frame rates of 25 Hz. However, this is only the case for a small working range, and even at 10 Hz, where $\tau = 124\,\mu s$ are required, in more than half of the usable bias range, this time constant requirement is exceeded. However, as this affects the low bias range where still some DORs occured, the range of time constants fully matching the requirements is free of DORs and hence fully usable. To achieve a vertical resolution of 3 cm which matches the horizontal resolution for 64 pixels, the whole bias range can be used at frame rates up to approx. 10 Hz. At 25 Hz, approx. one third of the bias range can be used without limitations, while for lower bias values smearing effects will occur.

Subfigure D) shows the noise levels for the working points marked by crosses in subfigure C). While the noise levels within the used bandwidth are approx. $3 \times 10^{-16}\,\mathrm{W\,Hz^{-1/2}}$ independent of the working point, again an excess noise hump as discussed in section 6.4 can be observed for higher frequencies. This hump is more pronounced for the working point at higher bias current, hence corresponding to the lower time constant. Therefore, this noise component seems to be coupled rather to the effective time constant than to the theoretical feedback from the lumped model as suggested for the DORs.

The time constant requirements of the camera demonstrator defined in section 7.4.1 were used to define the optical signal power spectral densities S_{sig}^{max} plotted in subfigure D) for frame rates of 10 Hz and 25 Hz, respectively. In combination with the noise level, the maximum achievable SNR was calculated for the optical window from 328 GHz to 368 GHz as

$$SNR = \frac{S_{sig}^{max}}{NEP} \tag{7.13}$$

resulting in

$$SNR^{25\,\mathrm{Hz}} = 82 \tag{7.14}$$

for 25 Hz and

$$SNR^{10\,\mathrm{Hz}} = 130 \tag{7.15}$$

According to equation 1.30, this equals achievable bit depths of 6.4 bit and 7 bit.

Time constant measurements were performed and evaluated following the setup and methods described in section 4.3.5. The resulting time constants are plotted in figure 7.5 versus the corresponding bias current.

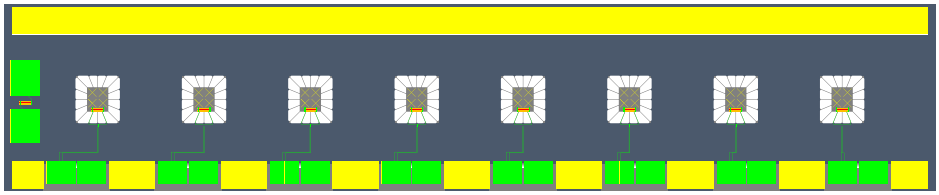

Figure 7.6: Top view on a sensor array consisting of eight 4AEL TES in a row. For effective thermal coupling to the cooling stage, the long edges are covered with a gold film that is thermally connected to the chip carrier using gold bonds.

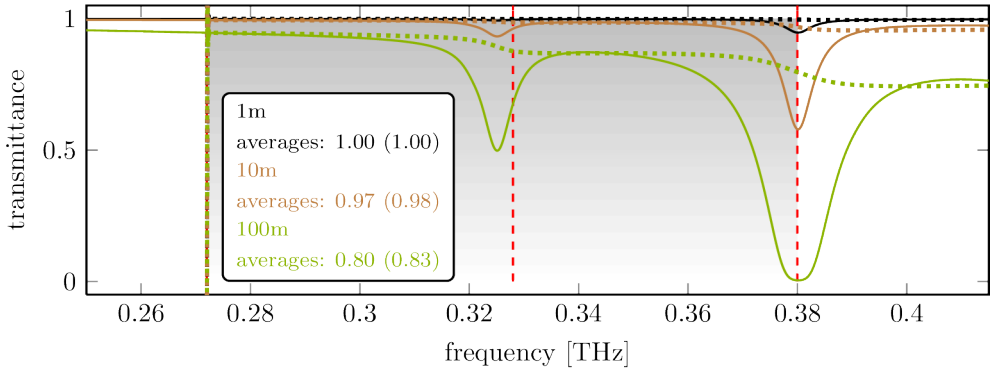

Figure 7.7: Transmittance of air at 295 K, 1013 mbar and 30 % relative humidity for different object distances. The shown data was calculated using [22]. The range from 272 GHz to 380 GHz is shaded. The dotted lines mark the average transmittance from 272 GHz to the current frequency. The average values for 380 GHz are shown in the legend.

7.4.3 THz imaging

The 4AEL TES were arranged on a chip consisting of eight TES pixels in a line as shown in figure 7.6. An additional thermistor is located at the left edge of the chip for testing purposes and the determination of T_c. To achieve a good thermal connection to the cooling stage, the edges of the chip are plated with gold pads. This chip design was used to integrate the 4AEL TES into the THz camera demonstrator, following the general setup concept described in section 4.2.

The chip is thermally connected to the chip carrier via gold bonds. The carrier itself consists of gold plated electrolytic copper and is directly connected to the cooling stage by copper bolts. A superconducting aluminum casing containing the chip and the carrier serves as thermal, magnetic and electromagnetic shielding. The THz radiation is coupled into the casing by eight feedhorn antennas which are integrated in the removable front cover. The demonstrator was equipped with optical filters with a bandpass from approx.

275 GHz to 380 GHz, which results in a only slightly reduced transmission compared to the 328 GHz to 368 GHz window even for distances of several 10 m, as can be seen from figure 7.7. Accordingly, the cut off frequency of the feedhorn antennas was adjusted by increasing the inner diameter of the cylindrical wave guide to 0.65 mm, which corresponds to a cut off frequency of approx. 270 GHz. This adjustment increases the maximum achievable SNR to at least

$$SNR^{25\,\mathrm{Hz}} = 130 \tag{7.16}$$

at 25 fps, which equals a bit depth of 7 bit.

The electrical contacts of the chip are attached by superconducting aluminum bond wires to a PCB which is screwed to the chip carrier. The whole module is connected via low resistive multi-pin connectors on this PCB to the electrical wiring outside of the casing. In the THz camera demonstrator system, eight modules are placed in a row on a temperature controlled ^{3}He evaporation cooler with a minimum base temperature of 350 mK. This cold stage is precooled and thermally shielded by two temperature stages at approx. 3 K and 50 K, respectively. These stages are cooled by pulse tubes, which produce unavoidable microphonic effects. Hence, the thermal coupling between the temperature stages and the pulse tubes is established by flexible copper wire, which allows to achieve a good thermal conductance and a weak mechanical coupling at the same time. Figure 7.8 shows a sectional view of the cryostat design.

An on-axis telescope was used as the objective of the camera. A main mirror of 1 m diameter was combined with a secondary mirror that was equipped with a tilting mechanism that allows for linear scanning with frame rates up to 25 Hz. A mechanical adjusting device allows to vary the position of the secondary mirror along the optical axis. By this, the focal distance of the system can be adjusted from 14 m to 20 m. According to equation 1.1, this results in a diffraction limited resolution of 1.5 cm to 2.1 cm depending on the chosen distance. Hence, the horizontal resolution is clearly limited by the number of sensors, which allow for approximately $r_{airy} \approx 3\,\mathrm{cm}$ for a FOV of 1 m width (see section 7.4.1) at 14 m. This will be compensated for in the near future with the setup of 128 sensors (which goes beyond the scope of this thesis). This will allow for resolutions down to 1.6 cm. As the sampling density as well as the diffraction limited resolution both scale linearly with the object distance, this relation applies to all focal lengths of the system.

A photograph of the entire demonstrator is shown in figure 7.8. The objective is mounted on an aluminum framework which includes the mechanism to vary the focal length. As an independent construction, it is not directly connected to the rest of the camera to avoid the transfer of mechanical vibrations. It can be moved separately for simplified transportation and allows for easy by a different objective, which makes the system very flexible in application. The main camera system contains a common power supply for all components, the electrical controlling units for temperature regulation and

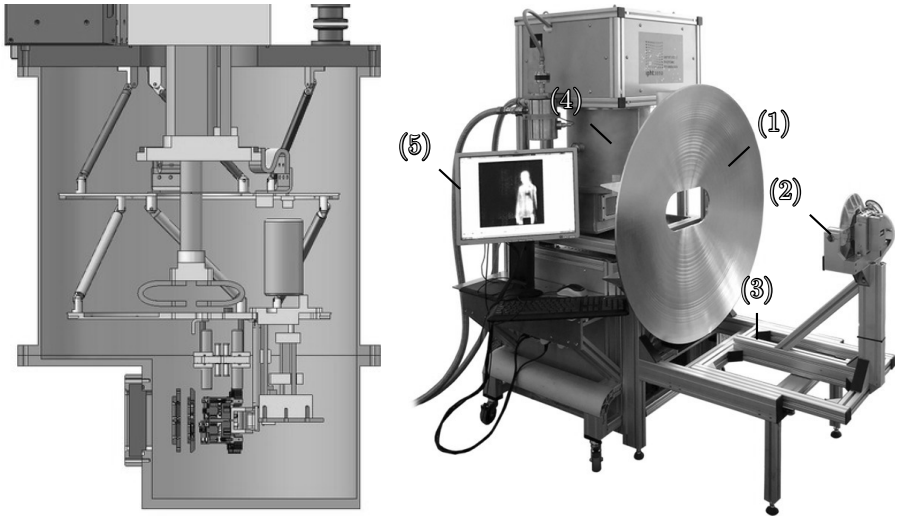

Figure 7.8: THz security camera demonstrator for 25 fps equipped with 8 sensor arrays (fig. 7.6). Left: Cryostat layout. Right: Primary mirror (1), the secondary mirror including the scanning mechanism (2), the objective framework for adjusting the focal length (3), the cryostat containing the sensors (4), and the system monitor showing the current THz video (5).

monitoring, the sensor settings and the data readout. The resulting THz video can be observed on a monitor.

To verify the achieved spatial resolution at the maximum frame rate of 25 fps, measurements with periodic test patterns were performed. To emulate the application setup of the camera, the test patterns were cut out of aluminum sheets, which reflect the background radiation at a room ambient temperature of 22 °C. The aluminum sheet was mounted in front of a heating plate, which was covered with eccosorb[118], a commercial efficient microwave absorber available as sheets of flexible foam. The plate was heated up to 37 °C, at which the thermal emission of the eccosorb simulates the human body. Hence, the radiation received from the slits and the remaining aluminum stripes in between equals the signals from the body and a hidden reflective object. Horizontal as well as vertical stripes were used to distinguish the different spatial resolutions in both directions. As discussed above, the horizontal resolution is limited by the amount of sensors, resulting in approximately 3 cm. This is in good agreement with the results of the test pattern with 30 line pairs per meter (30 lp/m), corresponding to a resolution of 3.3 cm. As can be seen in figure 7.9, The horizontal as well as the vertical lines can be clearly separated even at the maximum frame rate. At 45 lp/m, the vertical lines merge into a fluctuating area of shades of gray. When moving the test pattern through the FOV, single lines appear and disappear due to the varying location relative to the sensor grid, stressing a serious advantage of video rate visualization: While periodic structures below

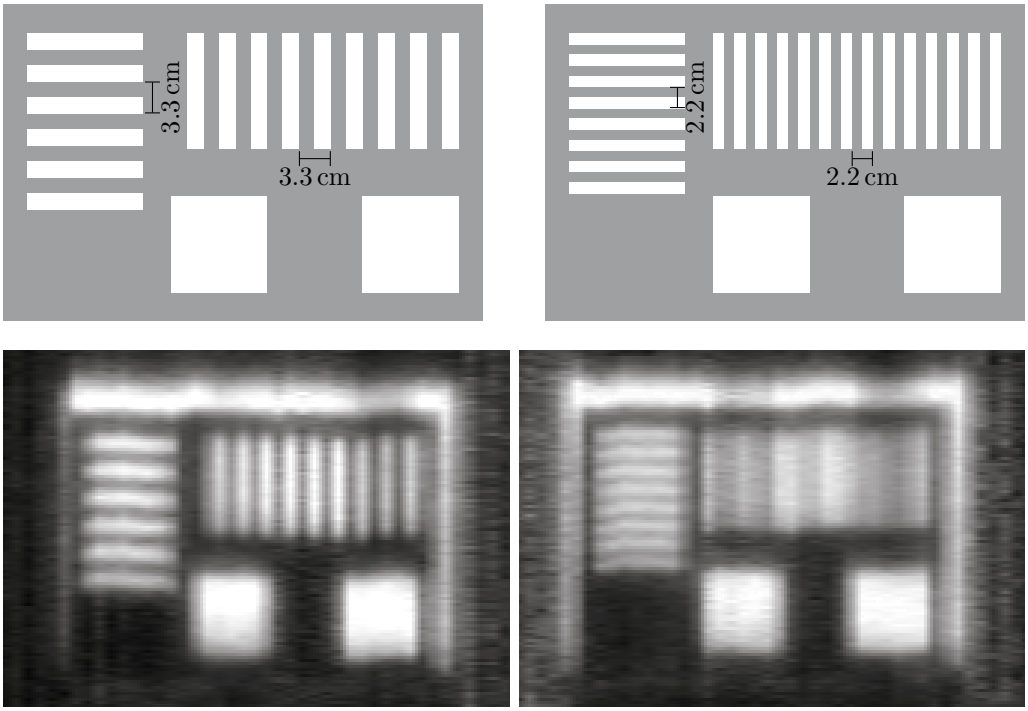

Figure 7.9: Upper pictures: Aluminum resolution test patterns with periodic slits. Left: 30 lp/m (line width of 1.7 cm). Right: 45 lp/m (line width of 1.1 cm). Below: THz images taken at 25 fps from a distance of 14 m. The test patterns are placed in front of a metal plate (bright frame) heated to 37 °C covered with eccosorb[118] to emulate the emission of the human body while the aluminum reflects the surrounding at room temperature (22 °C). While the horizontal lines which are orthogonal to the scanning direction can be separated in both cases, the vertical lines can only be resolved for 30 lp/m.

the resolution limit are smeared on single frames, they vary in intensity when watched as a video stream when moving due to the aliasing effect[108]. This oftentimes allows for detecting such small structures from a series of frames, while it can not be discovered on a still framing. The horizontal lines can still be distinguished, which confirms a resolution close to the theoretical limit of the optical system at the maximum frame rate.

The fact that the resolution is not limited by the speed of the sensors is also stressed by the comparability of images taken at different frame rates. Figure 7.10 shows a person hiding different objects under a T-shirt and a pullover, recorded from a distance of 14 m. No difference can be observed in the achieved resolution at 3 fps and 25 fps, which for example can be deduced from the separability of the fingers in the images. As the scanning speed and hence the scanned distance per time is by more than a factor of eight

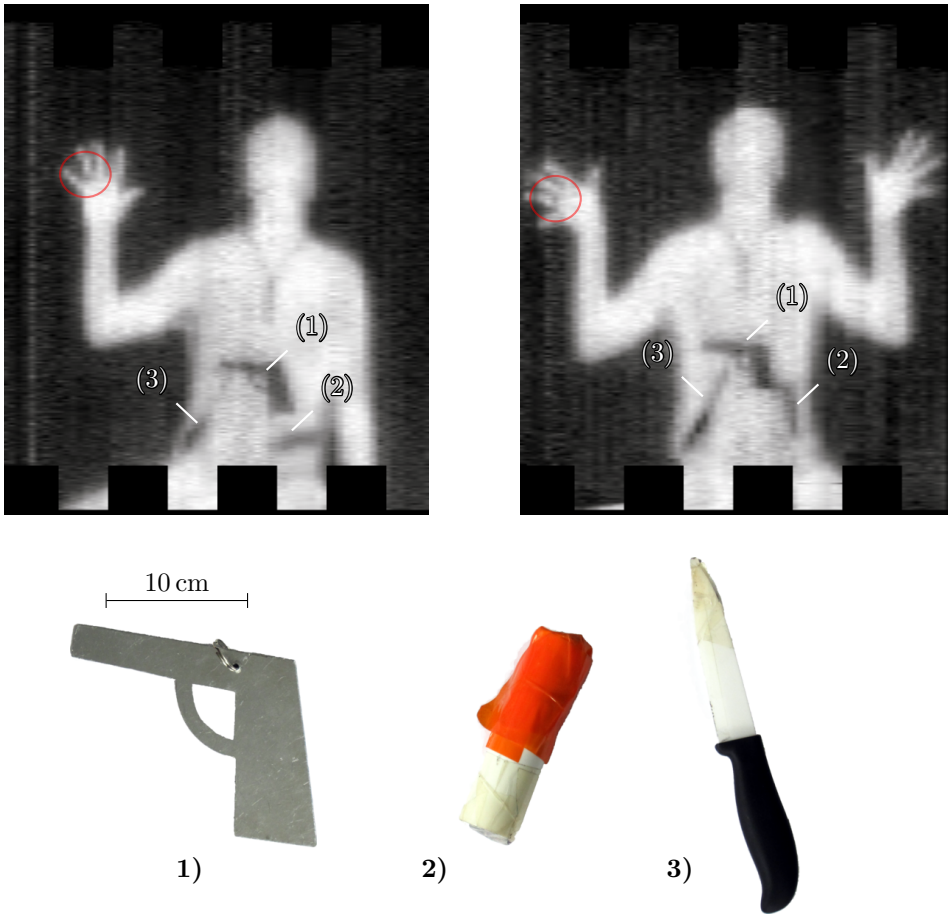

Figure 7.10: THz images taken from 14 m distance, taken at 3 fps (left) and 25 fps (right). A dummy handgun made of aluminum (1), a plastic tube filled with screws to imitage a pipe bomb (2) and a ceramic knife (tip wrapped with adhesive tape for safety reasons) (3) hidden at the body under a t-shirt and a pullover can be detected. Even the wedding ring can be vaguely seen (marked by a red circle).

different for these rates, the time constants of the sensor still are not dominating the resolution. This allows for a smooth reproduction of movements in front of the camera and hence is a significant enhancement compared to the demonstrator presented in section 6.5, for which the resolution at 10 fps was already visibly degraded. The images in figure 7.10 do also again stress the importance of the capability of taking video frames while the screened person is moving: Depending on the viewing direction, objects oftentimes change their visibility in the THz images. The hidden ceramic knife for example shows up mainly by its handle in the left image, as the blade is oriented in a small angle with respect to the line of sight and can be barely seen. Therefore, an object could be missed on a single frame, while it will show up in a video as soon as the viewing direction changes, for example as the person slightly turns the body.

The demonstrator discussed in section 6.5 showed occasional distortions of the images. This was caused by unpredictable instabilites of the signal, caused when temperature fluctuations shifted the working point into a DOR. While this could be compensated for due to the spiral scanning by temporarily switching of the affected sensor, single distorted frames could not be avoided. Additionally, such effects lead to substantial aggravation for line scanners. Due to the lack of redundancy, unstable channels would have to be deactivated and hence cause a local worsening of the resolution. This could be drastically improved by the significant reduction of the DORs with the 4AEL TES, which led to higher stability of the sensor signals.

8 Single absorber TES

8.1 Motivation

The results of the previous chapters show a significant improvement of the TES concerning their applicability for fast THz cameras. Multi pixel sensor arrays could be implemented, and the single TES showed low enough time constants and noise levels to obtain videos at frame rates of up to 25 Hz that allow to detect objects of different materials hidden at the body under clothing in real time. The achieved time constants were low enough to avoid significant degradation of the resolution, and the amount of DORs could be reduced strong enough to operate larger numbers of sensors simultaneously. Real time imaging at full video rate could be successfully demonstrated with a linearly scanning sensor line of 64 sensors, assembled of identical modules of 8 TES each.

However, strong bias dependency of the time constants of the 4AEL TES limits the possibilities of common biasing of the TES, which is a precondition for the efficient implementation of larger sensor arrays. It allows to reduce the number of electrical wires to the cold stage and hence increases the maximum number of usable sensors concerning the maximum acceptable heat load and system complexity. Further, the cost of implementation is reduced, as up to date large portions of the system setup require manual labor. Finally, also the controlling electronics and software is simplified due to the smaller number of free parameters. Hence, in this chapter an alternative TES design concept will be discussed which provides time constants below 50 µs throughout the whole working range, as required for real time full body scanning at a frame rate of 25 hertz and with 1.6 cm lateral resolution, defined in section 7.4.1. It will in particular take advantage of the findings of section 6.3 concerning the time constant dependencies on the geometrical structure.

8.2 Comb structures

The improvements achieved by the 4AEL design concerning DORs are remarkable, and it could be shown that it is suitable for full video rate passive THz imaging. However, the strong dependency of the time constants on the working point still demands a compromise between the width of the working range and the minimum achievable lateral resolution. The analysis of the effects of the geometrical TES design structure suggested to reduce the distribution of the components on the TES platform to the possible minimum (see section 6.3.2), which is supported by the analytical analysis of distributed TES structures

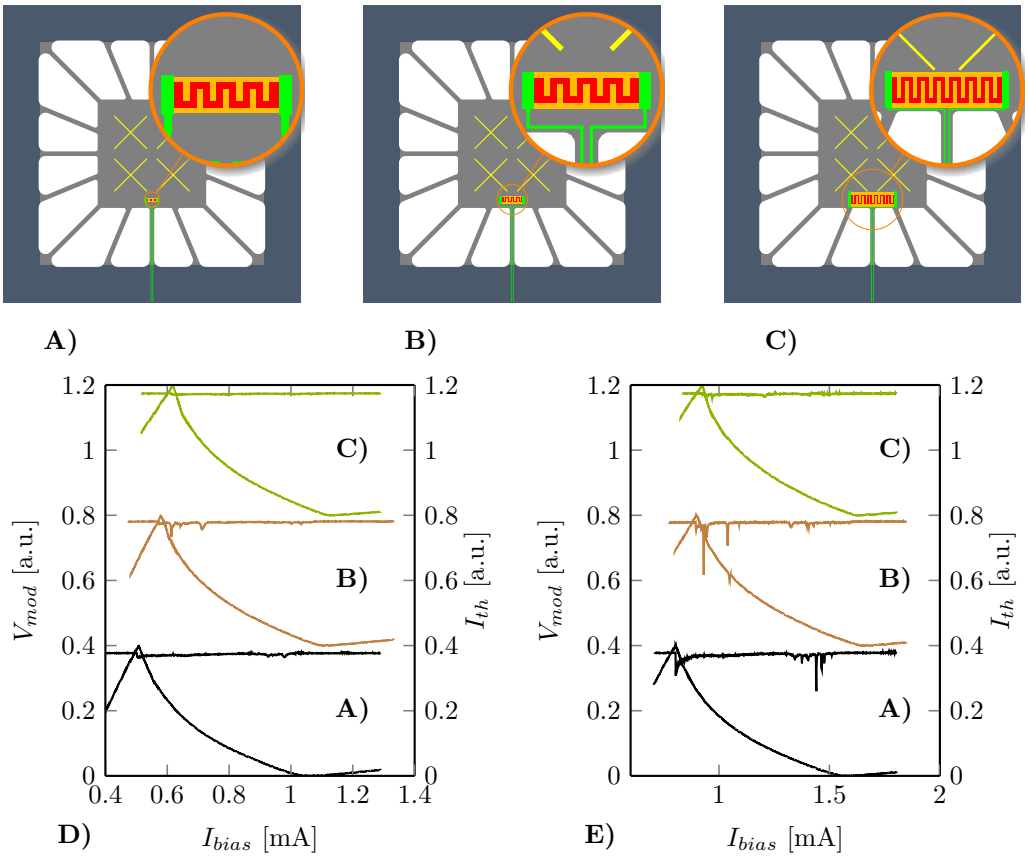

Figure 8.1: A) to C) 4AE TES with variing thermistor size as shown in figure 7.3 additionally equipped with normal conducting comb structures on top of the thermistors. Below: Measured M-I curves combined with the corresponding I-I curves for $\frac{T_{bath}}{T_c} = 93\,\%$ (D) and $82\,\%$ (E) depending on the thermistor area (vertically shifted for better visualization).

.

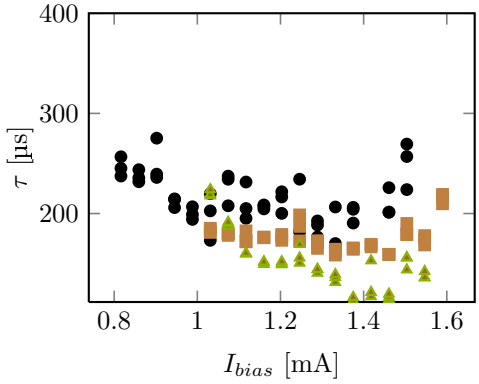

Figure 8.2: Measured time constants for the 4AE+comb TES with different thermistor sizes: 100 µm times 25 µm (black symbols), 200 µm times 50 µm (brown symbols) and 400 µm times 100 µm (green symbols).

in [92]. Unfortunately, the strong increase of the DORs with smaller thermistor sizes and the resulting use of a rather large thermistor limit the possibilities to concentrate the thermal platform, absorbers and thermistor to a small area.

An alternative means to reduce excess noise and instabilities at stronger feedback without the use of improved coupling in between thermistor and membrane and hence without the necessity of large thermistors was to slow down the TES by reducing α [99]. This could be achieved by adding normal metal structures to the thermistor surface, which were reported to directly tune α [93]. Excess noise features could be successfully reduced by such structures in TES calorimeters, as reported by [114][119]. As it was usually used to intentionally increase the time constants for calorimeters, this method is expected to increase the theoretical lower limit of the time constants of the bolometers discussed here due its their limiting effect on the feedback strength. However, as the FEM models showed that the time constants are not just limited by the feedback strength but also the geometrical extents. Hence, the effect of normal metal comb structures on TES with different thermistor sizes was analyzed.

To directly compare the effect on DORs a set of TES as shown in figure 7.3 was equipped with normal metal comb structures similar to those used in [119]. These structures were created from the same layer as the SP, hence resulting in a good thermal connection to the SP. Rectangular stripes starting in alternation from the left and the right SP of the thermistor span most of the width of the TES orthogonal to the current flow direction, leaving a meander-like area of the thermistor uncovered. The modified designs are shown in figures 8.1 A) to C). The M-I curves of these TES were measured at the same temperature levels as the TES without comb structures in section 7.3. The resulting curves are shown in figure 8.1 D) and E). The direct comparison to the results

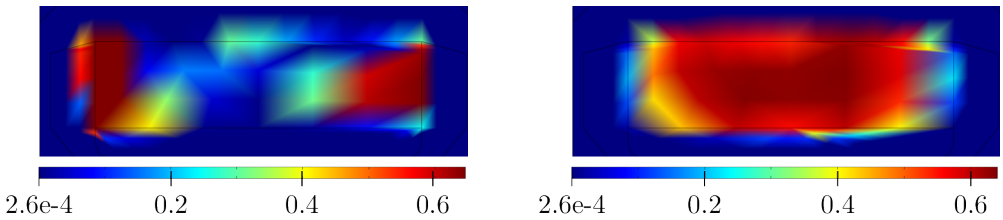

Figure 8.3: Lateral square resistance distribution over the thermistor in FEM simulations. Left: Working point showing instabilities. Right: Neighboring working point with stable parameter convergence using the same resistance scale in $\Omega/\square$.

without comb structures shown in figure 7.3 shows that again a significant reduction of the DORs can be achieved by adding the comb structures. Even for the small thermistor the number of DORs is strongly reduced. The corresponding time constants at $\frac{T_{bath}}{T_c} = 82\,\%$ are plotted in figure 8.2.

Different from the predictions e.g. in [93], no significant differences in the transition widths could be measured between the TES with and without the comb structures. Also no strong differences in the time constant levels could be observed. In general, a weak convergence of the levels could be observed with respect to the thermistor area, as the time constants of the smaller thermistor were slightly reduced, while those of the large thermistor were increased. Also the tendency of the time constants to increase with decreasing bias was maintained. Hence, the comb structure does not seem to substantially affect the decoupling from the substrate, which is expected to cause this behavior. The FEM simulations in section 5.2.4 showed distorted working ranges similar to DORs in which locally unstable solutions occurred. In these working ranges, a separation of the thermistor into regions with different electrical resistances could be observed (see figure 8.3). Though this model is strongly simplified compared to the real physical system of such a TES, this similarity suggests a possible physical reason of the DORs and the effects of the comb structures. Effects of a segmentation of the thermistor into elements of fluctuating resistances have been analyzed by [115] using a numerical percolation model, which allowed to describe noise effects due to the segmentation of a thermistor. The results of this model were in good qualitative agreement with the noise effects observed in measurements. As for a given resistance of the thermistor in the transition range the number of different segmentation patterns in principle is unlimited, new degrees of freedom occur that can cause variations of the thermal conductance in between different areas of the thermistor and local resistance fluctuations. Hence, noise due to phase border oscillations or resistance switching effects might occur, but also the degree of segmentation itself is expected to influence the noise level, as discussed in [94]. The limitation of the current path by comb structures to the meander shaped uncovered part of the thermistor reduces the degrees of freedom in this case and enforces normal conducting areas in the covered regions, which reduces the occurence of noise effects[115].

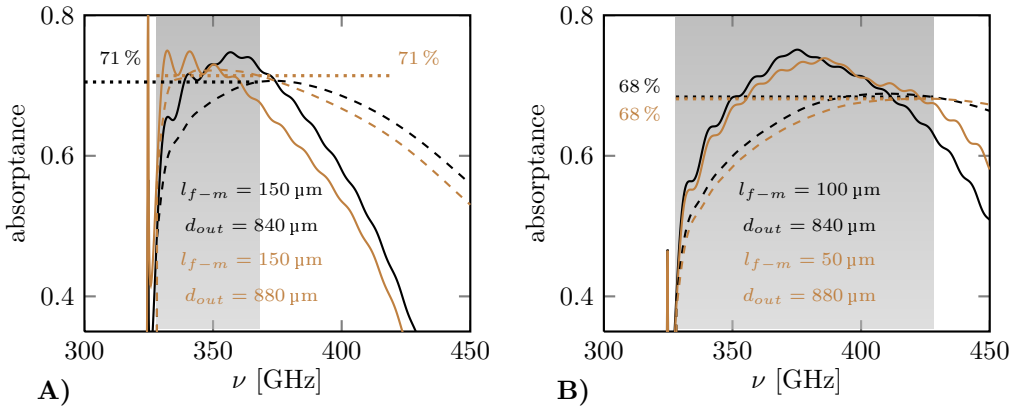

Figure 8.4: Electro-magnetic simulation of the 1A-model. The absorptance $A(\nu_{opt})$ is plotted as solid lines, its average $\bar{A}$ in the interval from the cutoff frequency of the feedhorn antenna to the respective frequency ν_{opt} as dashed lines. Selected values with high absorptances are selected for the diameter of the output cone of the feedhorn d_{out} and l_{f-m} (see figure 5.1). Subfigure A) refers to a bandwidth of 40 GHz, B) to 100 GHz.

8.3 Radiation coupling

To make use of the reduced DORs without the disadvantage of rather high time constants, a new TES design was created that combines comb structures with small area thermistors that allow for a compact design of the thermal platform. As this implies the use of only one dipole cross absorber, electro-magnetic FIT simulations of such an absorber configuration were performed to evaluate the achievable efficiency and hence the practical applicability of such TES designs. The used model is derived from the model described in section 5.2.1, and uses a single pair of dipole absorbers. Hence, it will be called 1A in the following. Again, the diameter d_{out} of the output cone of the feedhorn as well as the distance l_{f-m} between feedhorn and membrane were varied. Figure 8.4 shows the frequency dependent absorptance combined with the corresponding bandwidth dependent averages. The presented data in sub-figure A) results from two combinations of d_{out} and l_{f-m} that resulted in the highest average absorptance within an optical bandwidth of $\Delta\nu_{opt} = 40\,\mathrm{GHz}$. Sub figure B) shows the corresponding results with the highest average for a bandwidth of $\Delta\nu_{opt} = 100\,\mathrm{GHz}$. The achieved coupling efficiencies of

$$\eta_{EM}^{40\,\mathrm{GHz}} \approx 71\,\% \tag{8.1}$$

for $\Delta\nu_{opt} = 40\,\mathrm{GHz}$ and

$$\eta_{EM}^{100\,\mathrm{GHz}} \approx 68\,\% \tag{8.2}$$

for $\Delta\nu_{opt} = 100\,\mathrm{GHz}$

are very close to the corresponding values for the 16A and the 4A design. A significant difference is the achieved bandwidth for a given set of geometrical parameters: The 16A setup achieved a high absorptance over a wide bandwidth with a fixed set of parameters. In contrast, for the 1A design for each chosen bandwidth the optimum set of parameters has to be determined individually. [64] suggested to overcome this by using an extended numerical optimization process include a vast set of parameters, and achieved improved absorptances and increased bandwidth results. While this goes far beyond the scope of this work, further optimizations for such designs are planned. However, as the found configurations already allow for good coupling, they can be used for a defined setup without signifcant losses in coupling.

8.4 Electro-thermal simulations

As the analysis in the previous section showed that a TES with a single crossed dipole absorber pair can achieve as good electro-magnetic coupling as designs with larger absorber areas as long as they are optimized for a certain bandwidth, a TES design was created using the 1A platform. To further improve the temperature homogeneity on the thermal platform which was found to contribute to the reduction of DORs, the thermal conductance was reduced by redesigning the spider leg structure accordingly. The resulting design is shown in figure 8.5. To come closer to the ideal lumped TES design, the thermistor size was scaled down by a factor of four compared to the 16A and the 4A TES. To compensate for the increased number of DORs found for small thermistors in section 7.3, comb structures were added to the surface as described above. They were combined with SP to reduce the risk of degradation and provide long term stability (see section 3.3). A list of the specific geometry parameters of the 1A design can be found in table 8.1. These values were used to calculate the heat capacities of the different components of the design based on the literature values given in table 4.1. To allow for a direct comparison to the previously discussed models, base temperature, critical temperature and transition width were assumed to be identical to those used for the simulations and calculations of the 16A and the 4A model. This allows to identify effects of the geometrical differences of the models. In addition, the heat capacity values were calculated without a scaling factor as it was the case for the previous models for consistency reasons. They are shown in table 8.2. The surface area of the circular thermal platform is given as equivalent square dimensions for practical reasons. In the FEM simulations, these heat capacities were used with a scaling factor of $K_C^{FEM} = 6$ (see equation 5.33) being applied, as it was found to fit the corresponding measurement results for the 16A and the 4A models.

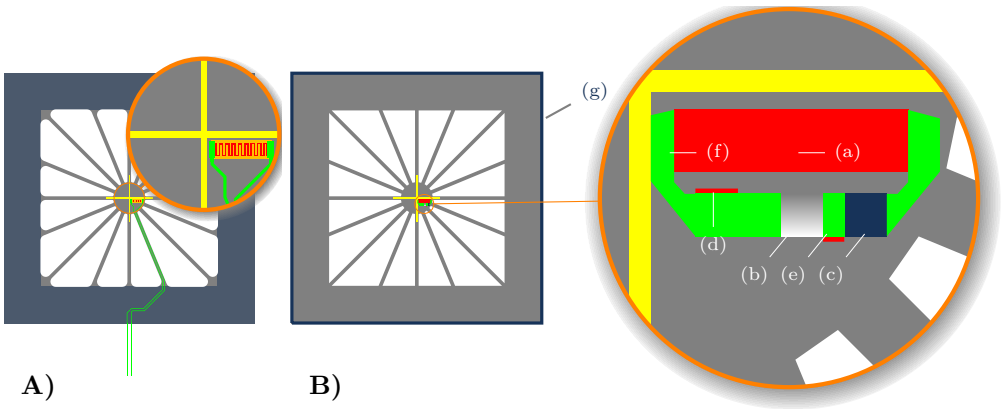

Figure 8.5: A) 1A TES with an uncovered thermistor area of 100 µm × 25 µm equipped with SP and normal conducting comb structures on top of the thermistors. B) Geometry of the FEM model used to simulate the behavior of the 1A TES. To improve the performance of the simulations, the spider leg structure is slightly simplified compared to fabricated TES. SP and comb structures are included only as heat capacity components into the thermistor. Superconducting wiring is omitted as it does not significantly contribute to the total heat capacity. The magnification on the right shows the electrical circuit that allows for a realistic modeling. It includes the thermistor (a), the shunt resistor (b), R_L (c) and the current nodes (d), (e) on the wiring (f). The blue frame (g) at the outer edge of the TES marks the thermal bath which is kept at the fixed temperature T_{bath}.

Table 8.1: Geometry parameters of the 1A design. Due to the non-rectangular shape of the platform, equivalent values were used for length and width that keep the surface area unchanged.

component	number	height [m]	length [m]	width [m]	total volume [m^3]
platform	1	$1{\cdot}10^{-6}$	$2.66{\cdot}10^{-4}$	$2.66{\cdot}10^{-4}$	$7.08{\cdot}10^{-14}$
thermistor	1	$1.08{\cdot}10^{-7}$	$1.1{\cdot}10^{-4}$	$2.9{\cdot}10^{-5}$	$3.45{\cdot}10^{-16}$
dipole	2	$2.1{\cdot}10^{-8}$	$4.3{\cdot}10^{-4}$	$1{\cdot}10^{-5}$	$1.81{\cdot}10^{-16}$
wiring	2	$1.5{\cdot}10^{-7}$	$1.5{\cdot}10^{-4}$	$6{\cdot}10^{-6}$	$2.7{\cdot}10^{-16}$
SP	2	$1{\cdot}10^{-7}$	$1.14{\cdot}10^{-4}$	$4{\cdot}10^{-6}$	$9.12{\cdot}10^{-17}$
comb	16	$1{\cdot}10^{-7}$	$2.1{\cdot}10^{-5}$	$2{\cdot}10^{-6}$	$6.72{\cdot}10^{-17}$

Table 8.2: Heat capacities of the 1A design based on the values given in table 4.1 and the geometry shown in table 8.1. The electron contribution of Mo is multiplied by 2.43 to reflect the effect of the superconducting transition.

component	C_{AuPd} $[\mathrm{J\,K^{-1}}]$	C_{Mo} $[\mathrm{J\,K^{-1}}]$	$C_{\mathrm{Si_3N_4}}$ $[\mathrm{J\,K^{-1}}]$	C_{Nb} $[\mathrm{J\,K^{-1}}]$	C_{total} $[\mathrm{J\,K^{-1}}]$
platform	0	0	$7.21 \cdot 10^{-15}$	0	$7.21 \cdot 10^{-15}$
thermistor	$7.42 \cdot 10^{-15}$	$9.78{\cdot}10^{-14}$	0	0	$1.05 \cdot 10^{-13}$
dipole	$5.55 \cdot 10^{-14}$	0	0	0	$5.55 \cdot 10^{-14}$
wiring	0	0	0	$3.98 \cdot 10^{-16}$	$3.98 \cdot 10^{-16}$
SP	$2.8 \cdot 10^{-14}$	0	0	0	$2.8 \cdot 10^{-14}$
comb	$2.07 \cdot 10^{-14}$	0	0	0	$2.07 \cdot 10^{-14}$
sum	$1.12 \cdot 10^{-13}$	$9.78{\cdot}10^{-14}$	$7.21 \cdot 10^{-15}$	$3.98 \cdot 10^{-16}$	$2.17 \cdot 10^{-13}$

The resulting total heat capacity C_{tot}^{1A} can be used in combination with the thermal conductance G^{1A} to calculate the thermal time constant as it is predicted by the lumped model as

$$\tau_0 = \frac{C_{tot}^{1A}}{G^{1A}} \tag{8.3}$$

An *I-I* curve was simulated without background radiation load to determine the Joule heating power. By combining equations 4.12, 4.38 and 4.39 to

$$G = G_0 \cdot T^n = \frac{n+1}{T} \cdot \frac{P_{el}}{1 - \left(\frac{T_{bath}}{T}\right)^{n+1}} \tag{8.4}$$

$$T = T_c + \Delta T_c \tag{8.5}$$

the thermal conductance G was calculated, resulting in

$$G \approx 1.7 \times 10^{-9}\,\mathrm{W\,K^{-1}} \tag{8.6}$$

which is about 44 % of the 4A value. The resulting calculated lumped model thermal time constant is

$$\tau_0^{lumped} = 130\,\mu\mathrm{s} \tag{8.7}$$

which is approx. 62 % of the corresponding 4A value. If the scaling of the heat capacity

is taken into account as $K_C^{FEM} = 6$, the thermal time constant increases to

$$\tau_0^{lumped,C\times 6} = 780\,\mu s \tag{8.8}$$

Similar to the 4A design, the thermistor contributes approximately half of the heat capacity of the thermal platform. However, if SP and comb structure are added to the thermistor as they are strongly thermally coupled to the latter, this increases to about 71 % (65 % for 4A including SP). in addition, due to the very close location of the thermistor to the absorber a stronger decoupling of these components can be expected for the 1A model, as far as the effect of the thermal conductance of the platform is concerned. To quantify this coupling and to separate it from boundary effects, an FEM model was created assuming ideal boundaries. Its results will be compared to measurement data, which allows to assign effects to the influence of the design geometry and to properties of the boundaries.

As the contribution of the wiring to the total heat capacity of the thermal platform is only approximately 0.2 % (see table 8.2), it is ignored in the simulation. As for the 4A model, the SP are taken into account as they provide about 13 % of the total heat capacity. Also the comb structure, which adds another 10 %, was included. A simplified electrical circuit containing all the relevant components was placed on the membrane in the near vicinity of the thermistor, as shown in figure 8.5. This circuit is identical to the one used for the 16A and the 4A model to ensure the comparability and does not contribute to joule heating, heat capacity and thermal conductance except from the thermistor. Only to fit the dimensions of the platform and the thermistor, it was completely scaled down by a factor of two, leaving all electrical properties unchanged. The additional SP and comb structures was included into the heat capacity of the thermistor without a geometric representation, as its close location to the thermistor and the small structures otherwise would significantly increase the simulation computing time, while no difference in the resulting TES behavior could be expected.

8.4.1 Temperature distribution and efficiency

A FEM simulation with a constant bias in the working range was performed to determine the temperature distribution on the platform. The resulting temperature distribution for $T_{bath} = 402\,mK$ is presented on the left in figure 8.6. As can be seen from the sub-figure on the right, the temperature gradient on the platform is strongly reduced compared to the 16A and 4A results: The maximum temperature difference on the platform is approximately 13 % of $T_c - T_{bath}$, while it was 46 % for the 16A TES and 42 % for 4A. Hence, the 1A model achieves a significantly better thermal homogeneity compared to the previous designs.

The Joule heating power difference ΔP_{el} between simulations with and without back-

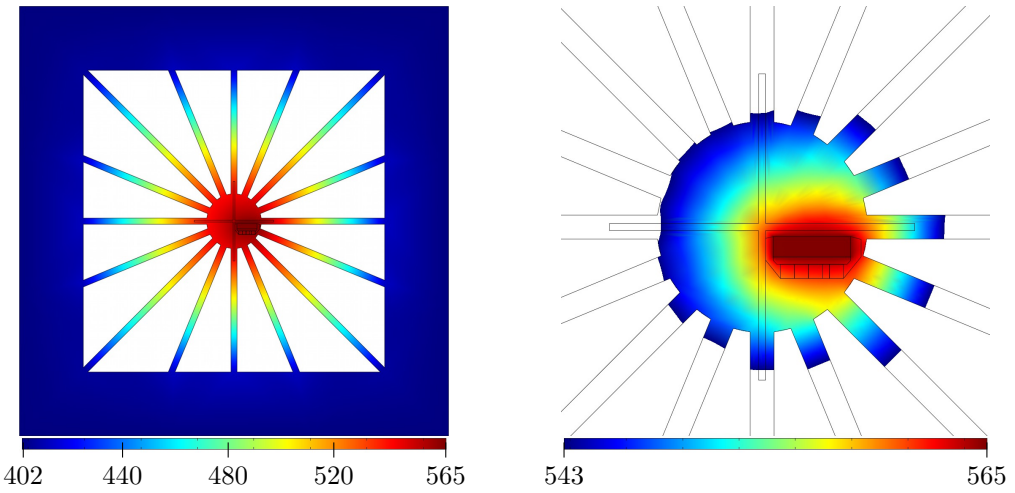

Figure 8.6: Left: Temperature distribution of the 1A comsol model in the transition range for $T_{bath} = 402\,\mathrm{mK}$ and $T_c = 564\,\mathrm{mK}$ under a background radiation power load of $P_{rad} \approx 36\,\mathrm{pW}$. The color scale marks the temperature levels in mK.
Right: A limited temperature range was used to visualize the gradient on the platform.

ground radiation, respectively, was adjusted to match the same value of

$$\Delta P_{el} = 3.2 \times 10^{-11}\,\mathrm{W} \tag{8.9}$$

as for the other models, to achieve comparable conditions. This was realized by scaling the total radiation power appropriately, which resulted in a value of

$$P_{rad}^{abs} \approx 3.6 \times 10^{-11}\,\mathrm{W} \tag{8.10}$$

corresponding to the intrinsic power efficiency of the 1A model of

$$\eta_{abs}^{1A} = \frac{\Delta P_{el}}{P_{rad}^{abs}} \approx 89\,\% \tag{8.11}$$

which is significantly higher than the values for the 16A design of 67 % and for the 4A design (70 %), in accordance with the reduced temperature gradient.

The bandwidth dependent overall efficiency of the 1A TES can be calculated by combining this efficiency with the coupling efficiency found in section 8.3, which results in

$$\eta_{TES}^{1A} = \eta_{EM}^{1A} \cdot \eta_{abs}^{1A} \approx 63\,\% \tag{8.12}$$

for an optical bandwidth of $\Delta\nu_{opt} = 40\,\mathrm{GHz}$, which is even above the results for the 16A TES (48 %) and the 4A TES (49 %).

For a bandwidth of $\Delta\nu_{opt} = 100\,\mathrm{GHz}$, still

$$\eta_{TES}^{1A} = \eta_{EM}^{1A} \cdot \eta_{abs}^{1A} \approx 60\,\% \tag{8.13}$$

can be achieved.

8.4.2 Time constants

To simulate the time dependent behavior of the TES, the same setup as described in section 5.2.6 was used: A rectangular signal was added to the background radiation power. To achieve consistent results, the same ratio of the signal amplitude to the applied background load was chosen as for the other simulations, which is 4.3 % as calculated in section 1.3. This resulted in a maximum signal difference at the thermistor of $(\Delta P_{sig})_{max} = 1.4 \times 10^{-12}\,\mathrm{W}$ as for the other models. The necessary amplitude at the absorber was

$$\delta P_{rad} = \frac{(\Delta P_{sig})_{max}}{\eta_{abs}^{1A}} \approx 1.5 \times 10^{-12}\,\mathrm{W} \tag{8.14}$$

A series of simulations was used to determine the effective time constant of the 1A TES. The left graph of figure 8.7 shows the resulting time constants referred to the bias current, and the *I-I* curve as reference. While in general the current response δI_{th} was used to determine the time constants, for values of I_{bias} close to or in the normal conducting range, the temperature response δT_{th} was used to approximate the time constants instead, as δI_{th} becomes very small in this range and finally fully vanishes once the normal resistance is reached, as discussed in detail in section 5.2.6.

The resulting thermal time constant τ_0 of

$$\tau_0^{FEM} \approx 773\,\mu\mathrm{s} \tag{8.15}$$

is marked in the figure by a dashed horizontal line. It is very close to the lumped model value derived from the total heat capacity and the thermal conductance of 780 µs (see equation 8.8), the difference is approx. 1 %.

The corresponding value of η_{τ_0}, is

$$\eta_{\tau_0}^{1A} = \frac{\tau_0^{FEM}}{\tau_0^{lumped,C\times 6}} \approx 99\,\% \tag{8.16}$$

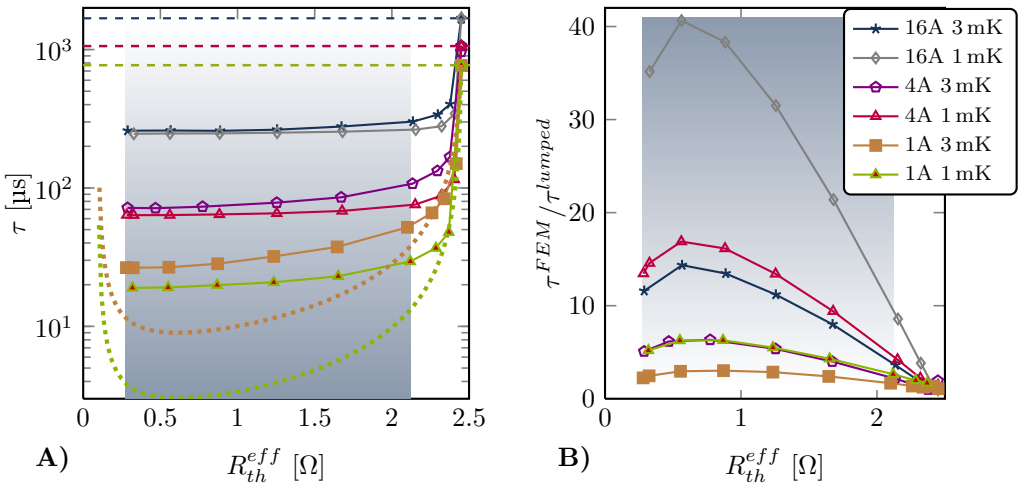

Figure 8.7: A) Time constants versus thermistor resistance. The symbols (legend in B) mark the FEM results. The thermal time constant levels are marked by dashed horizontal lines. The dotted lines represent the lumped model predictions for the 1A TES. B) The time constant ratio of FEM results and lumped model predictions is plotted versus the thermistor resistance. The same working range (shaded) as in figure 6.8 is evaluated (A and B).

compared to 84 % and 64 % for the 4A and the 16A model, respectively. As the deviation of these time constants results from the deviation of the model from the ideal lumped structure, the high value for the 1A model confirms its improved compliance with the lumped model.

Despite this better matching to the lumped model predictions, within most of the transition range, the course of the simulated effective time constants of the 1A TES still shows significantly smaller variations than predicted by the lumped model, as it was the case for the 16A and 4A design, though the mismatch is decreased. In the shaded area of figure 8.7, the simulated time constants vary from 27 µs to 52 µs for $\Delta T_c = 3\,\mathrm{mK}$, which corresponds to a rise by 96 % with respect to the minimum value. In the same range, the lumped model predicts a rise by 245 % from 9.0 µs to 31 µs. For $\Delta T_c = 1\,\mathrm{mK}$ the variation of the simulation results is still smaller: The values range from 19 µs to 29 µs, which corresponds to an increase by 55 % referred to the minimum value. The associated lumped model predicts a rise by 268 % from 3.0 µs to 11 µs.

Obviously, there is still a considerable mismatch of the absolute values of the minima between lumped model and simulation (cf. table 8.3). While the predicted minimum values differ by a factor of 3 for the used transition widths, the simulation results in a ratio of 1.4. While the tendency is obvious (the values for 16A and 4A are 1.05 and 1.1, respectively), still a limitation of the lower limit of the time constants can be observed, which can not be explained by the lumped model. As the FEM model is set up with ideal

Table 8.3: Comparison of the time constant characteristic of the 1A, 4A and the 16A models based on simulations ("FEM") and lumped model calculations ("lumped"). The used symbols are defined in section 6.3.2.

design	ΔT_c	τ_{min}^{FEM}	$\frac{\tau_0^{FEM}}{\tau_{min}^{FEM}}$	ϱ^{FEM}	τ_{min}^{lumped}	ϱ^{lumped}	$\frac{\varrho^{lumped}}{\varrho^{FEM}}$	$\frac{\tau_{min}^{FEM}}{\tau_{min}^{lumped}}$
1A	3 mK	27 µs	29	96 %	9 µs	250 %	2.6	2.9
1A	1 mK	19 µs	41	55 %	3 µs	270 %	4.9	6.3
4A	3 mK	71 µs	15	50 %	11 µs	340 %	6.8	6.3
4A	1 mK	64 µs	17	19 %	3.8 µs	380 %	20	17
16A	3 mK	259 µs	6.4	16 %	18 µs	420 %	26	14
16A	1 mK	246 µs	6.7	7.3 %	6.1 µs	380 %	52	41

interfaces, this difference has to be attributed to the still not ideal thermal coupling on the platform due to the extended geometry, similar to the 16A and 4A designs. Nevertheless, the improved coupling manifests itself in the considerably lower absolute limit of the time constants that is achieved in the 1A model compared to the previous models. The better matching can also be found in the ratio of the time constant values of the lumped model and the simulation, respectively, as visualized in figure 8.7 B).

For each transition width, the time constants of the 1A model are closer to the predictions of lumped model than the 4A values. The difference becomes even more evident in comparison to the 16A values.

Also the general course of the time constants affirms this improvement: While the predicted relative rise of the time constants ϱ^{lumped} (see equation 6.19) in the marked area results in similar values for all designs and both transition widths as can be seen from column ϱ^{lumped} in table 8.3, the corresponding rise in the simulated data, represented by ϱ^{FEM} as defined in equation 6.20 shows a substantial variation, which is also reflected by the ratio of ϱ^{lumped} to ϱ^{FEM} (column $\frac{\varrho^{lumped}}{\varrho^{FEM}}$). In general, for each transition width, this ratio is significantly smaller for the 1A model compared to the 4A model, which again shows smaller values than the 16A TES. This again confirms the smaller deviation from the lumped model for the 1A design.

8.5 Measurements

For verification of the simulation results, 1A TES were fabricated as described in section 3.1.1. The used design is shown in figure 8.5. For isolating the effect of the comb structure in this design, also a bare variant without comb structures was fabricated, called 1Ab in the following. In the simulations discussed above, the same parameters were assumed as for the 4A and 16A design. Hence, for best comparability and to exclude effects resulting from different production conditions, the compared TES were fabricated on

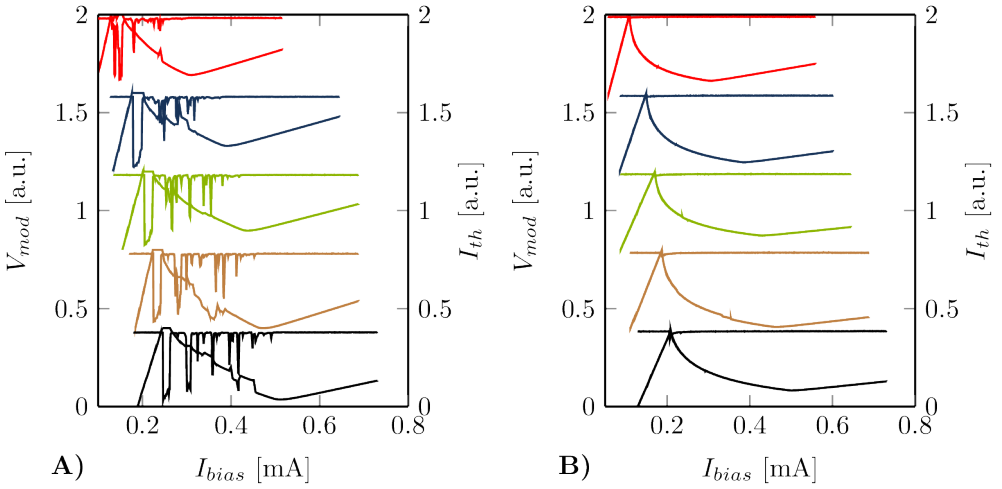

Figure 8.8: M-*I* curves combined with the corresponding *I*-*I* curves for the 1A and 1Ab design at different bath temperatures (from top to bottom: 502 mK, 462 mK, 432 mK, 402 mK, 362 mK). The curves are shifted in y direction for better visualization. A) 1Ab: Without comb structures on the thermistor. B) 1A: With comb structures.

the same wafer. The corresponding measurements are discussed and compared to the simulation results in this section.

V-*T* measurements as described in section 4.3.2 were used to determine the *R*-*T* characteristic of the 4A TES. This resulted in $T_c = 561$ mK for 1Ab without comb structure and $T_c = 548$ mK for 1A with comb structure. With respect to the found reproducibility of approx. ± 1 mK within the same cool down cycle for each T_c value, the result of 1Ab is nearly identical to the result of the 16A (564 mK) and the 4A (565 mK) TES. With comb structure, the reduction of T_c amounted to 3 %. The transition width in both cases was approx. (2 ± 1) mK. Hence, no significant lateral T_c variation throughout the thermistor is caused by the comb structure.

The 1Ab TES showed strong DORs for all measured temperature levels in the lower transition and for lower temperatures even throughout the whole transition range, as can be seen in figure 8.8 A). The number and strength of the DORs vastly exceeds the effects observed for the 4AEL TES, and is even significantly stronger than for the 4A TES, despite the small platform and reduced thermal conductance of the spider leg structure due to the small thermistor area (see section 7.3). In contrast, the 1A TES with comb structures showed only weak DORs throughout the transition range, as shown in figure 8.8 B). They did mainly become noticeable by a slightly increased noise level, while the modulation amplitude of the SQUID was unaffected. This stresses the necessity of the comb structures for this design, as they allow to operate the TES in the whole transition

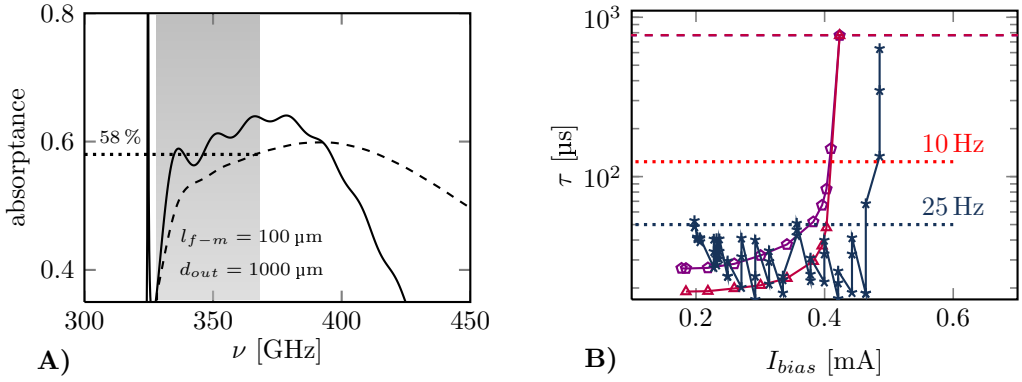

Figure 8.9: A) Electro-magnetic simulation of the 1A-model using the feedhorn configuration of the 4A TES. The absorptance $A(\nu_{opt})$ is plotted as a solid line, its average $\bar{A}$ in the interval from the cutoff frequency of the feedhorn antenna to the respective frequency ν_{opt} as a dashed line. B) Measured time constants for the 1A TES (stars) compared to the FEM simulation results for $\Delta T_c = 3\,\mathrm{mK}$ (pentagons) and $\Delta T_c = 1\,\mathrm{mK}$ (triangles). Lines are added to guide the eye. The dashed lines mark τ_0 resulting from the simulations, the dotted lines mark the 50 µs and 124 µs levels which are required for frame rates of 10 Hz and 25 Hz, respectively.

range and hence facilitating the operation of arrays in common working points.

The measurements on 1A TES were performed with the same feedhorn configurations as for the 4A design. Hence, a reduced sensitivity had to be expected, as predicted by the corresponding electro-magnetic FIT simulation. The result is shown in figure 8.9 A), which corresponds to an expected radiation power of $3.4 \times 10^{-11}\,\mathrm{W}$. However, the measured received radiation power of $7 \times 10^{-12}\,\mathrm{W}$ significantly went below this value. First FIT simulations including the superconducting wiring suggested a strong influence of the exact wiring location and length on the TES membrane due to the closeness to the center of the radiation lobe and its large relative coverage of the platform surface compared to the absorber. The promising possibility to freely vary the location and direction of the wiring on the membrane and to attach appropriately designed stub filters offers many degrees of freedom[101]. Hence, this can be expected to lead to a solution that involves an absorptance that is close to the value predicted in section 8.3. However, this requires extensive simulations that go beyond the scope of this thesis. As these adjustments are not expected to influence other properties of the TES due to the low thermal conductance and heat capacity of the wiring, further measurements on the unchanged 1A TES were performed to verify the general applicability of the 1A design as a future TES design for the THz video camera that allows to increase the working range while achieving the necessary time constants.

Measurements with a rectangular radiation signal were performed to determine the step response of the TES. The same setup and evaluation method as described in section

4.3.5 was used to identify the time constants to ensure comparability of the results for the different designs. The results are presented in figure 8.9 B).

In agreement with the simulation results, the measured time constants exhibit a fast drop in the uppermost transition range. A shift of this drop referred to the bias current compared to the simulation results can be observed in figure 8.9. This is due to the reduced optical radiation load, which is compensated for by Joule heating. Below this drop, the measured time constants cover the range of

$$\tau^{meas} = (35 \pm 15)\,\mu\text{s} \tag{8.17}$$

The high relative variation of the measurement data is due to the time constants approaching to the limits of the measurement setup (see section 4.3.5). The measurement data nicely fits in the range of the simulation results between $\Delta T_c = 1\,\text{mK}$ and $\Delta T_c = 3\,\text{mK}$, Though it does not follow the trend of continuous reduction of the time constants for decreasing bias current. Instead, at low bias currents, even a slight increase of the values can be observed, indicating a decoupling of the thermistor similar to the observations in the 4AEL TES. However, for the 1A TES this effect is weaker and the time constants do not exceed 50 µs, which allows to fully achieve the sampling requirements defined in section 7.4.1 and hence the required optical resolution without smearing effects. This suggests that also for this design, the idealized FEM model still allows good general predictions, while for fitting the exact trend throughout the transition range, it comes to its limits as boundary effects become relevant.

The direct comparison of the time constants to the results for the 4A TES shown in equation 6.23 reveals a scaling factor of

$$\chi_{4A}^{1A} = \frac{\tau^{4A}}{\tau^{1A}} \approx 2 \tag{8.18}$$

Hence, the time constant level could be further improved by the 1A design, while achieving a strongly reduced level of DORs.

To predict the achievable sensitivity, the parameters found above were compared to noise measurements. Due to the reduced sensitivity, the measured noise without background load, which will be called "blind noise" in the following, was used to model the noise under different load conditions. The necessary electrical bandwidth is given by the need to sample 256 rows per frame and 25 fps:

$$\Delta\nu_{el}^{1A} = \frac{1}{2} \cdot f_{sample} = \frac{256 \cdot 25}{2} = 3200\,\text{Hz} \tag{8.19}$$

The measured blind noise base level in this bandwidth was $2.2 \times 10^{-16}\,\text{W}\,\text{Hz}^{1/2}$. Using equation 4.60, the photon noise was calculated to achieve the total noise level. In case of the optical bandwidth of 40 GHz as used in the testing setup, for the reduced effective background load of 7 pW at the thermistor as measured for the 1A TES this resulted

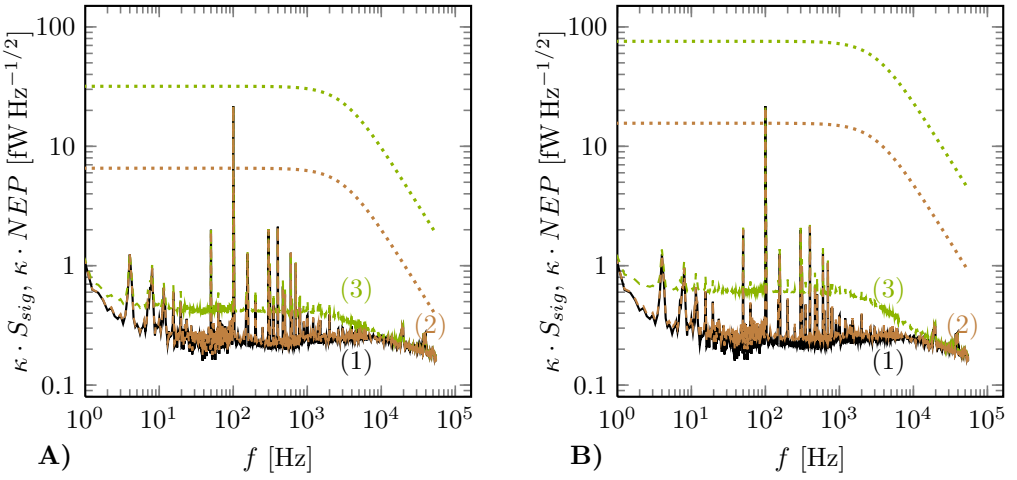

Figure 8.10: Measured NEP of 1A with background radiation load from 0.4 K (1) combined with the optical signal power spectral density S_{sig}^{max} (dotted lines for 10 Hz (red) and 25 Hz (blue) frame rate). A) For $\Delta\nu_{opt} = 40$ GHz, the calculated NEP for background radiation loads of 7 pW (2) and 41 pW (3) are shown. B) $\Delta\nu_{opt} = 100$ GHz, the calculated NEP for background radiation loads of 7 pW (2) and 39 pW (3) are shown. All graphs are scaled by $\kappa(\omega_{el})$.

in a total noise level of 2.3×10^{-16} W Hz$^{1/2}$. As discussed above, by optimizing the superconducting wiring of the TES higher optical efficiencies are probable. Hence, also the noise level for the aspired efficiency as predicted by the simulation in section 8.4.1 was calculated. For the corresponding effective background radiation load of 41 pW, the total noise level amounts to 4.2×10^{-16} W Hz$^{1/2}$. The different noise levels are plotted in figure 8.10. In addition, the signal power spectral density S_{sig}^{max} is shown. Using the maximum signal difference of approx 4.3 % of the effective background load ΔP_{el} as defined in section 1.3, it is calculated as given in equation 4.69 by

$$S_{sig}^{max} = 0.043 \cdot \frac{\Delta P_{el}}{\sqrt{\Delta\nu_{el}}} \tag{8.20}$$

This results in a signal to noise ratio of

$$SNR = \frac{S_{sig}^{max}}{NEP} \tag{8.21}$$

with

$$SNR^{1A}_{40\,\mathrm{GHz},reduced} = 28 \tag{8.22}$$

which equals 4.8 bit at 25 fps for the reduced effective background load. At the aspired efficiency, the 1A TES will achieve

$$SNR^{1A}_{40\,\mathrm{GHz},max} = 76 \tag{8.23}$$

corresponding to 6.3 bit at 25 fps.

The larger bandwidth of the demonstrator of 100 GHz further increases the resulting SNRs due to the linear dependency of the signal compared to the square root dependency of the photon noise. Hence, this results in

$$SNR^{1A}_{100\,\mathrm{GHz},reduced} = 67 \tag{8.24}$$

which equals 6.1 bit at 25 fps for the reduced effective background load. At the aspired efficiency, the 1A TES will achieve

$$SNR^{1A}_{100\,\mathrm{GHz},max} = 137 \tag{8.25}$$

which equals 7.1 bit at 25 fps. While the results for the current wiring scheme are not yet satisfactory for the THz camera, the aspired improved efficiency will lead to similar SNRs as achieved by the 4AEL TES, while DORs are further reduced and the time constants significantly reduced throughout the whole working range. Therefore, the 1A TES is a promising candidate for future camera systems.

References

[1] *Summary of the White House Review of the December 25, 2009 Attempted Terrorist Attack*. http://www.whitehouse.gov/sites/default/files/summary_of_wh_review_12-25-09.pdf (see p. 9).

[2] http://www.rapiscansystems.com/en/products/ps/productsrapiscan_secure_1000_dual_pose (see p. 9).

[3] *Röntgenverordnung - RöV*. http://www.bfs.de/de/bfs/recht/rsh/volltext/1A_Atomrecht/1A_14_RoeV_1011.pdf (see p. 9).

[4] *Commission Implementing Regulation (EU) No 1147/2011 of 11 November 2011 amending Regulation (EU) No 185/2010 implementing the common basic standards on civil aviation security as regards the use of security scanners at EU airports*. http://eur-lex.europa.eu/LexUriServ/LexUriServ.do?uri=OJ:L:2011:294:0007:0011:EN:PDF (see p. 9).

[5] *ACLU Backgrounder on Body Scanners and "Virtual Strip Searches"*. http://www.aclu.org/technology-and-liberty/aclu-backgrounder-body-scanners-and-virtual-strip-searches. Jan. 2010 (see p. 9).

[6] 112th Congress of the USA. *FAA Modernization and Reform Act Of 2012*. www.gpo.gov/fdsys/pkg/CRPT-112hrpt381/pdf/CRPT-112hrpt381.pdf (see p. 9).

[7] *Italian airport security axing body scanners*. http://www.euronews.com/2010/09/23/italian-airport-security-axing-body-scanners (see p. 9).

[8] R. Appleby. "Passive Millimetre Wave Imaging what it can and cannot do". In: *International Forum on Terahertz Spectroscopy and Imaging*. 2006. (See p. 10).

[9] *TSA Takes Next Steps to Further Enhance Passenger Privacy*. http://www.tsa.gov/press/releases/2011/0720.shtm (see p. 10).

[10] W. S. Holland et al. "SCUBA-2: the 10 000 pixel bolometer camera on the James Clerk Maxwell Telescope". *Monthly Notices of the Royal Astronomical Society* 430, pp. 2513–2533, 2013. DOI: 10.1093/mnras/sts612. (See pp. 10, 23).

[11] A. Rogalski and F. Sizov. "Terahertz detectors and focal plane arrays". *Opto-electronics Review* 19, 346–404, 2011. DOI: 10.2478/s1177201100333. (See p. 11).

[12] C. Baker, T. Lo, W. R. Tribe, B. E. Cole, M. R. Hogbin, and M. C. Kemp. "Detection of Concealed Explosives at a Distance Using Terahertz Technology". *Proceedings of the IEEE* 95, pp. 1559–1565, 2007. (See p. 11).

[13] *Recommendation V.431-7 (05/00): Nomenclature Of The Frequency And Wavelength Bands Used In Telecommunications*. English. http://www.itu.int/dms_pubrec/itu-r/rec/v/R-REC-V.431-7-200005-I!!PDF-E.pdf. Iternational Telecommunication Union (ITU), May 2000 (see p. 12).

[14] E. Heinz, T. May, D. Born, G. Zieger, A. Brömel, S. Anders, V. Zakosarenko, T. Krause, A. Krüger, M. Schulz, F. Bauer, and H.-G. Meyer. "Development of passive submillimeter-wave video imaging systems for security applications". In: *Millimetre Wave and Terahertz Sensors and Technology V*. Ed. by Neil A. Salmon and Eddie L. Jacobs. Vol. 8544. Proc. of SPIE. 2012. P. 854402. DOI: 10.1117/12.976849. (See p. 12).

[15] J. E. Bjarnason, T. L. J. Chan, A. W. M. Lee, M. A. Celis, and E. R. Brown. "Millimeter-wave, terahertz, and mid-infrared transmission through common clothing". *Applied Physics Letters* 85, pp. 519–521, 2004. (See p. 12).

[16] R. Appleby and H. B. Wallace. "Standoff detection of weapons and contraband in the 100 GHz to 1 THz region". *Ieee Transactions On Antennas and Propagation* 55, pp. 2944–2956, 2007. DOI: 10.1109/TAP.2007.908543. (See pp. 12, 14, 146).

[17] K.E Peiponen, J. A. Zeitler, and M. Kuwata-Gonokami, eds. *Terahertz Spectroscopy and Imaging*. Vol. 171. Springer Series in Optical Sciences. Springer, 2013. (See p. 12).

[18] R. Appleby. "Passive millimetre-wave imaging and how it differs from terahertz imaging". *Philosophical Transactions of the Royal Society of London Series A-mathematical Physical and Engineering Sciences* 362, pp. 379–392, 2004. DOI: 10.1098/rsta.2003.1323. (See p. 12).

[19] J. Xu, K. W. Plaxco, and S. J. Allen. "Absorption spectra of liquid water and aqueous buffers between 0.3 and 3.72 THz". *The Journal Of Chemical Physics* 124, p. 036101, 2006. DOI: 10.1063/1.2151267. (See p. 13).

[20] S.I. Alekseev, A.A. Radzievsky, and M.C. Logani M.K. ANDZiskin. "Millimeter-Wave Dosimetry of Human Skin". *Bioelectromagnetics* 29 Center for Biomedical Physics,Temple UniversityMedical School, Philadelphia, Pennsylvania, pp. 65–70, 2008. (See pp. 14, 146).

[21] X. Xin, H. Altan, A. Saint, D. Matten, and R. R. Alfano. "Terahertz absorption spectrum of para and ortho water vapors at different humidities at room temperature". *Journal Of Applied Physics* 100, p. 094905, 2006. DOI: 10.1063/1.2357412. (See p. 14).

[22] S. Paine. *am Atmospheric Model*. https://www.cfa.harvard.edu/~spaine/am/. 2013 (see pp. 16, 145, 163).

[23] E. Hecht. *Optik*. 3rd ed. Oldenbourg Wissenschaftsverlag, 2001. (See p. 20).

[24] F. Sizov and A. Rogalski. "THz detectors". *Progress in Quantum Electronics* 34, pp. 278 –347, 2010. DOI: http://dx.doi.org/10.1016/j.pquantelec.2010.06.002. (See pp. 22, 23).

[25] M. O. Reese. "Superconducting Hot Electron Bolometers for Terahertz Sensing". PhD thesis. Yale University, 2006. (See p. 22).

[26] C. Wang, G. Thummes, and C. Heiden. "A two-stage pulse tube cooler operating below 4 K". *Cryogenics* 37, pp. 159–164, 1997. DOI: 10.1016/S0011-2275(96)00112-9. (See p. 22).

[27] *TransMIT GmbH*. www.transmit.de (see p. 22).

[28] *Chase Research Cryogenics Ltd.* http://www.chasecryogenics.com/ (see p. 22).

[29] W. B. Lewis. "Fluctuations In Streams of Thermal Radiation". *Proceedings of the Physical Society of London* 59, pp. 34–40, 1947. DOI: 10.1088/0959-5309/59/1/307. (See p. 23).

[30] E. Heinz, T. May, D. Born, G. Zieger, K. Peiselt, A. Brömel, S. Anders, V. Zakosarenko, T. Krause, A. Krüger, M. Schulz, and H.-G. Meyer. "Development of passive submillimeter-wave video imaging systems". In: *Passive and Active Millimeter-Wave Imaging XVI*. Ed. by David A. Wikner and Arttu R. Luukanen. Vol. 8715. Proc. of SPIE. 2013. 87150E. DOI: 10.1117/12.2018848. (See p. 23).

[31] University Corporation for Atmospheric Research High Altitude Observatory. *Samuel P. Langley*. http://www.hao.ucar.edu/education/bios/langley.php. 2013 (see p. 24).

[32] H. Lindner, H. Brauer, and C. Lehmann. *Taschenbuch der Elektrotechnik und Elektronik*. 7th ed. Fachbuchverlag Leipzig, 1999. (See p. 26).

[33] D. H. Andrews, W. F. Brucksch, W. T. Ziegler, and E. R. Blanchard. "Attenuated Superconductors I. For Measuring Infra-Red Radiation". *Review of Scientific Instruments* 13 Issue 7 ; http://dx.doi.org/10.1063/1.1770037 (12 pages), p. 281, 1942. DOI: 10.1063/1.1770037. (See p. 27).

[34] Johns Hopkins University. *Notes on Ms. 443 Andrews Family Papers*. http://old.library.jhu.edu/collections/specialcollections/manuscripts/msregisters/ms443.html. 2011 (see p. 27).

[35] P. L. Richards. "Bolometers For Infrared And Millimeter Waves". *Journal Of Applied Physics* 76, pp. 1–24, 1994. (See p. 27).

[36] J. Clarke, G. I. Hoffer, P. L. Richards, and N.-H. Yeh. "Superconductive bolometers for submillimeter wavelengths". *Journal of Applied Physics* 48, pp. 4865–4879, 1977. DOI: 10.1063/1.323612. (See p. 28).

[37] K. D. Irwin. "An Application Of Electrothermal Feedback For High-Resolution Cryogenic Particle-Detection". *Applied Physics Letters* 66, pp. 1998–2000, 1995. (See p. 28).

[38] M. D. Niemack et al. "A kilopixel array of TES bolometers for ACT: Development, testing, and first light". *Journal of Low Temperature Physics* 151, pp. 690–696, 2008. DOI: 10.1007/s10909-008-9729-2. (See p. 28).

[39] D. Bintley, M. MacIntosh, W. Holland, J. Dempsey, P. Friberg, H. Thomas, P. Ade, R. Sudiwala, K. Irwin, G. Hilton, M. Niemack, M. Amiri, E. Chapin, and M. Halpern. "Commissioning SCUBA-2 at JCMT and Optimising the Performance of the Superconducting TES Arrays". *Journal of Low Temperature Physics* 167, pp. 152–160, 2012. DOI: 10.1007/s10909-012-0601-z. (See p. 28).

[40] J. E. Carlstrom et al. "The 10 Meter South Pole Telescope". *Publications of the Astronomical Society of the Pacific* 123, pp. 568–581, 2011. DOI: 10.1086/659879. (See pp. 28, 134).

[41] S. Anders, T. May, V. Zakosarenko, K. Peiselt, E. Heinz, M. Starkloff, G. Zieger, E. Kreysa, G. Siringo, and H. G. Meyer. "Cryogenic bolometers for astronomical observations in the sub-mm range". *Microelectronic Engineering* 88, pp. 2205–2207, 2011. DOI: 10.1016/j.mee.2010.11.010. (See pp. 28, 41).

[42] M. D. Audley et al. "SCUBA-2: A large-format TES array for submillimetre astronomy". *Nuclear Instruments & Methods In Physics Research Section A-Accelerators Spectrometers Detectors And Associated Equipment* 520, pp. 479–482, 2004. (See pp. 28, 134).

[43] A. T. Lee, P. L. Richards, S. W. Nam, B. Cabrera, and K. D. Irwin. "A superconducting bolometer with strong electrothermal feedback". *Applied Physics Letters* 69, pp. 1801–1803, 1996. (See p. 29).

[44] S. F. Lee, J. M. Gildemeister, W. Holmes, A. T. Lee, and P. L. Richards. "Voltage-biased superconducting transition-edge bolometer with strong electrothermal feedback operated at 370 mK". *Applied Optics* 37, pp. 3391–3397, 1998. (See pp. 29, 80, 81).

[45] M. Seifart. *Analoge Schaltungen*. 5th ed. Verlag Technik Berlin, 1996. (See p. 30).

[46] Jan Mathias Gildemeister. "Voltage-Biased Superconducting Bolometers for Infrared and mm-Waves". PhD thesis. University of California, Berkeley, 2000. (See p. 36).

[47] *Supracon AG*. http://supracon.com (see p. 37).

[48] John Clarke and Alex I. Braginski, eds. *The SQUID Handbook*. WILEY-VCH, 2004. (See pp. 37, 150, 153).

[49] T. May, V. Zakosarenko, R. Boucher, E. Kreysa, and H.-G. Meyer. "Superconducting bolometer array with SQUID readout for submillimetre wavelength detection". *Superconductor Science and Technology* 16, p. 1430, 2003. (See p. 39).

[50] Giorgio Siringo et al. "A New Facility Receiver on APEX: The Submillimetre APEX Bolometer Camera, SABOCA". *the messenger (ESO)*, pp. 20–23, 2010. (See p. 39).

[51] T. May, S. Anders, V. Zakosarenko, M. Starkloff, H.-G. Meyer, G. Thorwirth, E. Kreysa, and N. Jethava. "A Superconducting Terahertz Imager". *IEEE/CSC & ESAS European Superconductivity News Forum* No. 1, 2007. (See p. 39).

[52] T. May, G. Zieger, S. Anders, V. Zakosarenko, M. Starkloff, H.-G. Meyer, G. Thorwirth, and E. Kreysa. "Passive stand-off Terahertz imaging with 1 Hertz frame rate". *Proceedings Of The Society Of Photo-optical Instrumentation Engineers (SPIE)* 6949 Terahertz For Military and Security Applications VI, 2008. DOI: 10.1117/12.777952. (See p. 39).

[53] Solveig Anders, Torsten May, Viatcheslav Zakosarenko, Michael Starkloff, Gabriel Zieger, and Hans-Georg Meyer. "Structured SiN membranes as platform for cryogenic bolometers". *Microelectronic Engineering* 86, pp. 913–915, 2009. (See p. 39).

[54] H. Meissner. "Superconductivity of Contacts With Interposed Barriers". *Physical Review* 117, pp. 672–680, 1960. DOI: 10.1103/PhysRev.117.672. (See pp. 41, 53).

[55] R. Holm and W. Meissner. "Messungen mit Hilfe von flüssigem Helium". *Zeitschrift fur Physik* 74 Berlin. Issue 11-12 ISSN 0939-7922, pp. 715–735, 1932. (See p. 41).

[56] *Ragnar Holm*. http://www.nad.riksarkivet.se/sbl/Presentation.aspx?id=13718 (see p. 41).

[57] *Walther Meißner*. http://www.av.ph.tum.de/Bios/WMeissner.php (see p. 41).

[58] L. Fabrega, A. Camon, I. Fernandez-Martinez, J. Sese, M. Parra-Borderias, O. Gil, R. Gonzalez-Arrabal, J.L. Costa-Krämer, and F. a Briones. "Size and dimensionality effects in superconducting Mo thin films". *Superconductor Science & Technology (SuST)* 24, 2011. (See p. 41).

[59] A. L. Woodcraft et al. "Electrical and optical measurements on the first SCUBA-2 prototype 1280 pixel submillimeter superconducting bolometer array RID B-9108-2009". *Review of Scientific Instruments* 78, p. 024502, 2007. DOI: 10.1063/1.2436839. (See p. 41).

[60] M. Kenyon, P. K. Day, C. M. Bradford, J. J. Bock, and H. G. Leduc. "Background-limited membrane-isolated TES bolometers for far-IR/submillimeter direct-detection spectroscopy". *Nuclear Instruments & Methods In Physics Research Section A-accelerators Spectrometers Detectors and Associated Equipment* 559, pp. 456–458, 2006. DOI: 10.1016/j.nima.2005.12.036. (See p. 41).

[61] C. Hollerith, B. Simmnacher, R. Weiland, F. Von Feilitzsch, C. Isaila, J. Jochum, W. Potzel, J. Hohne, K. Phelan, D. Wernicke, and T. May. "Energy calibration of superconducting transition edge sensors for x-ray detection using pulse analysis". *Review of Scientific Instruments* 77, p. 053105, 2006. DOI: 10.1063/1.2202911. (See p. 42).

[62] T. May, G. Zieger, S. Anders, V. Zakosarenko, H.-G. Meyer, M. Schubert, M. Starkloff, M. Rößler, G. Thorwirth, and U. Krause. "Safe VISITOR: VISible, Infrared and Terahertz Object Recognition for security screening applications". *Proc. SPIE* 7309, 2009. (See p. 42).

[63] R. Boucher, T. May, T. Wagner, V. Zakosarenko, S. Anders, and H. G. Mayer. "Structural and electrical properties of AuPd/Mo bi-layer films for transition edge sensors". *Superconductor Science & Technology* 19, pp. 138–142, 2006. (See p. 42).

[64] Ge Wu. "Analyse und Optimierung von ebenen frequenzselektiven Flächen". PhD thesis. Bergische Unversität Wuppertal, 2007. (See pp. 43, 59, 114, 116, 174).

[65] Gabriel Zieger, Solveig Anders, Harijanto Bone, Jan Dellith, Detlef Born, Torsten May, and Hans-Georg Meyer. "Degradation in molybdenum thin films and Mo/AuPd bilayers and its reduction by sidewall passivation". *Superconductor Science & Technology*, 2012. DOI: doi:10.1088/0953-2048/25/12/125005. (See p. 46).

[66] S.J.B. Reed. *Electron Microprobe Analysis*. Cambridge University Press, 1997. (See p. 47).

[67] Joseph R. Davis. *Heat-resistant materials*. ASM International. ISBN 0871705966. Russell Township, Geauga County, Ohio: ASM International, 1997. Pp. 361–365. (See p. 49).

[68] L. De Rosa, C.R. Tomachuk, J. Springer, D. B. Mitton, S. Saiello, and F. Bellucci. "The wet corrosion of mobybdenum thin film - Part I: Behavior at 25∘C". *Materials and Corrosion* 55, pp. 602–609, 2004. (See p. 49).

[69] H. Oikawa. "Ellipsometric Investigation of Corrosion of Deposited Thin Molybdenum Film". *Japanese Journal of Applied Physics* 14, pp. 629–635, 1975. (See p. 49).

[70] R. Boucher, T. Wagner, S. Anders, T. May, and H. G. Meyer. "Disorder control of TC in thin film Mo". *Superconductor Science & Technology* 24, p. 035031, 2011. (See p. 51).

[71] J. M. Martinis, G. C. Hilton, K. D. Irwin, and D. A. Wollman. "Calculation of T-c in a normal-superconductor bilayer using the microscopic-based Usadel theory". *Nuclear Instruments & Methods In Physics Research Section A-accelerators Spectrometers Detectors and Associated Equipment* 444 Technol Fdn; European Space Technol Ctr; Space Res Org Netherlands Volume 444, Issues 1–2, 7 April 2000, Pages 23–27, pp. 23–27, 2000. DOI: 10.1016/S0168-9002(99)01320-0. (See p. 53).

[72] G. Brammertz, A. A. Golubov, P. Verhoeve, R. den Hartog, A. Peacock, and H. Rogalla. "Critical temperature of superconducting bilayers: Theory and experiment". *Applied Physics Letters* 80, pp. 2955–2957, 2002. DOI: 10.1063/1.1470712. (See p. 53).

[73] L. Fabrega, I. Fernandez-Martinez, M. Parra-Borderias, O. Gil, A. Camon, R. Gonzalez-Arrabal, J. Sese, J. Santiso, J.-L. Costa-Kraemer, and F. Briones. "Effects of Stress and Morphology on the Resistivity and Critical Temperature of Room-Temperature-Sputtered Mo Thin Films". *Ieee Transactions On Applied Superconductivity* 19, pp. 3779–3785, 2009. DOI: 10.1109/TASC.2009.2027609. (See p. 53).

[74] G. C. Hilton, J. M. Martinis, K. D. Irwin, N. F. Bergren, D. A. Wollman, M. E. Huber, S. Deiker, and S. W. Nam. "Microfabricated transition-edge x-ray detectors". *Ieee Transactions On Applied Superconductivity* 11, pp. 739–742, 2001. DOI: 10.1109/77.919451. (See p. 54).

[75] Ch. Kittel. *Einführung in die Festkörperphysik*. 13th ed. Oldenbourg Wissenschaftsverlag GmbH, 2002. (See pp. 61, 62).

[76] Frank Pobell. *Matter and Methods at Low Temperatures*. 3rd ed. Springer-Verlag, 2007. (See pp. 60–62, 67, 156).

[77] C. A. Bryant and P. H. Keesom. "Low Temperature Specific Heat of Molybdenum". *J. Chem. Phys. 35, ; doi:10.1063/1.1701213 (2 pages) — Cited 2 times* 35, pp. 1149–50, 1961. (See p. 61).

[78] B.M. Boerstoel, J. J. Zwart, and J. Hansen. "Specific Heat of Palladium, Platinum,gold and Copper Below 30k". *Physica* 54, pp. 442–&, 1971. DOI: 10.1016/0031-8914(71)90189-3. (See p. 61).

[79] M. Winter. *webelements.com*. www.webelements.com (see p. 61).

[80] W. Holmes, J. M. Gildemeister, P. L. Richards, and V. Kotsubo. "Measurements of thermal transport in low stress silicon nitride films". *Applied Physics Letters* 72 zitat jethava, pp. 2250–2252, 1998. (See pp. 61, 66, 67, 101).

[81] Ch. Enss and S. Hunklinger. *Tieftemperaturphysik*. Springer-Verlag, 2000. (See p. 62).

[82] J. Bardeen, L. N. Cooper, and J. R. Schrieffer. "Theory of Superconductivity". *Phys. Rev.* 108, pp. 1175–1204, 1957. DOI: 10.1103/PhysRev.108.1175. (See p. 62).

[83] Werner Buckel and Reinhold Kleiner. *Supraleitung - Grundlagen und Anwendungen*. 6. Wiley-VCH, 2004. (See p. 62).

[84] H. F. C. Hoevers, M. L. Ridder, A. Germeau, M. P. Bruijn, P. A. J. de Korte, and R. J. Wiegerink. "Radiative ballistic phonon transport in silicon-nitride membranes at low temperatures". *Applied Physics Letters* 86, p. 251903, 2005. (See p. 66).

[85] H. F. C. Hoevers. "Thermal physics of transition edge sensor arrays". *Nuclear Instruments & Methods In Physics Research Section A-accelerators Spectrometers Detectors and Associated Equipment* 559, pp. 702–705, 2006. DOI: 10.1016/j.nima.2005.12.109. (See p. 66).

[86] W. Wasserbach. "Phonon Dislocation Scattering and Low-temperature Lattice Thermal-conductivity of Niobium and Tantalum Single-crystals Deformed At Low-temperatures". *Physica Status Solidi B-basic Research* 128, pp. 453–466, 1985. DOI: 10.1002/pssb.2221280210. (See p. 67).

[87] G. Ventura and L. Risegari. *The Art of Cryogenics - Low-Temperature Experimental Techniques*. Elsevier, 2008. (See pp. 67, 78).

[88] *Agilent Technologies, Inc.* http://www.agilent.com (see pp. 76, 82).

[89] *Virginia Diodes, Inc. (VDI).* http://vadiodes.com/ (see p. 76).

[90] *Tektronix, Inc.* http://www.tek.com (see p. 76).

[91] *National Instruments Corporation*. http://www.ni.com (see p. 76).

[92] I. J. Maasilta. "Complex impedance, responsivity and noise of transition-edge sensors: Analytical solutions for two- and three-block thermal models". *Aip Advances* 2, p. 042110, 2012. DOI: 10.1063/1.4759111. (See pp. 78, 93, 103, 132, 150, 155, 158, 171).

[93] J. N. Ullom, W. B. Doriese, G. C. Hilton, J. A. Beall, S. Deiker, W. D. Duncan, L. Ferreira, K. D. Irwin, C. D. Reintsema, and L. R. Vale. "Characterization and reduction of unexplained noise in superconducting transition-edge sensors". *Applied Physics Letters* 84, pp. 4206–4208, 2004. DOI: 10.1063/1.1753058. (See pp. 80, 84, 153, 171, 172).

[94] K. M. Kinnunen, M. R. J. Palosaari, and I. J. Maasilta. "Normal metal-superconductor decoupling as a source of thermal fluctuation noise in transition-edge sensors". *Journal of Applied Physics* 112, p. 034515, 2012. DOI: 10.1063/1.4745908. (See pp. 80, 84, 155, 172).

[95] P. Khosropanah, R. A. Hijmering, M. Ridder, M. A. Lindeman, L. Gottardi, M. Bruijn, J. van der Kuur, P. A. J. de Korte, J. R. Gao, and H. Hoevers. "Distributed TES Model for Designing Low Noise Bolometers Approaching SAFARI Instrument Requirements". *Journal of Low Temperature Physics* 167, 2012. DOI: 10.1007/s10909-012-0550-6. (See pp. 80, 84).

[96] Massimiliano Galeazzi. "Fundamental Noise Processes in TES Devices". *IEEE Transactions on Applied Superconductivity (preprint)*, 2010. (See pp. 80, 84).

[97] J. C. Mather. "Bolometer Noise - Non-Equilibrium Theory". *Applied Optics* 21, pp. 1125–1129, 1982. (See p. 81).

[98] J. Zmuidzinas. "Thermal noise and correlations in photon detection". *Applied Optics* 42, pp. 4989–5008, 2003. (See p. 81).

[99] J. Hubmayr et al. "Stability of Al-Mn Transition Edge Sensors for Frequency Domain Multiplexing". *Ieee Transactions On Applied Superconductivity* 21, pp. 203–206, 2011. DOI: 10.1109/TASC.2010.2090630. (See pp. 84, 155, 156, 171).

[100] *CST microwave studio*. http://www.cst.com/Content/Products/MWS/Overview.aspx (see p. 89).

[101] M. Kummer. *Grundlagen der Mikrowellentechnik*. 2nd ed. ISBN 3-341-00687-7. VEB Verlag Technik Berlin, 1989. (See pp. 89, 91, 183).

[102] COMSOL Inc. *COMSOL Multiphysics*. http://www.comsol.com/ (see p. 93).

[103] Comsol AB. *Comsol Multiphysics user's guide*. 2006. (See p. 96).

[104] J. W. Fowler et al. "Optical design of the atacama cosmology telescope and the millimeter bolometric array camera". *Applied Optics* 46, pp. 3444–3454, 2007. DOI: 10.1364/AO.46.003444. (See p. 134).

[105] E. Kreysa, J. W. Beeman, and E. E. Haller. "Micromachined Bolometer-Arrays with Silicon-Nitride Membranes". *Submillimetre and Far-Infrared Space Instrumentation, Proceedings of the 30th ESLAB Symposium held in Noordwijk, 24-26 September 1996. Edited by E.J. Rolfe and G. Pilbratt. ESA SP-388. Paris: European Space Agency, 1996., p.111*, 1996. (See p. 134).

[106] J. F. Johansson. "Fundamental Limits for Focal-Plane Array Efficiency". *Astronomical Society of the Pacific Conference Series: Multi-Feed Systems for Radio Telescopes*. 75 Workshop held in Tucson, Arizona, May 16-18, 1994. Editors, Darrel T. Emerson John M. Payne; Publisher, Astronomical Society of the Pacific, San Francisco, California, 1995. LC 1994. 0-937707-94-5., p.34, p. 34, 1995. (See p. 134).

[107] T. May. "Molybdenum-gold/palladium transition edge sensors for sub-millimetre wave instruments in astronomy and security". PhD thesis. Technische Universität Berlin, 2014. (See p. 134).

[108] R. Gonzalez and R. Woods. *Digital image processing*. 2nd ed. Prentice Hall Press, 2002. (See pp. 135, 166).

[109] Prof. Dr. Horst Stöcker, ed. *Taschenbuch der Physik*. 4th ed. Verlag Harri Deutsch, 2000. (See p. 136).

[110] M. J. Griffin, J. J. Bock, and W. K. Gear. "Relative performance of filled and feedhorn-coupled focal-plane architectures". *Applied Optics* 41, pp. 6543–6554, 2002. (See pp. 139, 140).

[111] E. Heinz, T. May, D. Born, G. Zieger, S. Anders, G. Thorwirth, V. Zakosarenko, M. Schubert, T. Krause, M. Starkloff, A. Krüger, M. Schulz, F. Bauer, and H.-G. Meyer. "Passive Submillimeter-wave Stand-off Video Camera for Security Applications". *Journal of Infrared, Millimeter and Terahertz Waves* 31, pp. 1355–1369, 2010. (See p. 146).

[112] R. H. Koch, V. Foglietti, J. R. Rozen, K. G. Stawiasz, M. B. Ketchen, D. K. Lathrop, J. Z. Sun, and W. J. Gallagher. "Effects of Radio-frequency Radiation On the DC Squid". *Applied Physics Letters* 65, pp. 100–102, 1994. DOI: 10.1063/1.113046. (See p. 150).

[113] Martin Podt. “Wideband Low-noise Integrated SQUID Systems”. PhD thesis. University of Twente, 2003. (See p. 150).

[114] M. A. Lindeman, S. Bandler, R. P. Brekosky, J. A. Chervenak, E. Figueroa-Feliciano, F. M. Finkbeiner, T. Saab, and C. K. Stahle. “Characterization and reduction of noise in Mo/Au transition edge sensors RID A-6258-2010”. *Nuclear Instruments & Methods In Physics Research Section A-accelerators Spectrometers Detectors and Associated Equipment* 520, pp. 348–350, 2004. DOI: 10.1016/j.nima.2003.11.264. (See pp. 153, 171).

[115] M. A. Lindeman et al. “Percolation model of excess electrical noise in transition-edge sensors”. *Nuclear Instruments & Methods In Physics Research Section A-accelerators Spectrometers Detectors and Associated Equipment* 559, pp. 715–717, 2006. DOI: 10.1016/j.nima.2005.12.114. (See pp. 153, 172).

[116] A. Luukanen, K. M. Kinnunen, A. K. Nuottajarvi, H. F. C. Hoevers, W. M. B. Tiest, and J. P. Pekola. “Fluctuation-limited noise in a superconducting transition-edge sensor”. *Physical Review Letters* 90, p. 238306, 2003. DOI: 10.1103/PhysRevLett.90.238306. (See p. 158).

[117] C. E. Shannon. “Communication In the Presence of Noise”. *Proceedings of the Institute of Radio Engineers* 37, pp. 10–21, 1949. DOI: 10.1109/JRPROC.1949.232969. (See p. 160).

[118] *Eccosorb®*. http://www.eccosorb.eu/products/eccosorb (see pp. 165, 166).

[119] J. G. Staguhn, S. H. Moseley, B. J. Benford, C. A. Allen, J. A. Chervenak, T. R. Stevenson, and W. T. Hsieh. “Approaching the fundamental noise limit in Mo/Au TES bolometers with transverse normal metal bars”. *Nuclear Instruments & Methods In Physics Research Section A-accelerators Spectrometers Detectors and Associated Equipment* 520, pp. 336–339, 2004. DOI: 10.1016/j.nima.2003.11.261. (See p. 171).

[120] Kile-team. *kile*. http://kile.sourceforge.net/ (see p. 210).

[121] M. Kohm. *KOMA-script documentation*. http://www.komascript.de, (see p. 210).

[122] *PGF*. http://sourceforge.net/projects/pgf/ (see p. 210).

[123] *gnuplot* (see p. 210).

[124] E. Ressler. *sketch*. (See p. 210).

[125] JabRef Development Team. *JabRef*. http://jabref.sf.net, 2013. (See p. 210).

[126] *biblatex*. http://www.khirevich.com/latex/biblatex/ (see p. 210).

[127] *debian*. http://debian.org (see p. 210).

Summary

Security screenings currently undergo fundamental changes. While the established combination of metal detectors and pat down searches was commonly used for years without substantial changes, in the last years a strong demand for expanded detection capabilities came up. This led to the recent development of new screening methods, like x-ray backscattering or microwave cabin scanners. While they could demonstrate detection capabilities with respect to different materials that went beyond the capabilities of metal detectors, they did not solve the problem of delays which occur due to the intense screenings for example in mass transportation. Additionally, they provoked a new discussion, as these methods imply the creation of images with the impression of nakedness. Also the active irradiation of the human body, though in relatively small doses, caused widespread irritation and unsettledness.

Therefore, a different approach was taken at IPHT. To combine the advances of expanded detection capabilities with a fast and flexible screening method and to avoid irradiation and the exposure of intimate details of the body, a concept for a passive terahertz camera was developed. Its general prerequisites are discussed in chapter 1. It involves the use of highly sensitive sensors, which are the subject of this thesis. The general properties, requirements and the applicability of superconducting transition edge sensors in bolometric mode is addressed in chapter 2. The common lumped model is introduced, which is used to predict the behavior of an ideal TES and referred to in the following chapters for comparison to measurements and simulation results.

Starting from an initial TES design, the so-called 16A design, which was used in a still very limited single pixel demonstrator, reasons for varying and unstable properties of the used TES were investigated in chapter 3. By performing analyses of the degradation process of the materials in the bilayer of the thermistor, its sensitivity to humidity and water in general could be classified. Molybdenum (Mo), which is used as superconducting material in the thermistor of the TES, was examined in a long-term study concerning the influence of water on its oxidation level, including effects of physical destruction. The results were compared to the found effects on bilayers of Mo and an alloy of gold and palladium (AuPd) which are used as a proximity system to tune the critical temperature of the thermistor to the desired working temperature. While a general effect of protection of the Mo by the covering AuPd layer could be observed, it also showed effects of physical destruction even after short exposition to water in case of defects in the AuPd layer, while pure Mo was only slightly affected after comparable exposition. In addition, effects of the oxidation process on the superconductivity parameters of the thermistors were determined. In this regard, strong effects on the critical temperature and the transition

width could be found even for states of low oxidation, which caused increased parameter variation. By applying sidewall passivation to the bilayer, this effect could be reduced strongly enough to ensure the applicability of the TES in multi-sensor arrays and stability also in the case of long term use.

A comprehensive characterization of the initial TES design in chapter 4 resulted in substantial differences to the predictions of the lumped model concerning the course and the absolute values of the time constants with respect to the working point. To analyze the reasons for this deviation and to be able to predict the results for adjusted designs, appropriate FEM models were introduced and discussed in chapter 5. By using a model with ideal boundaries it could be shown that even in the case of zero thermal boundary resistance, the initial TES design deviates strongly from the lumped model due to the distribution of the heat capacity resulting from its extended geometry and the corresponding finite coupling strength of the components on the membrane to the thermistor. By introducing a single scaling factor to the total heat capacity of the TES, the model could reproduce the measured behavior based on bulk values of the literature material parameters. The model also predicted a strong influence of the internal thermal conductance in the thermistor on instabilities of the TES, which occurred in the model as well as in measurements.

These FEM models were used to evaluate an improved design called 4A with reduced heat capacity and better thermal coupling of the absorbers to the thermistor. It could be shown that this redesign led to a significant reduction of the time constants by a factor of 3.6 while the same radiation coupling efficiency as with the 16A design could be achieved with adequately adjusted feedhorn antennas. The corresponding results are presented in chapter 6 in combination with measurements, that confirmed the simulation results.

Based on this improved TES redesign, a demonstrator of a terahertz camera was set up that is capable of taking images from up to 10 m distance at 10 fps. To conform to the need of keeping the system cost-efficient, the number of sensors was limited to 20. Still high quality imaging could be ensured due to an adapted array design that met the special demands of the used spiral scanning. Details about the array design, the demonstrator setup and the sensor performance in this system are presented in section 6.5. While still limited in the field of view to a disc of approx. 1 m diameter, it could be shown that moving images could be realized with the 4A TES design in this camera demonstrator. Images taken at 10 fps were used to illustrate the achieved detection capabilities.

However, this demonstrator also stressed the disadvantages resulting from operating ranges observed in the 16A and 4A designs that exhibited increased noise and instabilities of the readout circuit, which led to temporary, but unpredictable outages of sensors in the case of slight working point variations due to temperature fluctuations of the cooling stage. Especially with respect to larger arrays, this effect in these so called distorted operating ranges (DORs) plays a critical role. Hence, in chapter 7, these distortions are quantified for different TES designs. A found relation to the base area of the thermistor is described. It was used for a modified 4A design, called 4AEL, that allowed to significantly reduce the DORs. The time constants for this design changed

strongly dependent on the working point which limited the usable operating range for high frame rates. Nevertheless, time constants down to 50 µs could be achieved.

Using the 4AEL, an improved demonstrator was set up equipped with 64 TES. Due to the reduced DORs, simultaneous operation of all 64 sensors could be realized while temporary outages were strongly reduced compared to the previous demonstrator system. Therefore, it was possible to use a line scanner which allowed to produce images without redundancy. Frame rates up to 25 Hz could be demonstrated without significant loss in spatial resolution with this system, as presented in section 7.4.

Due to the time constant variation mentioned above the operating range of the 4AEL TES was limited in the case of high frame rates, which made individual biasing of the single sensors necessary. To overcome this restriction for future systems, a design called 1A was created that achieves low time constants throughout the whole operating range, which could be verified by simulations and measurements. By adding normal conducting comb structures to the surface, DORs could be further reduced. This combination allows for common biasing of larger numbers of sensors. While in first measurements presented in chapter 8 the optical coupling efficiency for this design was still reduced in comparison to the previously discussed designs, significant improvements can be expected by optimizing the electric wiring and adding matched filter structures. Electro-magnetic simulations predict an even higher optical coupling efficiency compared to the 16A and 4A designs if the intrinsic power efficiency of the TES is taken into account.

While the necessary optimization of the wiring of the 1A TES clearly goes beyond the scope of this work, the simulation results are promising concerning sensitivity, speed and stability, and the time constant measurements showed the great advantage of a wide operating range. Hence, after successful adjustment of the wiring these sensors will be suitable for the next demonstrator system which is under construction at the moment. It will scan a field of view of one times two meters and hence can map a person as a whole within one frame, at a frame rate of 25 Hz. The wide stable operating range of the 1A TES allows for common biasing and hence to increase the number of sensors to 128 without additional bias lines. Considering the results of section 7.4, stable video imaging with high detection capabilities and at a lateral resolution of approx. 2 cm from distances up to 20 m can be expected.

Samenvatting

Veiligheidscontroles ondergaan momenteel fundamentele veranderingen. De gebruikelijke combinatie van metaaldetectoren en aftasten werd zonder grote veranderingen jarenlang toegepast. In de afgelopen jaren onstond echter een sterke vraag naar uitgebreidere detectiemogelijkheden. Dit leidde tot de recente ontwikkeling van nieuwe screening methoden, die gebruik maken van röntgenstraling of millimetergolven. Hoewel deze methodes gevoelig zijn voor materialen die niet door metaaldetectoren herkend worden, hebben ze de vertragingen die optreden als gevolg van de intensieve screenings, zoals die bijvoorbeeld in massatransport optreden, niet opgelost. Bovendien ontstond een nieuwe discussie, doordat deze methoden de indruk wekken naaktbeelden te produceren. Ook de actieve bestraling van het menselijk lichaam, hoewel in relatief lage dosis, zorgde op grote schaal voor irritatie en onbehagen.

Om deze redenen werd aan het IPHT voor een andere aanpak gekozen. Er werd een passieve terahertzcamera ontwikkeld die een uitgebreide, snelle en flexibele opsporingsmogelijkheid zonder actieve bestraling en het zichtbaar maken van intieme details mogelijk maakt. De algemene vereisten aan zo'n systeem worden in hoofdstuk 1 besproken. Hierbij worden zeer gevoelige sensoren, die het onderwerp van dit proefschrift zijn, ingezet. De algemene eigenschappen, voorwaarden en de toepasbaarheid van deze supergeleidende transition edge sensoren in de bolometrische modus worden in hoofdstuk 2 behandeld. Het algemene lumped model, dat gebruikt wordt om het gedrag van een ideale TES te voorspellen, wordt geïntroduceerd en in de volgende hoofdstukken gebruikt voor het vergelijken van metingen met simulatieresultaten.

Uitgaande van een eerste TES ontwerp, het zogenaamde 16A ontwerp, dat werd ingezet in een nog zeer eenvoudige één-pixel demonstrator, werden de oorzaken voor de variërende en instabiele eigenschappen van de gebruikte TES in hoofdstuk 3 onderzocht. Door de analyse van de degradatie van de materialen in de bilaag van de thermistor, kon de gevoeligheid voor vocht en water in het algemeen worden bepaald. Molybdeen (Mo), dat als supergeleidend materiaal in de thermistor van de TES wordt gebruikt, werd in een lange-termijn studie onderzocht betreffende de invloed van water op zijn oxidatie en zijn fysische vernietiging. De resultaten werden vergeleken met de gevonden effecten op bilagen bestaande uit Mo en een legering van goud en palladium (AuPd), die worden gebruikt als een proximity systeem om de kritische temperatuur van de thermistor op de gewenste bedrijfstemperatuur in te stellen. Hoewel een algemene bescherming van de Mo-laag door de afdekkende AuPd-laag kon worden vastgesteld, werd ook deze combinatie na een korte blootstelling aan water, in het geval van defecten in de AuPd laag vernietigd en dan zelfs sneller dan zonder AuPd laag. Verder werd het effect van het

oxidatieproces op de supergeleidende parameters van de thermistors bepaald. Hierbij werden zelfs bij een lage oxidatiegraad grote veranderingen in de kritische temperatuur en de overgangsbreedte gevonden, met een grotere parameter variatie tot gevolg. Door het passieveren van de zijwanden van de bilaag kon dit effect zo sterk worden vermindert dat de TES in multisensor-arrays, ook in het geval van langdurig gebruik, ingezet kunnen worden.

Een uitgebreide karakterisiering van het oorspronkelijke TES ontwerp in hoofdstuk 4, resulteerde in wezenlijke verschillen met de voorspellingen van het lumped model betreffende het verloop en de absolute waarden van de tijdconstanten als functie van het werkpunt. In hoofdstuk 5 werden passende FEM modellen geïntroduceerd en besproken om deze afwijkingen te verklaren en het gedrag van aangepaste ontwerpen te kunnen voorspellen. Door het gebruik van een model met ideale grenzen kon worden aangetoond dat zelfs zonder thermische weerstand aan het grensvlak, het oorspronkelijke TES ontwerp sterk afwijkt van het lumped model. Dit wordt veroorzaakt door de lokale verschillen in de warmtecapaciteit op de chip en de bijbehorende begrenste koppelingssterkte van de componenten op het membraan aan de thermistor. Door de invoering van een schaalfactor voor de totale warmtecapaciteit van de TES, kon het model het gemeten gedrag, op basis van de literatuurwaarden van de bulk-materiaalparameters, reproduceren. Het model voorspelde eveneens een grote invloed van de thermische geleiding in de thermistor op instabiliteiten van de TES, die zowel in het model als bij de metingen optraden.

Deze FEM modellen werden gebruikt om een verbeterd ontwerp (het 4A ontwerp) met kleinere warmtecapaciteit en betere thermische koppeling van de absorber aan de thermistor te evalueren. Het nieuwe ontwerp leidde tot een duidelijke vermindering van de tijdconstanten met een factor 3,6 terwijl, met goed ingestelde hoornantennes, hetzelfde stralingskoppelingsrendement als bij het 16A ontwerp kon worden bereikt. De bijbehorende resultaten worden in hoofdstuk 6 in combinatie met metingen die de simulaties bevestigen, beschreven.

Op basis van het verbeterde TES ontwerp, werd een terahertzcamera demonstrator gebouwd die in staat is om beelden op maximaal 10m afstand met 10 fps te maken. Het aantal sensoren werd beperkt tot 20 om de systeemkosten te beperken. Desondanks kon een hoge beeldkwaliteit worden gegarandeerd door een aangepast array-ontwerp dat aan de bijzondere eisen van de gebruikte spiraalscanner voldoet. Het array-ontwerp, de demonstrator en de prestaties van de sensor in dit systeem worden in paragraaf 6.5 uitvoerig besproken. Met een beperkt beeldveld van ca. 1 m diameter, kon worden aangetoond dat met deze camera demonstrator bewegende beelden kunnen worden gerealiseerd met het 4A ontwerp. Opnames met 10 fps werden gebruikt om de bereikte detectiemogelijkheden te illustreren.

Deze demonstrator banadrukte echter ook dat bij de 16A en de 4A ontwerpen bij bepaalde instellingen een hoger ruisniveau en een slechtere stabiliteit optreden. Die leidde tot een tijdelijke, maar onvoorspelbare uitval van sensoren bij kleine veranderingen van deze instellingen, die weer door kleine temperatuurvariaties veroorzaakt werden. Vooral

voor grotere arrays speelt dit verschijnsel in deze zogenaamde distorted operating ranges (DORs) een cruciale rol. In hoofdstuk 7 worden daarom deze storingen gekwantifiseerd voor verschillende TES ontwerpen. Een beschrijving van de gevonden relatie tussen de oppervlakte van de thermistor en deze storingen werd gebruikt voor een verandert 4A ontwerp (4AEL), met een duidelijke verminderdering van de DORs. De tijdconstanten van dit ontwerp hingen sterk af van het werkpunt wat het bruikbare werkbereik voor hoge beeldsnelheden beperkt. Niettemin konden tijdconstanten van 50 µs worden bereikt.

Gebruik makend van het 4AEL ontwerp, werd een verbeterde demonstrator uitgerust met 64 TES gebouwd. Door de vermindering van de DORs, konden gelijktijdig alle 64 sensoren worden ingezet, terwijl in vergelijking met de vorige demonstrator de tijdelijke uitval van sensoren sterk verminderd was. Derhalve was het mogelijk om een lineare scanner te gebruiken voor het maken van beelden zonder redundantie. In paragraf 7.4 wordt getoond dat met dit systeem beeldsnelheden tot 25 Hz konden worden gerealiseerd zonder signicant verlies in ruimtelijke resolutie.

Door de eerder genoemde variatie van de tijdconstante was het werkgebied van de 4AEL TES voor hoge beeldsnelheden beperkt, wat het noodzakelijk maakte iedere sensor apart te biasen. Om voor toekomstige systemen deze beperking op te heffen, werd TES 1A, met kleine tijdconstanten in het hele werkgebied, ontworpen, wat door simulaties en metingen bevestigd werd. Door de toevoeging van normaal geleidende kamstructuren op het oppervlak, kon DORs verder worden verminderd. Deze combinatie maakt het mogelijk gemeenschappelijk grotere aantallen sensoren te biasen. Terwijl in eerte metingen, zoals gepresenteerd in hoofdstuk 8, het optische koppelingsrendement voor dit ontwerp nog verminderd was in vergelijking met de eerder besproken ontwerpen, kunnen significante verbeteringen worden verwacht door het perfectioneren van de elektrische bedrading en het toevoegen van aangepaste filters. Elektromagnetische simulaties voorspellen een nog hoger optisch koppelingsrendement vergeleken met de 16A en 4A ontwerpen, als rekening wordt gehouden met het interne koppelingsrendement van de TES.

Terwijl de noodzakelijke perfectionering van de bedrading van de 1A TES buiten de reikwijdte van dit proefschrift valt, zijn de simulatieresultaten veelbelovend betreffende gevoeligheid, snelheid en stabiliteit, en de bepaling van de tijdconstantes toonden het grote voordeel van een groot werkbereik. Na succesvolle aanpassing van de bedrading zijn deze sensoren geschikt voor het volgende demonstratorsysteem dat op dit moment gebouwd wordt. Dit zal met een framerate van 25 Hz een beeldveld van één bij twee meter scannen en daarmee een persoon kompleet kunnen afbeelden. Het grote stabiele werkbereik van de 1A TES maakt een gemeenschappelijke biasing en daarmee het vergroten van het aantal sensoren tot 128 zonder extra biasleidingen mogelijk. Gezien de resultaten in paragraaf 7.4, kunnnen stabiele video-opnames met goede detectiemogelijkheden bij een laterale resolutie van ca. 2 cm en afstanden tot 20 m worden verwacht.

List of Abbreviations

$\Delta\nu_{el}$ electrical bandwidth, see equation 4.63

$\Delta\nu_{opt}$ bandwidth of electromagnetic radiation

ΔT_c superconducting transition width, $\Delta T_c = T_c^{90} - T_c^{10}$

η_{τ_0} ratio of the thermal time constants of the FEM model and the lumped model, see equation 5.32

η_{abs} on-chip power efficiency of the TES, see equation 5.24

η_{EM} electromagnetic power efficiency of the TES, see equation 5.4

η_{TES} total power efficiency of the TES, $\eta_{TES} = \eta_{EM} \cdot \eta_{abs}$

κ $\equiv \kappa(\omega_{el}) = \frac{1}{\sqrt{1+\omega_{el}^2 \cdot \tau^2}}$, see equation 4.68

ν_{opt} frequency of electromagnetic radiation

ϕ_0 magnetic flux quantum, $\phi_0 = \frac{h}{2e}$

ψ_{th} scaling factor for k_{th} in FEM simulations, see equation 5.20

σ electrical conductivity

σ_{th}^{NC} electrical conductivity of the thermistor in the normal conducting state

θ_D Debye temperature, see section 4.3.1

$A(\nu_{opt})$ frequency dependent absorptance, see equation 5.2

C heat capacity, see section 4.3

c specific heat capacity, see section 4.3

c speed of light in vacuum, $c = 299\,792\,458\,\mathrm{m\,s^{-1}}$

c_{abs} specific heat capacity of the absorber, see equation 5.13

c_{mem} specific heat capacity of the membrane, see equation 5.14

c_{th} specific heat capacity of the thermistor, see equation 5.12

d_{AP} aperture diameter

d_{out} output diameter of the output cone of the feedhorn antenna, see figure 5.1

G thermal conductance, see equation 2.2

I-I curve $I_{th}(I_{bias})$: Current-current characteristic of the TES, see section 4.3.4

k thermal conductivity, see equation 4.9

k_{abs} thermal conductivity of the absorber, see equation 5.16

k_{abs}^{eff} effective thermal conductivity of the absorber including the subjacent membrane, see equation 5.19

K_C^{FEM} common scaling factor of the heat capacities in the FEM model with respect to the bulk literature values, see equation 5.33

k_{mem} thermal conductivity of the membrane, see equation 5.17

k_{mem}^0 temperature independent term of k_{mem}, see equation 5.17

k_{th} thermal conductivity of the thermistor, see equation 5.15

k_{th}^{eff} effective thermal conductivity of the thermistor including the subjacent membrane and a scaling factor, see equation 5.20

l^4He liquid helium-4

L_0 Lorentz constant, $L_0 = 2.443 \times 10^{-8}\,\mathrm{V^2\,K^{-2}}$

l_{f-m} distance between output cone opening of the feedhorn antenna and the averted Si_3N_4 membrane surface, see figure 5.1

$P_{bb}(T)$ Power emitted by a blackbody at the temperature T, see equation 1.2

R-T curve $R(T)$: resistance-temperature characteristic of the thermistor, see section 4.3.2

R_0 parasitic on-chip resistance in series with the thermistor, see section 2.4

r_{airy} radius of the airy disc, see equation 1.1

R_L readout resistance in series with the thermistor (outside of the chip), see section 2.4

r_{min} spatial resolution: minimum distance of two separable objects

R_n normal state resistance of a superconductor, just above the superconducting transition.

R_{sh} (ohmic resistance of the) shunt resistor, see section 2.4

S_{sig}^{max} signal power spectral density $S_{sig}^{max} = \frac{(\Delta P_{sig})_{max}}{\sqrt{\Delta\nu_{el}}}$

$SNR \equiv SNR_{max}$ (maximum) signal to noise ratio, see equations 1.31 and 4.70

T_{bath} fixed temperature of the thermal bath, see section 2.2

T_c critical temperature of a superconductor, $T_c = \frac{T_c^{90}+T_c^{10}}{2}$

T_c^{10} temperature in the superconductors transition with a resistance of 10 % of R_n

T_c^{90} temperature in the superconductors transition with a resistance of 90 % of R_n

V-T curve $V(T)$: Voltage-temperature characteristic of the thermistor, see section 4.3.2

$V_{SQUID} \equiv V_{SQUID}(\phi)$: transfer function of a SQUID, see equation 7.1

τ_0 thermal time constant, see equation 2.25

Si_3N_4 silicon nitride

fps frames per second

at% atomic percent: fraction of a certain type of atoms of the total amount of atoms

AuPd gold-palladium alloy of 50 at% each

DOR distorted operating range

EPMA energy dispersive electron probe micro-analyzer, see section 3.3.2

ETF electrothermal feedback

FEM finite element method

FIT finite integration technique

FOV field of view

IPHT Leibniz Institute of Photonic Technology in Jena, Germany

M-I curve modulation-current characteristic, see section 7.2

nETF negative electrothermal feedback

SP sidewall passivation

TES transition edge sensor(s), see section 2.3

THz terahertz (radiation), see section 1.2

Acknowledgements

Writing a Ph.D. thesis itself as well as the preceding work is not possible without the support of numerous people. I would like to thank everybody who was involved in this process. Your help is greatly appreciated!

First of all, I would like to thank Prof. Horst Rogalla and Prof. Hans-Georg Meyer for the opportunity to write this thesis and being my supervisors. I further want to thank Prof. Meyer for the chance to work in the productive atmosphere of his department of quantum detection at the IPHT in Jena on an exciting subject of practical relevance and for the uncomplicated access to a set of modern tools and techniques.

Thank you Torsten for the faith and the uncomplicated support which allowed me to realize this project.

And thanks to Marco, Detlef, Torsten and Erik as well as Anika, Katja, Sven, Oliver, Julia and many others for hours of discussions and ideas; Thomas, Simon and Detlef for deep insights into practical cryogenics.

Solveig and Sven I would like to thank for sharing their knowledge about many details of thin film technology and the fabrication of my samples, which also included the work of many others. So many thanks to Uwe, Wolfgang, Katrin, Steini, Dirk and everybody else in the clean room for your professional work, you keep things running!

Thanks to Jan and his colleagues for SEM and EPMA measurements and fruitful discussions. Further, my thanks go to Günter and Katja for answering many questions concerning optics and Anika for insights into optical filter technologies.

Thanks to Marco for help with electromagnetic simulations and practical assistance. Thank you, Matthias for helpful discussions about SQUIDs and Jürgen for assistance in the design of wafer masks. Special thanks go to Slava for having good ideas about just everything.

Many thanks to Hari and Norman for a lot of measurements and to Hari for many shared night shifts. Thank you Anja for sample separation and very good honey, Florian, Silke, Heike, Marion and Angelika for myriads of important little and not so little things. Thanks to Frank and the electronics group, especially Marco, André and Torsten for support in many ways concerning electronics and software. Thank you everybody in the workshop for uncomplicated help and professional realization of my constructions.

Thanks to Alex for interesting discussions about English grammar and Rob for translating the summary of this thesis into Dutch, as well as to everybody who was involved in proofreading.

And many thanks to all of you for your open and helpful manner. It is a pleasure to work with you!

Very special thanks go to my wife and the rest of family. You made me become who I am today and thus are the very basis of this work. Thank you for your support, your love and for just being there. Many thanks also to Markus, Martin, Marcus, Robert, Johanna, Nico and Matthias for being reliable friends.

This work was written in LaTeXusing kile[120]. Templates come from the KOMA-script[121], and plots and graphics were produced using pgf/tikz[122] and gnuplot[123], 3d graphics with sketch[124].

References were managed in Jabref[125] saved and displayed using BibTeXand biblatex[126]. All computer work is based Debian[127]. Thanks to the community!